Nanostructures in a ferritic and an oxide dispersion strengthened steel induced by dynamic plastic deformation

Zhang, Zhenbo; Pantleon, Wolfgang; Mishin, Oleg; Tao, Nairong

Publication date:
2015

Document Version
Publisher's PDF, also known as Version of record

Citation (APA):
Zhang, Z., Pantleon, W., Mishin, O., & Tao, N. (2015). Nanostructures in a ferritic and an oxide dispersion strengthened steel induced by dynamic plastic deformation. DTU Wind Energy. (DTU Wind Energy PhD; No. 0045(EN)).

Nanostructures in a ferritic and an oxide dispersion strengthened steel induced by dynamic plastic deformation

DTU Vindenergi
PhD Report2015

Zhenbo Zhang

DTU Wind Energy PhD-0045 (EN)

January 2015

DTU Vindenergi
Institut for Vindenergi

Author: Zhenbo Zhang

Title: Nanostructures in a ferritic and an oxide dispersion strengthened steel induced by dynamic plastic deformation

Department: Department of Wind Energy

Abstract

Nanostructured metals and alloys are expected to have much higher strength and better irradiation tolerance than their counterparts with a coarse-grained structure. Therefore, nanostructuring is suggested to be a promising approach to improve the properties of structural materials for advanced fission and fusion reactors. In this study, two candidate steels for nuclear reactors, namely a ferritic/martensitic steel (modified 9Cr-1Mo steel) and an oxide dispersion strengthened (ODS) ferritic steel (PM2000), were nanostructured by dynamic plastic deformation (DPD). The resulting microstructure was characterized in detail, and the annealing behavior regarding the thermal stability and microstructural response was investigated across several length scales by electron backscatter diffraction (EBSD), transmission electron microscopy (TEM), high resolution TEM (HRTEM), and scanning TEM (STEM).

A nanoscale lamellar structure with a ⟨100⟩+⟨111⟩ duplex fibre texture develops in both the modified 9Cr-1Mo steel and PM2000 during DPD to high strains. The strength is improved significantly, but the thermal stability is largely reduced. A very pronounced orientation dependent recovery and recrystallization take place, when both steels after DPD are annealed. Both oriented nucleation and oriented growth of ⟨111⟩ oriented lamellae are demonstrated to account for such an orientation dependence. The underlying mechanisms are discussed, including the differences in stored energy, structural variation, and recovery processes. Higher strain rates are demonstrated to be able to facilitate the structural refinement; nevertheless, the general annealing behavior resembles that of the material after deformation at low strain rate.

In addition to the microstructure of the matrix materials, the oxide nanoparticles in PM2000 were systematically investigated with respect to their structure in the as-received, substantially deformed and annealed material. The majority of oxide nanoparticles in PM2000 are orthorhombic YAlO$_3$ (YAP) and have a cuboid-on-cube orientation relationship with the ferrite matrix. Annealing at 1300 °C and above leads to considerable coarsening; the orientation relationship between YAP/Fe changes into a pseudo-cube-on-cube relationship. It is remarkable that YAP nanoparticles with diameters smaller than 20 nm are substantially deformed during DPD. The average equivalent strain of the YAP nanoparticles is about 1.2 estimated in the sample after DPD to a strain of 2.1. Mechanical twinning is found to be the dominant deformation mechanism for the YAP nanoparticles. Nanovoids are found to form at the YAP/Fe interface at low strain. With increasing strain, these nanovoids become closed around the smaller particles which are considerably deformed, whereas those voids associated with the undeformed, larger particles remain open. When a sample with substantially deformed YAP nanoparticles is annealed, the morphology of the deformed particles changes dramatically leading to the formation of much smaller YAP particles distributed in the ferrite matrix. These findings provide insight in the strengthening mechanism and ductility of ODS steels, and, most importantly, open a novel approach to refine oxide nanoparticles in ODS steels by a combination of thermomechanical treatments.

DTU Wind Energy PhD-0045 (EN)
January 2015

Project period:

2011.10-2015.01

Education:

Doctor of Philosophy

Supervisors:

Wolfgang Pantleon
Oleg V. Mishin
Nairong Tao

Project No.:

44530

Sponsorship:

Sino Danish Center for Education and Research

Pages: 196

Referencer: 219

ISBN: 978-87-93278-27-1

Danmarks Tekniske Universitet
DTU Vindenergi
Nils Koppels Allé
Bygning 403
2800 Kgs. Lyngby
Telefon

www.vindenergi.dtu.dk

Nanostructures in a ferritic and an oxide dispersion strengthened steel induced by dynamic plastic deformation

Zhenbo Zhang

A thesis submitted in fulfillment of the requirements
for the degree of Doctor of Philosophy
Technical University of Denmark, 2015

Department of Wind Energy
Technical University of Denmark
Denmark

Preface

This thesis is submitted in partial fulfillment of the requirements for the PhD degree at the Technical University of Denmark. The project was funded by the Sino-Danish Center for Education and Reseach and carried out within the Section for Materials Science and Advanced Characterization, Department of Wind Energy, under the supervision of Assoc. Prof. Dr. Wolfgang Pantleon (Department of Mechanical Engineering, DTU), Dr. Oleg V. Mishin (Department of Wind Energy, DTU), and Dr. Nairong Tao (Institute of Metal Research, Chinese Academy of Science). This study was conducted during the period from October 2011 to January 2015.

Zhenbo Zhang

January 2015

List of publications

Z.B. Zhang, O.V. Mishin, W. Pantleon, Compression behavior of a ferritic-martensitic Cr-Mo steel, in: S. Fæster, et al. (Eds.), Proc. of the 33rd Risø International Symposium on Materials Science: Nanometals, DTU, Roskilde, 2012, 423-430.

Z.B.Zhang, O.V. Mishin, N.R. Tao, W. Pantleon, Nanoscale lamellae in an oxide dispersion strengthened steel processed by dynamic plastic deformation. *IOP: Mater. Sci. Eng.*2014 (63) 012065

Z.B. Zhang, O.V. Mishin, N.R. Tao, W. Pantleon, Evolution of oxide nanoparticles during dynamic plastic deformation of ODS steel, in: S. Fæster, et al. (Eds.), Proc. of the 35th Risø International Symposium on Materials Science: New Frontiers of Nanometals, DTU, Roskilde, 2014, 423-430.

Z.B.Zhang, O.V. Mishin, N.R. Tao, W. Pantleon, Effect of dynamic plastic deformation on the microstructure and annealing behavior of a modified 9Cr-1Mo steel. *Mater. Sci. Technol.*2015 (31) 715-721

Z.B. Zhang, O.V. Mishin, N.R. Tao, W. Pantleon, Microstructure and annealing behavior of 9Cr-1Mo steel after dynamic plastic deformation to different strains. *J. Nucl. Mater.* 2015(458) 64-69

Z.B. Zhang, Y.B. Zhang, O.V. Mishin, N. R. Tao, W. Pantleon, D. Juul. Jensen, Orientation dependent recrystallization behavior of nanostructured 9Cr-1Mo steel. *In preparation*

Acknowledgement

Foremost, I wish to express my gratitude to Drs. Wolfgang Pantleon and Oleg V. Mishin, who have supervised this work and provided me with constant support and many inspiring discussions. I am also thankful to my co-supervisor, Dr. Nairong Tao, for introducing me to the dynamic plastic deformation technique and his guidance during my stay at the Institute of Metal Research, CAS, China.

I am grateful to Prof. Dorte Juul Jensen for proving me the opportunity to do my PhD project in the MAC section, and her constant support and encouragement during my work at DTU Wind. I also thank Dr. Niels Hansen for many useful discussions during my PhD work. Senior scientists Drs. Hilmar Kjartansson Danielsen, Søren Fæster, and Xiaoxu Huang are acknowledged for their help with electron microscopy and useful discussions. Drs. Chuanshi Hong, Fengxiang Lin, Tianbo Yu, Xiaodan Zhang, Yubin Zhang are acknowledged for their help and valuable discussions. I am grateful to the very skilled secretary and technicians, Helle Hemmingsen**,** Lars Lorentzen, Preben Olesen, and especially Gitte Christiansen for her help with TEM foil preparation. I am also indebted to Dr. Fengkai Yan and Mr. Xiao Si at IMR, for their help with the DPD process.

Finally, I would like to acknowledge my family and friends but especially my beloved wife, Haihua Yan, for their enduring support during my graduate studies. A special thank you to my dear daughter, Zimo Anne Zhang, for the endless happiness you bring to me.

Dansk resume

Nanostrukturer i et ferritisk og et oxiddispersionsstyrket stål induceret af dynamisk plastisk deformation

Nanostrukturerede metaller og legeringer forventes at vise meget højere styrke og bedre bestrålingstolerance end deres modparter med en grovkornet struktur. Derfor er nanostrukturering foreslåettil at være en lovende tilgang for at forbedre egenskaberne af konstruktionsmaterialer til avancerede fissions- og fusionsreaktorer. I denne undersøgelse er to stål som er kandidater til atomreaktorer, et ferritisk/martensitisk stål (modificeret 9Cr-1Mo stål) og et oxiddispersionsstyrket (ODS) ferritisk stål (PM2000), blevet nanostruktureret ved dynamisk plastisk deformation (DPD). Den resulterende mikrostruktur blev karakteriseret i detaljer, og opførslen under varmebehandling blev undersøgt med hensyn til termisk stabilitet og ændringer i mikrostrukturen over flere længdeskalaer ved elektron backscatter diffraction (EBSD), transmissionselektronmikroskopi (TEM), høj opløsnings TEM (HRTEM) og scanning TEM (STEM).

En lamelstruktur på nanoskalaen med en ⟨100⟩+⟨111⟩ duplex fiber tekstur udvikler sig i både det modificerede 9Cr-1Mo stål og PM2000 under DPD til høje tøjninger. Styrken øges betydeligt, men den termiske stabilitet bliver stærkt reduceret. Restituering og rekrystallisation er stærkt orienteringsafhængig, når de to stål opvarmes efter DPD. Både orienteret kimdannelse og orienteret vækst af ⟨111⟩ orienterede lameller påvises at udgøre en sådan orienteringsafhængighed. De underliggende mekanismer, herunder forskelle i lagret energi, strukturel variation, og restitueringsprocesser diskuteres. Højere tøjningshastigheder påvises at være i stand til at fremkalde strukturforfining, men den generelle opførsel under varmebehandling ligner materialet efter deformation med mindre tøjningshastigheder.

Ud over mikrostrukturen af matrixmaterialer blev oxidnanopartiklerne i PM2000 systematisk undersøgt med hensyn til deres struktur i materialet som modtaget og i høj deformeret og i varmebehandlet tilstand. Størstedelen af oxidnanopartiklerne i PM2000 er orthorhombisk $YAlO_3$ (YAP), som har et cuboid-on-cube orienteringsforhold til ferrit matrix. Varmebehandling ved 1300 °C og derover fører til betydelig vækst, og orienteringsforholdet mellem YAP/Fe skifter til et pseudo-cube-on-cube forhold. Det er

bemærkelsesværdigt, at YAP nanopartikler med diametre mindre end 20 nm deformerer væsentligt under DPD. Den gennemsnitlige ækvivalente tøjning af YAP nanopartikler er ca. 1.2 skønnet i prøven efter DPD til en tøjning af 2.1. Mekanisk induceret tvillingsdannelse viser sig at være den dominerende deformationsmekanisme for YAP nanopartikler. Nanohulrum findes at dannes ved YAP/Fe-grænsefladen ved lav tøjning. Med stigende tøjning, bliver disse nanohulrum lukket omkring de mindre partikler, som er væsentligt deformeret; derimod forbliver hulrummene forbundet med udeformerede, større partikler åbne. Når en prøve med væsentligt deformerede YAP nanopartikler varmes op, ændrer morfologien af de deformerede partikler sig dramatisk og fører til dannelsen af meget små YAP partikler fordelt i ferrit matricen. Disse resultater giver indsigt i styrkeøgningsmekanismer og duktilitet af ODS stål, og, endnu vigtigere, åbner de en ny tilgang til at forfine oxid nanopartikler i ODS stål ved en kombination af termomekaniske behandlinger.

Contents

Chapter 1

Introduction

To meet the increasing world-wide demand for sustainable energy while reducing the reliance on the fossil fuels but maintaining the economic efficiency and reliability, extensive international collaborations have been conducted on developing advanced fission and fusion energy. One of the major challenges in realizing such advanced nuclear energy is to develop high performance structural materials for fuel cladding and blanket components [1-3]. Ferritic and martensitic steels are considered to be promising structural materials for constructing the components in advanced fission and fusion reactors, due to their low thermal expansion, high thermal conductivity, irradiation tolerance and corrosion resistance [4-6]. To enhance the swelling resistance and improve the upper limit of service temperature, oxide nanoparticles were introduced into conventional ferritic and martensitic steels, forming oxide dispersion strengthened (ODS) steels with prominent properties [7-9].

The properties of metals and alloys can in general be altered to a large extend by varying their internal defect content, such as dislocations, boundaries and interfaces, etc. One way to increase the strength is by structural refinement via plastic deformation, when original grains are subdivided by dislocation boundaries [10]. Furthermore, it has been suggested that irradiation-induced swelling can be reduced in materials with well-refined microstructures. Therefore, these materials may exhibit improved irradiation tolerance compared to their coarse-grained counterparts [11-15]. It is however known that substantial structural refinement by plastic deformation is often accompanied by deteriorated ductility and reduced thermal stability of the material [16, 17]. For structural materials exposed to elevated temperatures, an optimal balance between the desirable and undesirable properties must be sought. The first objective of this study is therefore to obtain nanostructured ferritic and martensitic steels with and without oxide dispersoids by plastic deformation, and to investigate the recovery and recrystallization behavior of the resulting microstructure. Dynamic plastic deformation (DPD) is chosen for this purpose because DPD has been demonstrated as an efficient technique for structural refinement [18]. Understanding of the microstructural evolution and related properties of this special group of steels during plastic deformation and subsequent heat treatments will allow optimization of their structure and properties by certain combinations of thermomechanical treatment.

Another ambition of this work is to study both the thermal and mechanical behavior of oxide nanoparticles in an ODS steel. ODS steels can be considered as a system which comprises three components, namely iron matrix, oxide nanoparticles and interfaces between them. It has been demonstrated that the extraordinary properties of ODS steels, such as excellent creep strength and irradiation tolerance, originate from the well-dispersed oxide nanoparticles and their interface with the iron matrix. Therefore, the effect of heat treatments on the character of the oxide nanoparticles and their interfaces is important for the properties of ODS steels. However, due to the complexity in characterizing the nanoscale oxide dispersoids embedded in a magnetic ferrite matrix, current understandings on these issues are far from complete. In addition, due to the fact that processing of ODS steels typically involves plastic deformation, the response of oxide nanoparticles, and their interactions with iron matrix and the related changes in the interface when the steel is subjected to plastic deformation are crucial issues, since any changes in these aspects may alter the mechanical properties and irradiation tolerance of the material. Little is known in these areas, especially about the behavior of the oxide nanoparticles during plastic deformation of ODS steels. Special efforts are made in the present work to investigate the plastic deformation induced structural evolution of the oxide nanoparticles and their interfaces. Findings and conclusions obtained are not only significant for monitoring the microstructure and properties of the ODS steel, but are also able to provide insight into the strengthening mechanism of nanodispersoid strengthened materials.

Chapter 2

Background

This chapter firstly provides the literature review regarding two groups of steels, namely ferritic/martensitic steels and oxide dispersion strengthened (ODS) steels, as candidate structural materials for nuclear reactors. The necessary theoretical and experimental background for the current study are then summarized, including the plastic deformation induced microstructure at different strains, plastic deformation techniques for fabricating nanostructured materials, general annealing behavior of deformed metals and the related theories of recovery and recrystallization, the effect of fine particles on the microstructural evolution during plastic deformation and subsequent annealing behavior. Furthermore, due to the significance of the oxide nanoparticles in the ODS steels, background information regarding their character and interfaces with matrix, strengthening mechanisms, etc., is also reported.

2.1 Ferritic/martensitic steels

The exceptional harsh environment in the core of a nuclear reactor requires that the structural materials are capable of sustaining a combination of high temperatures, high stresses, a chemically aggressive coolant and intense radiation fluxes. Heat resistant ferritic/martensitic stainless steels are considered to be candidates for the fuel cladding materials in advanced fission reactors and blanket components in future fusion reactors. This is mainly due to the fact that, compared to austenitic stainless steels with face-centered cubic (*fcc*) crystal structure, ferritic/martensitic steels with body-centered cubic (*bcc*) crystal structure have the following advantages [6, 19, 20]: higher self-diffusion coefficient, lower He concentrations in the absence of Ni (Ni is inevitable element for austenitic steel and will be transmuted to He by thermal neutrons), etc. The better swelling resistance of ferritic/martensitic steel also benefit from the martensitic transformation induced very fine martensitic lath structure, where helium bubbles could form on nanoscale.

High Cr-alloyed (9-12%) ferritic/martensitic steels were first considered for elevated temperature in-core applications [5]. Cr is a ferrite-stabilizing element, which provides little solid solution strengthening in iron, but can improve the oxidation and corrosion resistance and form carbides to stabilize the microstructure at elevated temperature [21]. Mo was added in these steels to further stabilize ferrite and provide strong solid solution strengthening. Then Cr-Mo alloyed ferritic/martensitic steels were developed on this purpose, and among them a 9Cr-1Mo steel (designated by ASTM as Grade 91) was the most widely used [6]. In 1970s, by adding some carbide formers vanadium and niobium and optimizing the contents of carbon and nitrogen, a modified 9Cr-1Mo steel (designated by ASTM as T91) was developed. The modified 9Cr-1Mo steel has been demonstrated to have good creep strength and corrosion resistance, and has been used most extensively in the power plant industry throughout the world [22, 23]. The upper bound temperature of this steel for long time operation is about 600 °C [6]. The acceptable range of compositions for the modified 9Cr-1Mo steel is listed as below [24].

Table 2.1 Acceptable composition range of the modified 9Cr-1Mo steel (wt.%)

C	Cr	Mo	V	Nb	Ni	Mn	N	Si	S	P
0.08-0.12	8.00-9.50	0.85-1.05	0.18-0.25	0.18-0.25	0.40 Max	0.30-0.60	0.03-0.07	0.20-0.50	0.01 Max	0.01 Max

Heat treatments of the modified 9Cr-1Mo steel start with normalization at around 1050 °C, so that the material is fully austenized and all precipitates are dissolved. To enable all the austenite to be transformed into martensite, the cooling rate should be higher than 6 K/min until the martensite finishing temperature is reached (around 200 °C) [24]. This can be normally accomplished by air cooling. The transformed martensite, which contains a very high dislocation density, is very strong and brittle. Tempering is necessary to achieve a balance between strength and ductility. When tempered, the martensite is transformed into ferrite with recovered dislocation structure, and the martensitic laths are replaced by elongated ferritic subgrains. In addition, $M_{23}C_6$ type carbides and MX type carbonitrides precipitate during tempering. Consequently, a tempered martensitic structure with widely distributed carbides and carbonitrides is formed. A sketch of the desired microstructure is shown in Fig. 2.1. The schematic diagram illustrates the developed microstructure interior of a prior austenite grain. There are prior austenite grain boundaries (PAGBs), martensitic lath and packet boundaries and subgrain boundaries, which are decorated with $M_{23}C_6$ type carbides. There is also nearly randomly distributed MX type carbonitrides throughout the material. Therefore, the tempered modified 9Cr-1Mo steel exhibits solid solution strengthening, precipitation hardening, boundary and dislocation strengthening. In addition, the $M_{23}C_6$ carbides, which locate at martensitic boundaries and PAGBs, stabilize the martensitic structure during exposure at elevated temperatures. The MX type particles in the interior of martensitic laths and subgrains pin dislocations, and thereby maintaining high strength at high temperatures [25].

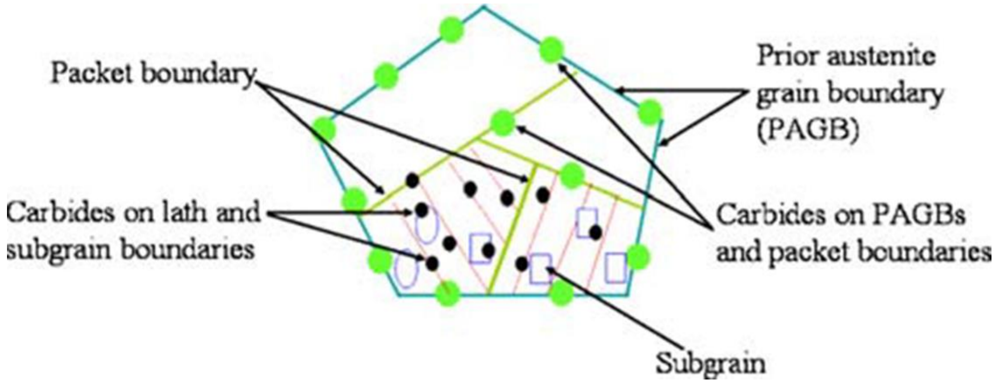

Fig. 2.1 Schematic of the microstructure of the tempered modified 9Cr-1Mo steel. (from [25]).

Safety issues concerning the waste disposal are important for developing nuclear reactors. In the fusion program, it was recognized that the decay of induced radioactivity produced by irradiation in a fusion environment could be accelerated by removing or diminishing elements such as Mo, Nb and Ni. This requirement leads to the concept of designing reduced activation ferritic/martensitic (RAFM) steels. It is expected that the RAFM steels can be safely handled at the end of their useful lifespan after a shorter cool down period less than 100 years rather than a cool down time of over 1000 years, which would be the case for the conventional Cr-Mo-Ni-Nb alloyed ferritic/martensitic steels [26, 27]. The modified 9Cr-1Mo steel has been used as guide and benchmark in designing RAFM steels. The Oak Ridge National Laboratory designed 9Cr2WVTa, for instance, was patterned after modified 9Cr-1Mo steel, with molybdenum replaced by tungsten and niobium replaced by tantalum [4]. There are also several other RAFM steels developed under the international collaborations, such as a F82H steel developed by the Japan Atomic Energy Agency[28], EUROFER97 produced in Europe within the framework of the European Fusion Development Agreement program [29], and a CLAM steel designated by the Chinese Institute of Plasma Physics [30]. Although the chemical compositions of these steels are slightly different, they have very similar microstructures, namely tempered martensite with fine precipitations. If only the microstructural evolution during thermomechanical treatment is considered, there is no essential difference among them, and therefore on this aspect the commercial modified 9Cr-1Mo steel is widely used for investigation.

2.2 Oxide dispersion strengthened steel

2.2.1 Why ODS steels

Development of advanced fission reactors and future fusion reactors requires structural materials able to operate at high temperatures and to sustain strong irradiation damage. Two key ingredients for irradiation-resistant alloys are (a) high creep strength, permitting operation at temperatures above the displacement damage regime, and (b) high volume density of stable nanoprecipitates that trap He in fine bubbles to avoid swelling and thereby enhancing the irradiation tolerance [1]. Oxide dispersion strengthened (ODS) ferritic/martensitic steels are promising materials with a potential to be used at elevated temperatures due to the addition of thermally stable oxide particle dispersion into the ferritic/martensitic matrix. Compared with the conventional second phase precipitates, oxide dispersoids are thought to be much more stable at high temperature since they are almost insoluble and can persist up to the melting temperature of the matrix material, which is the premise behind the ODS alloys.

The high creep strength of the ODS steels is due to the dispersed oxide particles which act as barriers to dislocation motion. In terms of particle strengthening, there are two distinguishable mechanisms due to interaction of dislocations with either penetrable or impenetrable obstacles [31]. For hard impenetrable particles (Fig. 2.2a), dislocations are forced to bow out between the particles, which is the primary effect responsible for particle strengthening. The dislocation bypasses the particles by forming dislocation loops around them, which is known as Orowan strengthening. For penetrable particles, dislocation can pass them by cutting through. This process requires stresses much higher than that required for motion through the matrix (Fig. 2.2b). I both cases, a stress increase is required to move dislocations through a matrix containing dispersed particles, although hard impenetrable particles provide generally a higher strengthening effect. The key parameters to describe dispersion strengthening are the interparticle spacing, λ, and the particle diameter, R. For a constant volume fraction of hard dispersoids with Orowan strengthening mechanism, the increase in resolved shear stress due to the dispersoids has a relationship with the particle diameter as $\tau_{OR} \propto 1/R$ [32]. Whereas for weak and penetrable dispersoids, the dislocation is forced to bow out less, and the relationship between the increased resolved shear stress and particle diameter at a constant volume fraction is $\tau_{OR} \propto \sqrt{R}$ [32]. Therefore, in a system with constant volume fraction of particles, small impenetrable particles results in greater strengthening effect, whereas for penetrable particles there is a critical size for strengthening, and either smaller or larger than this size leads to weaker strengthening effect. Oxide particles in ODS steels are generally thought to be impenetrable with Orowan strengthening mechanism. At elevated temperatures, dislocations gain new degree of freedom for their motion, and they can circumvent obstacles by climb or more easily cross slip, which both are pronounced thermally activated processes. To achieve higher creep strength, fine dispersoids are thought be able to pin dislocations by exerting even attractive interactions on them [33].

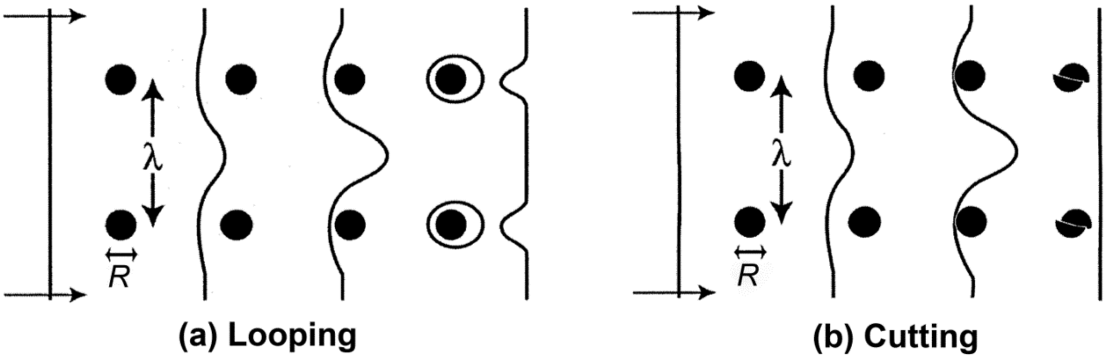

Fig. 2.2 Schematic diagrams of the interactions between a dislocation and an array of precipitates: (a) dislocation passes by precipitates via forming Orowan loops, (b) dislocation cuts through precipitates.

Besides the enhanced creep strength, the irradiation tolerance may also benefit from the well-dispersed nanoscale particles. A comprehensive schematic diagram (Fig. 2.3) illustrates the envisaged cause for a high irradiation tolerance of ODS steels [1]. The primary irradiation damage caused by the displacement cascades, consists of self-interstitial atoms (SIAs) and vacancies, and the transmutation product helium. In ODS alloys, the high density of nanoparticles and dislocations provides irradiation damage resistance. This results from trapping He in fine bubbles, maintaining high stable sink densities for defect annihilation at the particle/matrix interface, which therefore diminishes the irradiation induced swelling and embrittlement. Grain boundaries are protected from an accumulation of high He concentrations. Therefore, a ductile facture is expected in ODS steels.

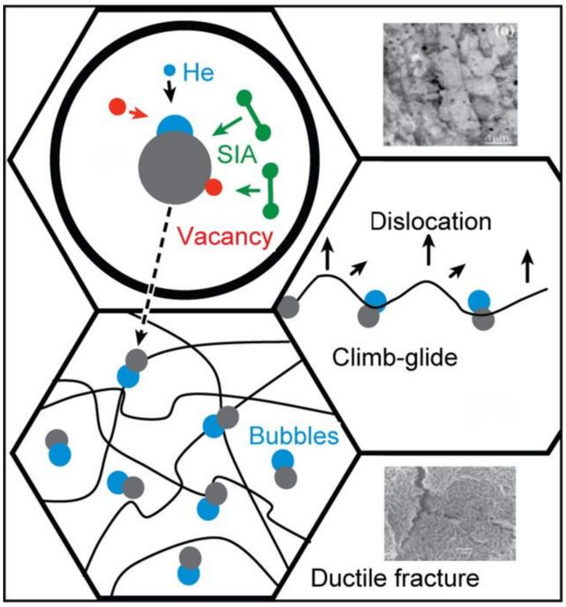

Fig. 2.3 Irradiation damage resistance in a nanostructured ODS ferritic alloy with high density of nanofeatures. SIA represents the irradiation induced self-interstitial atoms. (From [1]).

2.2.2 Overview of some ODS steels

Mechanical alloying is employed to produce the ODS steels. This involves high energy ball milling of pre-alloyed material powders and oxide powders, and is followed by hot consolidation [34]. Mechanical alloying was first developed by John Benjamin at the International Nickel Company around 1966 [35] for producing ODS superalloys. Research and development of the ODS ferritic/martensitic steels as structural materials for nuclear reactors started in the late of 1980s [7]. For ODS ferrtic/martensitic steels, yttria is introduced as dispersoids during ball milling, however, during hot consolidation, other alloy elements from matrix, like Ti, Al, etc., may become incorporated in the dispersoids and result in the formation of other oxide compounds [36].

Several ODS ferritic/martensitic steels have been developed for fission and fusion applications in the United States [37, 38], Japan [8, 39] and Europe [29]. Commercial ODS products, including MA956 and MA957 [40, 41] (developed by International Nickel Company) and PM2000 [34] (developed by Plansee GmbH in Austria) were available but only used in limited quantities. ODS EUROFER [42], 12YWT [43], 14YWT [44] were developed in collaboration between laboratories and industry. Among these types of ODS steels, the matrix of MA956 and PM2000 are ferrite, while others mentioned above have a ferritic/martensitic matrix. This is due to the fact both

MA956 and PM2000 contain more than 20 wt. % Cr as ferrite stabilizer, which can stabilize the ferrite to melting temperature. Since their relatively simple microstructure with pure ferrite and oxide dispersoids compared to the tempered martensitic steels, they are used as model materials for fundamental research on ODS steels.

Besides extensive investigations of mechanical properties and irradiation performance of a variety of ODS steels, characterization of the oxide nanoparticles and their relationships with matrix at various conditions is also an active research field. However, due to the complicated process in fabricating ODS steels, and the inherent structural uncertainty when oxide particles are only a few nanometers, and the difficulty in characterizing the nanoscale particles embedded in ferrtic matrix, there have been lots of controversial issues in the identification of oxide nanoparticles even in the identical material. Because of the crucial importance of the oxide nanoparticles for ODS steels, various techniques, including high resolution transmission electron microscopy [45, 46], scanning transmission electron microscopy [44, 47], energy dispersive X-ray spectroscopy [44, 48], three dimensional atom probe tomography [37], etc., have been employed to investigate the oxide nanoparticles. However, there are still substantial discrepancies on the structure of oxide nanoparticles and their interfaces with matrix, and systematic work is necessary to clarify these issues.

2.3 Advantage of fine structure in enhancing irradiation tolerance

Fig. 2.4 illustrates the envisaged different fate of irradiation induced defects in materials with a conventional grain size and a nanostructure [49]. In a conventional material, self-interstitial atoms caused by irradiation quickly move to the surface instead of meeting with the vacancies. Vacancies slowly agglomerate, forming immobile voids that cause swelling and embrittle the material. In a nanostructured material, on the other hand, the interstitial defects get stuck in boundaries. Virtual interstitials re-emitted from boundaries annihilate with vacancies, leaving a healed crystal. An enhanced irradiation tolerance due to a higher density of interfaces and grain boundaries in ultrafine grained and nanostructured materials have been proved by atomic simulation [11] and experimental results [12-15]. Singh [12] showed that the void nucleation is delayed, void concentration is lowered, and void volume swelling is reduced by decreasing the grain size of an austenitic steel under irradiation. Furthermore, Chimi *et al.* [13] reported that irradiation induced defects are thermally unstable in nanocystalline Au, which suggests the propensity in using nanocrystalline as irradiation-resistant material. According to Rose *et al*. [14] drastic reduction in defect cluster happens in nanocrystalline Pd and ZrO_2 with grain sizes less than 50 nm, and no defect clusters were observed in the sample with grain sizes smaller than 30 nm. Recently, Song *et al*. [15] carried out some work on the irradiation response of ultrafine grained modified 9Cr-1Mo steel produced by equal channel angular extrusion, and the results demonstrated that the swelling rate of ultrafine grained material is three times lower than its counterpart with a conventional grain size. The enhanced irradiation tolerance reported in these articles is expected to originate from the mechanism shown in Fig. 2.4. For metallic materials, a very important method to achieve ultrafine grained or nanostructured materials is plastic deformation to high strains. Therefore, structural refinement behind the plastic deformation should be introduced.

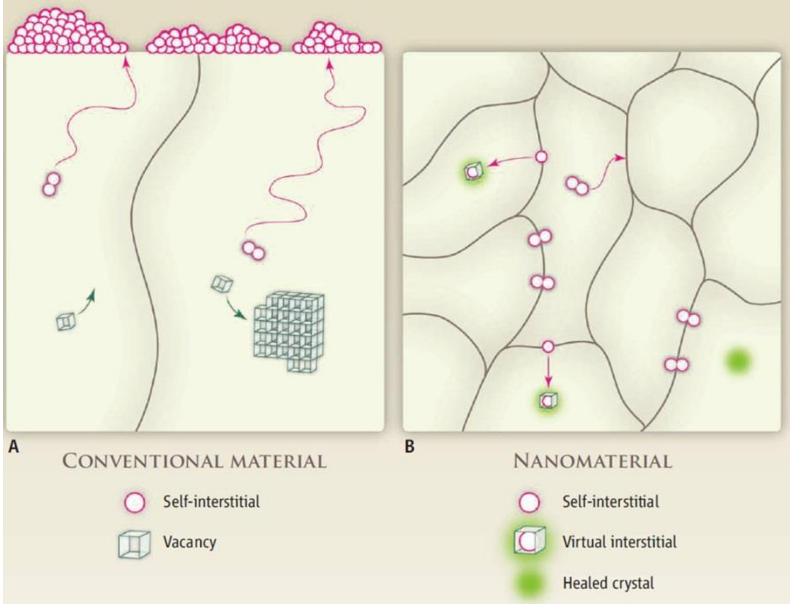

Fig. 2.4 Schematic diagram illustrating the different fate of irradiation induced defects, namely self-interstitial atoms and vacancies, in (a) conventional material, (b) nanostructured material. (From [49]).

2.4 Plastic deformation induced microstructural evolution

In this section, microstructural and textural evolution induced by plastic deformation is described. Since the materials investigated in this work have *bcc* structure, the literature data used to illustrate the underlying mechanisms is preferentially based on the results from *bcc* materials. Due to the fact that, the microstructural evolution of *bcc* materials and *fcc* materials with medium to high stacking fault are similar, some results for *fcc* materials are also extracted when there are no results on *bcc* materials with good quality available.

2.4.1 Some basics of plastic deformation

2.4.1.1 Dislocation and slip

Dislocation is a line defect in materials. The movement of dislocations constitutes the fundamental basis for understanding the plastic behavior of crystalline materials. Metallic materials, even in the annealed state, contain a statistical density of dislocations, which can be determined by thermodynamic principles. The stress to cause plastic deformation can be reduced by a factor of 1000 if deformation can be achieved by the movement of dislocations, rather than moving complete lattice planes simultaneously [50]. For this reason, plastic deformation of metals depends on the generation and subsequent movement of dislocations. Dislocations are characterized by Burgers vectors, denoted by b. The Burgers vector can be considered a slip vector because its direction is the slip direction and its magnitude is the magnitude of the slip displacement caused by its movement of the dislocation. The direction of dislocation motion is always parallel to b. There are two basic types of dislocations, namely edge dislocation and screw dislocation. Edge dislocation was firstly proposed by Orowan, Polanyi and Taylor, in 1934, and screw dislocation was proposed by Burgers in 1939. A defining characteristic of an edge dislocation is that its Burgers vector is always perpendicular to the dislocation line, while a screw dislocation has its Burgers vector parallel to the dislocation line. Edge and screw dislocations are two extreme cases. A dislocation in reality may be neither parallel nor perpendicular to the slip direction, i.e. it has a mixed character.

The plane, in which a dislocation moves, is called a slip plane. Generally the slip plane is the plane of greatest atomic density, and the slip direction it the closest packed direction within the slip plane. The slip plane together with the slip direction establishes a slip system. In the *fcc* structure, {111} planes and ⟨110⟩ directions are the close-packed systems. The *bcc* structure is not a close packed structure, so there is no one plane of predominant atomic density. The ⟨111⟩ direction of the *bcc* structure is just as close packed as ⟨110⟩ direction in the *fcc* structure. Therefore, *bcc* metals obey the general rule that slip direction is the close packed direction, but they do not have a definite slip plane. Slip in *bcc* metals is found to occur on the {110}, {112}, and {123} planes while the slip direction is always ⟨111⟩, which is usually denoted as pencil-glide.

2.4.1.2 Orientation and texture

Crystallographic orientation of crystalline materials indicates how atomic planes in a volume of crystals are positioned in relation to a fixed reference. To describe an orientation in real case, two systems are required, namely the sample coordinate system and the crystal coordinate system. One of the most common sample systems relates to a rolled product, and hence the directions associated with the external shape are the rolling direction (RD), the direction normal to the rolling plane (ND), and the transverse direction (TD). Other samples, such as tensile and compressed piece, swaged rod, or drawn wire, have only uniaxial symmetry, hence it is only necessary to specify one axis in the specimen coordinate system. For the crystal coordinate system, Miller indices are usually used. The orientation of a crystal is then defined as the position of the crystal coordinate system with respect to the specimen coordinate system. For instance, if a crystal has its (111) plane parallel to the rolling plane and $\langle 110 \rangle$ direction parallel to the rolling direction, its orientation can be described as $(\bar{1}11)\langle 110 \rangle$ in Miller indices. Grain orientations in polycrystals, whether naturally occurring or fabricated, are rarely randomly distributed. For most crystalline materials, there is a propensity for the occurrence of certain orientations during crystallization from a melt or during further thermomechanical processes. This tendency is known as preferred orientation, which is usually termed texture. There are two broad categories of textures commonly known as sheet and fibre textures. To describe a sheet texture of a rolled material, it is necessary to know crystallographic planes aligned in the rolling plane of the sheet and crystallographic directions aligned with the rolling direction. A fibre texture can be completely described by crystallographic directions aligned parallel to the fibre axis.

The difference in crystallographic orientation between two crystallites in a polycrystalline material is called misorientation. The orientation between two coordinate systems can be defined by the angle-axis pair $\theta\langle uvw \rangle$. One coordinate system can be superimposed onto the other by rotating by an angle θ around the common axis $\langle uvw \rangle$. This angle-axis pair notation is normally used to describe the misorientation of grain boundaries.

2.4.2 Microstructural evolution from low to high strains

For metals and alloys with medium to high stacking fault energy, plastic deformation takes place predominantly by the multiplication and movement of dislocations. Dislocations within the structure can reduce their elastic strain energy by forming arrays or boundaries [51]. The formation of dislocation boundaries, in the form cell, subgrain or grain boundaries, is associated with changes in the lattice orientation. The deformation-induced structural refinement has its cause in the multiplication of dislocations that interact and are stored in the form of low-angle dislocation boundaries and high-angle boundaries, which together subdivide the structure on a finer and finer scale as the strain increases [10, 52].

Fig. 2.5 shows a typical microstructure of IF steel after deformation to low strains [53]. As seen from the TEM images and the corresponding sketches, at small strains, a dislocation cell block structure forms where cell blocks are delineated by extended planar dislocation boundaries, which are generally referred as geometrically necessary boundaries (GNBs). The cell blocks are further subdivided into cells by cell boundaries, which are termed incidental dislocation boundaries (IDBs) [10]. As the strain increases, the spacing between both the cell block boundaries and the cell boundaries decreases and the misorientation angle across them increases. At large strains the structure became a typical lamellar structure, with nearly planar lamellar boundaries and short interconnecting boundaries. A typical lamellar structure is shown in Fig. 2.6 [54].

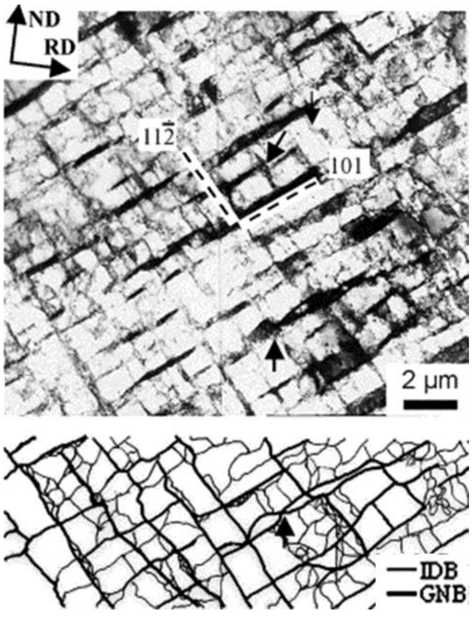

Fig. 2.5 Deformation microstructure of IF steel after cold rolling to a thickness reduction of 10%. Sketch below the figures illustrates the cell block structure composed of GNBs and IDBs. Dashed lines mark the traces of crystallographic planes. (From [53]).

The cell block boundaries in the materials deformed to low strains and lamellar boundaries after deformation to high strains are both thought to be GNBs, since they delineate regions where distinct dislocation slip systems are active. Cell boundaries at low strains and interconnecting boundaries at high strains are both thought to be IDBs, which originate from mutually trapping of gliding dislocations [10, 51]. With increasing strain, the average boundary spacing of both GNBs and IDBs decreases and their mean misorientation angle increases [55], leading to a microstructural evolution towards a finer and finer scale.

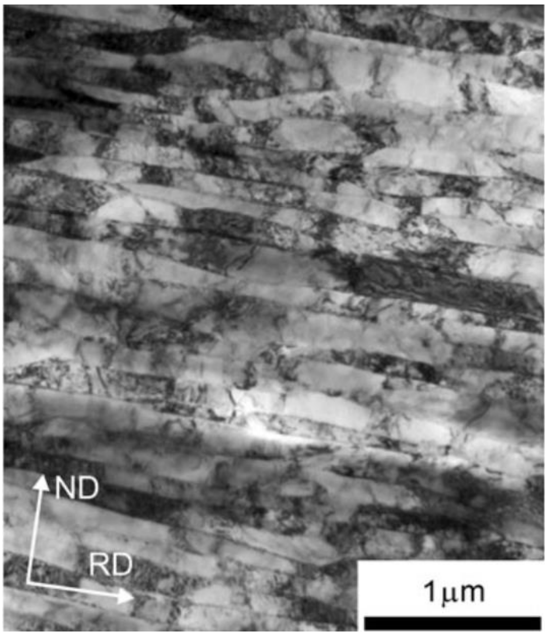

Fig 2.6 Microstructure of IF steel after rolling to a thickness reduction of 99.2% with a combination of warm and cold rolling. The microstructure is characterized by lamellar boundaries nearly parallel to the rolling direction and interconnecting boundaries. (From [54]).

In addition to the evolution of the microstructural morphology with strain, the stored energy also changes with increasing strain. Fig. 2.7 shows the estimated stored energy based on the different methodologies (DSC and TEM). It shows that the obtained value of the stored energy very much depends on the measuring methods. Nevertheless, an evident tendency that the obtained stored energy increases with increasing strain is common for all measurements. The stored energy has a strong effect on the annealing behavior of deformed materials.

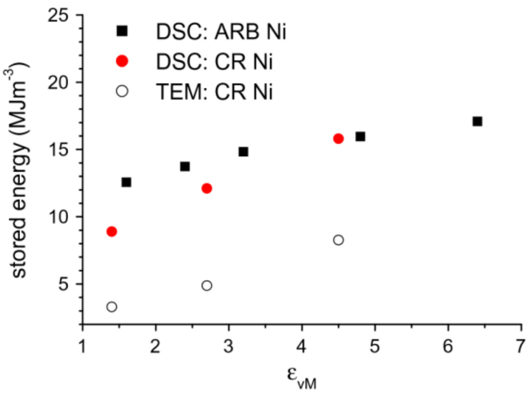

Fig. 2.7 Stored energy measured by differential scanning calorimetry (DSC) and from TEM measurements for Ni deformed by cold rolling and accumulated roll bonding to different strains (From [56]).

2.4.3 Orientation dependent deformation microstructure

The morphology of the deformation induced microstructure depends strongly on the crystallographic orientation [57]. The correspondence between grain orientation and deformation-induced structure of is illustrated in Fig. 2.8 for pure aluminum after tension to a small strain [58]. Three types of characteristic microstructures were identified. Each occupies a specific region in the stereographic triangle which is related to the specific crystallographic direction of grains along the tensile axis. Type 1 is a cell block structure with GNBs delineating the grains. The GNBs are almost parallel to a slip plane. Type 2 is a cell structure, divided by cell boundaries forming a nearly equiaxed network of cells. Type 3 is a cell block structure, which is similar to Type 1, but the GNBs do not lie on slip planes.

This orientation dependence of the dislocation structure is not only found after tensile deformation, but also after rolling [53] and compression [59]. Such orientation dependence is pronounced in *bcc* metals and alloys as well [53, 60]. Therefore, the orientation dependence of deformation-induced microstructure is thought to be universal of all metallic material. The relation between the grain orientation and deformation-induced microstructure is thought to originate from the interaction of different sets of mobile dislocations, as the activated slip systems have strong dependence on grain orientation [61]. The relationship between grain orientations and resulting dislocation patterns may lead to different annealing response of deformed grains with different orientations.

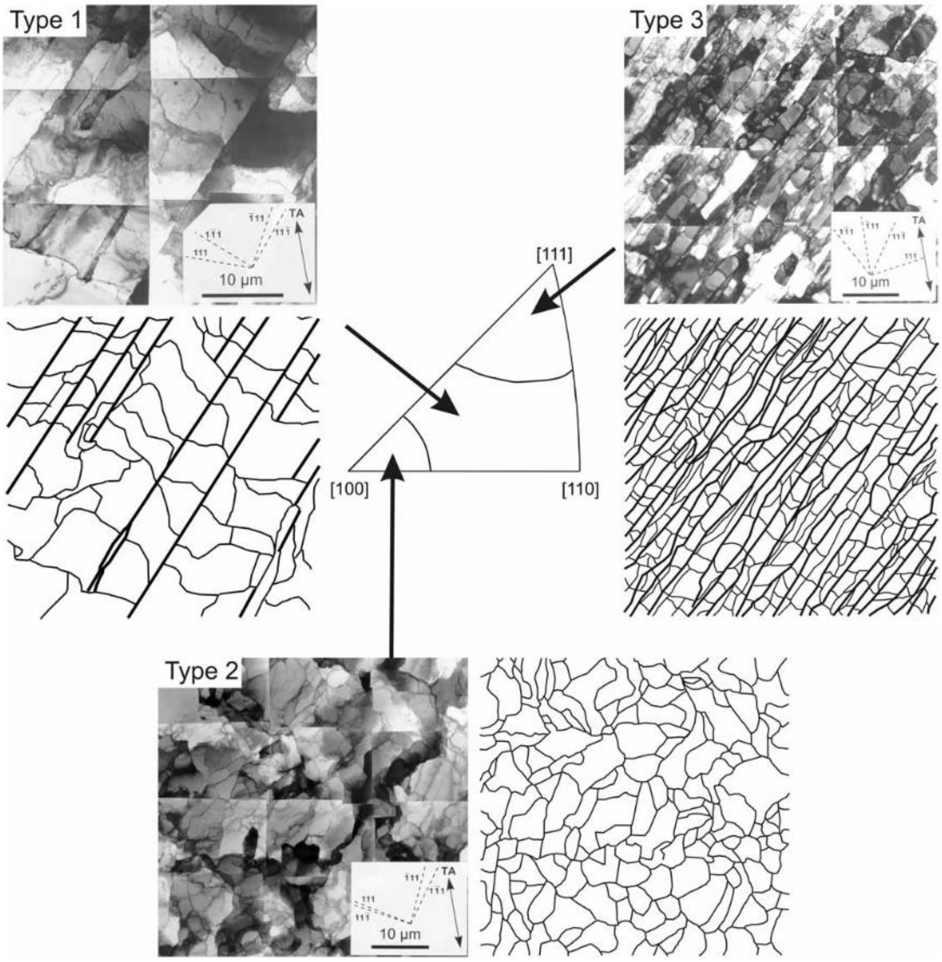

Fig. 2.8 Microstructural types in grains of different orientations in polycrystalline pure aluminum deformed in tension to a strain of 0.14. The inverse pole figure used to present the orientation of grains is constructed along the tensile axis. (From [62]).

2.4.4 Deformation texture

During plastic deformation, the change in grain orientation is not random. Reorientation is a consequence of the fact that deformation occurs on the most favorably oriented slip systems (metals with medium to high stacking fault energy) and the interplay with boundary conditions. Consequently grains of deformed metal acquire preferred orientations. Thus metals develop deformation textures.

For metals and alloys with *bcc* structure, fibre textures are usually formed, due to the fact that dislocations in *bcc* materials exhibit ⟨111⟩ pencil gliding. Fig. 2.9 shows some important texture components of *bcc* metals and alloys after rolling in Euler space.

Among them the α and γ fibres are the most typical texture components of cold rolled ferritic steels [63].

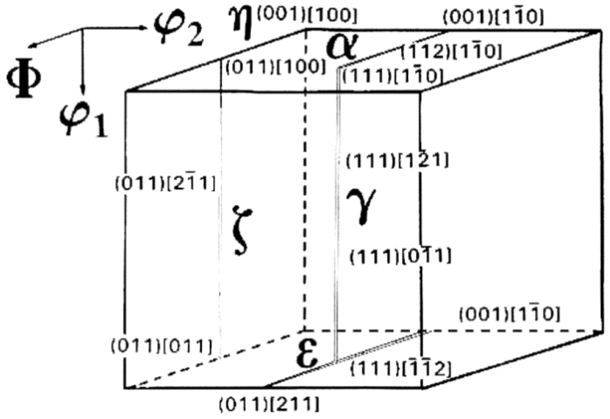

Fig. 2.9 Some important fibre texture components of *bcc* material represented in the reduced Euler space. α: ⟨110⟩ // RD; γ: {111} // ND; η: ⟨001⟩ // RD; ε: ⟨110⟩ // TD; ζ: ⟨110⟩ // ND. RD, ND, and TD are rolling, normal, and transverse directions, respectively. (From [63]).

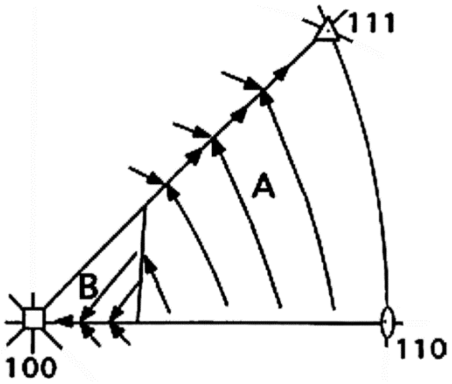

Fig. 2.10 Stereographic triangle illustrating the changes in the crystallographic direction of the CA of a *bcc* crystal deforming by ⟨111⟩ pencil glide during uniaxial compression.

According to Taylor’s theory, the textural evolution of *bcc* metallic materials subjected to uniaxial tension and compression can be predicted. When reorientation is dominated by single slip, the active slip plane rotates towards the CA, whereas in tension it is the active slip direction that tends to align with the axis of the applied stress [64]. A diagram in Fig. 2.10, shows the lattice rotation of *bcc* crystals deforming by ⟨111⟩ pencil glide during compression. Compression causes a rotation of orientations in region B away from [111] toward [100], whereas orientations in region A rotate towards

[111]. When they reach the [100]-[111] symmetry line, simultaneous slip with [111] and $[11\bar{1}]$ Burgers vectors causes a net rotation toward [111]. Consequently, *bcc* materials compressed to high strains develop a ⟨100⟩+⟨111⟩ pronounced duplex fibre texture [65].

2.4.5 Techniques for nanostructuring

According to the classic Hall-Petch theory on boundary strengthening, the yield strength of metallic materials closely related to their grain size. The Hall-Petch relation is described as:

$$\sigma_y = \sigma_0 + k_1 d^{-½}$$

where σ_y is the yield strength, σ_0 is the friction stress, d is the grain size, and k_1 is a strengthening coefficient. Accordingly, the strength of materials can be largely increased by refining the grain size (boundary spacing). Therefore, structural refinement by plastic deformation to high and ultrahigh strains has been explored extensively in metallic materials. During the last two-three decades, several plastic deformation techniques have been developed, including equal channel angular extrusion [66], high pressure torsion [67], accumulative rolling bonding [68], etc., which are able to deform the material to equivalent strains up to a magnitude of 10^2. Ultrafine grained material with grain sizes in sub-micrometer range or nanostructured material can be produced using these techniques.

However, structural refinement by conventional plastic deformation techniques due to dislocation activities is sluggish, since dynamic recovery caused by dislocation annihilation is very pronounced at high strain [69], which inhibits further refinement by dislocation boundaries. It is well known that dynamic recovery is a thermally activated process [70], therefore this process could be suppressed by increasing strain rate and/or decreasing deformation temperature. By suppressing the dislocation annihilation with the other dislocation with opposite sign, the dislocation density at a given strain can be improved. Therefore a higher density of dislocation boundaries forms. More efficient grain refinement has been achieved in materials deformed at high strain rate (10^2-10^3 s^{-1}) and liquid nitrogen temperature [71, 72].

Another approach to facilitate grain refinement is to introduce strain gradients into plastic deformation, since the density of geometrically necessary dislocations is proportional to the strain gradient [73]. Surface mechanical grinding treatment was developed for this purpose, and a much finer structure could be obtained on the sample surface than that deformed with conventional method [74]. In terms of strain gradient, besides those could be introduced by specific deformation technique, in plastically non-homogeneous material comprising hard and soft phases, such as particle strengthened alloys, strain gradient will generate around the interface due to strain heterogeneity between them. As a result, such strain gradient exerts certain effect on the microstructural evolution.

2.4.6 Particle effect on the deformation microstructure

The density and arrangement of dislocations in deformed materials containing particles is dependent on whether or not these particles deform. For weak and deformable particles which cannot withstand the stress to form Orowan loops, dislocations can shear the particles leading to slip concentration on the softened slip planes [75]. Thus no extra dislocations are generated at the particles. For non-deformable particles, plastic strain incompatibilities emerge between the two phases. This strain is accommodated by the generation of dislocations at the particle-matrix interface. These dislocations are termed geometrically necessary dislocations (GND). These extra dislocations were observed in the oxide dispersion strengthened metals [76]. The increase in the dislocation density for the alloys containing non-deformable particles is pronounced at small strains, while at large strains the dislocation density is high even far from particles, the effect of particles on dislocation density might be less significant [77].

The presence of non-deformable fine particles has certain effects on the deformation-induced cells and subgrain structures. It is known that dislocation cell and subgrain structures result from the dislocation arrangement and dynamic recovery, and therefore any factors affecting the accumulation of dislocations should have influence on them [78]. Non-deformable particles could hinder the dislocations movement and reduce dynamic recovery. Besides, the free path of dislocations will also be affected. If the interparticle spacing is smaller than the usual moving distance of dislocations, the dislocation cell size and misorientations across dislocation boundaries will therefore be affected. For instance, more homogeneous structure with more diffuse dislocation cells was observed in the copper containing fine particles and small interparticle spacing [79]. However, for Al with A_2O_3 as dispersoids but large interparticle spacing, the developed cell structure was not found to be significantly different from that in pure aluminum [80]. Barlow *et al.* [81, 82] report that in aluminum with fine alumina particles, the deformation structure evolves faster, characterized by smaller cell size and higher misorientation at given strains, than in pure aluminum.

For small particles at low strains, plastic relaxation generally involves generation of prismatic dislocation loops, which are of lower energy than Orowan loops [73]. Even if the Orowan loops form at a low strain, they would be relaxed by forming prismatic dislocations. This is why Orowan loops are rarely observed. For larger particles (normally with size larger than 100 nm), complex dislocation structures are formed around the particles and local lattice rotation takes place due to the plastic heterogeneity between the particles and matrix [83]. This will result in a region with a microstructure different from that far away from the particle. This region is commonly termed particle deformation zones (PDZ) [83]. This PDZ is usually of higher stored energy density, and has a strong effect on the subsequent recrystallization behavior.

2.5 Recovery and recrystallization of deformed material

Plastically deformed metals and alloys are not thermally stable, since substantial energy is stored in the material during plastic deformation. Therefore, thermal treatment is usually necessary for cold deformed materials, since the thermal stability of deformed material should be checked if the material is supposed to serve at elevated temperature. More generally, the microstructure and mechanical properties of the deformed materials could be modified by appropriate annealing.

2.5.1General background on recovery and recrystallization

When cold deformed materials are annealed, their microstructure and properties can be partially restored to their initial state. This restoration involves a sequence of processes, namely recovery, recrystallization, and grain growth. These three processes are generally defined as [84]: Recrystallization is the formation of new almost dislocation free grains in a deformed material by the formation and migration of high angle boundaries driven by the stored energy of the deformation structure. High angle grain boundaries are those with misorientation higher than 10-15°; Recovery is conventionally defined as all annealing processes taking place before recrystallization, and it proceeds without long range migration of high angle boundaries; Grain growth is a process involving the migration of grain boundaries with the driving force solely coming from the reduction of grain boundary area.

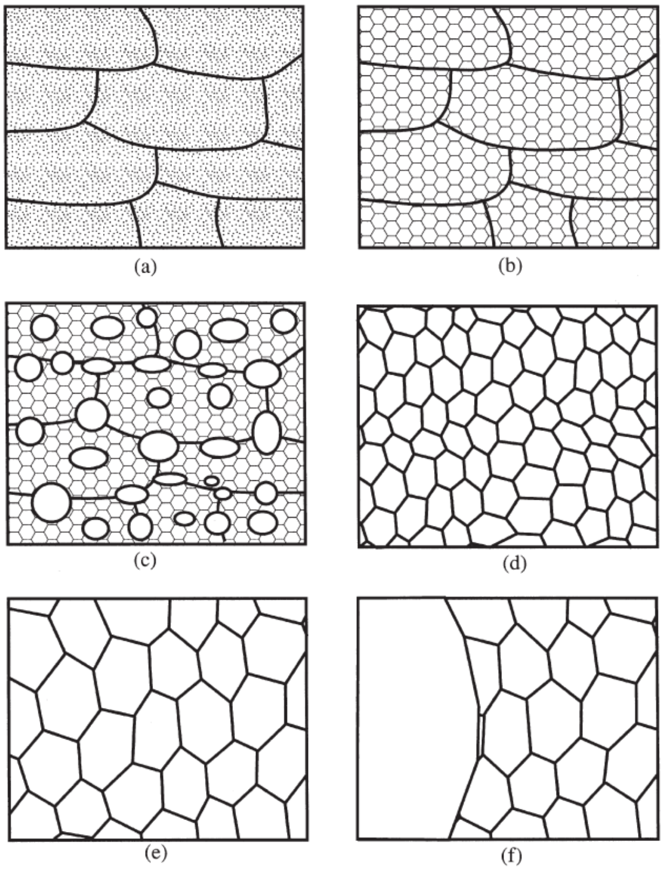

Fig. 2.11 Schematic diagrams illustrating the main annealing processes: (a) deformed state, (b) recovered, (c) partially recrystallized, (d) fully recrystallized, (e) grain growth, and (f) abnormal grain growth. (From [78]).

Fig. 2.11 schematically shows the main processes involved when the cold deformed materials are annealed [78]. Recovery is due to mutual annihilation of dislocations with opposite Burgers vectors and rearrangement of dislocations to lower their energy, for example by the formation of subgrain boundaries. The microstructural changes during recovery are relatively homogeneous, as shown in Fig. 2.11b. By extending the annealing time or increasing the annealing temperatures, recrystallization occurs with new dislocation free grains formed within the deformed or recovered structure. The prerequisites for a subgrain to become a new grain are: it should have a large size and possess a high misorientation angle with the neighboring structure. Then these new grains grow and consume the deformed matrix, resulting in a recrystallized structure with a very low dislocation density (Fig. 2.11d). Further annealing leads to grain growth or abnormal grain growth during which smaller grains are consumed and larger grains grow.

Recovery and recrystallization are both driven by the energy stored during plastic deformation, During both processes this energy is reduced. Therefore these processes are largely affected by the deformation-induced microstructure. The transition from recovery to recrystallization is sometimes difficult to identify, as recovery plays an important role in nucleating recrystallization, especially in highly strained materials [85]. Recently, Yu *et al.* [86] found that triple junction motion, which involves short range migration of high angle boundaries, is an important mechanism contributing to recovery in highly strained aluminum. Thus the border between the recovery and recrystallization is blurred in the materials deformed to high strains.

2.5.2 Recrystallization texture

During recrystallization, the texture of the deformed materials can be changed dramatically in the sense that the previous deformation texture is replaced by a different texture. The recrystallization- induced texture evolution has been the subject of extensive studies for many years, since texture is largely responsible for the anisotropic properties of the thermomechanically treated products, and simultaneously its origin is of much scientific interest.

There are two major factors determining the nature of the recrystallization texture: (i) orientations of the recrystallization nuclei; and (ii) the relative nucleation and growth rates of the recrystallizing grains [78]. It is generally assumed that the recrystallization textures have their origin in either a preferred nucleation of grains with a particular orientation, which is known as oriented nucleation (ON), or the preferred growth of grains with specific orientations from a relatively randomly oriented nuclei, which is termed oriented growth (OG) [87]. Originally, the ON and OG theories were developed to explain the strong cube texture in cold rolled and annealed *fcc* metallic materials [88].

The ON theory has also been employed to interpret the strong ⟨111⟩//ND fibre texture of the cold rolled low carbon steel after recrystallization. Cold rolled *bcc* steels usually develop two strong texture components, namely ⟨111⟩//ND texture and ⟨110⟩//RD texture. The higher stored energy in the ⟨111⟩//ND fibre after deformation is thought to be the main reason contributing to an advantage in recovery and preference in nucleation [89-92]. Consequently, deformation structure with other texture components are consumed by ⟨111⟩ oriented recrystallizing grains.

2.5.3 Particle effects on recovery and recrystallization

Particles are able to pin dislocations and boundaries, thereby retarding the dislocation rearrangement as well as subgrain and grain boundary movement during recovery and recrystallization. On the other hand, PDZs form around large particles. These regions with more pronounced lattice rotation and higher dislocation density are preferential nucleation sites. Particles stimulated nucleation (PSN) has been observed in many metals [93]. Retardation and acceleration effects depend on the particle size and interparticle spacing. For particles with diameter smaller than 25 nm and interparticle spacing less than 8 nm, particles show retardation effect on recovery and recrystallization [80, 94, 95]. Whereas particles with sizes larger than 1 μm and interparticle spacing larger than 0.3 μm, an acceleration effect due to PSN is observed [93, 96, 97]. For particles with diameter between 25 nm and 1 μm, both retardation and acceleration effects were reported [94, 98].

The orientation of the recrystallization nuclei produced by PSN will in general be different from those produced by conventional recrystallization mechanism. According to [78], if the PSN is the dominant recrystallization mechanism, recrystallized grains form either a weak texture or are randomly oriented. Whereas in some cases, PSN can lead to very strong textures, which are however still different from those in materials without PSN [99].

2.5.4 Changes of mechanical properties

The strength of materials can be largely increased via structural refinement by plastic deformation, and the structure-strength relationship is described by the classical Hall-Petch relation (see section 2.4.4). Compared to materials with a coarse-grained structure, the strength of the ultrafine grained and nanostructured counterpart produced by severe plastic deformation is largely improved. However, with increasing strain, the work hardening rate is reduced due to dynamic recovery [69]. According to Considere’s criterion [100], when the work hardening rate is lower than the flow stress, strain localization occurs in a sample under tension, leading to necking and quick failure. Such a lack of work hardening capability is the main reason for the deteriorated ductility of the metallic materials after cold deformation to high strains.

Recovery and recrystallization lead to reduced dislocation density and coarsened structure, and therefore a decreased strength. Since material regains the capability to store extra dislocations, the work hardening rate of the material is enhanced after annealing. In this manner, the ductility of the material is restored to a certain extent, which depends on the fraction of recrystallized regions. Such a trade-off between the strength and ductility can be optimized by tailoring the extent of recovery and the fraction of recrystallization in the highly deformed and annealed material. A bimodal grain size distribution with recrystallized grains in micrometer size embedded in the matrix of nanocrystalline and ultrafine grains achieved has the potential to achieve a good combination of both high strength and high ductility [16]. A typical example of the trade-off between strength and ductility for nanostructured 316L steel is shown in Fig. 2.12 [101], and decent synergies of strength and ductility could be obtained by certain thermomechanical treatments.

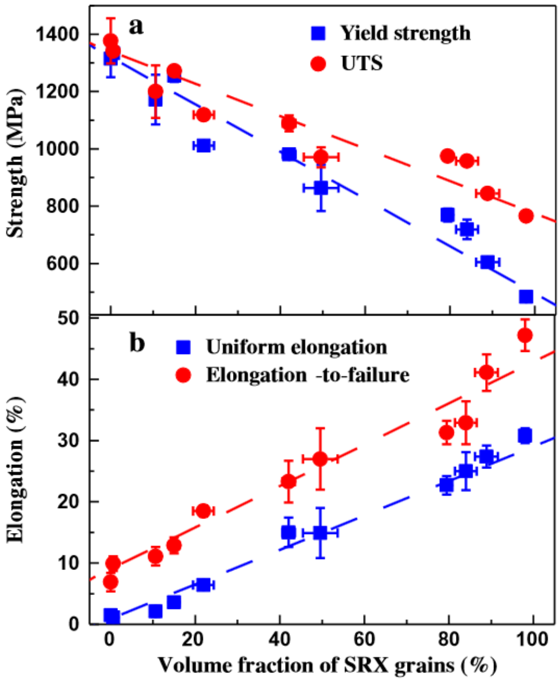

Fig. 2.12 Mechanical properties of a 316L steel after dynamic plastic deformation to a strain of 1.6. Strength and ductility of the material depend on the volume fraction of recrystallized grains (SRX). (From [101]).

2.6 Overview of this thesis

In the present study, two steels with potential applications for nuclear reactors, namely modified 9Cr-1Mo ferrtic/martensitic steel with carbides strengthened, and oxide dispersion strengthened (ODS) ferrtic steel, were nanostructured by plastic deformation at high strain rates, and the resulting microstructure and annealing behavior of the nanostructured steels were studied in detail.

Chapter 3 introduces the materials and techniques applied in this study. Dynamic plastic deformation (DPD) was employed to refine the structure of the steels. After nanostructuring, the materials were annealed at a variety of temperatures to examine the thermal stability of the nanostructured steels, and to investigate the evolution of microstructure and mechanical properties during annealing. Transmission electron microscopy (TEM), electron backscattered diffraction (EBSD) were used to characterize the microstructural and textural evolution of the steels during DPD and subsequent annealing. Besides, techniques including high resolution TEM (HRTEM), scanning TEM (STEM), electron dispersive X-ray spectrum (EDS), were extensively applied to study the character of the oxide dispersoids in the as-received ODS steel, and their behavior during annealing and plastic deformation. Mechanical properties of the deformed and annealed materials were evaluated by tensile tests and Vicker’s hardness measurements.

Chapter 4 reports the studies of the modified 9Cr-1Mo ferrtic/martensitic steel. The microstructure evolution in this steel subjected to DPD was characterized from low to high strains. The microstructure of this steel was transformed from a coarse tempered martensitic structure to a nanoscale lamellar structure after DPD to high strains. The nanostructured steel was then annealed at elevated temperatures to reveal its thermal stability, recovery and recrystallization behavior. A pronounced orientation dependent recovery and recrystallization phenomenon was found and investigated in detail. It is established that both oriented nucleation and oriented growth contribute to this orientation dependence. Furthermore, the effect of strain rate on the work hardening, plastic deformation induced microstructure and the subsequent annealing behavior of this modified 9Cr-1Mo steel was analyzed, in order to verify the results and conclusions obtained on the DPD-processed steel could be expanded to this steel deformed by conventional techniques.

Chapter 5 reports the studies of the ODS ferrtic steel. Since the oxide dispersoids are of vital importance, the character of the oxide nanoparticles in the as-received and high temperature annealed samples including their crystallographic structure and the interface with the ferrite matrix was identified. Nanostructured ODS steel was obtained by DPD to high strains, and resulting microstructure is in general resembled to that of DPD-processed modified 9Cr-1Mo steel. Similar orientation dependent recrystallization behavior was identified in the nanostructured ODS steel as well, and the same mechanism as that of modified 9Cr-1Mo steel was suggested. Remarkably, the oxide nanoparticles mainly with diameters smaller than 20 nm were found to be substantially deformed to large strains. The deformation mechanism of the oxide nanoparticles was revealed, and the co-deformation behavior of oxide nanoparticles and ferrite matrix was characterized at different strains. Furthermore, the effect of interfacial character between the oxide nanoparticles and the matrix, and imposed strain rates on the deformation of oxide nanoparticles was clarified. Interestingly, when the sample with deformed oxide nanoparticles was annealed, the morphology of the oxide nanoparticles changed significantly, and the oxide particles were found to be largely refined compared to those in the as-received material.

In Chapter 6, a general comparison of deformed microstructure and annealing behavior between these two steels was given. The difference due to the initial microstructure and the dispersoids was analyzed.

Chapter 7 summarized the main findings of this study and conclusions were presented. An outlook and perspective coming from this study were also given in this chapter.

Chapter 3

Materials and experimental techniques

This chapter briefly introduces the two materials studied in this work. Then the deformation techniques including dynamic plastic deformation (DPD) and quasi static compression (QSC) is described. Methods for evaluating mechanical properties of the as-received, deformed and subsequently annealed materials are presented. Characterization techniques including EBSD, conventional TEM, HRTEM, and STEM are described.

3.1 Materials

3.1.1 Modified 9Cr-1Mo steel

The modified 9Cr−1Mo steel (X10CrMoVNb9−1) was supplied by Remystahl Gmbh & Co KG in the form of a hot-extruded rod, normalized at 1040 °C for 1.4 h, tempered at 770 °C for 5 h and finally stress-relieved at 740 °C. The chemical composition of the modified 9Cr−1Mo steel determined by glow discharge optical emission spectroscopy (GDOES) is shown in Table 1.

Table 1 Chemical composition (wt. %) of modified 9Cr−1Mo steel as determined by GDOES

C	Cr	Mo	V	Ni	Nb	W	Si	Mn	P	S	Fe
0.11	8.20	0.98	0.20	0.16	0.07	0.01	0.31	0.51	0.02	<0.01	Balance

3.1.2 PM2000

An ODS ferritic steel, PM2000, was received in the form of a hot-extruded bar with a diameter of 13 mm [102], initially produced in Plansee GmbH Austria with the nominal composition shown in Table 2 [102]. This steel was produced using mechanical alloying of the components using high energy ball milling to produce a solid solution containing uniform yttria. After ball milling, the powder was consolidated by hot isostatic pressing and then extruded into bars [103].

Table 2 Nominal chemical composition (wt. %) of PM2000.

Cr	Al	Ti	Y_2O_3	Fe
20	5.5	0.5	0.5	Bal.

3.2 Deformation technique

3.2.1 Dynamic plastic deformation

DPD is an axisymmetric deformation technique established at the Institute of Metal Research, Chinese Academy of Science, Shenyang, China [71]. The set-up is illustrated in Fig. 3.1. A cylindrical sample is placed on the lower anvil, and compressed by a falling upper anvil (20 kg). This deformation process is dynamic, i.e. the strain rate varies during the deformation process, with the maximum strain rate mainly depending on the release height of the falling hammer. The sample can be compressed by several strokes to a desired strain. The thickness reduction in each pass can be controlled by a large ring with a certain thickness placed around the sample on the lower anvil to stop the hammer at a certain height. The deformation temperature can be changed, from an elevated temperature to the temperature of liquid nitrogen.

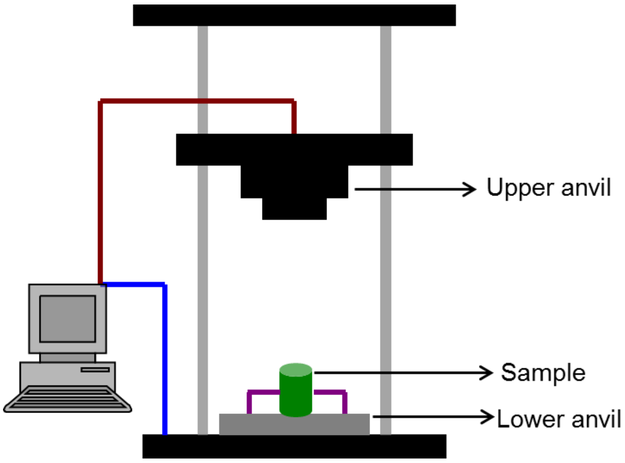

Fig.3.1 A schematic illustration of the DPD set-up.

In this work, the modified 9Cr-1Mo steel and PM2000 are deformed by DPD at room temperature to different strains. Cylindrical samples were machined from the bars with a diameter of Ø9×12 mm and Ø6×9 mm for modified 9Cr-1Mo steel and PM2000, respectively. The compression axis (CA) of the samples is along the initial extrusion axis of the bars. The release height of the hammer was 1.9 m. The initial strain rate imposed on the sample was estimated to be about 10^2-10^3 s^{-1}. Samples were deformed to equivalent strains ranging from 0.2 to 2.3 by different number of passes. The microstructure is quite homogeneous across the samples after DPD to a strain of 1.4 and above, whereas for the samples deformed to lower strains, microstructural analysis was conducted near the sample center.

3.2.2 Quasi static compression

In order to reveal the strain rate effect on the microstructure, annealing behavior and mechanical properties of the investigated materials, QSC was carried out at room temperature with initial strain rates ranging from 10^{-4} s^{-1} to 10^{-1} s^{-1}. QSC was conducted on an Instron testing machine at the Department of Wind Energy, DTU. To eliminate the friction stress on the top and bottom contacting surface of the compressed samples, MoS_2 was used as lubricant.

3.3 Mechanical tests

3.3.1 Tensile test

Tensile tests of the samples after DPD and subsequent annealing were conducted using an Instron 5848 MicroTester in IMR, Shenyang. Dog-bone shaped tensile test specimens with a gauge section of $5 \times 1 \times 0.5$ mm^3 were prepared and tested at room temperature with an initial strain rate of 5×10^{-3} s^{-1}.A MTS LX300 laser extensometer was used for measuring engineering strain during the test.

3.3.2 Hardness test

A Struers DuraScan fully automatic hardness tester was used for Vickers hardness measurement. The tester was equipped with a diamond indenter of a pyramidal shape, have a square base and an angle of 136^o between opposite faces. A load of 1000 g and a dwell time of 10 s were used. The hardness values were derived by measuring the diagonals of the indentation.

3.4 Characterization

3.4.1 Electron backscattered diffraction

EBSD in a scanning electron microscope is a widely used technique for texture measurements. EBSD is based on acquisition and analysis of backscattered Kikuchi diffraction patterns from the surface of a specimen. As illustrated in Fig. 3.2 [104], a stationary electron beam of electrons hits the specimen surface, and backscattered electrons are diffracted at crystal lattice planes within the probe volume according to Bragg's law. In order to reduce the path length of backscattered electrons and maximize these electrons escape from the specimen, the sample is 20^o inclined to the incident beam. In this case, diffraction pattern arise from typically up to 50 nm thick layer from the sample surface.

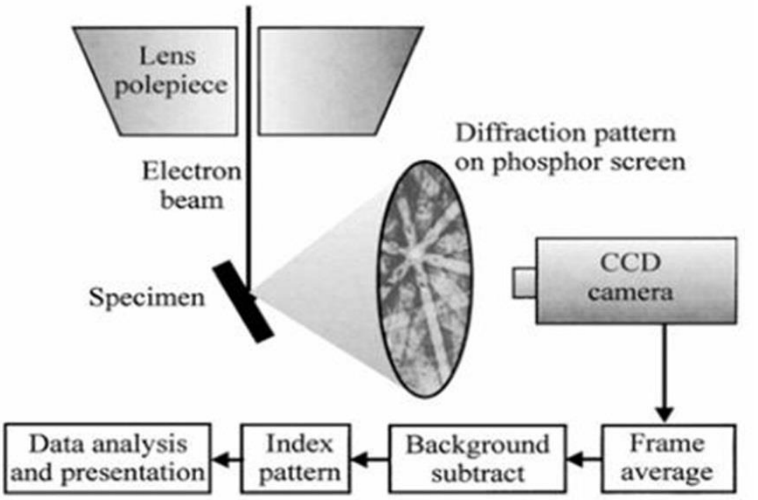

Fig. 3.2 Schematic diagram of a basic EBSD set-up. (From [104]).

In this study, a Zeiss Supra-35 FEG SEM, equipped with an HKL Channel 5 EBSD system, was used for texture analysis and orientation mapping. The microscope was operated at 20 kV for EBSD acquisition, and the nominated spatial and angular resolution were about 20 nm and 1^o, respectively. Samples for EBSD analysis were grinded and mechanically polished followed by electropolishing in a solution of ethanol (70%), water (12%), 2-butoxy-ethanol (10%), and perchloric acid (8%) at about -10 °C for about 30 seconds with a voltage of 25 V. For data acquisition, the step size varied between samples after different treatments: the smallest step size of 20 nm was used for the samples after DPD to a strain of 2.3, whereas larger step sizes were used after lower strains and for the annealed conditions. The HKL Channel 5 software was used to process the EBSD data. During data processing, the minimum misorientation angle to define a boundary was set to be 2^o. Low angle boundaries (LABs) and high angle boundaries (HABs) were defined as boundaries with misorientation between 2^o and 15^o, and larger than 15^o, respectively.

Recrystallized grains were identified automatically from the EBSD data by the DRG program developed by Wu *et al.*[105]. The recrystallizing grains must fulfil the following criteria: 1) The internal misorientation within a recrystallizing grain should be smaller than 2^o; 2) the size of recrystallizing grains should be larger than a critical value (in this study an equivalent circular diameter (ECD) of 3 μm was used); 3) the recrystallizing grains should be at least partially surrounded by HABs.

3.4.2 Transmission electron microscopy

TEM is a very powerful and versatile technique for characterizing microstructures. It can be used not only to image microstructures and defects, but also to gain information from about the crystal structure, crystallography, lattice parameters, etc, of the constituent phases in the microstructure. A schematic diagram of a TEM illustrating the electron waves is shown in Fig. 3.3. There are three principle planes, namely the sample plane, the image plane and the focal plane of the objective lens. When an electron beam passes through the thin specimen, interacts with the specimen and enters the objective lens, the transmitted and diffracted beams satisfying the Bragg condition are focused at the back focal plane of the objective lens and form an electron diffraction pattern there. The resulting diffraction pattern reflects (part of) the reciprocal space, which is mathematically obtained from the real space by Fourier transformation.

In the present study, two types of TEM techniques were used, namely conventional TEM and high resolution TEM (HRTEM). For conventional TEM characterization with the main purpose of imaging and diffraction analysis, a JEM 2000FX transmission electron microscope, equipped with a LaB6 filament and a charge-coupled device (CCD) camera, was used. It was operated at an accelerating voltage of 200 kV, and the best point resolution was 0.3 nm.

To achieve a higher resolution for more detailed characterization, especially for analyzing nanoscale oxide particles in PM2000, HRTEM was used. A JEM 3000F TEM, with a field-emission electron gun, was operated at 300 kV, and the point resolution was 0.19 nm. The obtained HRTEM images were analyzed in the Gatan DigitalMicrograph software. For assistance, a software suite CaRIne Crystallography 3.1 was used to construct the crystal structures and simulate the diffraction pattern of oxide nanoparticles.

HRTEM images are phase-contrast images and result from the interference of the transmitted and diffracted electron beams. Fast Fourier transformation (FFT) is used to construct the spatial frequency on the back focal plane of the electron microscope. In this study, the software of Gatan DigitalMicrograph is employed for FFT processing. FFT patterns are analogous to the selected area electron diffraction patterns in conventional TEM, which can be used to identify the orientation relationship between different components. Fourier mask filtering is widely used to produce a contrast-enhanced image by applying a suitable spatial frequency filter in the Fourier space. If the transmitted and the diffracted beams interfere on the image plane, the reciprocal space can be reconstructed in real space to form an image corresponding to its inverse fast Fourier transformation (IFFT). Generally, Fourier mask filtering is used to select certain spatial frequencies in reciprocal space and reconstruct a direct specimen image from the filtered spatial frequencies by applying the FFT-IFFT transformation.

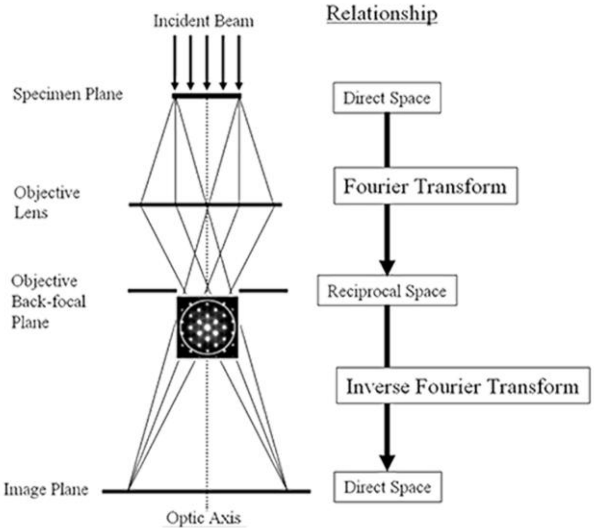

Fig.3.3 A simplified schematic diagram of a TEM and the mathematical relationships described the three principle planes: specimen plane, objective back focal plane and image plane.

In addition, scanning TEM (STEM) was employed to analyze the oxide nanoparticles in PM2000. For this technique, the electron beam is focused on to a narrow spot which is scanned over the sample in a raster. The obtained STEM images mainly show the mass contrast, where regions with lower density and/or including lighter elements are imaged with darker contrast and vice versa. As oxygen atoms is lighter than iron atoms, oxide particles appear to be darker than the iron matrix. Hence STEM is very suitable for analysis of the oxide nanoparticles in PM2000. Besides, scanning of an electron beam across the sample enables mapping by energy dispersive X-ray (EDX) spectroscopy and electron energy loss spectroscopy. EDX was used to determine the chemical composition of the oxide nanoparticles in PM2000. A FEI Tecnai F30 transmission electron microscope equipped with a Schottky field-emission electron gun and operated at 300 kV was used for this purpose. This microscope enables mass contrast imaging by detection of the electrons scattered to a high-angle annular dark-field (HAADF) detector, and thereby reducing the normal diffraction contrast. The collection angle of the HAADF detector is between 55-245 mrads, with a camera length of 200 mm. This microscope was also equipped with an EDX system from EDAX, containing a Li-drifted Si detector, with an energy resolution which was measured to 130 eV.

TEM foils with large electron-transparent regions were prepared using a modified window technique developed by Chistiansen *et al.*[106]. Samples were cut from the section of interest and grinded to 100 μm in thickness and electropolished in a solution of ethanol (70%), water (12%), 2-butoxy-ethanol (10%), and perchloric acid (8%) using the modified window technique. To enable HRTEM characterization, the foils were further thinned and cleaned by ion milling. Ion milling was conducted on a Gatan precise ion milling system, operating at 3.5 kV.

Chapter 4

Microstructure and annealing behavior of a nanostructured ferritic/martensitic steel

In this chapter, the microstructural evolution and mechanical behavior of a modified ferritic/martensitic modified 9Cr-1Mo steel compressed by DPD at room temperature from low to high strains are studied, and the annealing behavior of the highly strained material is analyzed and discussed in detail.

Significant structural refinement is achieved in the modified 9Cr-1Mo steel by DPD, and a nanoscale lamellar structure is obtained after DPD to a strain of 2.3. The strength of the modified 9Cr-1Mo steel is significantly improved by DPD, however, the thermal stability of this DPD-processed steel is reduced. Annealing at 600 °C and above for 1 hour leads to a considerable reduction in strength as a result of pronounced recovery and recrystallization. The processes of recovery and recrystallization in the DPD-processed steel strongly depend on the crystallographic orientation of the deformed microstructure. This issue is explored by detailed EBSD and TEM characterization, with regard to the underlying mechanism of oriented nucleation and/or oriented growth.

To clarify the effect of strain rate on the deformed microstructure and mechanical properties of the modified 9Cr-1Mo steel, samples of the DPD-processed modified 9Cr-1Mo steel are compared with those processed by quasi static compression (QSC) at a wide range of strain rates. The work hardening behavior of the modified 9Cr-1Mo steel for different strain rates is analyzed, and the difference in the microstructural parameters of the DPD-processed and QSC-processed material is revealed. The effects of strain rate on the subsequent annealing behavior are described.

4.1 Microstructural evolution of the modified 9Cr-1Mo steel during DPD

In this subsection, the initial microstructure is first reported, and then the microstructural and textural evolution with strain from 0.2 to 2.3 is described in detail.

4.1.1 Microstructure: as-received modified 9Cr-1Mo steel

The microstructure of the as-received modified 9Cr-1Mo steel characterized by EBSD is shown in Fig. 4.1a. In this misorientation map, LABs (2–15°) and HABs (>15°) are presented as thin grey and bold black lines, respectively. The distribution of misorientation angles of all boundaries is shown in Fig.4.1b, and the fraction of HABs is measured to be 46%. The steel was delivered in the quenched and tempered state, and thus its microstructure is characterized as tempered martensite. Prior austenite grain boundaries (PAGB) are preserved during quenching and tempering, and some of them are indicated in the boundary map (Fig.4.1a). Martensitic boundaries originating from the martensitic phase transformation during quenching keep their characters after tempering.

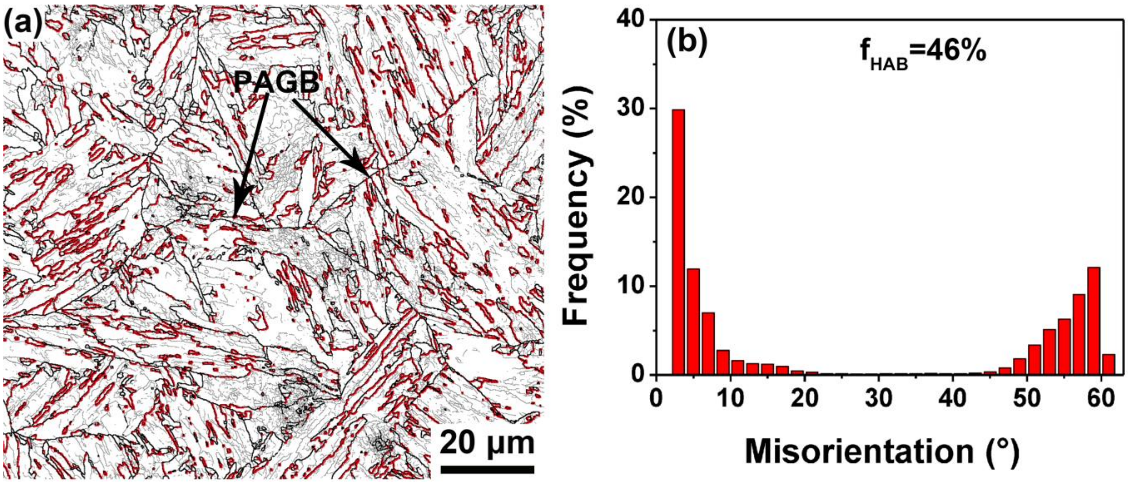

Fig.4.1 (a) Misorientation map obtained by EBSD from the as-received modified 9Cr-1Mo steel. Thin gray and bold dark lines show LABs (2–15°) and HABs (>15°), respectively. Boundaries with either 60°⟨111⟩, 60°⟨110⟩, or 49.5°⟨110⟩ misorientations are shown in red. Prior austenite grain boundaries (PAGB) are indicated by arrows. (b) Distribution of misorientation angles obtained from the boundaries in (a).

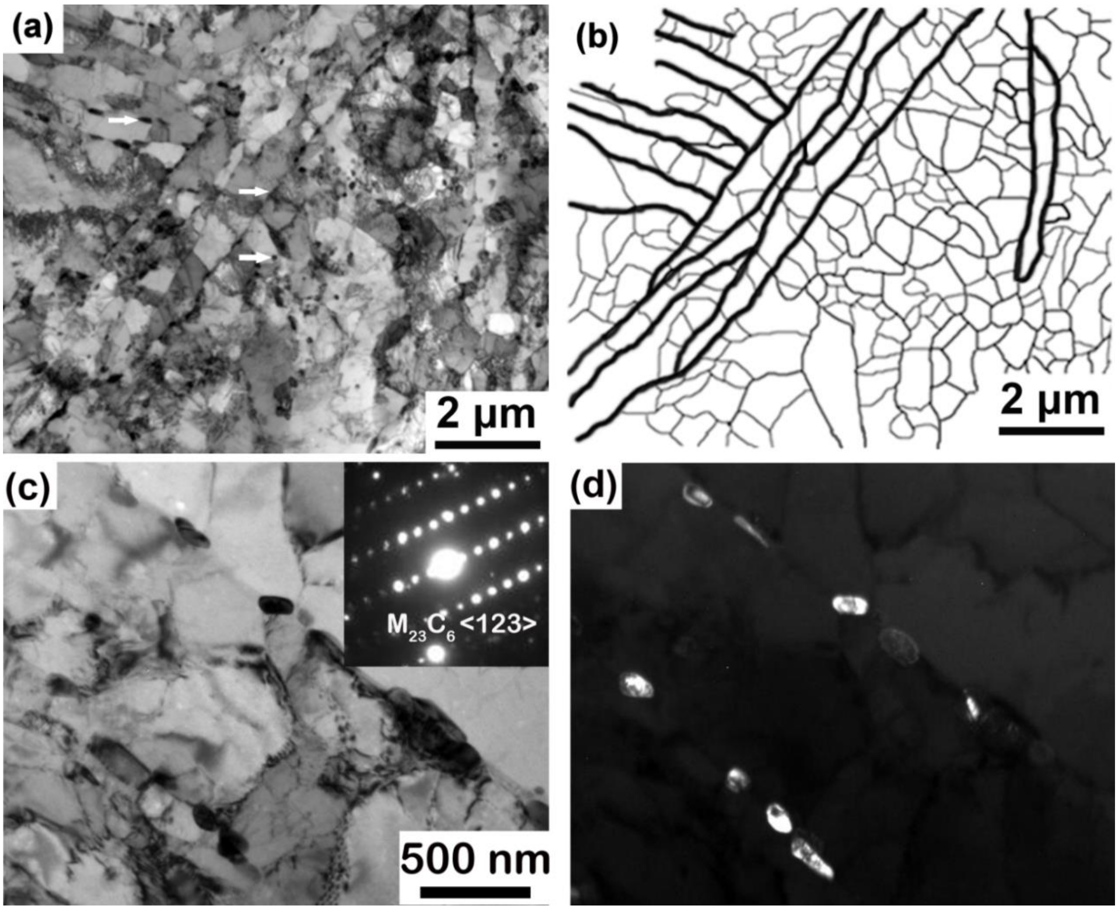

Fig. 4.2 Microstructure of the modified 9Cr-1Mo steel in the as-received condition: (a) Bright field TEM image and (b) a corresponding sketch of the microstructure. (c) A bright field TEM image and (d) a corresponding dark field image based on diffraction from carbide, showing carbide particles located at the martensitic boundaries. Some carbides are indicated by arrows in (a). Martensitic boundaries are represented in bold black lines in (b). The selected area diffraction pattern in (c) demonstrates that the particles are $M_{23}C_6$ type carbides.

In low carbon steel, the orientation relationship between lath martensite (α') and austenite (γ) can be rationalized by Kurdjumov-Sachs (K-S) relationship [107, 108]. It is expressed as: $(111)\gamma//(011)\alpha'$, $[\bar{1}01]\gamma//[\bar{1}\bar{1}1]\alpha'$. Due to the cubic symmetry, there are 24 equivalent martensite variants which can develop in a single austenite grain. Based on this orientation relationship between the martensitic variants, a three-level hierarchical structure is usually used to describe a typical martensitic structure, containing martensitic lath, block, and packet [108, 109]. A martensitic lath is a single martensite lamella with a high density of dislocations. A block is a family of laths of the same martensitic variant and with small misorientations between them. A packet consists of blocks with the same habit plane ({111}γ) in the same austenite grain. There are four different {111}γ habit planes, and all of them in a single prior austenite grain. Therefore, the martensitic block boundaries (MBB), i.e. boundaries between different martensitic variants, have some specific misorientations, which can be revealed by EBSD. According to the K-S orientation relationship, there are six possible martensitic variants in each packet (having the same {111}γ habit plane), and only four different misorientation relationships between them can develop, namely 60°⟨111⟩, 60°⟨110⟩, 49.5°⟨110⟩ and 10.53°⟨110⟩ [109]. In the misorientation map obtained by EBSD (Fig. 4.1a), boundaries with misorientations deviating by less than 5° from these particular orientation relationships are classified as MBBs, and are shown in red in the boundary map. In order to avoid confusion with the LABs developed during tempering of martensite, only those boundaries with high misorientation angles are taken into account. Thus 10.53°⟨110⟩ is not highlighted in the map. It is evident that the majority of MBBs are HABs. This is the reason for the significant HABs fraction in the as-received microstructure (seen in Fig. 4.1b).

TEM analysis of the as-received modified 9Cr-1Mo steel indicates that whereas subgrains have developed within the martensitic laths after tempering, former martensite laths can still be recognized in the microstructure (see Fig. 4.2a, b). The average width of such martensitic laths is about 750 nm, and the average subgrain boundary spacing is about 650 nm. The dominant particle type in the microstructure is $M_{23}C_6$ carbides (Fig. 4.2c). These particles are mainly observed at PAGBs and martensitic boundaries (Fig. 4.2c, d), while much smaller MX type carbonitride particles are distributed randomly in the matrix.

4.1.2 Microstructure: DPD to a low strain (ε_{vM}=0.2)

TEM images in Fig. 4.3 show the microstructure of the modified 9Cr-1Mo steel compressed by one stroke of DPD to a strain of 0.2. It is clear that the dislocation density in this microstructure is much higher compared to that before deformation (Fig. 4.2c). Although lots of dislocation tangles and dislocation boundaries form in the interior of the initial martensitic laths (Fig. 4.3b), most of the martensitic boundaries can still be recognized. Therefore, after deformation to such a low strain, the general feature of the tempered martensite is preserved, with new dislocation boundaries and dislocation tangles developed in the martensitic structure.

Most of the carbides are still visible after deformation, as shown in Fig. 4.4, and they are still located at the martensitic boundaries. Besides, it is seen that the dislocation density is higher in the regions near the carbides, which is typical when strain gradients emerge due to a heterogeneous deformation of two components. These dislocations generated to accommodate the elastic strain gradient are called geometrically necessary dislocations (GND) [73].

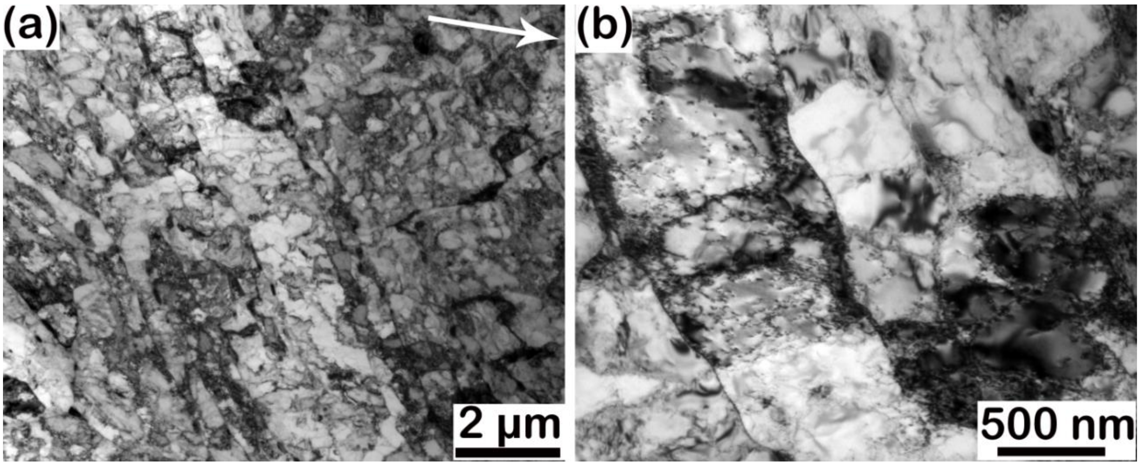

Fig. 4.3 TEM images of the modified 9Cr-1Mo steel in longitudinal section after DPD to a strain of 0.2: (a) overview of the microstructure, (b) magnified image showing more details. The CA is indicated by the arrow.

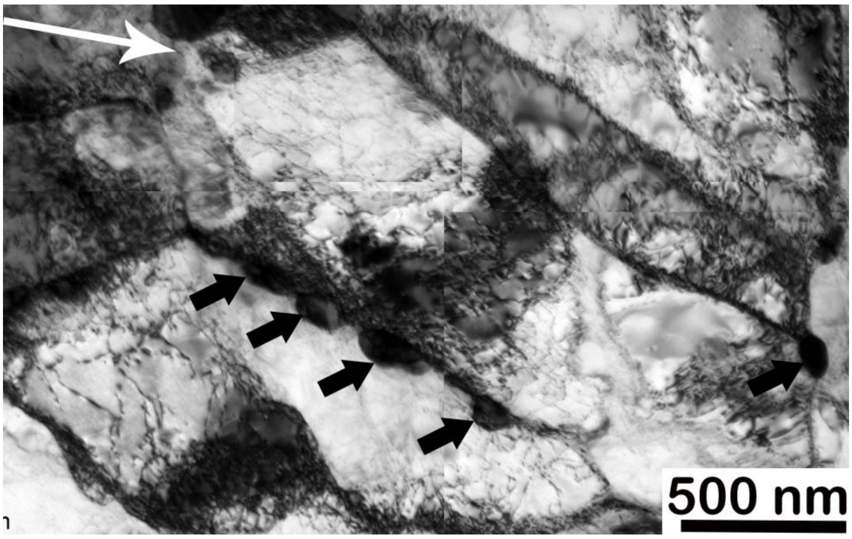

Fig. 4.4 TEM image of the modified 9Cr-1Mo steel in longitudinal section after DPD to a strain of 0.2, showing the microstructure around carbides (indicated by black arrows). The CA is indicated by the white arrow.

4.1.3 Microstructure: DPD to a medium strain (ε_{vM}=0.5)

After DPD to a strain of 0.5, the microstructure of the modified 9Cr-1Mo steel further refined, as shown in Fig. 4.5. A very fine dislocation cell structure is developed, and the initial martensitic boundaries and PAGBs are no longer distinguishable. This suggests that the tempered martensitic structure has been transformed into a typical dislocation cell structure. The dislocation cells are slightly elongated in the compression plane. It is evident from Fig. 4.5b that some dislocation boundaries are quite sharp with relatively clean cell interiors (having lower dislocation density), whereas in other regions dislocation cell boundaries are not well-developed and the microstructure is still in the form of dislocation tangles.

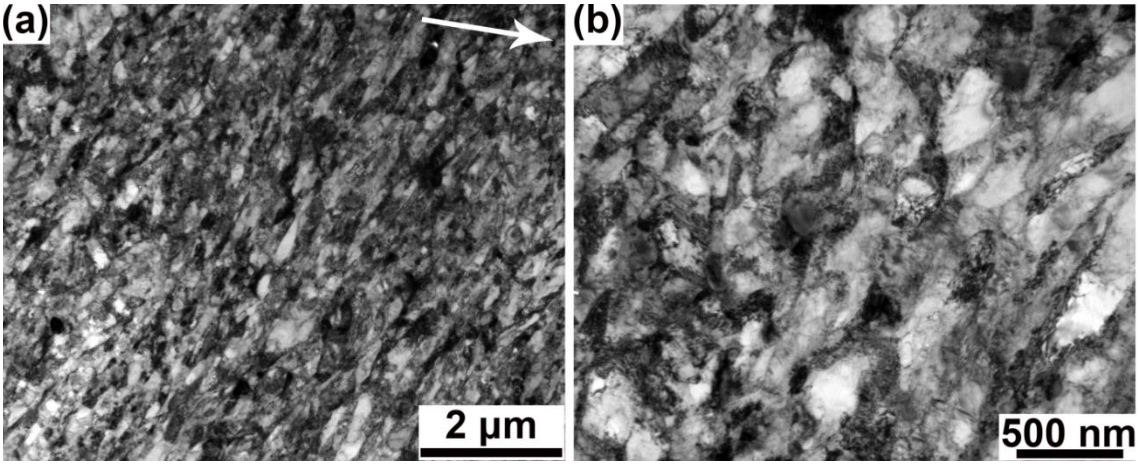

Fig. 4.5 TEM images of the modified 9Cr-1Mo steel in longitudinal section after DPD to a strain of 0.5: (a) an overview of the microstructure, (b) magnified image showing more details. The CA is indicated by the white arrow.

At this stage, the carbides become less visible, which can be a result of two processes: (i) the interference in recognizing carbides due to the high density of dislocations; and (ii) dissolution or partial dissolution of some carbides due to plastic deformation [110-112]. Based on selected area diffraction (SAD) patterns, a dark field image with the diffraction only from the carbides can be obtained (Fig. 4.6b), and thus the locations of the carbides are revealed clearly (Fig. 4.6c). A higher density of dislocation is seen in the regions around the carbides. Well-developed dislocation cell structure with a relatively low dislocation density interior is seen around some particles. Besides, the microstructure indicates that the initial boundaries become bended around some of the particles. These features are quite different from the microstructure in the regions without carbide particles. This suggests that the higher density of GNDs stored around the carbides at this strain may affect the microstructure evolution in the neighborhood. This is considered to be an important influence from the carbide particles on the microstructure evolution of modified 9Cr-1Mo steel deformed to medium strains.

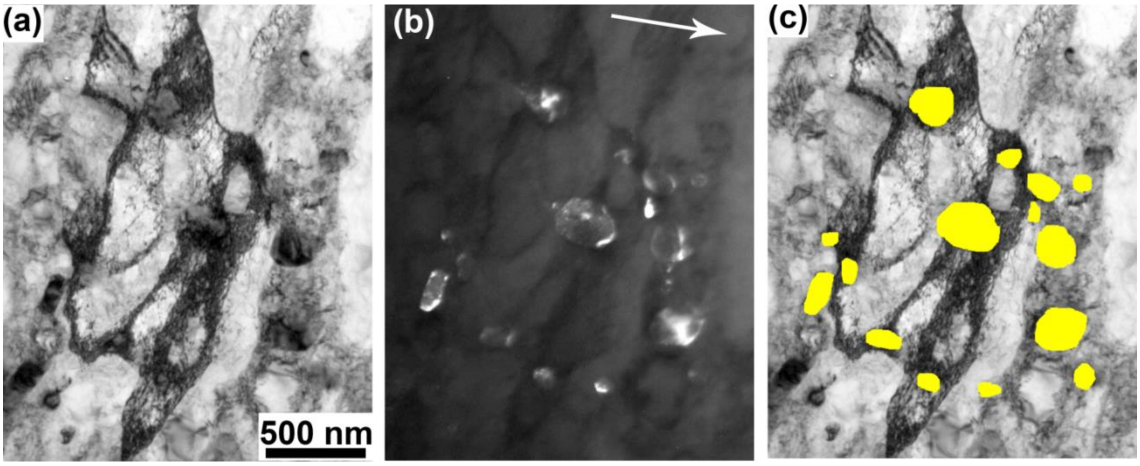

Fig. 4.6 Microstructure of the modified 9Cr-1Mo steel in longitudinal section after DPD to a strain of 0.5: (a) Bright field and (b) its corresponding dark field TEM images, (c) the same bright field image with carbides highlighted in yellow. The CA is indicated by the white arrow.

4.1.4 Microstructure: DPD to high strains (ε_{vM}=1.4 and 2.3)

With increasing DPD strain, the microstructure of the modified 9Cr-1Mo steel is further refined, the misorientations across the dislocation cell boundaries increase, and the nearly equiaxed cell structure gradually evolves into a lamellar structure. As shown in Fig. 4.7, lamellar boundaries nearly perpendicular to the CA are present in the sample after DPD to a strain of 1.4. The features of the initial martensitic structure totally vanish after deformation to this strain, and no martensitic boundaries can be recognized any longer. However, a dislocation cell structure still exists in some regions.

After DPD to a strain of 2.3, an ultrafine lamellar structure is observed in the modified 9Cr-1Mo steel, with lamellar boundaries nearly perpendicular to the CA (Fig. 4.8a). Compared to the microstructure after DPD to a strain of 1.4, the lamellar spacing is finer and the boundaries between the lamellae are sharper. Fig. 4.8b shows the distribution of the lamellar thicknesses measured for 530 lamellae. The mean thickness of the lamellae is about 98 nm. Thus after this strain a real nanostructure is obtained in the modified 9Cr-1Mo steel. More details of the microstructure are presented in Fig.4.8c at a higher magnification. It can be seen that the deformation-induced boundaries can be classified into two categories: (i) lamellar boundaries approximately perpendicular to the CA, which are usually defined as extended geometrically necessary boundaries (GNBs) [55], and (ii) boundaries that interconnect the GNBs, which are termed as incidental dislocation boundaries (IDBs) [55]. These two types of boundaries are highlighted in Fig.4.8d, where GNBs and IDBs are represented by bold and thin lines, respectively. Within the lamellae, there is a high density of dislocations. This structure is typical for *bcc* and *fcc* metals with medium to high stacking fault energies after plastic deformation to high strains [10, 52]. It is clear that although the initial modified 9Cr-1Mo steel has a martensitic structure, the final microstructure after DPD to high strains resembles the deformed microstructure of materials with conventional grain structures in the initial condition.

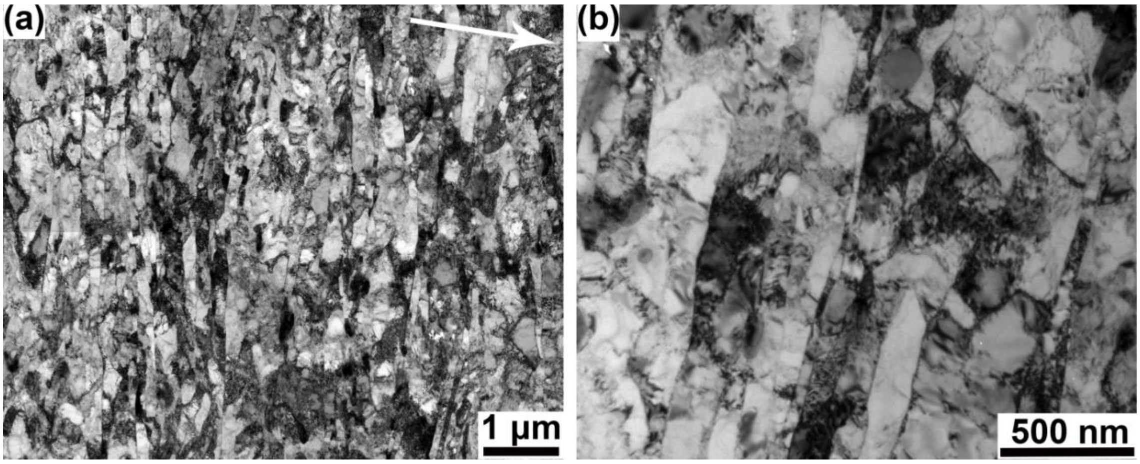

Fig. 4.7 TEM images of the modified 9Cr-1Mo steel in longitudinal section after DPD to a strain of 1.4: (a) an overview of the microstructure, (b) magnified image showing more details. The CA is indicated by the arrow.

TEM images in Fig. 4.9 reveal the effect of carbide particles on the microstructure around them. It is clear that the lamellar boundaries bend around some relatively large particles (Fig. 4.9a), thereby forming so-called particle deformation zones (PDZs) [84]. The formation of pronounced PDZs depends on the particle size [98], and no appreciable PDZ is found in this work around the particles smaller than 100 nm. However, another important microstructural feature can be observed around such small particles. From the two examples presented in Fig. 4.9b,c, it can be seen that in addition to the high dislocation density in the neighboring matrix, lamellae in the vicinity of such carbides are much thinner than those in region far from carbides. These much thinner lamellae are thought to originate from the suppression of dynamic recovery in the neighborhood due to the pinning at carbides. The underlying mechanism will be discussed in the section 4.1.6.

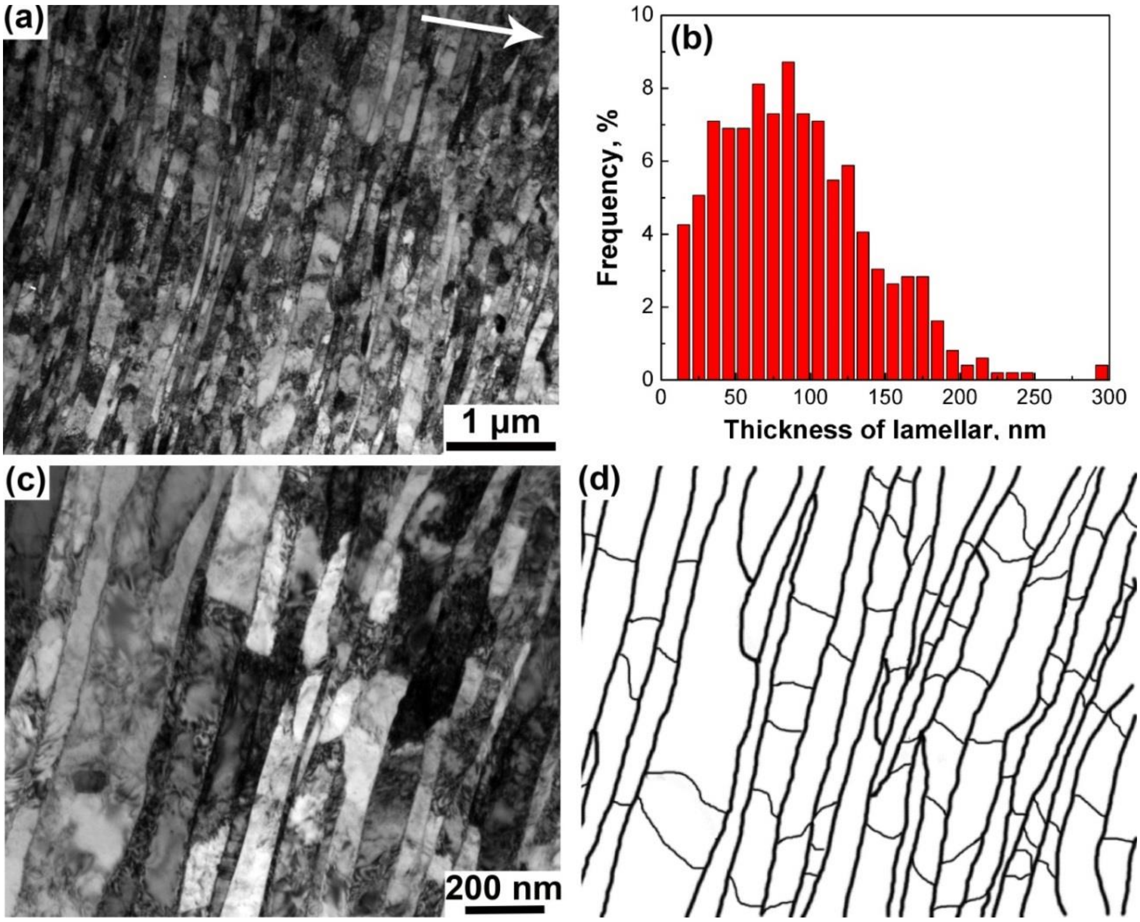

Fig. 4.8 TEM images of the modified 9Cr-1Mo steel in longitudinal section after DPD to a strain of 2.3: (a) general overview of the microstructure at a low magnification; (b) distribution of thicknesses along the CA of 530 measured lamellae. (c) bright field image at a higher magnification showing more details; and (d) the corresponding sketch of (c), in which extended planar boundaries and interconnecting boundaries are represented by bold and thin lines, respectively. The CA is indicated by the arrow.

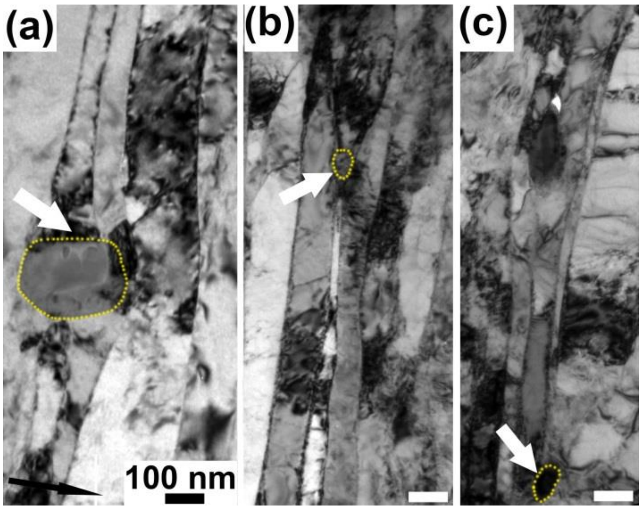

Fig. 4.9 TEM images of the 9Cr–1Mo steel in longitudinal section after DPD to a strain of 2.3 showing the microstructure in the vicinity of (a) coarse carbide particle and (b, c) small carbide particles marked by dashed lines and white arrows. The CA is indicated by the black arrow.

4.1.5 Evolution of the microstructural parameters

Complementary to the TEM observations, more microstructural parameters can be analyzed from EBSD data. Fig. 4.10 shows orientation maps obtained by EBSD of the modified 9Cr-1Mo steel after DPD to strains of 0.5, 1.4 and 2.3. At a strain of 0.5 (Fig. 4.10a), the initial martensitic structure is almost vanished. A high frequency of LABs (white lines) is formed, which results in a significant decrease of the fraction of HABs, from 46% in the received condition to 23% after DPD. The boundary spacing of HABs and LABs drops dramatically (Fig. 4.11a), from 1110 nm and 2040 nm, to 210 nm and 810 nm, respectively, i.e. a significant structural refinement is achieved.

With increasing strain to 1.4, the microstructure becomes less equiaxed, as shown in Fig. 4.10b. The fraction of HABs increases to 34%, which indicates that a large fraction of deformation-induced dislocation boundaries develop high misorientations. The spacings between boundaries with misorientation angles above 2° and between boundaries with misorientations angles above 15° decrease to 400 nm and 149 nm, respectively. In the material deformed to a strain of 2.3, a very fine lamellar structure is developed, and the fraction of HABs further increases to 50%.

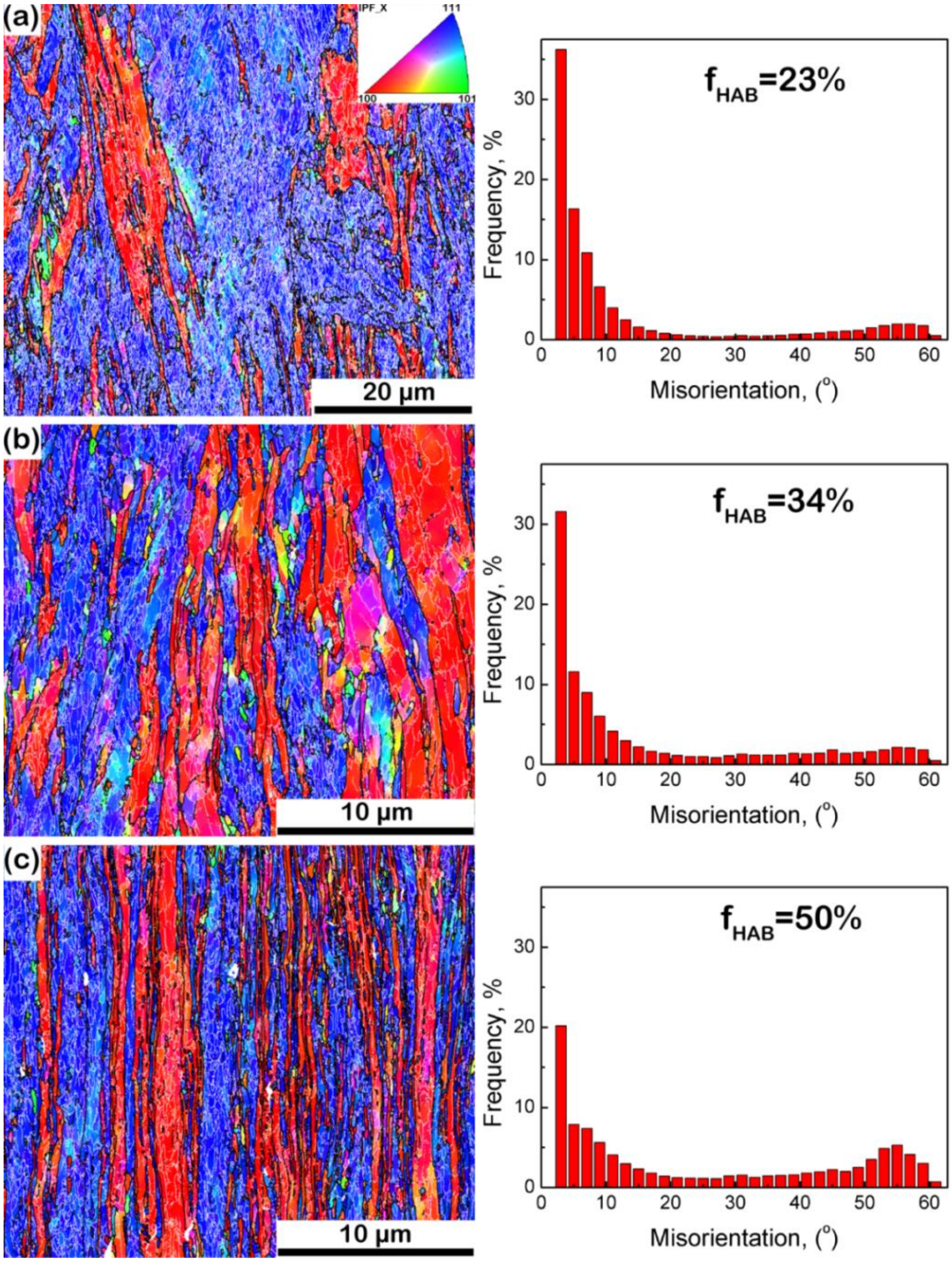

Fig. 4.10 Orientation maps obtained by EBSD of the 9Cr–1Mo steel in longitudinal section after DPD to different strains: (a) 0.5, (b) 1.4, and (c) 2.3. These orientation maps represent the crystallographic direction along CA according to the inverse pole figure in the inset in (a). Thin white and bold dark lines show LABs (2–15°) and HABs (>15°), respectively. The CA is horizontal. The distributions of misorientation angles of all boundaries obtained from the corresponding orientation maps are shown on the right side.

Quantitative determination of the boundary spacing along the CA (Fig. 4.11a) shows that the spacing between boundaries with misorientation above 2° is 111 nm, which is slightly higher than that measured in TEM images. This is typical when comparing the results of TEM and EBSD measurements of the boundary spacing [113], because in the EBSD analysis boundaries with misorientation less than 2° are disregarded due to the limited angular resolution of the EBSD technique. The boundary spacing between HABs also decreases significantly to 200 nm. Fig.4.11a reveals the general trends for the boundary spacing and the fraction of HABs with increasing of strain during DPD: the boundary spacing and the fraction of HABs drop dramatically when the material is deformed to 0.5. The boundary spacings decrease slowly with a further increase in strain to 2.3, whereas the fraction of HABs gradually increases.

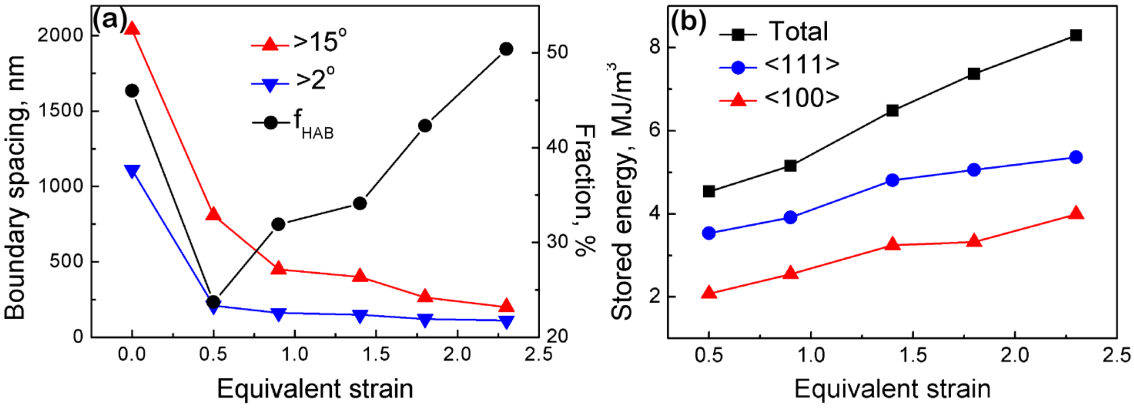

Fig. 4.11 Microstructural parameters of the modified 9Cr-1Mo steel deformed by DPD: (a) Spacings between boundaries with misorientation angles above 2°, and above 15° (HABs), and fraction of HABs after DPD to different strains. (b) Stored energy in the whole measured area (marked “Total”), and the subsets representing either ⟨100⟩ or ⟨111⟩ texture components calculated from the samples after DPD to different strains.

Another important parameter of the deformed material is the deformation texture. In the orientation maps colored according to the crystallographic direction along the CA, it is seen that blue and red colors dominate, which means that the majority of crystals are oriented in such a way that either ⟨100⟩ or ⟨111⟩ directions are along CA. {001}, {110} and {111} pole figures obtained by EBSD on the sample deformed to a strain of 2.3 shown in Fig. 4.12 demonstrate a very pronounced ⟨100⟩+⟨111⟩ duplex fibre texture with a little stronger ⟨100⟩ component and a weaker ⟨111⟩ component.

A TEM image from the sample after DPD to a strain of 2.3 is shown in Fig. 4.13. The orientations of the individual lamellae were determined by SAD patterns, and the ⟨100⟩ and ⟨111⟩ oriented lamellae are separated by dash lines. This duplex fiber texture is common for *bcc* metallic materials after uniaxial compression, which can be predicted by the classic Taylor-Bishop-Hill theory [64].

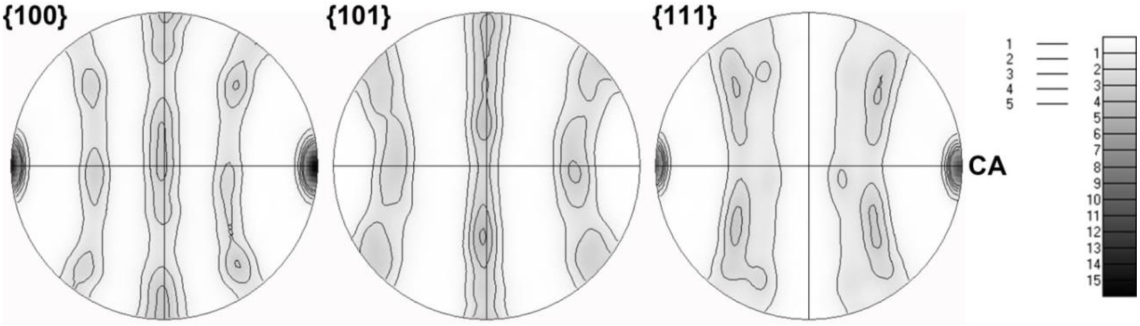

Fig. 4.12 {001}, {101} and {111} pole figures obtained by EBSD of the modified 9Cr-1Mo steel after DPD to a strain of 2.3. CA is horizontal.

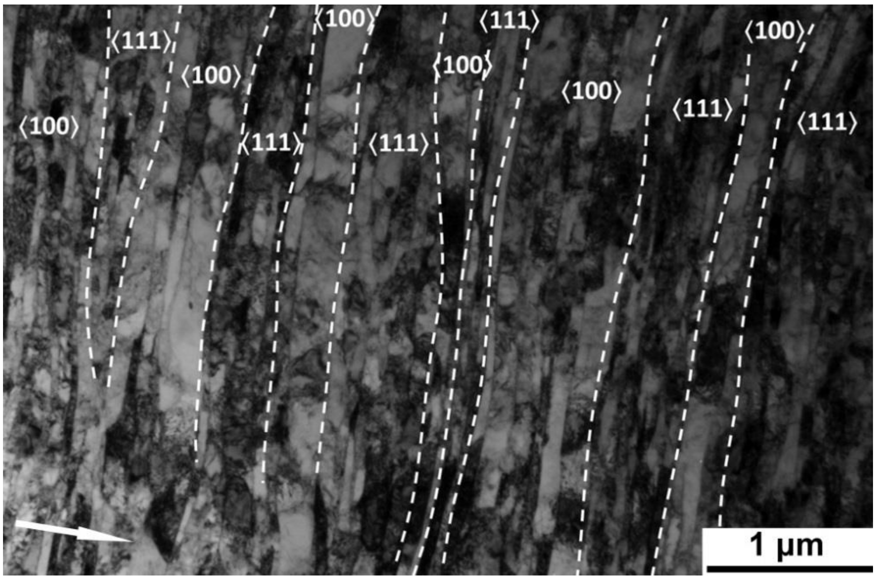

Fig. 4.13 A TEM image from the longitudinal section of the modified 9Cr-1Mo steel to a strain of 2.3, showing lamellar structures with dashed lines between alternating ⟨100⟩ and ⟨111⟩ texture bands. The orientations of the lamellae are determined by SAD patterns. The CA is indicated by an arrow.

For ⟨111⟩ pencil glide with all possible slip planes, crystals with either ⟨100⟩ or ⟨111⟩ directions aligned with the CA are expected to be stable, while grains with other orientations will rotate to one of stable orientations. The texture development during DPD can be described by the classic Taylor type model, i.e. there is no essential difference between DPD and normal compression. It is well known that Taylor's theory is based on finding the slip systems in individual grains which can geometrically produce a specific shape change with the least expenditure of work. Taylor's factor, *M*, is used to define the ratio between the magnitude of total slip and the externally applied strain, which is expressed as [114]:

$$M = \frac{\sum_l d\gamma_l}{d\varepsilon} \tag{4.1}$$

where $d\gamma_l$ are the incremental amounts of slip on the activated systems and $d\varepsilon$ is the increment of the applied equivalent strain. It is obvious that Taylor factor *M* is orientation dependent. Its values for ⟨100⟩ and ⟨111⟩ oriented *bcc* crystals for pencil glide under compression are 2.1 and 3.2, respectively [115], which are the lowest and highest values among all orientations. This considerable difference between the two orientations with respect to the Taylor factors indicates that lamellae of the ⟨111⟩ fibre texture component undergo appreciably larger incremental slip than lamellae of the ⟨100⟩ fibre texture component when the sample is deformed to a given strain. Consequently, the work done at individual grains with higher Taylor factor is large and one may expect to have higher stored energy after deformation to a specific strain.

The stored energy can be estimated based on the microstructural parameters [116]. For plastically deformed structures in medium to high stacking fault energy metallic materials, the stored energy can be estimated from the misorientation angles and spacings between the dislocation boundaries. The stored energy density due to dislocation boundaries can be obtained by multiplying the specific boundary energy (γ) with the boundary density (S_v). The stored energy is expressed as:

$$u_s = S_v * \gamma + u(\rho_0) \tag{4.2}$$

where $u(\rho_0)$ is the energy due to individual dislocations which do not form dislocation boundaries. For metallic materials after deformation to high strain, $u(\rho_0)$ is generally very small compared to the other contribution and will be neglected. For calculation of the dislocation boundary energy, the Read-Shockley equation can be used [117]:

$$\gamma = \begin{cases} \gamma_m(\theta/\theta_m)[1-\ln(\theta/\theta_m)] & :\theta \le \theta_m \\ \gamma_m & :\theta > \theta_m \end{cases} \tag{4.3}$$

where γ_m is the energy per unit area of a HAB, θ is the boundary misorientation angle, and θ_m is the misorientation angle above which the energy of the boundary becomes independent of the misorientation angle. For deformation-induced dislocation boundaries θ_m is widely used to be 15° [78].

The required microstructural parameters can be obtained by either EBSD or TEM. In the misorientation maps obtained by EBSD, the boundary misorientation is acquired, and the boundary density (S_v) can be derived. To estimate the stored energy in the modified 9Cr-1Mo steel after DPD, the EBSD data are used to determine the misorientation angle of individual boundaries and the boundary density. To be more specific, if the number of misorientation angles above 2° acquired in an EBSD orientation map is defined as N_n, and the EBSD step size is P, then the total boundary length of the measured region can be estimated as $N_t=N_n\times P$. Then $S_v=N_t/A$, where A is the area of the map. It should be mentioned here that any stereological influence on the estimated area density based on the measured boundary length is neglected in the present work. The energy per unit area of HAB of *bcc* iron is 617 mJ/m^2 [118]. With these parameters the stored energy of the deformed modified 9Cr-1Mo steel can be obtained. To compare the stored energy of ⟨100⟩- and ⟨111⟩-oriented lamellae, their stored energy was calculated separately. This was realized in Channel 5 software, by creating subsets with components of either ⟨100⟩ or ⟨111⟩ fibre texture, and allowing a 10° deviation to define the texture components. The calculated values are shown in Fig. 4.11b.

This figure shows that the total stored energy and stored energy of the ⟨100⟩- and ⟨111⟩ subsets increase with increasing DPD strain. It should be mentioned that since the boundaries between ⟨100⟩- and ⟨111⟩-oriented lamellae were not taken into consideration when separating the ⟨100⟩ and ⟨111⟩ subsets, contributions from those boundaries were missed in calculating the separated subsets, and this is why the stored energy per unit area of both ⟨100⟩- and ⟨111⟩-oriented regions is smaller than the total stored energy. However, this treatment should not affect the analysis aiming at revealing the difference in stored energy between both components. Considering the data for the ⟨100⟩- and ⟨111⟩ subsets, it is apparent that the stored energy of ⟨111⟩-oriented regions is much higher than that of ⟨100⟩-oriented regions at all strains, which is consistent with the prediction based on the Taylor factor that larger work done in the ⟨111⟩ lamellae. Specifically, the stored energy density of ⟨111⟩-oriented regions is about 70% higher than that of ⟨100⟩-oriented regions for a strain of 0.5. Both densities increase with increasing strain, and after DPD to a strain of 2.3 the stored energy density of ⟨111⟩-oriented lamellae is about 35% larger than that of ⟨100⟩-oriented lamellae. This significant difference in the stored energy density between the ⟨100⟩ and ⟨111⟩ texture components should affect the annealing behavior of the deformed material. This will be studied in detail in section of 4.2.

4.1.6 Discussion

The results obtained for the modified 9Cr-1Mo steel subjected to DPD demonstrate that the tempered martensitic structure is transformedd into a typical dislocation cell structure after DPD to medium strain, and that a nanoscale lamellar structure forms after DPD to high strains. This proves that DPD is a very efficient technique for refining the microstructure of the modified 9Cr-1Mo steel to nanoscale. Besides this special technique, the initial microstructure also plays an important role in the structural refinement. Several methods can be used to enhance the structural refinement at a given strain, for instance, by introducing a high dislocation density in the initial structure, by reducing the initial grain size (i.e. by increasing the surface area density of boundaries), and by increasing the number density of dispersoids into the initial structure, etc. [119]. It is well documented that through the martensitic transformation a high density of dislocations and martensitic boundaries can be introduced in the initial microstructure. Consequently an ultrafine grain structure can be easily obtained in martensitic steels after cold rolling to medium strains [120-122]. It is evident that the modified 9Cr-1Mo steel with tempered martensitic structure also contains a high density of dislocations and a high frequency of martensitic boundaries, which facilitate the structural refinement during plastic deformation compared to the materials with initially a clean grain structure. This is one reason that the modified 9Cr-1Mo steel is refined to the nanostructure after DPD to a strain of 2.3.

The structural refinement could also be enhanced by the presence of particles in the modified 9Cr-1Mo steel. It has been shown that a higher density of dislocations, mainly GNDs, is present around carbide particles after DPD to low and medium strains. The particles do not only act as a source in initiating dislocations, but also confine the dislocation motion to shorter distances. Both processes will facilitate structural refinement. When the material is deformed to high strains, dynamic recovery becomes more pronounced. Besides the dislocation annihilation with other dislocations, triple junction motion is thought to be an important contributor to dynamic recovery leading to a saturate state with stationary lamellar thickness [123]. Fine particles, which are able to pin triple junctions to some extent, could suppress the related dynamic recovery, and thereby enhancing the structural refinement and achieving a finer microstructure [86]. The carbides in modified 9Cr-1Mo steel are supposed to play such a role when the material was deformed to high strains. It was shown in Fig. 4.9 that some carbides sitting at triple junctions are associated with much thinner lamellae, which indicates a pinning effect on the triple junctions. Due to this pinning effect, thin lamellae can be preserved, instead of becoming destroyed by triple junction motion. Therefore, formation of nanoscale lamellar structure is supposed to benefit from the fine particles in the material.

4.2 Annealing behavior of the nanostructured modified 9Cr-1Mo steel

As a structural material for high temperature applications, the thermal stability of nanostructured modified 9Cr-1Mo steel is of crucial importance. Exposure at high temperatures is, however, expected to lead to an increase in the grain size, which will cause the loss of strength and radiation resistance. The purpose of this section is to study the annealing response of the DPD-processed modified 9Cr-1Mo steel to a strain of 2.3 and to investigate recovery and recrystallization within the nanoscale lamellar structure.

4.2.1 Evolution during isochronal annealing

The microstructural evolution during annealing at different temperatures for 1 h is shown in Fig. 4.15. It is seen that annealing at temperatures below 650 °C leads to structural coarsening without any pronounced recrystallization. This coarsening results in significant softening of the material as seen from the obtained Vickers hardness values in Fig. 4.16a. As expected, the boundary spacing increases with increasing annealing temperature (Fig. 4.16b). After annealing at 550 °C for 1 hour, the material almost maintains a lamellar structure, with minor structural coarsening, during which the average spacing of boundaries with misorientation angles above 2° ($d_{\theta>2^\circ}$) increases from 110 nm to 170 nm. No recrystallization takes place during annealing at 600 °C for 1hour. However, the structural coarsening at this temperature is considerable, and the average $d_{\theta>2^\circ}$ increases to 271 nm. In contrast to the boundary spacing, the texture is less sensitive to the annealing treatment, demonstrating no significant changes until the annealing temperature is increased to ≥ 650 °C (Fig. 4.17).

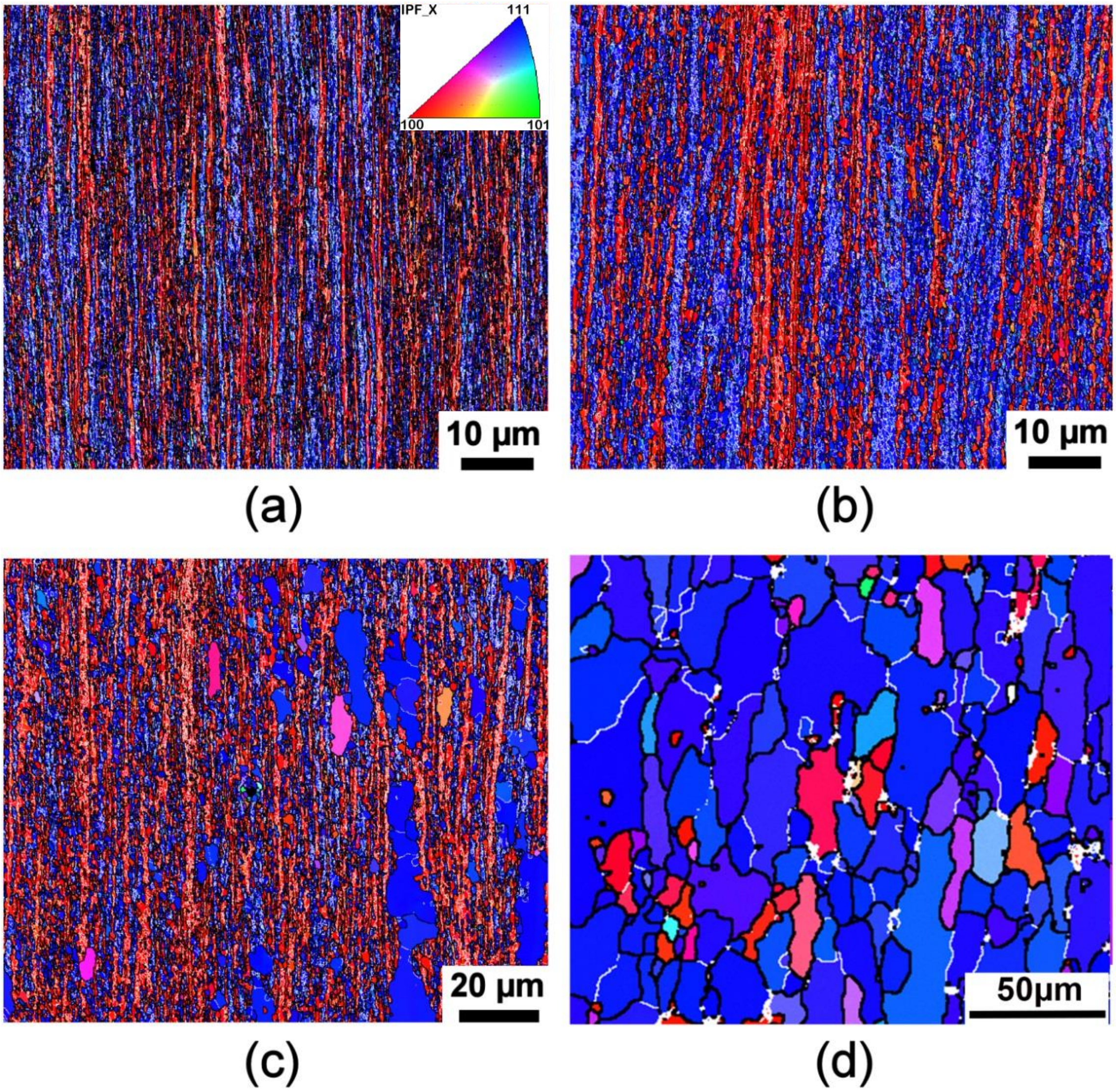

Fig. 4.15 Orientation maps from the longitudinal section of the modified 9Cr-1Mo steel obtained by EBSD deformed by DPD to a strain of 2.3 after annealing at different temperatures for 1 h: (a) 550 °C, (b) 600 °C, (c) 650 °C and (d) 700 °C. Different colors in the maps correspond to different crystallographic directions along the CA as shown in the inset in (a). LABs and HABs are shown as white and black lines, respectively.

TEM images of the DPD-processed sample after annealing at 600 °C for 1 hour are shown in Fig. 4.18. Whereas most subgrains become less elongated during the coarsening, there are regions where highly elongated subgrains, similar to those in the as-deformed material, are still present. A region with such highly elongated subgrains is marked by dash lines in Fig. 4.18a. Orientation analysis based on SAD patterns obtained from the framed region in Fig. 4.18a indicates that the region which coarsen less (Fig. 4.18b), i.e. maintaining a structure with elongated subgrains, belongs to the ⟨100⟩ fibre texture component. It should be emphasized that the phenomenon that the material with the highly elongated structure is of the ⟨100⟩ texture component is a typical feature of the material annealed at 600 °C for 1 hour, and very frequently observed in the microstructure. The average thickness of the preserved lamellae is about 260 nm, which is much coarser than the lamellar thickness that prior to annealing. Therefore, significant coarsening also occurs in this lamellar structure. Although recovery results in coarsening of both ⟨100⟩- and ⟨111⟩-oriented lamellae, there is an appreciable difference between the recovered lamellae of the different texture components.

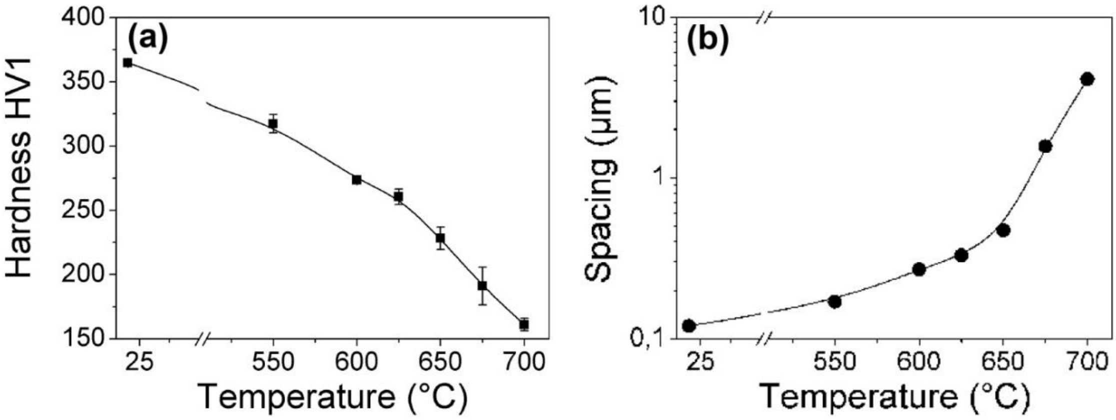

Fig. 4.16 Effects of isochronal annealing at different temperatures for 1 h on (a) Vickers hardness and (b) boundary spacing $d_{\theta>2°}$ measured by EBSD along the CA of the modified 9Cr-1Mo steel DPD-processed to a strain of 2.3.

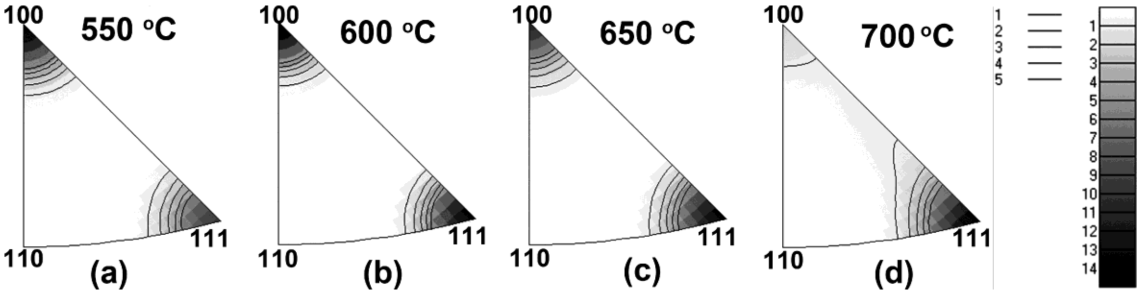

Fig. 4.17 Inverse pole figures show the crystallographic direction of the CA after isochronal annealing at different temperatures for 1 h obtained by EBSD from the modified 9Cr-1Mo steel deformed by DPD to a strain of 2.3.: (a) 550 °C, (b) 600 °C, (c) 650 °C and (d) 700 °C.

Annealing at 650 °C for 1 h results in recrystallization by nucleation and growth (see Fig. 4.15c) with an area fraction of recrystallized material of 12%. The annealing also results in a slope change in the softening curve in Fig. 4.16a, which is indeed expected as the dominating process changes from recovery to recrystallization [124]. As is evident from Fig. 4.15c, most of the recrystallizing grains have orientations of the ⟨111⟩ fibre texture component, and the intensity of the ⟨111⟩ texture component increases at the expense of the ⟨100⟩ texture component. With increasing temperature to 675 °C, f_{Rex} increases to 73%, and after annealing at 700 °C the material is almost fully recrystallized (f_{Rex}=99%, see Fig. 4.15d). The texture of this almost fully recrystallized sample is a combination of a strong ⟨111⟩ component and a weak ⟨100⟩ fibre texture component (see Fig. 4.17d).

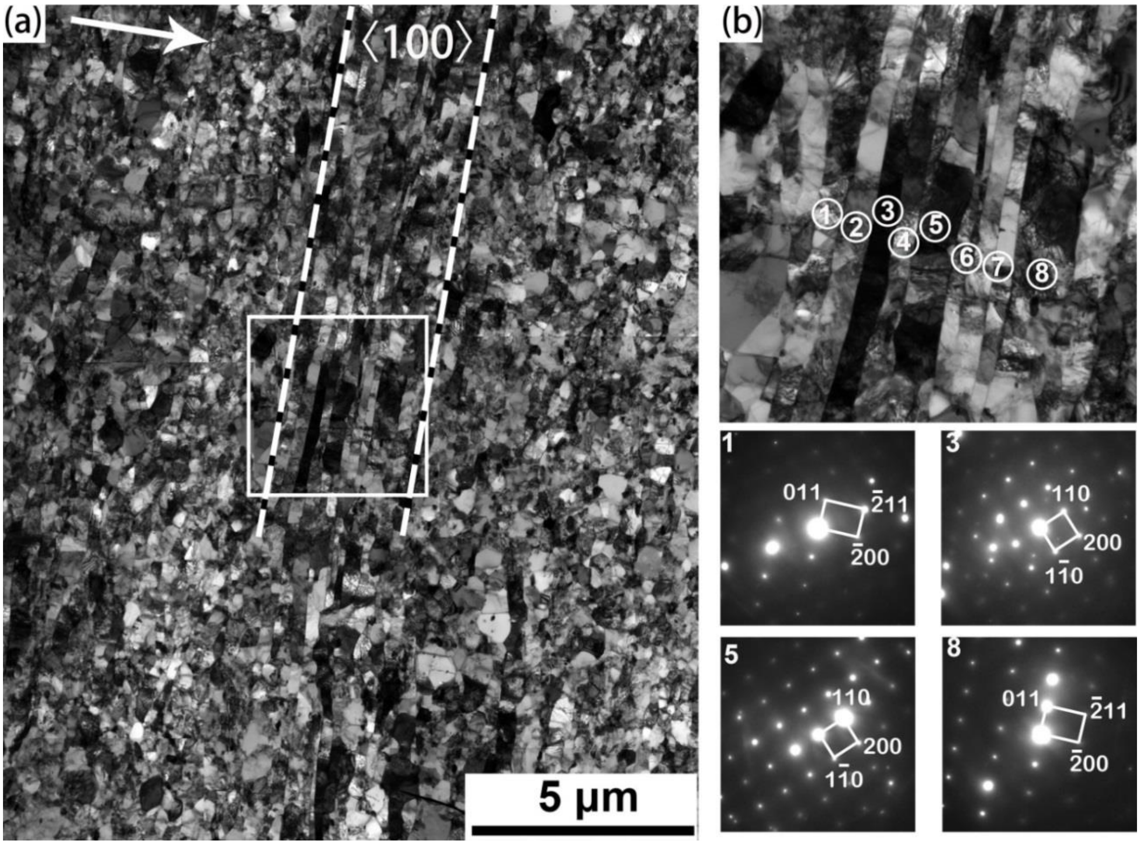

Fig. 4.18 TEM images and selected area diffraction (SAD) patterns from the longitudinal section of the modified 9Cr-1Mo steel deformed by DPD to a strain of 2.3 and annealed at 600 °C for 1 hour. (a) TEM image showing the recovered structure, and (b) enlargement of the framed region in (a). SAD patterns were obtained in the selected regions in (b), which are marked by numbered circles. Four indexed diffraction patterns with numbers corresponding to those in (b) are presented as examples to illustrate the orientations of the lamellae. The initial CA is indicated by the arrow in (a).

A TEM image showing the microstructure of the partially recrystallized DPD-processed modified 9Cr-1Mo steel is given in Fig. 4.19. After annealing at 650 °C for 1 hour, a large fraction of recrystallized grains can be seen in the TEM image (Fig. 4.19a). In the corresponding sketch (Fig.4.19b), large white regions represent the recrystallized grains with bold black boundaries separating them from the deformed structure. SAD analysis demonstrates that the recrystallized grains are of the ⟨111⟩ texture component, and as an example the diffraction patterns from grain I is presented. It is also evident that some isolated lamellae survived even though they are surrounded by recrystallizing grains, as indicated by circles II and III in Fig. 4.19a. These remaining lamellar structures have ⟨100⟩ directions along the CA, which means even in the partially recrystallized state some lamellae with the ⟨100⟩ orientations are still preserved. In addition, the boundaries between the survived lamellae and the recrystallized grains are quite straight (such as region II in Fig. 4.19a). This might be an impeding factor for the boundary migration and preventing the recrystallizing grains from invading into the ⟨100⟩-oriented lamellae.

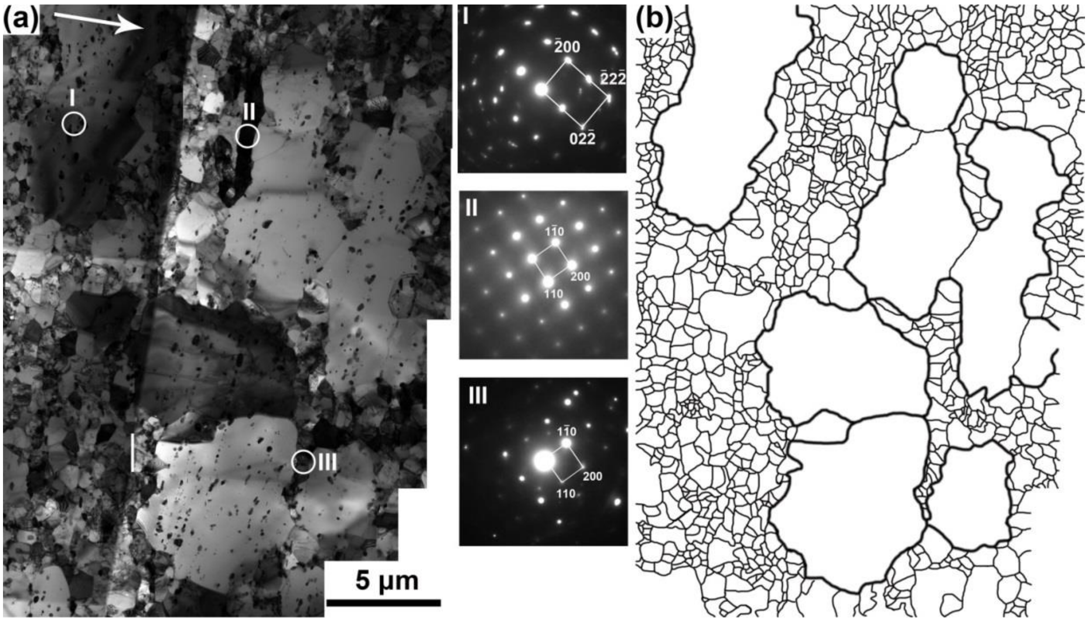

Fig. 4.19 (a) Bright field TEM image and SAD patterns from the longitudinal section of the modified 9Cr-1Mo steel deformed by DPD to a strain of 2.3 after annealing at 650 °C for 1 hour and (b) the corresponding sketch. Three indexed SAD patterns are from the regions marked I, II, and III in (a) to show their orientations, I: ⟨111⟩//CA; II: ⟨100⟩//CA; III: ⟨100⟩//CA. In (b), thin black lines represent the subgrain boundaries, whereas bold black lines represent boundaries between recrystallized grains and their surrounding recovered structure. The initial CA is indicated by the arrow in (a).

4.2.2 Evolution during isothermal annealing

As shown in subsection 4.2.1, few recrystallized grains emerge during annealing for 1 hour at 650 °C, while the sample annealed at 700 °C is almost fully recrystallized. To characterize in detail both recovery and recrystallization during isothermal annealing, the evolution of microstructure and texture was studied at an intermediate annealing temperature of 675 °C. From Fig. 4.20(a) it is apparent that a number of small (mean size 4.2 μm) recrystallizing grains are present in the microstructure already after 15 min of annealing at 675 °C. The area fraction of the recrystallizing grains in this condition is 1.3% and it is seen that most of recrystallizing grains have blue color, i.e. they have ⟨111⟩ directions along the CA. The hardness is reduced dramatically, from 365 HV1 in the DPD sample to 243 HV1 after 15 min of annealing (Fig. 4.21a). Further annealing increases the number, average size and area fraction of recrystallizing grains, and additionally coarsens the structure and softens the material (Fig. 4.21a, b). It is seen that recrystallization occurs very heterogeneously and that the recrystallizing grains form bands aligned almost perpendicular to the CA (Fig. 4.20b). Similar to the isochronal annealing results, recrystallization nuclei form preferentially in regions with orientations belonging to the ⟨111⟩ fibre texture component, and the ⟨111⟩ oriented recrystallizing grains consume the deformed structure leading to a strong ⟨111⟩ recrystallized texture. To conduct a quantitative analysis, the number frequency, size and area fraction of the recrystallizing grains with ⟨100⟩ and ⟨111⟩ orientations obtained from EBSD data after isothermal annealing are plotted in Fig. 4.22.

Fig. 4.22a shows the number of recrystallizing grains in different texture components per unit volume (N_V). N_V is obtained by: (i) measuring the number density per unit area N_A and the average equivalent diameters d_{ECD} of recrystallizing grains in each texture components, and then (ii) N_V can be calculated as $N_V=N_A/ d_{ECD}$. Here, the stereology factor is neglected for both texture components. The result (Fig. 4.22a) indicates that for all annealing durations N_V for recrystallizing grains in ⟨111⟩ texture component is much greater than that of ⟨100⟩ recrystallizing grains. Besides, the ECD of the ⟨111⟩ recrystallizing grains is significantly larger than that of the ⟨100⟩ grains (see Fig. 4.22b). For instance, the average recrystallized grain size after annealing for 30 min is 6.5 μm and 3.7 μm for the ⟨111⟩ and ⟨100⟩ grains, respectively. After 90 min at 675 °C, the average recrystallized grain size increases to 9.0 μm and 5.7 μm for the ⟨111⟩ and ⟨100⟩ components, respectively. The advantage in both the size and the frequency of recrystallizing ⟨111⟩ grains results in a higher area fraction of recrystallized regions from the ⟨111⟩ fibre texture component (Fig. 4.22c).

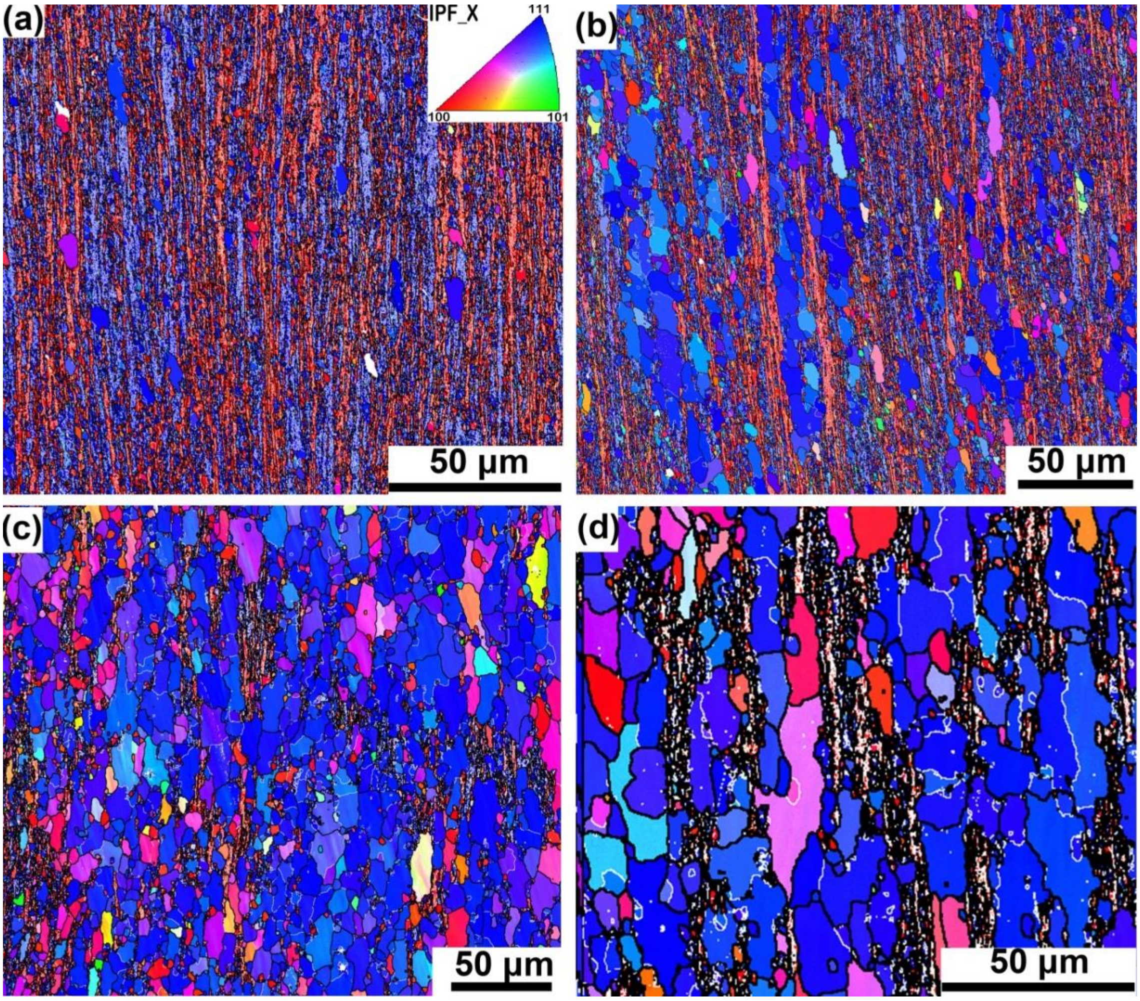

Fig. 4.20 Orientation maps obtained by EBSD from the longitudinal section of the modified 9Cr-1Mo steel deformed by DPD to a strain of 2.3 and annealed at 675 °C for (a) 15 min, (b) 30 min, (c) 60 min and (d) 90 min. They are colored according to the crystallographic direction along the CA using the color code in the inverse pole figure (see the inset). LABs and HABs are shown as white and black lines, respectively.

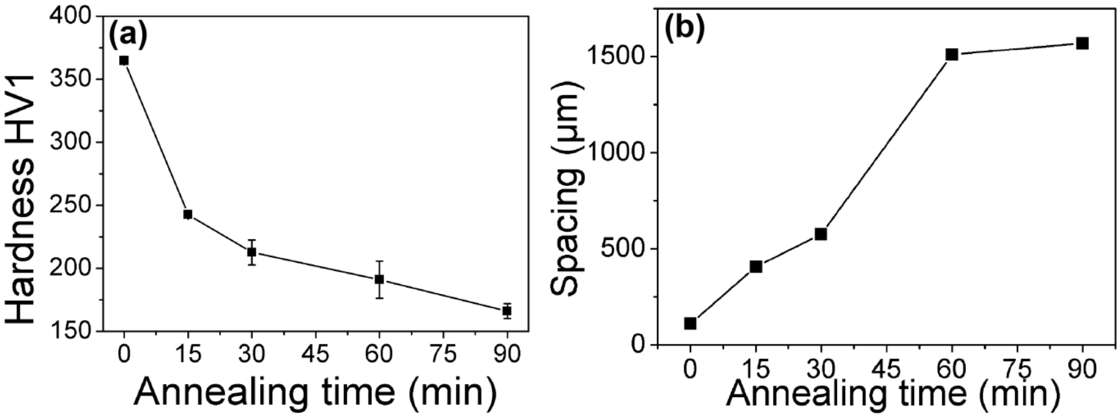

Fig. 4.21 (a) Vickers hardness and (b) the boundary spacing $d_{\theta>2°}$ of the modified 9Cr-1Mo steel after DPD to a strain of 2.3 and annealed at 675 °C.

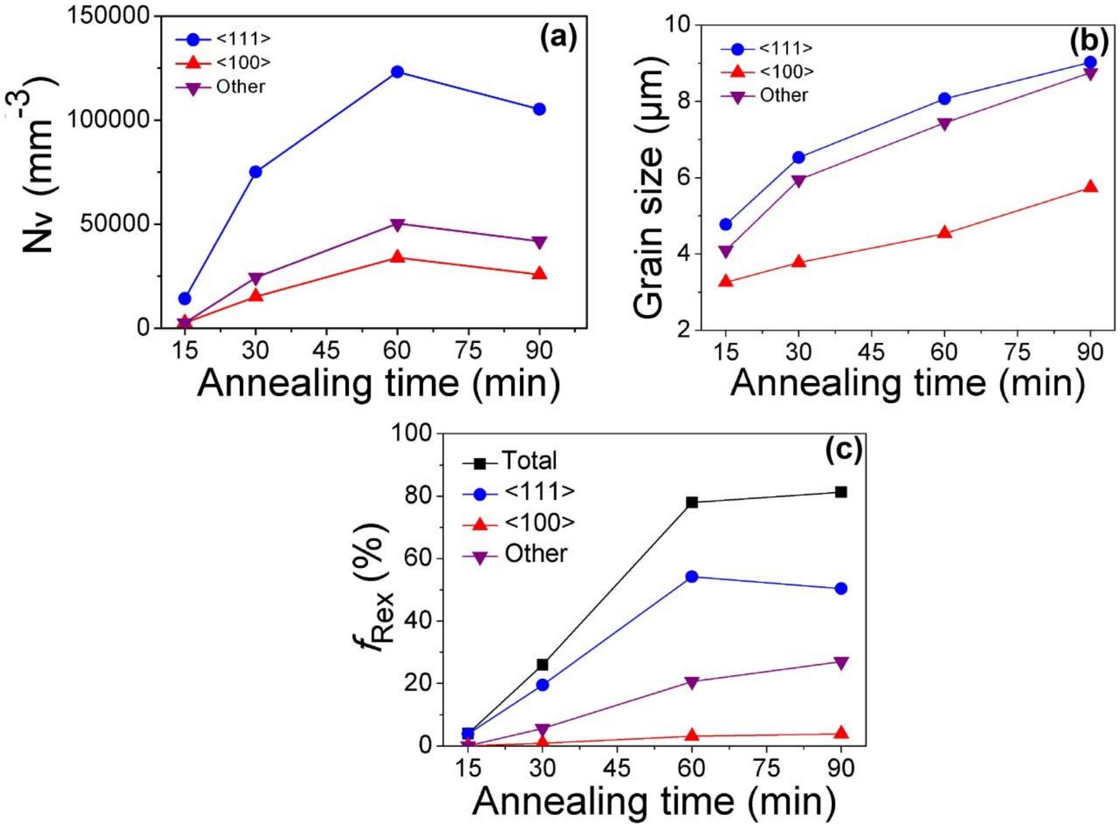

Fig. 4.22 Parameters of recrystallized grains with different crystallographic orientations in the modified 9Cr-1Mo steel after DPD to a strain of 2.3 and annealed at 675 °C for different periods of time: (a) number per unit volume; (b) average grain size expressed as equivalent circular diameter; (c) area fraction.

4.2.3 Discussion

The compression texture of the modified 9 Cr – 1 Mo steel is characterized by a combination of strong ⟨100⟩ and ⟨111⟩ fibre texture components, which is typically observed in compressed *bcc* materials [65, 125]. The HAB spacing in the initial material prior to DPD is about 2.4 μm. After compression to a strain of 2.3, the spacing between HABs existing prior to deformation is expected to drop to 240 nm, which is reasonably consistent with the observed width of the texture bands, ~0.3 μm. Therefore, it is suggested that most boundaries between the ⟨100⟩ and ⟨111⟩ oriented bands originate from the initial microstructure. The majority of initial HABs are either prior austenite grain boundaries or martensitic block boundaries. During recrystallization this duplex texture evolves to a strong ⟨111⟩ texture, which is also in agreement with published literature [65, 126]. Although the evolution of the texture in our DPD processed steel is consistent with the previous findings in compressed *bcc* materials, the present work reveals two important and original observations related to DPD:

1) DPD of the given *bcc* steel leads to a structural refinement on the nanoscale;
2) Significant differences are observed in the recovery and recrystallization behavior between the ⟨100⟩ and ⟨111⟩ oriented regions.

4.2.3.1 Recovery

Similar to previous observations on other heavily deformed materials [26-28], recovery in the modified 9Cr–1Mo steel is accompanied by coarsening of the deformed microstructure. The driving force for the coarsening is the reduction of the dislocation boundary energy. Indeed, estimations of the stored energy density based on the EBSD data indicate that the coarsening significantly reduces the energy (see Fig. 4.23) and that this reduction is more pronounced in the ⟨111⟩ bands, for which the initial stored energy was greater than that in the ⟨100⟩ bands. This observation is in agreement with recent findings that [26] during annealing of heavily rolled commercial purity aluminum high-energy bands recover more than low-energy bands. The result of the stronger recovery within the ⟨111⟩ regions in the DPD-processed 9Cr–1Mo steel is that by the onset of recrystallization there is almost no difference in the stored energy between the ⟨111⟩ and ⟨100⟩ bands. A further observation is that the stored energy associated with the interfaces between the ⟨111⟩ and ⟨100⟩ bands is reduced very fast. This is reflected in the difference between the total stored energy and average stored energy of the ⟨100⟩ and ⟨111⟩ oriented regions.

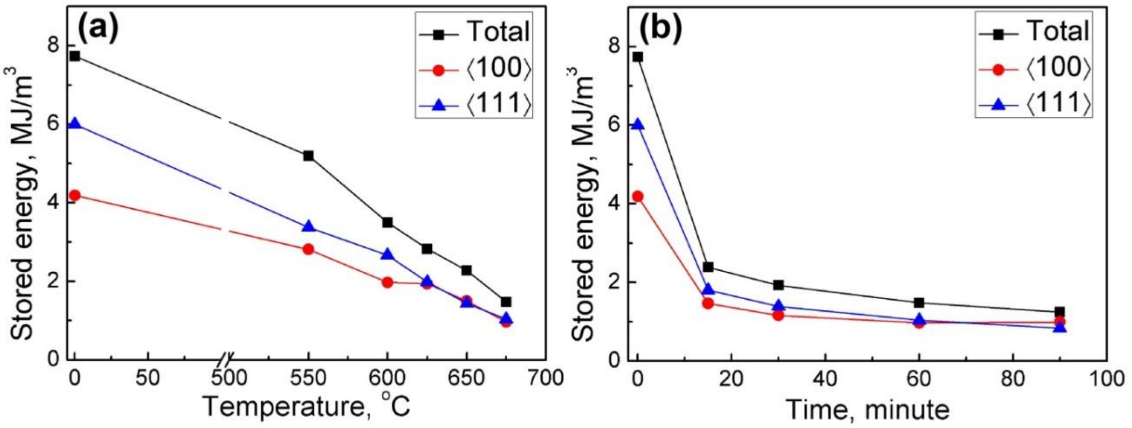

Fig. 4.23 Evolution of the stored energy density during (a) isochronal and (b) isothermal annealing of the modified 9Cr-1Mo steel after DPD to a strain of 2.3. The stored energy density, within the ⟨100⟩ and ⟨111⟩ fibre texture components and the total stored energy was obtained from the EBSD data, based on the methodology described in the section of 4.1.5. Recrystallized regions were discarded when calculating the stored energy for partially recrystallized samples.

This is illustrated in the following. If in a map the area fractions of the ⟨100⟩ and ⟨111⟩ oriented regions are $f_{\langle 100\rangle}$ and $f_{\langle 111\rangle}$ respectively, the stored energy density of them are $u_{s\langle 100\rangle}$ and $u_{s\langle 111\rangle}$, respectively, and the stored energy density of the total area is u_{stotal}, the stored energy density of the boundaries between the ⟨111⟩ and ⟨100⟩ bands is

$$u_{sinterface} = u_{stotal} - (u_{s<100>} * f_{<100>} + u_{s<111>} * f_{<111>}) \tag{4.4}$$

Fig. 4.24 shows that $u_{\mathrm{sinterface}}$ decreases significantly during annealing at 600°C and above. The decrease in the stored energy density should be caused by a decrease of the area density of these boundaries. The average spacing measured between the ⟨111⟩ and ⟨100⟩ oriented bands is shown in Fig. 4.24. These band spacings increase dramatically during annealing at 600°C and above for 1 hour, which demonstrates a very good correlation with the evolution of the stored energy. This indicates that during annealing at these temperatures, a large number of boundaries between ⟨111⟩ and ⟨100⟩ oriented bands are removed from the microstructure. It is also evident from Fig. 4.15b that the initial ⟨111⟩ and ⟨100⟩ oriented bands evolve into a more equiaxed necklace-shaped structure, despite no recrystallization occurring at this temperature. The considerable reduction in the area density of the boundaries between the ⟨111⟩ and ⟨100⟩ oriented bands during recovery is attributed to the high mobility of these boundaries having high misorientations across them and to a high energy stored in these boundaries which subdivide volumes belonging to different texture components.

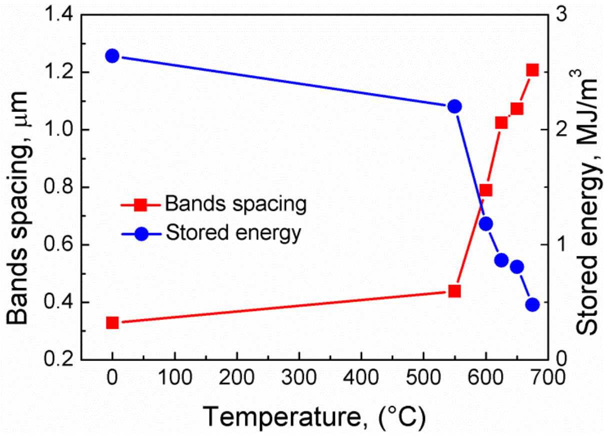

Fig. 4.24 Stored energy density calculated for boundaries between the ⟨111⟩ and ⟨100⟩ oriented bands, and the average thickness of the ⟨111⟩ and ⟨100⟩ oriented bands measured along CA using the intercept length method, from the modified 9Cr-1Mo steel after DPD to a strain of 2.3 and isochronal annealing for 1 hour at different temperatures.

4.2.3.2 Nucleation

Nuclei are observed after 1h at annealing temperatures of 650 °C and higher. Regardless of the annealing temperature, it is found that ⟨111⟩ nuclei develop within ⟨111⟩-oriented lamellae in the deformed and recovered microstructure, and likewise ⟨100⟩ nuclei form within ⟨100⟩-oriented lamellae. These observations are consistent with the standard concept of nucleation, where nucleation is closely related to the microstructure in which it occurs by e.g. subgrain growth, subgrain coalescence or strain-induced boundary migration, all resulting in nuclei having orientations of the actual nucleation sites [78].

The number of nuclei formed with ⟨111⟩ orientations is about 5 times as high as those with ⟨100⟩ orientations. Altogether, 59% and 15% of the all nuclei after annealing at 675° for 1 h have ⟨111⟩ and ⟨100⟩ orientation, respectively. In contrast, for randomly oriented material with *bcc* crystalline lattice, one should expect 6% and 5% of nuclei with these orientations respectively (as calculated allowing 10° from the ideal orientation). This means that both ⟨111⟩ and ⟨100⟩ grains nucleate preferentially compared to the nucleation with random orientation. In the present modified 9Cr-1Mo steel after DPD to a strain of 2.3, the ⟨111⟩ and ⟨100⟩ components represent 37% and

49% respectively of all orientations in the deformation texture, and this distribution changes very little due to recovery. Even taking these numbers into account, it becomes clear that nucleation of ⟨111⟩ grains is preferential. In a previous work on *bcc* materials [127-131], oriented nucleation has been reported to be the main reason for developing recrystallization textures with a pronounced γ-fibre containing ⟨111⟩ axes parallel to the normal direction (⟨111⟩//ND) after rolling. According to the work by Sanchez-Araiza *et al.* [130], who studied texture evolution during recrystallization in a warm-rolled low-carbon steel, oriented nucleation is due to a higher stored energy in the deformed ⟨111⟩//ND-oriented microstructure as compared to regions of other orientations. Similar ideas were proposed by others as well [89, 90, 132].

For the compressed modified 9Cr-1Mo steel studied in the present work, it is also found that after deformation the stored energy density in the ⟨111⟩ regions is higher, ~6 MJ/m^2, than that in the ⟨100⟩ regions, ~4 MJ/m^2. However, during recovery the stored energy decreases in both types of regions and this reduction is found to be more pronounced in the ⟨111⟩ regions (see Fig. 4.23). As a result, when recrystallization starts, the stored energy in both ⟨111⟩ and ⟨100⟩ regions is rather similar, 1 – 2 MJ/m^2. Thus, when nucleation starts there is no significant difference in the stored energy between the ⟨111⟩ and ⟨100⟩ regions. It is therefore apparent that preferential nucleation of ⟨111⟩ grains cannot be rationalized based on the large difference in the stored energy density revealed for the different texture bands in the as-deformed material. It is also obvious that coarsening occurring during recovery will affect nucleation, in particular because coarsening does not occur homogeneously. Some regions coarsen more than others even for the same ⟨hkl⟩ orientations, and if a certain subgrain has coarsened more than its neighbors, it may have an advantage during nucleation. Therefore, although the stored energy density in the ⟨111⟩ and ⟨100⟩ oriented bands is similar when recrystallization starts, the difference observed after deformation may indirectly affect the nucleation via recovery.

The most remarkable difference seen between the recovered ⟨111⟩- and ⟨100⟩-oriented regions is in their different morphology. As shown in Fig. 4.18, subgrains within the recovered ⟨111⟩ regions are almost equiaxed, whereas the ⟨100⟩ regions largely retain the lamellar morphology with elongated subgrains. It is therefore suggested that the preferential nucleation of the ⟨111⟩ grains may be related to easier nucleation in the more equiaxed structures as compared to a structure with planar elongated boundaries.

4.2.3.3 Growth

Besides oriented nucleation, oriented growth is also an important process leading to significant texture changes during recrystallization. If oriented growth occurs, grains/nuclei of certain orientations grow faster than those of other orientations, as is often observed in *fcc* metals [133]. For compressed and rolled *bcc* materials, either no oriented growth is observed at all [128, 134] or it is observed to become significant only in later stages of recrystallization when ⟨111⟩//ND oriented grains consume deformed/recovered regions of other orientations [135]. To analyze whether there is an oriented growth for the present steel, an extended Cahn-Hagel approach [136] was applied for the series of partially recrystallized samples annealed for various times at 675 °C.

The Cahn-Hagel method is widely used to measure true growth rates of recrystallized grains. The method is based on measurements of the volume fraction of the recrystallized material (V_v) and the interfacial area density between recrystallized and deformed material (S_v). By introducing S_v, the effects from the impingement between recrystallizing grains are largely eliminated. The mean growth rate, given by Cahn-Hagel, can be expressed as [137]:

$$\langle G \rangle = \frac{1}{S_v} \bullet \frac{dV_v}{dt} \tag{4.5}$$

where t is the annealing time.

Juul Jensen extended the Cahn-Hagel method by introducing different crystallographic orientations into the equation, yielding to an extended Cahn-Hagel equation [136]:

$$\langle G \rangle_i = \frac{1}{S_{v,i}} \bullet \frac{dV_{v,i}}{dt} \tag{4.6}$$

where i refers to a specific orientation or a texture component within a given angular range.

In this study, $S_{v,\langle 100 \rangle}$ and $S_{v,\langle 111 \rangle}$ are the volume densities of the boundaries between recrystallized material of the ⟨100⟩ and ⟨111⟩ fibre texture components and the deformed matrix, which can be determined from the EBSD data using the linear intercept method. The $V_{v,\langle 100\rangle}$ and $V_{v,\langle 111\rangle}$ are the volume fractions of the recrystallized materials of ⟨100⟩ and ⟨111⟩ orientations, respectively. To obtain the differential result of $dV_{v,i}/dt$, the evolution of each $V_{v,i}$ with time is fitted into the Johnson-Mehl-Avrami-Kolmogorov equation:

$$V_{v,i} = V_{v,\infty}(1-\exp(-k\cdot t^{\beta})) \tag{4.7}$$

where $V_{v,\infty}$, k, and β are fitting constants. By fitting this equation, the evolution of $V_{v,\langle 100\rangle}$ and $V_{v,\langle 111\rangle}$ with time t can be determined (shown in Fig. 4.25) and thus the $dV_{v,\langle 100\rangle}/dt$ and $dV_{v,\langle 111\rangle}/dt$ can be calculated as well. The average growth rates for recrystallized grains with ⟨100⟩ and ⟨111⟩ texture components are shown in Fig. 4.26. For recrystallized grains of the different texture components, the average growth rate decreases with time as $\langle G\rangle_i = \langle G\rangle_{0,i}t^{-r}$, which corresponds to a linear decrease in the log-log coordinates.

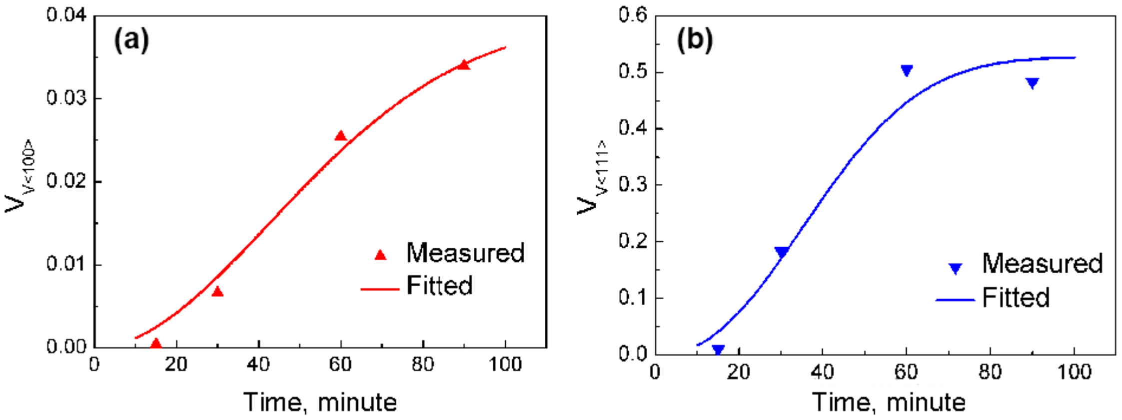

Fig. 4.25 Measured (from EBSD data) and fitted (based on Eq. (4.7)) volume fractions of the recrystallized materials with annealing time at 675 °C of modified 9Cr-1Mo steel after DPD to a strain of 2.3 (a) ⟨100⟩ texture component $V_{v\langle 100\rangle}$ and (b) ⟨111⟩ texture component $V_{v\langle 111\rangle}$.

It is evident that the growth rate of recrystallized grains of the ⟨111⟩ fibre texture component is much higher than that of the ⟨100⟩ fibre texture component in the beginning of recrystallization. More specifically, the average growth rate of the ⟨111⟩-oriented recrystallized grains is about four times higher than that of the ⟨100⟩-oriented during annealing at 675 °C for 15 min. This difference becomes smaller during annealing for longer time (see Fig.4.26). It should be mentioned here that as the V_v

becomes very high after annealing for 60 min and 90 min (73%, 82%, respectively), the S_v is very low at these stages, which results in large experimental uncertainties. Besides, V_v of ⟨100⟩-oriented recrystallizing grains is small for the entire annealing process, which may also cause some errors. Nevertheless, Fig. 4.26 demonstrates that the ⟨111⟩-oriented recrystallized grains have an advantage in growth compared to the ⟨100⟩-oriented recrystallized grains, i.e. oriented growth does take place during recrystallization of this modified 9Cr-1Mo steel after DPD. This finding is consistent with the size advantage of ⟨111⟩-oriented recrystallizing grains shown in Fig. 4.22b.

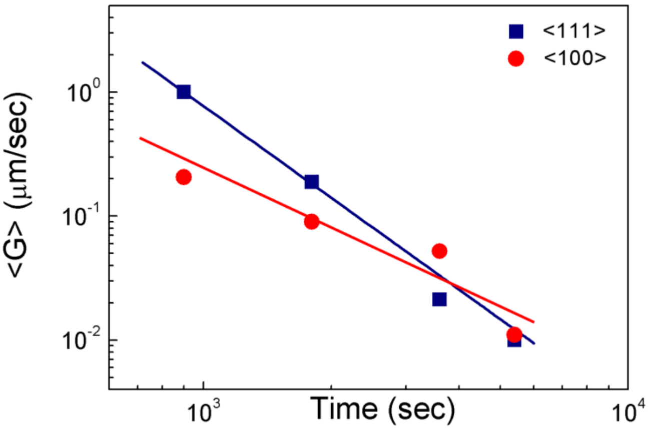

Fig. 4.26 Growth rates of ⟨100⟩ and ⟨111⟩ oriented recrystallizing grains calculated based on the extended Cahn-Hagel method using the EBSD data for the modified 9Cr-1Mo steel after DPD to a strain of 2.3 and annealed at 675 °C for different periods of time.

Whereas the extended Cahn-Hagel method gives impingement-corrected average growth rates, this statistical method cannot explain why the ⟨111⟩ grains grow faster than the ⟨100⟩ grains at the early stages of recrystallization. To observe changes during annealing in more detail, the present author investigated several regions in a partially recrystallized microstructure containing 16 grains of the ⟨111⟩ fibre texture component, and followed their growth after an additional annealing step. As the microstructure evolved rather rapidly at 675 °C (see Fig. 4.20), the annealing temperature for the present investigation was chosen to be 650 °C, which enabled slower evolution and thus better control in this particular experiment. No re-polishing was done after before and after this additional annealing step. Examples of maps showing the structural evolution during the additional annealing step are given in Fig. 4.27. The maps show that recrystallizing ⟨111⟩ grains grow preferably into the ⟨111⟩ matrix, and that the migrating ⟨111⟩/⟨111⟩ boundaries are mostly HABs. Interestingly, although ⟨111⟩/⟨100⟩

boundaries are also HABs, most of these boundaries do not move during the additional annealing treatment.

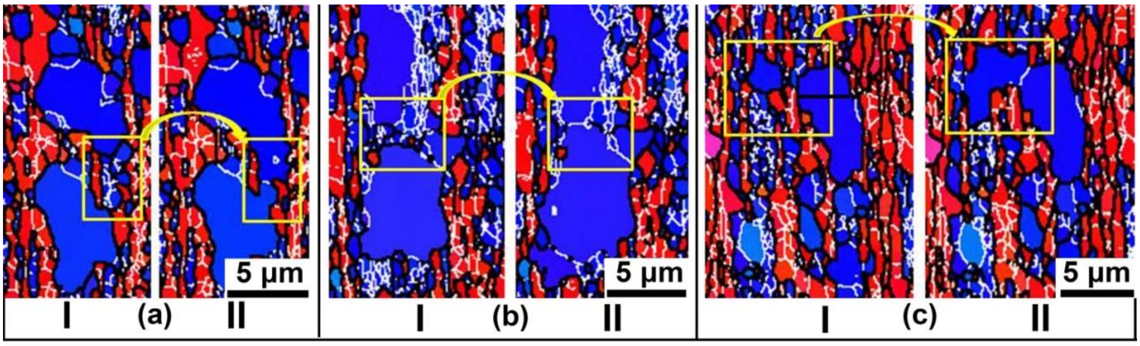

Fig. 4.27 Three regions mapped in the longitudinal section of the modified 9Cr-1Mo steel after DPD to a strain of 2.3 and annealed at 650 °C for 1 hour and again for 1 more hour (total annealing time 2 hours). "I" refers to the initial state and "II" refers to that after annealing for an additional 1 hour. The frames show regions where boundary migration is observed. Different colors in the maps correspond to different crystallographic directions of CA as shown in the inset in Fig. 4.20(a). LABs and HABs are shown as white and black lines, respectively.

Considering all boundaries between the 16 recrystallizing ⟨111⟩ grains, identified in this ex-situ annealing experiment, and their neighboring matrix, it is apparent that there is a significant difference between ⟨111⟩/⟨111⟩ and ⟨111⟩/⟨100⟩ boundaries: their distributions are dominated by 2-60° ⟨111⟩ and 40-60° ⟨110⟩ misorientations, respectively (Fig. 4.28). In addition, the angular distribution of the ⟨111⟩/⟨111⟩ boundaries is much broader than that of the ⟨111⟩/⟨100⟩ boundaries. To quantitatively analyze the fast growing ⟨111⟩ grains, Fig. 4.29 shows the distribution of misorientations across only those boundaries that migrate during the additional annealing step. This distribution shows that the LABs, as expected, are much less mobile, and that most of the migrating boundaries can be described as 20-60° ⟨111⟩ boundaries.

There are several possible reasons for the faster migration of the ⟨111⟩/⟨111⟩ boundaries, i.e. ⟨111⟩ recrystallizing grains growing into ⟨111⟩ oriented matrix. A higher stored energy in the ⟨111⟩ matrix than in the ⟨100⟩ matrix can theoretically lead to such a preference. However, for the present sample, this reason can be ruled out, because when recrystallization occurs the difference in stored energy between the ⟨111⟩ and ⟨100⟩ is marginal (see Fig. 4.23). Other theoretically possible reasons relate to higher mobility and/or lower energy of the ⟨111⟩ boundaries separating ⟨111⟩ recrystallizing grains from the ⟨111⟩ matrix. Concerning the higher mobility, previous experiments for rolled *bcc* material indicated that 27°⟨110⟩ boundaries might have higher mobility [128]. Such boundaries are not at all predominant in the present compressed sample (see Fig. 4.28). This relates to the deformation mode chosen for the present experiment which produces textures that do not contain many 27° ⟨110⟩ boundaries. The observation that the distributions of misorientation angles and axes for the migrating boundary segments are very broad (see Fig. 4.29), points to the fact that high-mobility low-energy boundaries, which are generally seen as clear extremes for certain misorientation relationships are not the only explanation for the preferential growth of the ⟨111⟩ grains observed in the present experiment. The morphology of the deformed/recovered microstructure, into which the ⟨111⟩ oriented recrystallizing grains grow, may also play a significant role. This has been previously observed in aluminum where preferential growth occurred in regions with dislocation boundaries favorably arranged with respect to the growing grains [138]. It is possible that a similar phenomenon may be important also for the present material.

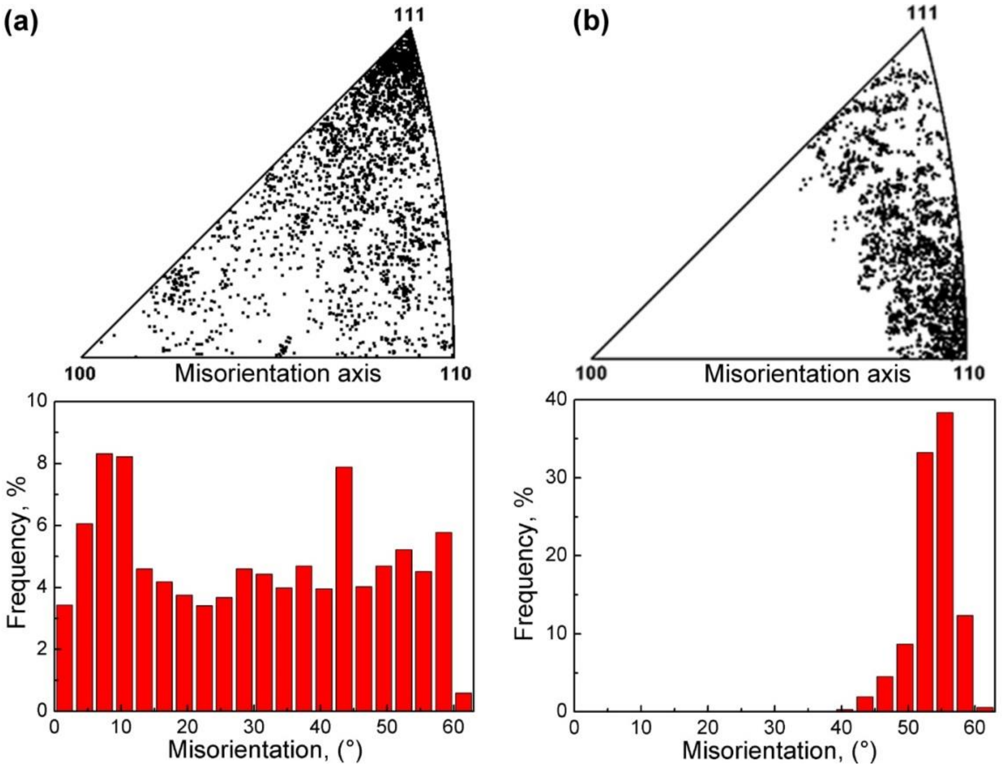

Fig. 4.28 Distribution of misorientation angles and axes for all boundaries formed between the matrix of either the (a) ⟨111⟩ or (b) ⟨100⟩ component and the 16 recrystallizing grains of the ⟨111⟩ fibre texture component identified in the ex-situ EBSD measurement of the modified 9Cr-1Mo steel after DPD to a strain of 2.3 and annealing at 650 °C for 1 hour and then additionally for 1 more hour.

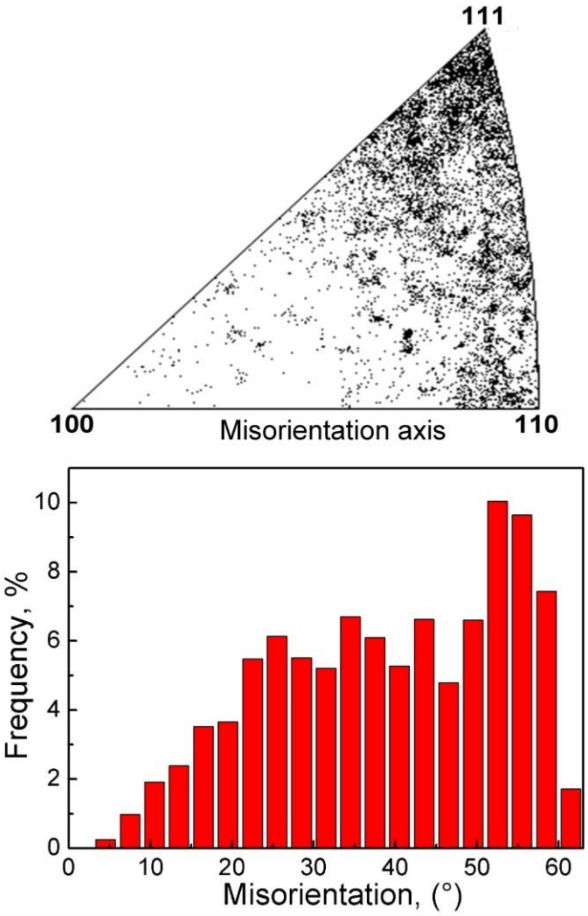

Fig. 4.29 Distribution of misorientation angles and axes for migrating boundary segments between the 16 recrystallizing grains of the ⟨111⟩ texture and the matrix in the modified 9Cr-1Mo steel after DPD to a strain of 2.3 and annealing at 650 °C for 1 hour and then additionally for 1 more hour.

4.2.4 Summary

1) DPD at strain rates of 10^2-10^3 s^{-1} leads to a refined lamellar microstructure in the modified 9Cr-1Mo steel with a spacing of ~100 nm between the lamellar boundaries. The texture is a duplex ⟨100⟩ + ⟨111⟩ fibre texture. The stored energy in the ⟨111⟩ texture bands in the deformed state is significantly higher than that in the ⟨100⟩ texture bands.

2) Recrystallization by nucleation and growth takes place after 1 h at temperatures of 650°C and above. Both oriented nucleation and oriented growth contribute to the development of a strong ⟨111⟩ recrystallization texture. It is shown that the fast recovery of the nanostructured modified 9Cr-1Mo steel significantly affects both the nucleation and growth. Differences in the stored energies between

different texture bands in the as-deformed material cannot directly explain the preferential nucleation of ⟨111⟩ grains in the ⟨111⟩ matrix and the faster growth of these grains.

3) It is suggested that the difference in recovery within the ⟨111⟩ and ⟨100⟩ bands leads to a more equiaxed morphology of subgrains in the recovered ⟨111⟩ bands as compared to the subgrains being highly elongated in the ⟨100⟩ recovered bands. Furthermore, it is proposed that this difference in morphology and the presence of significant variations in the size of the well recovered equiaxed subgrains may facilitate oriented nucleation of the ⟨111⟩ nuclei. Although the stored energy is similar for all parts of the recovered microstructure when recrystallization starts at around 650 °C, the initial difference in stored energy indirectly affects the difference in nucleation via the differences in recovery.

4) It is shown that ⟨111⟩ oriented grains preferentially grow into the ⟨111⟩ matrix at high rates. As the misorientation distribution across the fast migrating boundaries is very broad, the preferential growth cannot be explained solely by the fast migration of low energy/high mobility boundaries surrounding the growing grains. It is suggested that also the morphology of the surrounding microstructure may be important.

4.3 Effect of strain rate on the deformation microstructure, annealing behavior and mechanical properties

The strain rate of DPD is relatively high (10^2-10^3 s^{-1}) compared to the conventional compression process. In order to analyze the effect of strain rate, quasi-static compression (QSC) with a wide range of strain rates is conducted to investigate the microstructure and mechanical properties of the modified 9Cr-1Mo steel after QSC. The strain rate dependence of the deformation-induced microstructure and mechanical properties is presented, and the effect of strain rate on the subsequent annealing behavior of the deformed material is described.

4.3.1 Effect of strain rate on the deformation microstructure

In this subsection, the microstructure of the modified 9Cr-1Mo steel after QSC with a strain rate of 10^{-4} s^{-1} to strains of 0.5 and 2.3 is introduced, and comparison with the microstructure of DPD-processed sample to the same strains is presented.

4.3.1.1 Strain of 0.5

The microstructure of the modified 9Cr-1Mo steel after QSC to a strain of 0.5 is shown in Fig. 4.30. This microstructure is generally similar to the microstructure of the DPD sample (Fig. 4.5 and Fig.4.10a),. During compression grains flatten, the dislocation density increases and new cell boundaries are introduced. The initial martensitic structure is transformed into a dislocation cell structure (Fig. 29b). The microstructural parameters obtained by EBSD from the QSC sample aresummarized in Table 4.1. Significant microstructure refinement is achieved after QSC with a boundary spacing of $d_{(\theta>2°)}$ and d_{HAB} decreasing from 1.11 μm and 2.43 μm in the as-received material to 0.29 μm and 0.93 μm respectively after QSC. Compared to the sample after QSC, the DPD sample shows finer boundary spacings for both $d_{(\theta>2°)}$ and d_{HAB} (see Table 4.1).

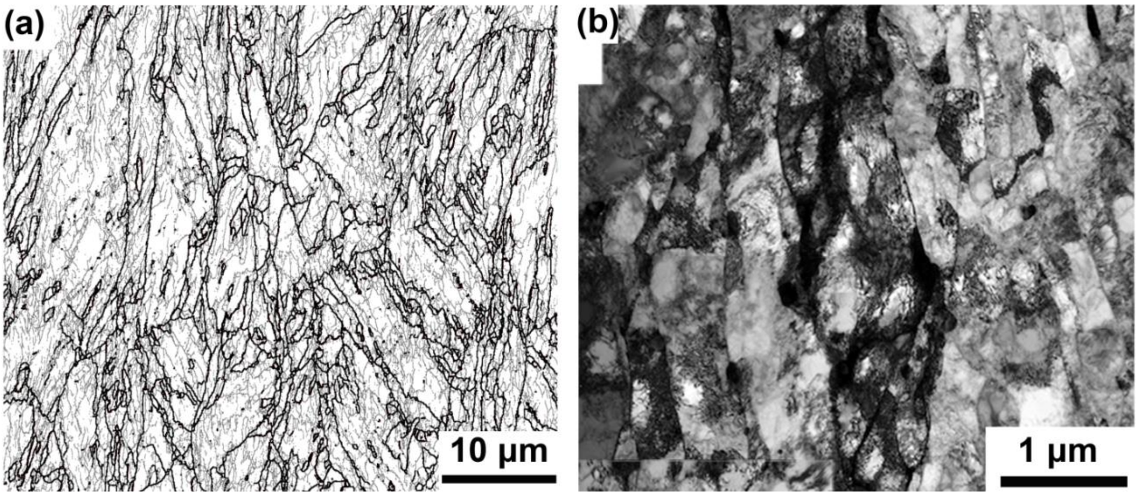

Fig. 4.30 Microstructure of the modified 9Cr-1Mo steel in longitudinal section after QSC to a strain of 0.5: (a) misorientation map obtained by EBSD. Thin gray and bold dark lines show LABs and HABs, respectively and (b) TEM bright image. The CA is approximately horizontal.

Table 4.1 Microstructural parameters (determined using EBSD) of the modified 9Cr-1Mo steels in different conditions

Condition	$d_{(\theta>2°)}$ (μm)	d_{LAB} (μm)	d_{HAB} (μm)	f_{HAB} (%)
As-received	1.11	2.04	2.43	46
DPD 0.5	0.21	0.25	0.81	23
QSC 0.5	0.29	0.38	0.93	29
DPD 2.3	0.111	0.60	0.200	38
QSC 2.3	0.120	0.61	0.224	30

The misorientation angle distributions for the DPD and QSC samples are similar (see Fig. 4.31), though the LAB fraction is slightly higher in the DPD sample (77%) than in the QSC sample (71%). A duplex ⟨111⟩ + ⟨100⟩ fibre texture, with a stronger ⟨111⟩ component and a weaker ⟨100⟩ component, is also observed in the sample after QSC to a strain of 0.5 (Fig. 4.32b). However, the texture is slightly stronger in the DPD sample than the QSC sample (Fig. 4.32a).

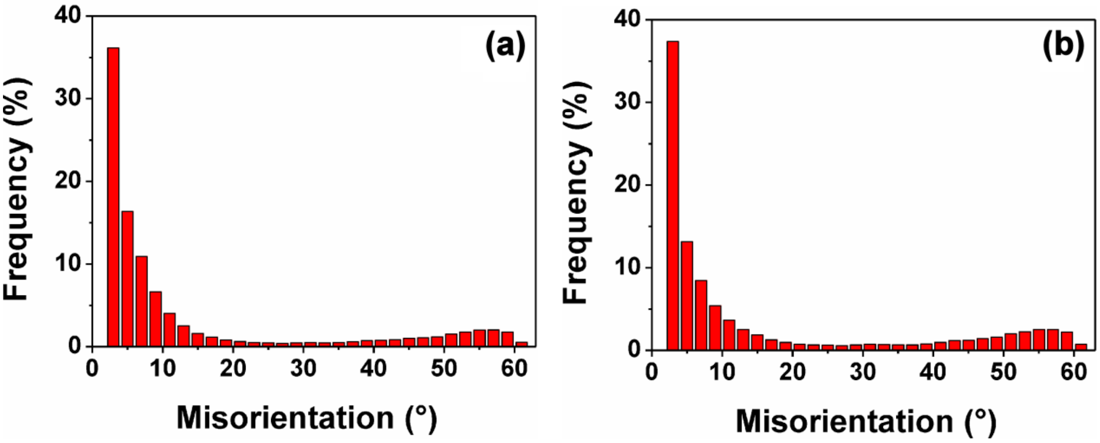

Fig. 4.31 Distribution of misorientation angles obtained by EBSD in the modified 9Cr-1Mo steel: (a) sample after DPD, and (b) sample after QSC, after an equivalent strain of 0.5.

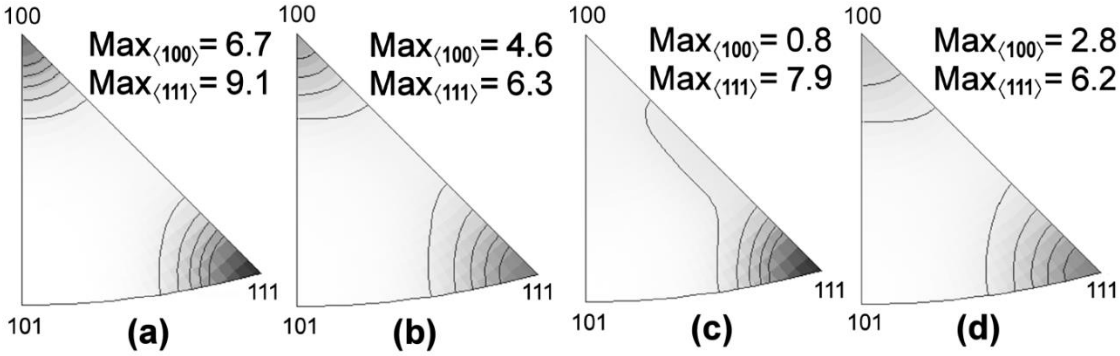

Fig. 4.32 Inverse pole figures showing the crystallographic orientation of the CA of the modified 9Cr-1Mo steel: (a) sample after DPD; (b) sample after QSC; (c) sample after DPD and annealing at 700 °C for 1 h; and (d) sample after QSC and annealing at 700 °C for 1 h. All samples are deformed to a strain of 0.5. Numbers represent the maximum intensity for the ⟨100⟩ and ⟨111⟩ components. Contour lines are given at 1, 2, 3, 4, and 5 times random.

4.3.1.2 Strain of 2.3

The microstructure is further refined after QSC to a strain of 2.3. A very fine structure with lamellar boundaries almost perpendicular to the CA is observed in this QSC sample (Fig. 4.33), which is similar to that in the sample after DPD (Fig. 4.10c). The pole figures obtained from the EBSD data of the QSC sample demonstrate a very pronounced duplex ⟨100⟩+⟨111⟩ fibre texture (as shown in Fig. 4.34), which is identical to the texture of the DPD-processed modified 9Cr-1Mo steel after the same strain (see Fig. 4.12). The microstructural parameters obtained by EBSD are summarized in the Table 4.1. The boundary spacing of the QSC-processed material is slightly larger than that of DPD-processed, with $d_{\theta>2°}$ = 120 nm and 111 nm, and d_{HAB} = 224 nm and 200 nm, for the QSC- and DPD-processed samples, respectively.

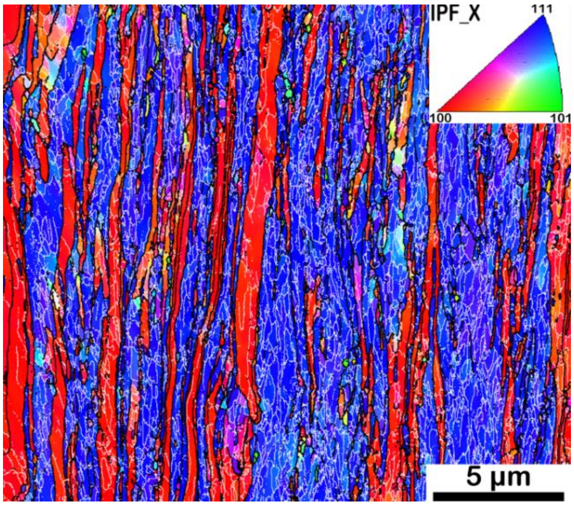

Fig. 4.33 Orientation map obtained by EBSD from the longitudinal section of the modified 9Cr-1Mo steel after QSC to a strain of 2.3: Different colors in the maps correspond to different crystallographic directions along CA as shown in the inset. LABs and HABs are shown as white and black lines, respectively. The CA is horizontal.

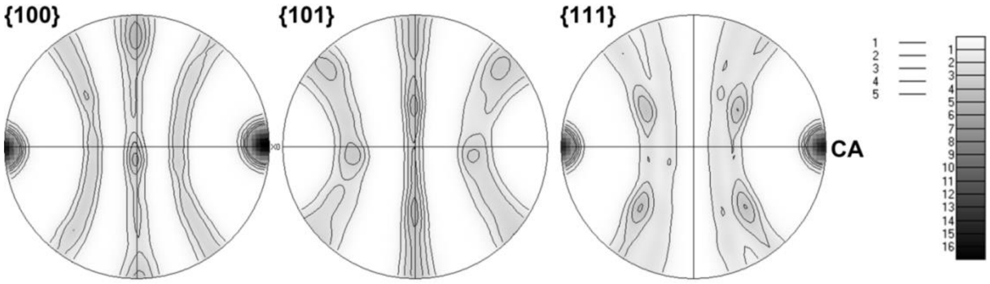

Fig. 4.34 Pole figures obtained by EBSD from the modified 9Cr-1Mo steel after QSC to a strain of 2.3. CA is horizontal.

4.3.2 Effect of strain rate on the subsequent annealing behavior

The microstructure of the modified 9Cr-1Mo steel after QSC is morphologically similar to that after DPD to the same strains. However, the microstructural parameters are slightly different for the DPD and QSC samples, which may result in different annealing behavior. In this subsection, comparative studies of the annealing behavior of the samples after QSC and DPD are presented.

4.3.2.1 Annealing after a strain of 0.5

Annealing at 675 °C for 1 h results in coarsening of the deformed microstructure and in the onset of recrystallization (Fig. 4.35). The $d_{(\theta>2°)}$ increases to approximately 0.4 μm, and the area fraction of recrystallized grains (f_{RX}) after this annealing treatment is estimated to be 2% and 8% in the QSC and DPD samples, respectively. After annealing at 700 °C for 1 h, f_{RX} is still rather small (6%) in the QSC sample, whilst the DPD sample is almost fully (95%) recrystallized (see Fig. 4.36 and Table 4.2).

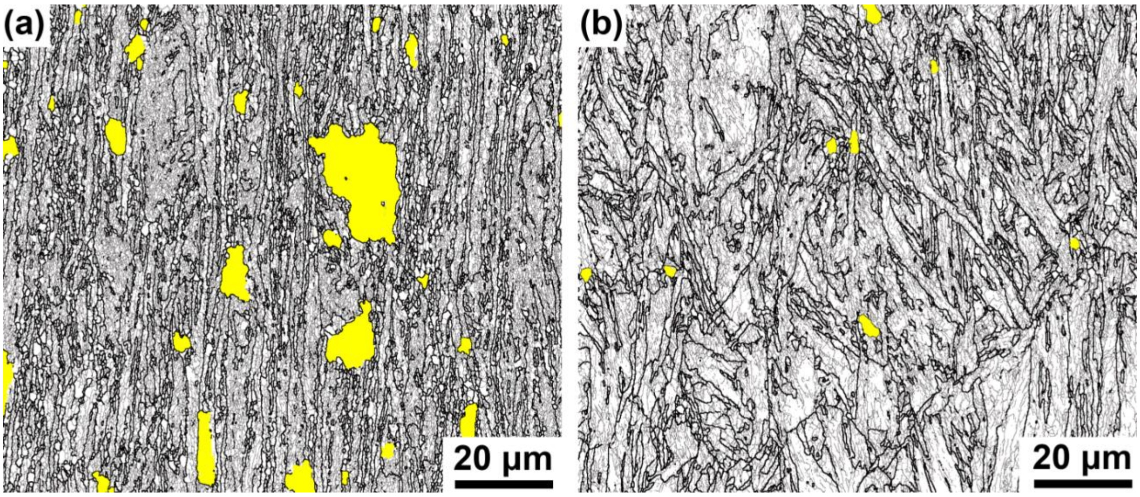

Fig. 4.35 Misorientation maps obtained by EBSD from the longitudinal section of the modified 9Cr-1Mo steel annealed at 675 °C for 1 h: (a) sample after DPD; and (b) sample after QSC. Thin gray and bold dark lines show LABs (2–15°) and HABs (>15°), respectively. Recrystallized grains are shown in yellow. The CA is horizontal.

To obtain information on the non-recrystallized (recovered) regions of the annealed samples, spacings between LABs were calculated excluding the contribution of the recrystallized regions. The resulting parameter d^*_{LAB} is inversely proportional to the surface density S_V of LABs in the recovered regions, and an increase in d^*_{LAB} thus characterizes the elimination of LABs during recovery of the deformed microstructure.

After annealing at 675 °C for 1 h, d^*_{LAB} for the DPD sample is 130% larger than d_{LAB} in the deformed microstructure, whereas for the QSC sample the increase is only 60%. This indicates that recovery is more pronounced in the DPD sample. Nevertheless, the recovered microstructure in the DPD sample is still more refined than that in the QSC sample (see d^*_{LAB} in Table 4.2). The difference between the samples is much greater after annealing at 700 °C, when d^*_{LAB} is found to increase by a factor of almost 5 after DPD, but only by a factor of 2 after QSC. It should however be noted that only a very small area (5%), classified as recovered, contributed to d^*_{LAB} for the DPD sample annealed 700 °C for 1 h. Therefore, statistics for this value in the latter condition are not as good as for the other annealed samples.

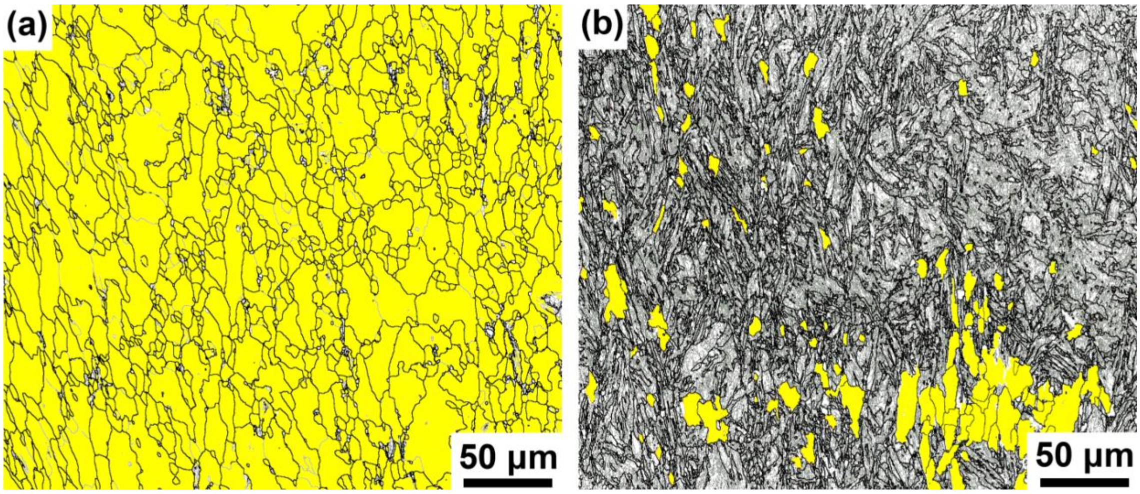

Fig. 4.36 Misorientation maps obtained by EBSD from the longitudinal section of the modified 9Cr-1Mo steel annealed at 700 °C for 1 h: (a) sample after DPD; and (b) sample after QSC. Thin gray and bold dark lines show LABs (2–15°) and HABs (>15°), respectively. Recrystallized grains are shown in yellow. The CA is horizontal.

Considering the fraction of HABs, it is apparent that f_{HAB} differs very little for both annealed conditions of the QSC sample, but increases significantly with increasing annealing temperature in the DPD sample (see Table 4.2). Whereas annealing at 675 °C for 1 h does not cause appreciable changes in crystallographic textures as compared to those in the deformed conditions, the ⟨100⟩ texture component weakens considerably in the samples annealed at 700 °C, especially in the annealed DPD sample (see Fig. 4.32c,d).

Table 4.2 Microstructural parameters (determined using EBSD) of the modified 9Cr-1Mo steel in different conditions

Condition	$d_{(\theta>2°)}$ (μm)	d_{LAB} (μm)	d^*_{LAB} (μm)	d_{HAB} (μm)	f_{HAB} (%)	f_{RX} (%)
DPD 0.5+675°C 1 h	0.37	0.60	0.55	0.96	38	8
QSC 0.5+675°C 1 h	0.43	0.61	0.60	1.45	30	2
DPD 0.5+700°C 1 h	3.4	15.2	1.22	4.4	78	95
QSC 0.5+700°C 1 h	0.61	0.88	0.83	1.97	31	6

4.3.2.2 Annealing after a strain of 2.3

The modified 9Cr-1Mo steel after QSC to a strain of 2.3 is annealed for 1 hour at temperatures in the range between 400 °C to 700 °C. An orientation map obtained by EBSD from the QSC sample after annealing at 675 °C for 1 hour is shown in Fig. 4.37. It is seen that the material is partially recrystallized with a recrystallization fraction of 19%. In this orientation map, most of recrystallizing grains are shown in blue, i.e. they belong to the ⟨111⟩ texture component. Therefore, the orientation dependent recrystallization behavior is very pronounced in the QSC-processed material, which is very similar to that of DPD-processed material.

Microstructural parameters of the two annealed samples obtained by EBSD are compared in Table 4.3. After annealing at 675 °C for 1 hour the fraction of recrystallization (f_{RX}) in the QSC sample is much less (19%) than that in the DPD sample (72%). The difference in the recrystallization fraction leads to a considerable difference in the measured boundary spacings for both $d_{(\theta>2°)}$ and d_{HAB} (see Table 4.3). However, the difference in the boundary spacings for the recovered materials ($d^*_{(\theta>2°)}$ and d^*_{HAB}) is much smaller. It is seen that the microstructural parameters of the QSC sample after annealing at 675 °C for 1 hour are comparable to that of the DPD sample after annealing at 650 °C for 1 hour (Table 4.3). Such a lower thermal stability of the DPD-processed sample, compared to the QSC sample, is due to the higher energy stored in the microstructure in the form of higher density of deformation-induced boundaries.

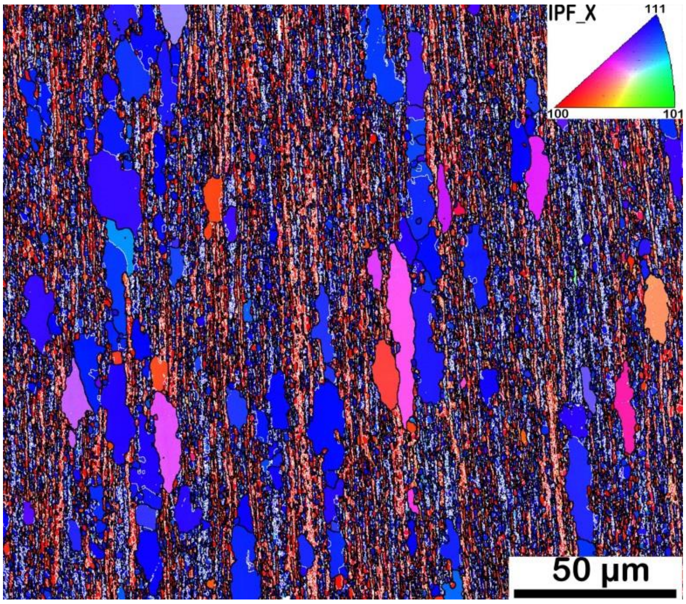

Fig. 4.37 Orientation map obtained by EBSD from the longitudinal section of the modified 9Cr-1Mo steel after QSC to a strain of 2.3 and annealing at 675 °C for 1 hour. Different colors in the maps correspond to different crystallographic directions along the CA as shown in the inset. LABs and HABs are shown as white and black lines, respectively, and the CA is horizontal.

Table 4.3 Microstructural parameters (determined using EBSD) of the modified 9Cr-1Mo steel at different conditions. $d^*_{(\theta>2°)}$ and d^*_{HAB} are the $d_{(\theta>2°)}$ and d_{HAB} in the recovered region, respectively.

Condition	$d_{(\theta>2°)}$ (μm)	d_{HAB} (μm)	$d^*_{(\theta>2°)}$ (μm)	d^*_{HAB} (μm)	f_{HAB} (%)	f_{RX} (%)
QSC 2.3+675°C 1h	0.530	0.876	0.448	0.727	49.4	19
DPD 2.3+675°C 1h	1.568	2.671	0.553	0.870	61.0	72
DPD 2.3+650°C 1h	0.471	0.772	0.426	0.693	49.4	12

4.3.3 Effect of strain rate on the mechanical properties

4.3.3.1 Mechanical properties of modified 9Cr-1Mo steel after DPD

Significant structural refinement due to DPD, as shown in section 4.1, results in enhanced strength and hardness of the modified 9Cr-1Mo steel. It is seen from Fig. 4.38 that Vickers hardness increases with increasing DPD strain. The hardness of the sample after DPD to a strain of 2.3 is about 365 HV1, which is about 80% higher than that of as-received sample (205 HV1). The hardness does not further increase when the strain increases to 3.1. This hardening correlates with the structural refinement, with the boundary spacing of $d_{\theta>2^\circ}$ decrease from 1110 nm to 110 nm as determined from the orientation maps obtained by EBSD. The microstructural refinement induced hardening is also evident in the stress strain curves. The tensile test results of the DPD-processed and the as-received material are shown in Fig. 4.38. The tensile strength increases from 675 MPa to 1247 MPa after DPD to a strain of 2.3, whereas the total elongation decreases from 21.5% to only 5.0%. The lack of ductility of the modified 9Cr-1Mo steel after DPD is very typical for many heavily deformed materials due to their very limited work-hardening capacity.

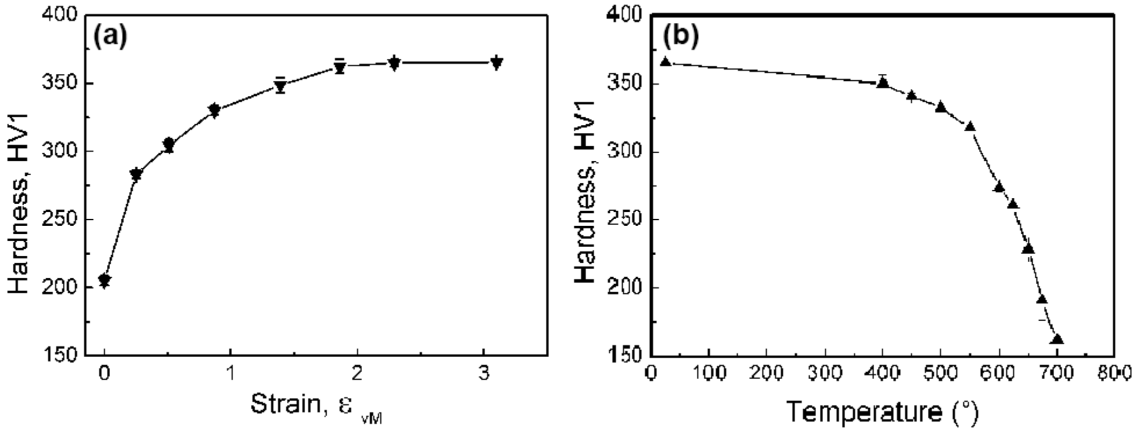

Fig. 4.38 Vickers hardness of the modified 9Cr-1Mo steel: (a) after DPD to different strains; and (b) after annealing for 1 hour at different temperatures of the sample processed by DPD to a strain of 2.3

Considerable structural coarsening occurs in the DPD-processed sample after annealing at 600 °C for 1 hour, which is demonstrated in section 4.2 in both EBSD and TEM results. This structural coarsening also leads to a reduction in the strength. It is seen in the Fig. 4.38b that the hardness is reduced to only 273 HV1 after annealing at 600 °C for 1 hour, and consequently the strength decreases to 940 MPa. Nevertheless, the ductility does not improve appreciably and the total elongation is still low, ~7%, as seen in Fig. 4.39. After this annealing treatment, the material is only recovered, which suggests that only recovery is not sufficient to considerably improve the ductility of the deformed modified 9Cr-1Mo steel. After annealing at 675 °C for 1 hour, the hardness of the material is further reduced to 228 HV1, and the tensile strength is only 811 MPa. Owing to the structural coarsening and recrystallization (f_{rex}=12%), the DPD-processed sample regains decent ductility, with the total elongation increasing to about 11%. Compared to the as-received material, the thermal stability is largely reduced after nanostructuring, due to the fact that no appreciable softening happens when the as-received modified 9Cr-1Mo steel after annealing at 700 °C for 10 hours [17].

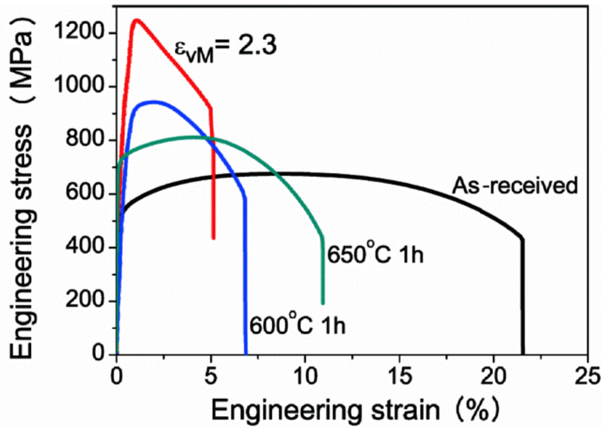

Fig. 4.39 Stress-strain curves for the modified 9Cr–1Mo steel in the as-received condition and after DPD to a strain of 2.3 in the deformed and annealed conditions.

In summary, significant strengthening due to the DPD induced structural refinement is achieved, however, tensile elongation is largely reduced compared with the modified 9Cr-1Mo steel in the as-received tempered martensite state. Compared to the as-received condition, the reduced the thermal stability is thought to be related to the destructed martensitic structure with carbide stabilized martensitic boundaries, and the high stored energy input in the sample during DPD. Therefore, it is suggested that even though the strength of the DPD-processed material is very high, this material cannot withstand annealing at the temperatures which can be reached in the advanced fission and fusion reactors.

4.3.3.2 Work hardening behavior

The effect of strain rates on mechanical properties and work hardening behavior of the modified 9Cr-1Mo steel were tested by quasi-static compression at different strain rates. The stress–strain curves obtained during compression for initial strain rates between 10^{-4} s^{-1} and 10^{-1} s^{-1} are shown in Fig. 4.40. The compression tests at different strain rates do not reveal considerable differences in the yield stress (0.2% proof stress), but the flow curves after yielding do display significant differences; there is an obvious tendency for strain rates below 10^{-1} s^{-1} that the flow stress at any particular strain is greater for higher strain rates. Fig. 4.40 also shows that the shape of the curve for a strain rate of 10^{-1} s^{-1} is different from that of the curves obtained at lower strain rates. In particular, it is evident that for plastic strains larger than 0.3, the flow stress becomes even smaller than those measured at the lower strain rates (Fig. 4.40). This behavior would imply a negative strain rate sensitivity, which however is not expected for the modified 9Cr-1Mo steel with no stress-induced transformation. One possible reason for the unusual behavior at 10^{-1} s^{-1} could be adiabatic heating during compression. Estimations of the adiabatic heating, taking into account the mechanical work and the heat transfer, indicate that whereas for the strain rates up to 10^{-2} s^{-1} the heating is not appreciable, at a strain rate of 10^{-1} s^{-1} the temperature of the deformed sample may increase by about 50 K. The details in calculating the increased temperature is given in the Appendix I. It is suggested, that this significant heating is responsible for the reduced flow stress recorded during deformation at 10^{-1} s^{-1}.

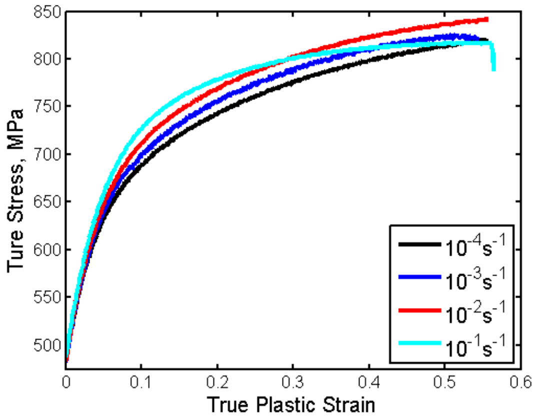

Fig. 4.40 True stress–true plastic strain curves of the modified 9Cr-1Mo steel compressed at different initial strain rates.

To clarify the cause for the different behavior at 10^{-1} s^{-1}, we conducted interrupted compression tests with loading–holding sequences. For instance, at a strain rate of 10^{-1} s^{-1}, the deformation occurs in 10 steps; in each step, the specimen is first compressed by 0.5 mm followed by holding (fixed crosshead positions) the specimen at this strain for 4 s under load. This holding step allows the heat generated during compression from the specimen to be transferred to the grips, thereby cooling the specimens to ambient temperature.

The results obtained during the loading–holding compression experiments for strain rates of 10^{-2} s^{-1} and 10^{-1} s^{-1} are presented in Fig. 4.41 along with the curves obtained during continuous compression. It is seen that for both strain rates, stress relaxation occurs during holding. In Fig. 4.41a no difference in the shape of the stress-strain curves for 10^{-2} s^{-1} between continuous and interrupted compression can be distinguished except for the stress relaxation during the interrupted compression test. It is therefore evident that at this strain rate heating during compression does not appreciably affect the flow stress. However, at 10^{-1} s^{-1} the stress in the interrupted compression test is much higher than that measured during continuous compression for strains larger than 0.2 (Fig. 4.41b). This provides strong evidence that at a strain rate of 10^{-1} s^{-1} adiabatic heating caused by the mechanical work during compression has significant influence on the flow stress of the modified 9Cr-1Mo steel. At a plastic strain of 0.55 the stress drop due to heating is estimated to be about 2%. A similar reduction is expected in the shear modulus. Since the temperature increases 50 K based on our calculation, the shear modulus would drop 2% according to the relationship between temperature and shear modulus of iron [139]. Therefore, the temperature dependence of the shear modulus appears to be the dominant factor causing the lower flow stress of the 10^{-1} s^{-1} sample seen at strains larger than 0.3.

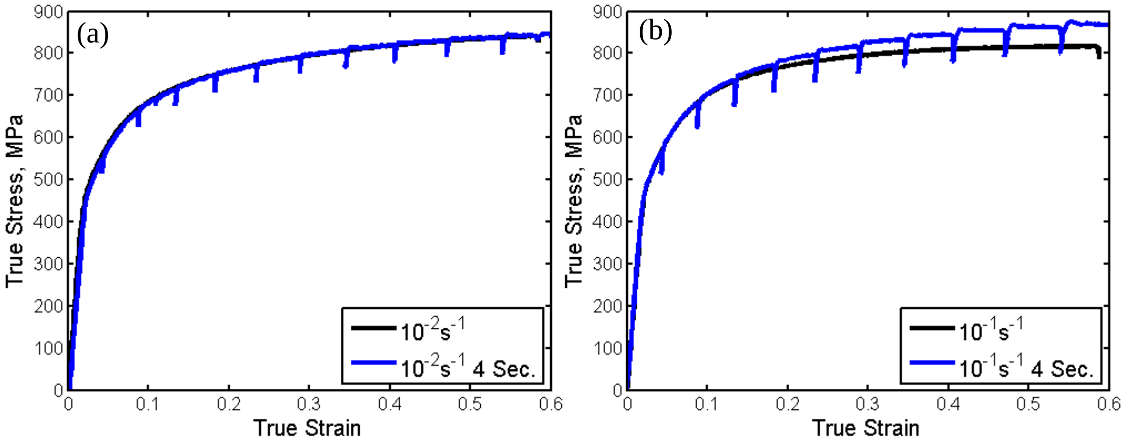

Fig. 4.41 Stress–strain curves for the modified 9Cr-1Mo steel obtained during continuous and interrupted compression tests at initial strain rates of (a) 10^{-2} s^{-1} and (b) 10^{-1} s^{-1}.

For a proper calculation of the intrinsic work-hardening rate at ambient temperature, it is important that there is no artifact due to adiabatic heating. Therefore, only the data from the interrupted test are considered for 10^{-1} s^{-1}. Fig. 4.42a presents modified true stress–true plastic strain curves obtained by omitting the short transient of the stress relaxation stages during the holding steps. Based on these curves, the work-hardening rate $\Theta = \partial\sigma / \partial\varepsilon$ was calculated and then plotted vs. the true stress in Fig. 4.42b. In this figure, two work-hardening stages can be clearly distinguished, for which the work-hardening rate decreases linearly with stress. As a linear decrease is usually attributed to odd-numbered stages of the work-hardening behavior, the stages are designated III and

III′ here to reflect their similar appearance.

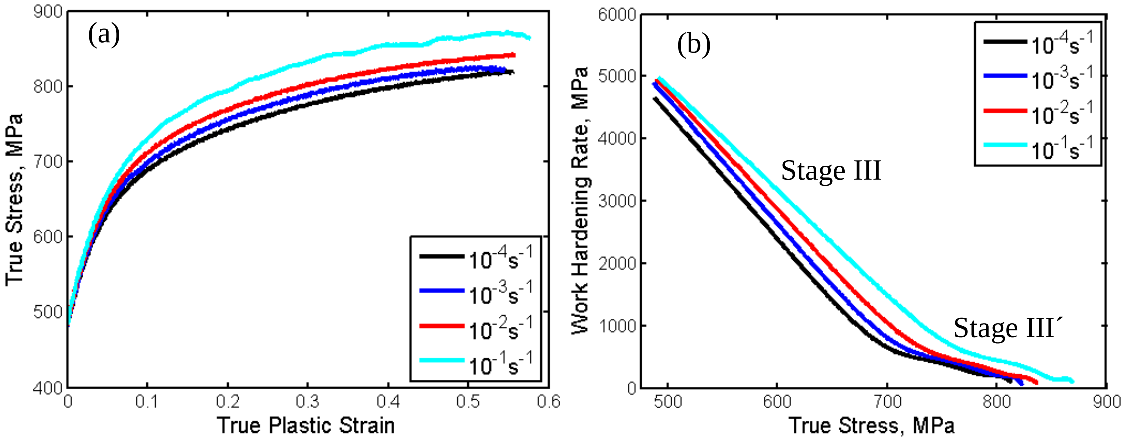

Fig. 4.42 Curves used for the analysis of the work-hardening behavior of the modified 9Cr-1Mo steel: (a) true stress vs. true plastic strain (without heating effect); (b) work-hardening rate vs. true stress.

The linear decrease in the work-hardening rate with increasing flow stress can be rationalized based on the Kocks–Mecking model for dislocation accumulation and annihilation [69, 140]. According to this model, accumulation of dislocations occurs by their mutual trapping leading to a work-hardening rate

$$\Theta = \left.\frac{\partial\sigma}{\partial\varepsilon}\right|_{\dot{\varepsilon},T} = \Theta_0\left(1-\frac{\sigma}{\sigma_s}\right) \qquad (4.8)$$

where Θ_0 is an athermal work-hardening rate and σ_s is the extrapolated saturation stress, at which Θ becomes zero. By fitting the experimental data to Eq. (4.8), Θ_0 and σ_s can be derived, independently for both stages. The fitting coefficients for all strain rates are summarized in Table 4.4. There is a systematic tendency that with increasing strain rate the saturation stress increases and that stage III extends to higher stresses.

Taking the data for the strain rate 10^{-2} s^{-1} as an example, the work hardening rate curve is plotted in Fig. 4.43a together with the fits for stages III and III′. Stress-strain curves calculated based on Eq. (4.7) and the coefficients Θ_0 and σ_s (Table 4.4) are shown in Fig. 4.43b along with the experimental curves. The fact that the calculated curves and the experimental data are almost identical implies that the Kocks–Mecking model can be employed to describe the flow and the work-hardening behavior of the modified 9Cr-1Mo steel studied in the present experiment.

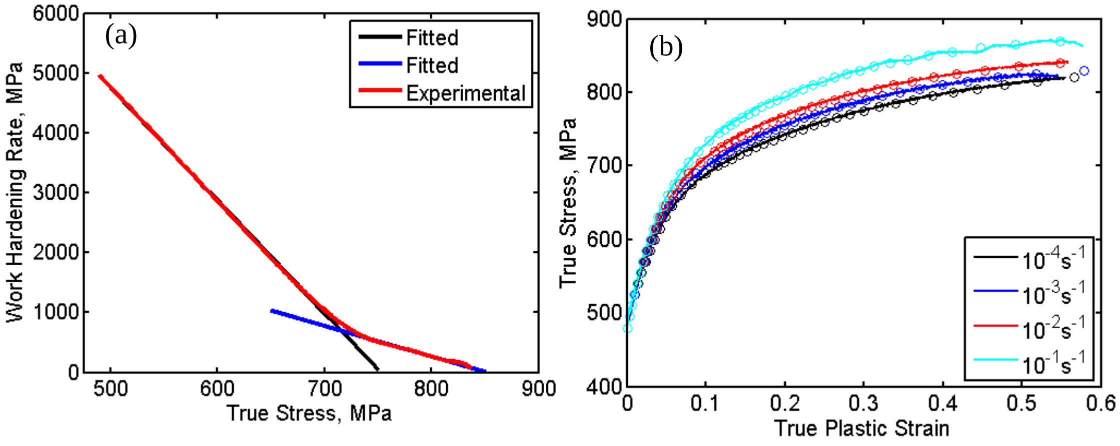

Fig. 4.43 Comparison of experimental and fitted values: (a) work-hardening rates versus true stress for a strain rate of 10^{-2} s^{-1}; (b) true stress–true plastic strain curves (open circles) based on the Kocks–Mecking model and the coefficients of Table 4.4. In (b) the solid line shows the experimental data and open symbols correspond to calculated data.

Table 4.4 Coefficients of Kocks–Mecking model for the stages III and III′ obtained by fitting and values for the intersection point characterizing the transition between the two stages.

	Stage III		Intersection point		Stage III′	
$\dot{\varepsilon}(s^{-1})$	σ_s (MPa)	Θ_0 (GPa)	σ_I (MPa)	Θ_I (MPa)	σ_s (MPa)	Θ_0 (GPa)
0.0001	719	14.4	685	684	834	3.6
0.001	736	14.3	700	706	844	4.0
0.01	752	14.1	714	724	856	4.4
0.1	787	13.3	740	797	882	4.9

Consequently, the work-hardening behavior of this steel can be rationalized in terms of mutual annihilation and mutual trapping of dislocations. (It should be mentioned that the dislocation density was already fairly high in the as-received material (Fig. 4.2) causing the high yield stress.) Although martensitic lath boundaries and precipitates may act as obstacles for dislocations, thereby affecting the work-hardening behavior, their influence is not considered to be significant in the present material. Based on the linearly decreasing work-hardening rate, it is concluded that the mean free path of dislocations is primarily controlled by interaction with other dislocations.

The saturation stresses of the modified 9Cr-1Mo steel vary systematically with the strain rate (Table 4.4). This dependence is characterized by the strain rate sensitivity $m = \partial \ln \sigma_s / \partial \ln \dot{\varepsilon}$. Fig. 4.44 presents the saturation stress as a function of strain rate; and strain rate sensitivities of 0.013 and 0.0075 are obtained for stages III and III′, respectively. Obviously, the lower value for stage III′ indicates that the annealing behavior during the later stage is less affected by thermal activation.

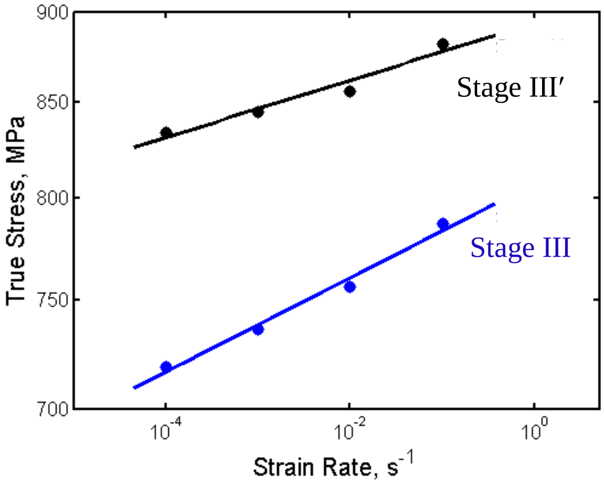

Fig. 4.44 Saturation stress vs. strain rate for stages III and III′

4.3.3.3 Strain of 0.5

The microstructure of the QSC sample is less refined than that of the DPD sample at a strain of 0.5 (Table 4.1). Consequently, the hardness of the QSC sample is lower than that of the DPD sample (see Fig. 4.45 and Table 4.5). However, the finer boundary spacing of the DPD sample indicates a higher stored energy, and thus the microstructure is more prone to recovery and recrystallization. This leads to a more pronounced softening during annealing at high temperatures, as shown in Fig. 4.45. It is seen that the hardness of the QSC sample is higher than that of DPD sample after annealing at 675 °C for 1 hour, and that a much larger difference is observed in the samples annealed at 700 °C for 1 hour, with 229 HV1 and 164 HV1 for the QSC and DPD samples, respectively.

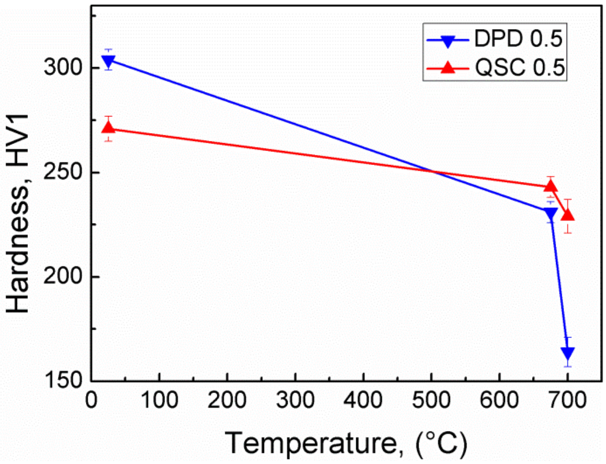

Fig. 4.45 The Vickers hardness of modified 9Cr-1Mo steel processed by either DPD or QSC to a strain of 0.5 during and annealed for 1 hour at different temperatures

Table 4.5 Vickes hardness of the modified 9Cr-1Mo steels in different conditions

Condition	DPD 0.5	QSC 0.5	DPD 0.5 675°C 1 h	QSC 0.5 675°C 1 h	DPD 0.5 700°C 1 h	QSC 0.5 700°C 1 h
Hardness (HV1)	304±5	271±6	231±9	243±5	164±7	229±8

4.3.3.4 Strain of 2.3

After deformation to a strain of 2.3, the QSC sample is still a little softer than the DPD sample, with Vickers hardness of 347 and 364 HV1, respectively. This is due to the coarser deformation structure of the QSC sample (Table 4.1). However, during isochronal annealing, the hardness of the QSC samples reduces less pronounced than DPD samples, especially for those annealed above 625 °C (Fig. 4.46). For instance, after annealing at 650 °C for 1 hour, the hardness of the QSC sample is about 243 HV1, whereas the hardness of the DPD sample is 228 HV1, and even a larger difference is observed after annealing at 675 °C for 1 hour: 220 HV1 and 190 HV1 for the QSC and DPD samples, respectively. The lower thermal stability of the DPD sample is again attributed to its higher stored energy introduced into the microstructure during deformation in the form of finer structure, which is the driving force for recovery and recrystallization.

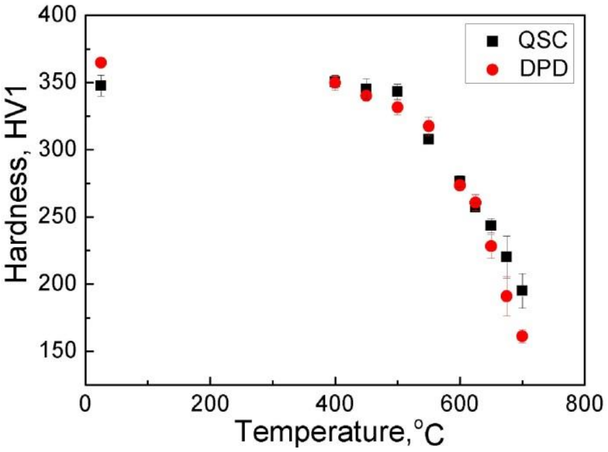

Fig. 4.46 The Vickers hardness of the modified 9Cr-1Mo steel after DPD or QSC to a strain of 2.3 during isochronal annealing for 1 hour at different temperatures

4.3.4 Discussion

4.3.4.1 Deformation microstructure and annealing behavior

The present work demonstrates that the strain rate has a considerable effect on microstructural parameters of the modified 9Cr-1Mo steel. For this material, the microstructure of the sample after DPD sample more refined by dislocation boundaries, and this greater refinement makes the DPD sample harder than the QSC sample after deformation to strains of both 0.5 and 2.3. The 9Cr–1Mo steel compressed via either DPD or QSC is found to develop duplex ⟨111⟩ + ⟨100⟩ fiber textures similar to those reported for other *bcc* materials deformed by compression [65, 141], and contains a well-refined microstructure due to subdivision by dislocation boundaries. This result obtained on the *bcc* material is similar to those previously reported for *fcc* nickel and aluminum [72, 142], for which the greater refinement after DPD was rationalized based on a higher density of dislocations stored after high strain rate deformation. Such a higher dislocation density results in a higher frequency of dislocation boundaries and in finer boundary spacing than those in the QSC material. Similarly, a larger amount of stored dislocations could explain the greater refinement observed in the DPD-processed steel investigated here, as compared to the QSC counterpart.

The results obtained in this work can be compared with those on the modified 9Cr–1Mo steel cold deformed by equal channel angular extrusion (ECAE) [143, 144]. Similar to our observations for the low-strain DPD sample, the initial tempered martensitic structure observed in [143] evolved into a nearly equiaxed subgrain structure already after a single pass through an ECAE die with 90° angle between channels (strain ~1.15). The deformation by ECAE appeared, however, to be less effective for structural refinement than DPD as the average subgrain size was found to be 0.4 µm after an ECAE strain of 1.15 and 0.2–0.3 µm and for strains of 3.8–4.6 [143, 144]. Thus, the subgrain size after a rather high strain by ECAE was similar to that obtained in our material processed by DPD to a strain of only 0.5. The more rapid refinement observed in our experiment compared to that by ECAE can be attributed to the higher strain rates during DPD, which accumulated a higher density of dislocations forming finely spaced dislocation boundaries [72, 142].

The difference in the stored energy between the samples after DPD and QSC can explain the differences observed in their annealing behavior. It is obvious that a deformed material with a higher stored energy is more prone to recrystallization than a sample with less stored energy. It is therefore not surprising that the area fraction of recrystallized grains after each heat treatment applied in this work is greater for the samples annealed after DPD. The difference in the recrystallization kinetics is significant after annealing at 675 °C for 1 h and becomes very large when the annealing temperature is increased to 700 °C. For the material after DPD to a strain of 2.3, significant structural coarsening and mechanical softening occurs during annealing at 600 °C and above, even though carbides show clear pinning effect on grain boundaries (Fig. 4.19). It is suggested that the strong dependence of the annealing behavior on the strain rate applied during processing of the modified 9Cr–1Mo steel should be taken into account when designing thermo-mechanical treatments for this material.

Although the recrystallization kinetics are different between the DPD and QSC processed samples due to the higher stored energy in the DPD sample, both samples demonstrate similar orientation dependence during recrystallization. Apparently, these similarities are due to similar deformation textures produced by compression, which appear insensistive to the strain rate in the range applied in the present work.

4.3.4.3 Mechanical properties

The modified 9Cr-1Mo steel exhibits weak strain-rate-dependent yielding behavior, whereas their post-yielding strain hardening is strongly rate-dependent, as demonstrated by the compression tests. The flow stress increases with increasing strain rate at given strain after yielding. In terms of the strength of materials during compression, the substructure evolution is supposed to play an important role. According to dislocation theory, the dislocation flux, which is the product of dislocation density and the velocity of mobile dislocations necessary to accommodate the deformation, is proportional to the imposed shear strain rate [145]:

$$\dot{\gamma} = b\rho_m \upsilon \tag{4.9}$$

Where b is the magnitude of the Burgers vector, υ is the average dislocation velocity, and ρ_m is the mobile dislocation density. Accordingly, higher strain rates relate to higher flux of dislocations. The work hardening rate reflects the rate of dislocation accumulation balanced by dislocation multiplication and dislocation annihilation. Dynamic recovery is strongly thermally activated, and hence a strain rate dependent process. Deformation at the high strain rate could suppress the dynamic recovery to some extent, and thereby enhance the work hardening rate at a given stress, as shown in Fig. 4.33b.

Adiabatic heating leads to a reduction of the flow stress, and this has been rationalized by the temperature dependent modulus of the modified 9Cr-1Mo steel. The Vickers hardness of the sample deformed at 10^{-1} s^{-1} is about 5% higher than that of the sample deformed at a strain rate of 10^{-4} s^{-1}, which indicates that adiabatic heating does not appreciably affect the microstructure evolution during compression of this steel. The specific structures that evolve during deformation are known to correlate with the flow stress achieved at given plastic strains, and the difference in the flow stress and hardness suggests that the substructure developed during deformation at different strain rates was indeed different. This difference becomes even more pronounced when the material is deformed by DPD at the much higher strain rate. After deformation to a strain of 0.5, the DPD sample is about 12% stronger than the QSC sample with a strain rate of 10^{-4} s^{-1}. The DPD processed sample is still about 5% stronger than the QSC sample after deformation to a strain of 2.3.

Structural refinement by DPD makes the modified 9Cr–1Mo steel harder and significantly increases its strength. After DPD to a strain of 2.3 the hardness increased from 205 HV1 to 365 HV1 and the UTS was almost doubled (from 675 MPa to 1247 MPa). These values after DPD are much larger than those in the ECAE-processed 9Cr–1Mo steel, where the hardness was only 320 HV0.1 even a strain of 4.6 [144]. Fan *et al*. [143] reported that the UTS after a strain of 2.5 was 1004 MPa, i.e. ~20% lower than the strength of our DPD sample deformed to a similar strain. The UTS of the sample after DPD to a strain of 2.3 was higher than that obtained during low strain rate deformation even after a strain of 3.8 by ECAE [143], which reflects the difference in the extent of structural refinement between the two deformation techniques, i.e. the finer boundary spacing after DPD compared to that after ECAE.

The significant strengthening of the modified 9Cr–1Mo steel by DPD is accompanied by a dramatic reduction in ductility, where the total elongation is only 5% after a strain of 2.3. The lack of ductility is typical for many heavily cold-deformed materials demonstrating very limited work-hardening capacity [17, 112]. Deformation at elevated temperatures or post-deformation heat-treatments can improve ductility (which can be important for further forming operations), but the strength in this case is not as high as in cold-deformed samples without additional annealing [17]. In the modified 9Cr-1Mo steel, annealing at 600°C for 1 h of the sample deformed to a strain of 2.3 leads to softening and a considerable loss of strength with a very minor increase in elongation (Fig. 4.39), which indicates that the coarsening of the deformed microstructure alone is detrimental for strength with only a small gain in ductility. In contrast, coarsening combined with partial recrystallization leads to significantly increased ductility and still comparatively high strength. Nevertheless, the material cannot be used for high temperature application, as is partially recrystallized, which is not stable at elevated temperatures.

4.4 Summary

The evolution of microstructure, texture and mechanical properties of a modified 9Cr-1Mo ferritic/martensitic steel during deformation at different strain rates and to different strains and during subsequent annealing have been analyzed in this chapter The main findings can be summarized as follows:

1. The microstructure of the modified 9Cr-1Mo steel is transformed from a tempered martensitic structure into a typical dislocation cell structure after DPD to a strain of 0.5. A nanoscale lamellar structure is developed after DPD to a strain of 2.1. After this strain, the DPD sample is characterized by a pronounced ⟨100⟩+⟨111⟩ duplex fibre texture along the CA.

2. The strength of the modified 9Cr-1Mo steel increases from 675 MPa in the as-received condition to 1247 MPa after DPD to a strain of 2.3. However, the thermal stability of this DPD-processed steel is reduced and significant structural coarsening and recrystallization take place during annealing for 1 hour at 600 °C and above.

3. Very pronounced orientation dependent recovery and recrystallization are observed during annealing of the nanostructured modified 9Cr-1Mo steel, resulting in a very strong ⟨111⟩ fibre texture after recrystallization. Both oriented nucleation in the ⟨111⟩ lamellae and oriented growth of ⟨111⟩ recrystallizing grains contribute to the strong recrystallized ⟨111⟩ texture.

4. After annealing at 600 °C for 1 hour, ⟨111⟩ oriented lamellae quickly evolve into nearly equiaxed subgrains, whereas most subgrains within ⟨100⟩ oriented lamellae are still highly elongated. This sluggish recovery of lamellae with the ⟨100⟩ texture component is suggested to be one main reason for the oriented nucleation. The considerably higher stored energy in the ⟨111⟩ oriented lamellae than that in the ⟨100⟩ oriented lamellae contributes to the more pronounced recovery within the ⟨111⟩ texture bands.

5. Analysis of growth rates of the ⟨111⟩ and ⟨100⟩ oriented recrystallizing grains by the extended Cahn-Hagel method demonstrates that the ⟨111⟩ grains have a considerably higher growth rate than the ⟨100⟩ grains.

6. Both the flow stress and the work hardening rate of the modified 9Cr-1Mo steel post yielding are strain rate dependent. The higher strain rate results in a higher flow stress, and a higher work hardening rate at a given strain. The microstructural parameters are also affected by the imposed strain rates. At strains of 0.5 and 2.3, the microstructure of the DPD-processed material is finer than that of the QSC-processed material. The thermal stability of the DPD sample is however lower than that of the QSC sample. Orientation dependent recrystallization is revealed for the sample after QSC during annealing as well, which indicates that this phenomenon is universal for this steel after compression to high strains.

7. .

Chapter 5

Microstructure and annealing behavior of a nanostructured oxide dispersion strengthened steel

An oxide dispersion strengthened (ODS) ferritic steel, PM2000, is studied in this chapter on the microstructural aspects of oxide nanoparticles and ferrite matrix prior to deformation, after deformation and after subsequent annealing. Since the oxide dispersoids distinguish ODS steels from other metals and alloys, the crystallographic structure of the oxide nanoparticles, their interface and their orientation relationship with the ferrite matrix prior to deformation are determined by HRTEM, and in addition, the evolution of the size, morphology, interface and orientation relationship during annealing at high temperatures were characterized.

The material is processed at room temperature by dynamic plastic deformation (DPD) with strain rates of 10^2-10^3 s^{-1}. A nanoscale lamellar structure is obtained after a strain of 2.1. Oxide nanoparticles with diameters less than 20 nm are found to be deformed, whereas no deformation is observed for larger dispersoids. The evolution of the oxide nanoparticles with increasing plastic strain was characterized in detail by TEM, HRTEM and STEM. The dominant deformation mechanism is revealed and the size-dependent deformation behavior of the oxide nanoparticles is discussed. The observation of deformed oxide particles contradicts the common view that oxide particles should be both strong and brittle, and that no plastic deformation is supposed to occur at ambient temperature.

Subsequent annealing is conducted on the DPD-processed material to investigate the thermal stability and the microstructural evolution of the nanostructured PM2000 during thermal treatment. Very pronounced orientation dependent recovery and recrystallization behavior were observed in the DPD-processed material, similar to those in the modified 9Cr-1Mo steel. Interestingly, the morphology of the deformed oxide nanoparticles changes dramatically, resulting in a significant refinement of the oxide nanoparticles compared to those in the initial material. These findings are thought to be able to open a methodology to tailor the properties by altering the microstructure of both the matrix and oxide nanoparticles via a thermomechanical treatment.

5.1 Microstructure of the as-received PM2000

5.1.1 Microstructure of ferrite matrix

The microstructure of PM2000 was characterized by EBSD and TEM. An orientation map and a misorientation distribution of the as-received PM2000 obtained by EBSD in a longitudinal section are shown in Fig. 5.1. It is seen that grains are not equiaxed but slightly elongated along the extrusion axis. The spacing of HABs along and perpendicular to the extrusion axis are 0.94 µm and 0.75 µm, respectively, i.e. the average grain size is in the submicrometer regime. The microstructure contains lots of LABs. The spacing of LABs along and perpendicular to the extrusion axis are about 0.58 µm and 0.37 µm, respectively. The misorientation angle distribution of all boundaries (Fig. 5.1b) shows that the fraction of boundaries with a misorientation angle less than 4° is the largest (20%), and that the material has a high fraction of HABs (53.7%). These microstructural features, with a grain size in the submicrometer range and a large fraction of HABs, originate from ball milling and the subsequent hot consolidation process [1, 34].A strong texture, with a stronger ⟨100⟩ fibre and a weaker ⟨110⟩ fibre along the extrusion axis, can be deduced from the orientations.

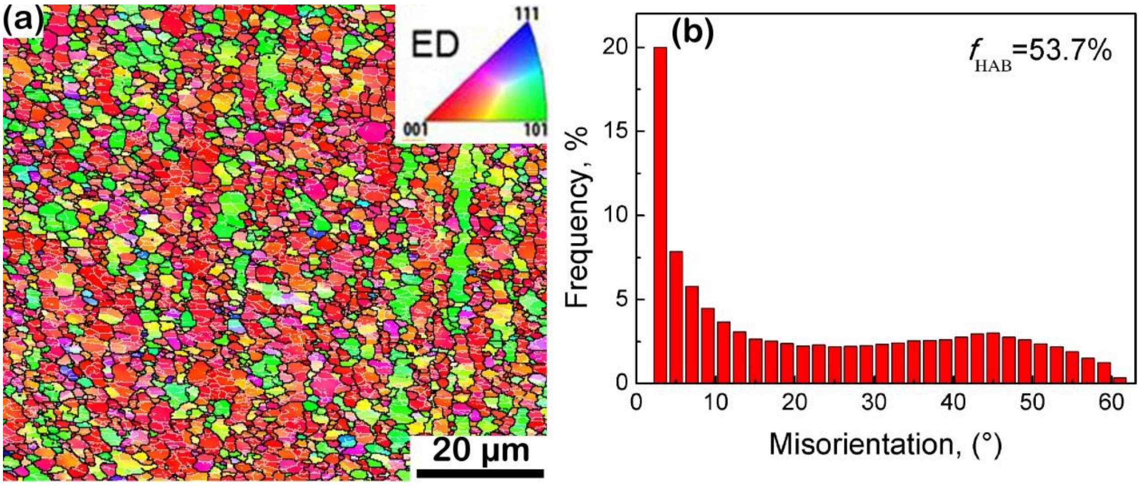

Fig. 5.1 (a) Orientation map obtained by EBSD in a longitudinal section of the as-received PM2000. The extrusion direction (ED) is vertical. It is colored according to the crystallographic direction along the ED using the color code in the inverse pole figure (see the inset). Black and white lines represent HABs and LABs, respectively. (b) Distribution of misorientation angles of the boundaries in the map(a).

A bright field TEM image (Fig. 5.2a) shows the microstructure in a longitudinal section of the as-received PM2000. This material is characterized by nearly equiaxed subgrains and a high dislocation density. A dark field TEM image (Fig. 5.2b) reveals a high frequency of well-dispersed oxide particles in the ferritic matrix.

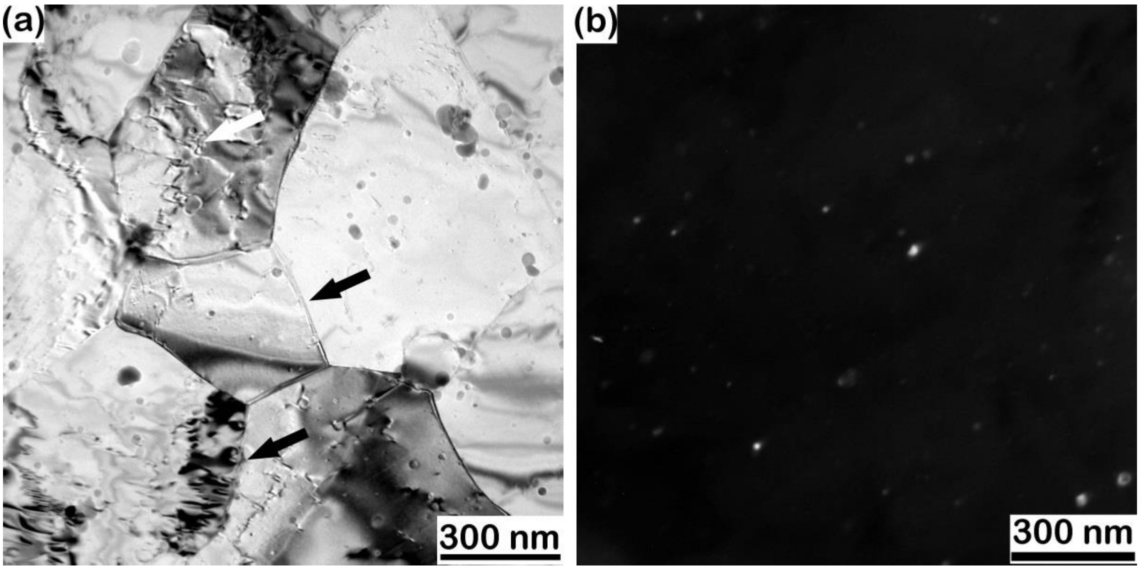

Fig. 5.2 TEM images from a longitudinal section of the as-received condition of PM2000: (a) a bright field image showing primarily a subgrain (indicated by black arrows) and a dislocation structure (indicated by while arrow). Particles are seen as dark features; (b) a dark field TEM image (from a different region), where the particles are seen as bright features. The extrusion direction is horizontal.

5.1.2 Structure of the oxide nanoparticles

Fig. 5.3a shows a bright field TEM image at a much higher magnification than Fig. 5.2a revealing more clear morphology and distribution of the oxide nanoparticles in the as-received PM2000. The oxide particles are nearly equiaxed, well-dispersed in the ferrite matrix and have a large size variation. The size distribution obtained by measuring 1196 oxide particles is shown in Fig. 5.3b, which demonstrates that the mean diameter of the oxide nanoparticles is about 14 nm and the standard deviation (STDEV) is 10 nm. This data is quite consistent with results reported by others on the same material [48].

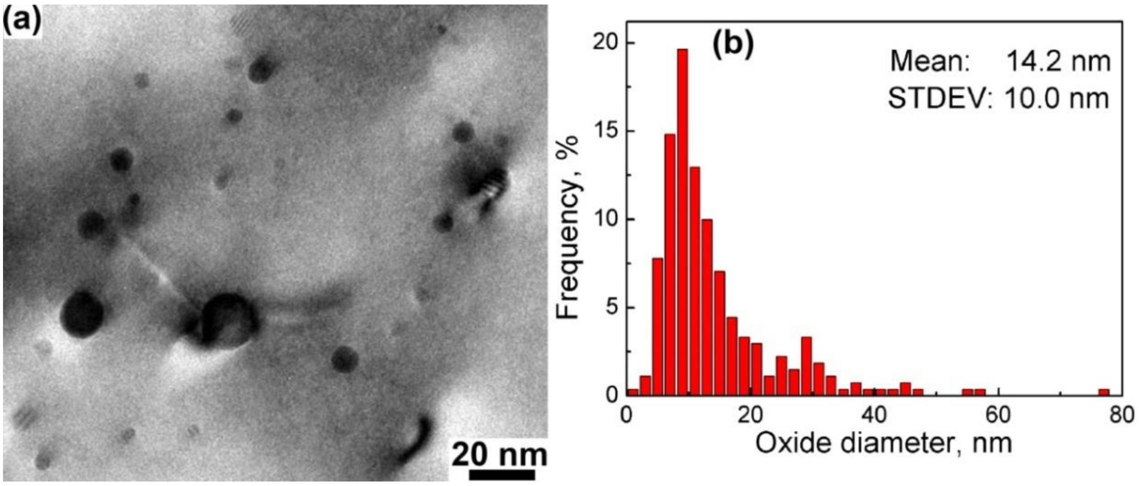

Fig. 5.3 (a) Bright field TEM image from the longitudinal section of the as-received PM2000 showing the dispersed oxide nanoparticles, and (b) size distribution of oxide nanoparticles measured from a number of TEM images.

The crystallographic structure of the oxide nanoparticles was systematically characterized by HRTEM. As the oxide nanoparticles are embedded in the ferrite matrix, it is difficult to obtain very clear imaging and electron diffraction of the oxide particles exclusively. To eliminate the interference in identifying the crystal structure of oxide nanoparticles due to the strong channeling effect of the ferrite matrix, oxide nanoparticles were extracted by carbon replica for HRTEM characterization. As described in section 3.1.2, PM2000 is produced by mechanical milling of yttria particles and pre-alloyed ferritic powders which contains 20 wt. % Cr and 5.5 wt. %Al. Since Al has a high affinity to oxygen [146], after mechanical alloying, consolidation and extrusion the oxide nanoparticles are no longer pure yttrium oxide. They have been determined to be yttrium-aluminum oxide by Electron Energy Loss Spectroscopy (EELS) [147] and Electron Dispersive X-Ray Spectroscopy (EDS) [48, 148, 149]. There are at least four different yttrium aluminum oxides known in the Y-Al-O system [150], namely $Y_4Al_2O_9$ (yttrium-aluminum-monoclinic, YAM), $YAlO_3$(yttrium-aluminum-hexagonal, YAH), $YAlO_3$ (yttrium-aluminum-perovskite, YAP) and $Y_3Al_5O_{12}$ (yttrium-aluminum-garnet, YAG). These variants complicate identification of the oxide nanoparticles in Al-alloyed ODS ferrtic steel and their relationships with the ferrite matrix [147, 148, 151-156]. To identify the character of the oxide nanoparticles in PM2000, Fast Fourier Transformation patterns of the HRTEM images were obtained and all of them were compared with simulated diffraction patterns of the four yttrium-aluminum oxides mentioned.

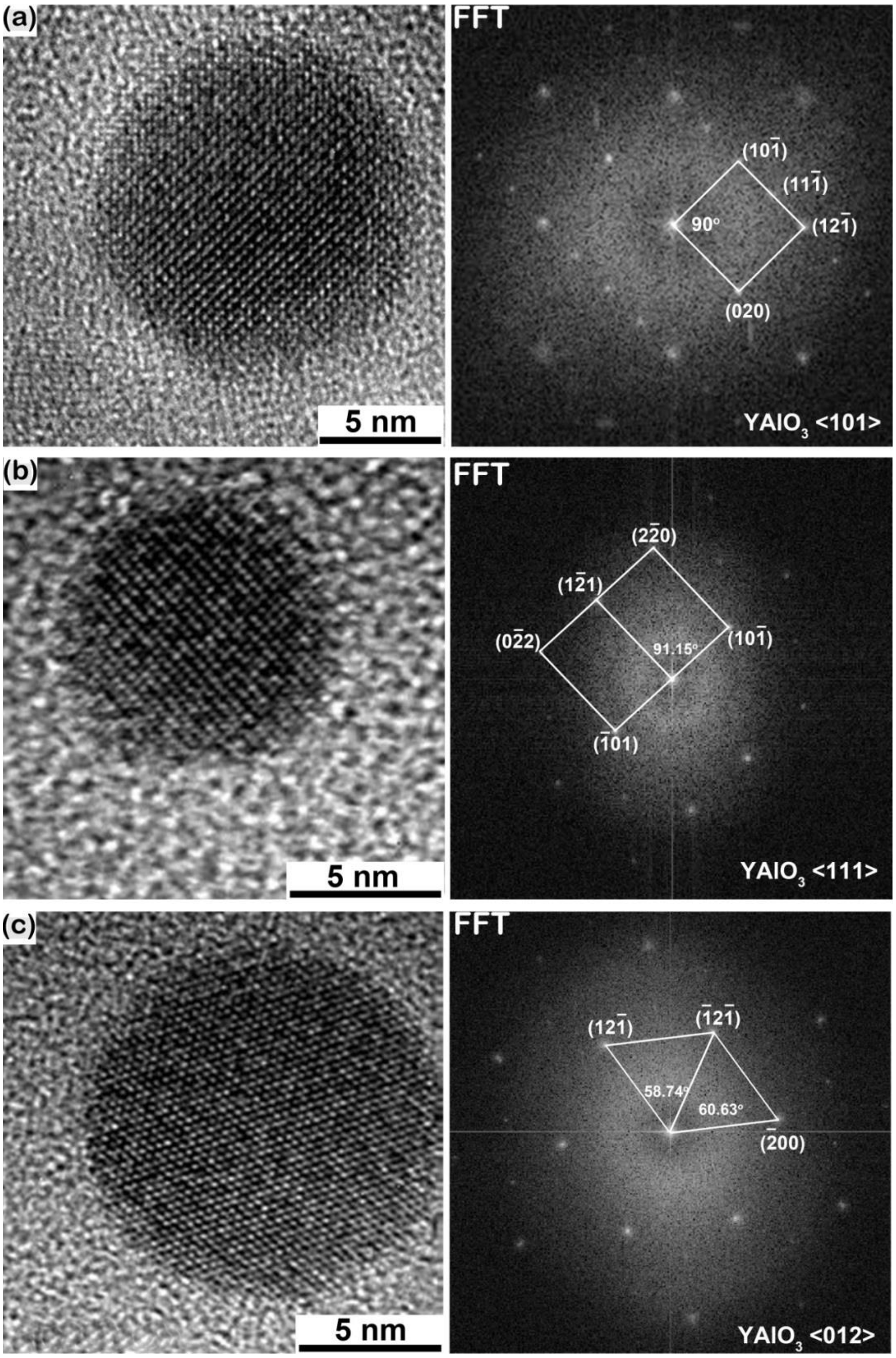

Fig. 5.4 HRTEM images and their corresponding FFTs of oxide nanoparticles in as-received PM2000 with incident electron beam along different zone axes of the oxide nanoparticles. By indexing the FFT patterns, the direction of incident electron beam is determined to be along (a) ⟨101⟩, (b) ⟨111⟩ and (c) ⟨012⟩zone axis of $YAlO_3$.

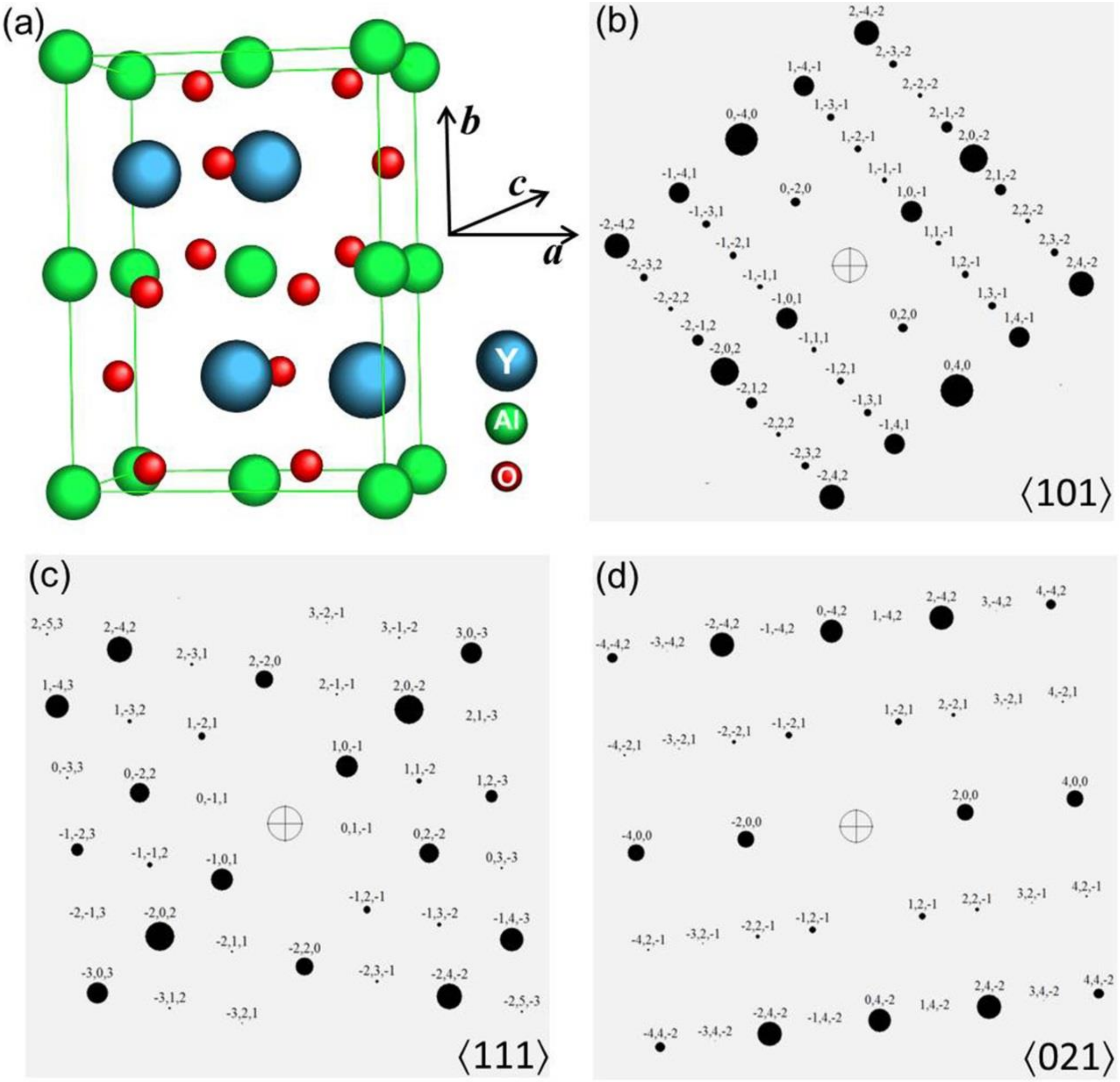

Fig. 5.5 (a) Schematic structure of the unit cell of $YAlO_3$and thesimulated diffraction patterns along different zone axes (b) ⟨101⟩, (c) ⟨111⟩ and (d) ⟨012⟩, which are consistent with those FFTs in Fig. 5.4 (a), (b), and (c), respectively. (CaRIne Crystallography 3.1 was used to construct the unit cell structure and simulate the diffraction patterns).

The software CaRIne Crystallography 3.1 was used to construct the unit cell structure of all the yttrium-aluminum oxides and simulate diffraction patterns along different zone axes by comparison. 30 oxide nanoparticles with diameters ranging from 4 nm to 35 nm were characterized. All the observed oxide nanoparticles are determined as $YAlO_3$, which has a space group of Pnma (group No. 206), with lattice parameters a=5.330 Å, b=7.375 Å and c=5.180 Å. Orthorhombic $YAlO_3$ has a perovskite structure and it is known as yttrium aluminum perovskite (YAP) [150], and will be abbreviated as YAP hereafter. Fig. 5.4 shows three examples of HRTEM images and corresponding Fast Fourier Transformation (FFT) patterns of oxide nanoparticles. The crystal lattice of these oxide nanoparticles is clearly seen from the HRTEM images. The electron beam incident direction is along the ⟨101⟩, ⟨111⟩ and ⟨012⟩ zone axes for Fig. 5.4a, b, and c, respectively. The unit cell structure of YAP and the electron diffraction patterns along the above three zone axes are shown in Fig. 5.5. It is evident that the simulated patterns and the FFTs of the HRTEMs are in very good agreement.

5.1.3 Interface and orientation relationship between oxide nanoparticles and ferrite

After clarification of the crystallographic structure of the oxide nanoparticles, their orientation relationship with ferrite matrix could be determined in PM2000. To obtain the relationship between YAP and ferrite, HRTEM characterization was conducted on conventional thin foils. Systematic characterizations were done, and three examples of the HRTEM images of the oxide nanoparticles and ferrite matrix are shown in Fig. 5.6.

In these HRTEM images, the three YAP nanoparticles are inspected along different zone axes, with the incident electron beam along three orientations, namely ⟨110⟩, ⟨221⟩, and ⟨112⟩ of the YAP. It is seen from the HRTEM images that all the particles have coherent lattices with the surrounding matrix. Their corresponding FFTs reveal that for all three particles, the parallel and coherent planes of YAP and ferrite are $(220)_{YAP}$ and $(110)_{Fe}$, respectively. This orientation relationship develops mainly because iron and YAP have very close lattice spacings for these crystallographic planes, with 2.12 Å, 2.24 Å and 2.21 Å for the $(110)_{Fe}$, $(220)_{YAP}$ and $(022)_{YAP}$ planes, respectively. Due to the fact that YAP has an orthorhombic structure, the $(220)_{YAP}$ plane only has one equivalent plane ($(2\bar{2}0)_{YAP}$). If a slight deviation is allowed, two more planes ($(022)_{YAP}$, $(0\bar{2}2)_{YAP}$) can be considered to be equivalent, whereas Fe has six equivalent(110) planes. Besides, angles between the individual $\{220\}_{YAP}$ planes are slightly different from that of $\{110\}_{Fe}$. Therefore, when one set of $\{220\}_{YAP}$ plane is parallel to a certain $\{110\}_{Fe}$ plane, the others of $\{110\}_{Fe}$ and $\{220\}_{YAP}$ planes are not exactly parallel. This issue can be more clearly illustrated in the reciprocal space of YAP and Fe along the ⟨111⟩ zone axis, where all six equivalent {110} planes are visible. It can be seen from Fig. 5.7 that, $(\bar{1}10)_{Fe}//(0\bar{2}2)_{YAP}$ and $(1\bar{1}0)_{Fe}//(02\bar{2})_{YAP}$, but other $\{110\}_{Fe}$ and $\{220\}_{YAP}$ planes are not parallel. Therefore, in this manner, if the viewing {110} plane of Fe is neither $(\bar{1}10)_{Fe}$ nor $(1\bar{1}0)_{Fe}$, no coherent information could be obtained from the orientation analysis. Two examples demonstrating this issue are shown in Fig. 5.8.

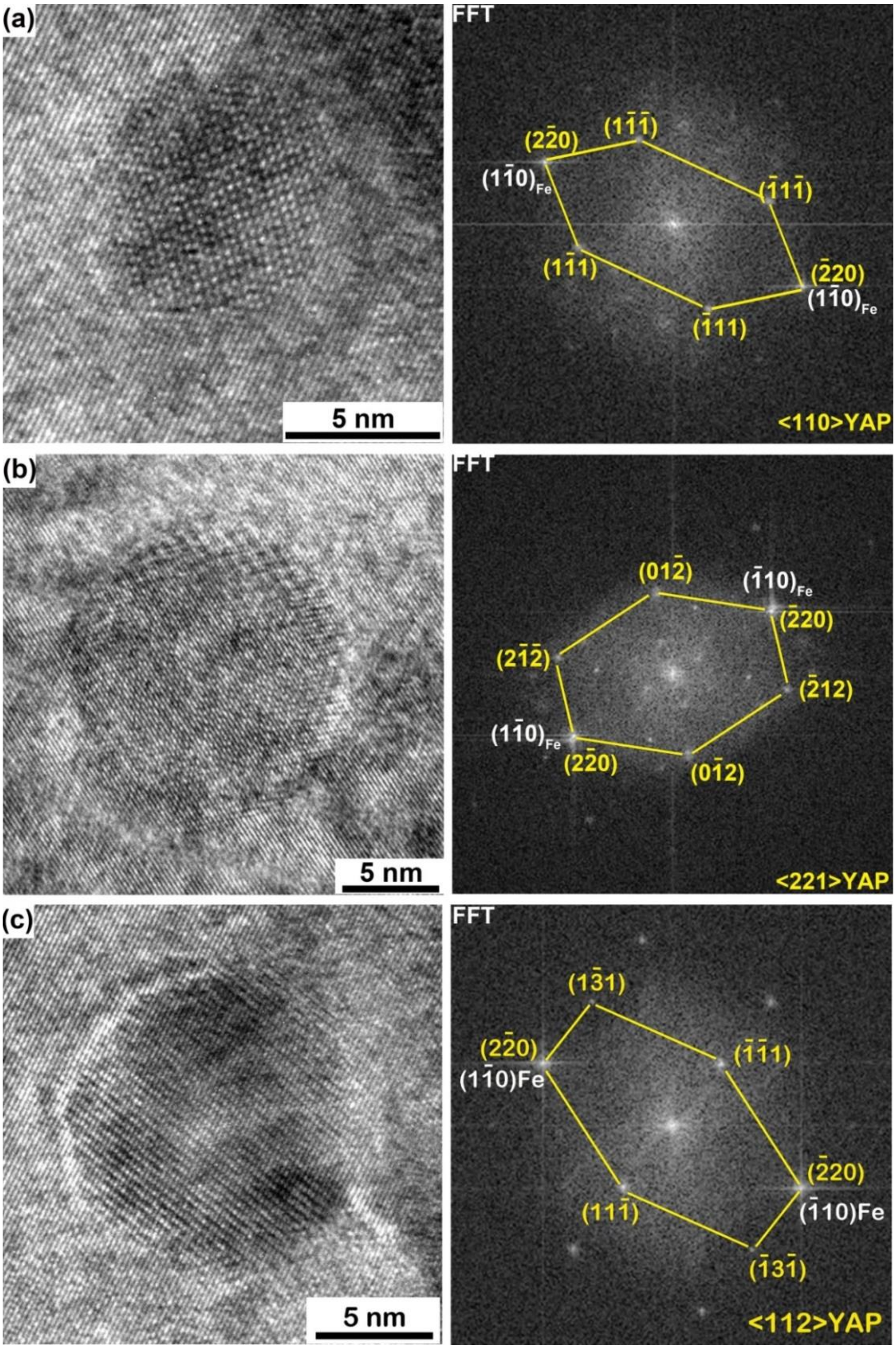

Fig. 5.6 HRTEM images of as-received PM2000 and the corresponding FFTs showing three YAP particles, with the electron beam along different zone axes of YAP, (a)⟨110⟩, (b) ⟨221⟩, and (c) ⟨112⟩, showing coherency with the ferritic matrix.

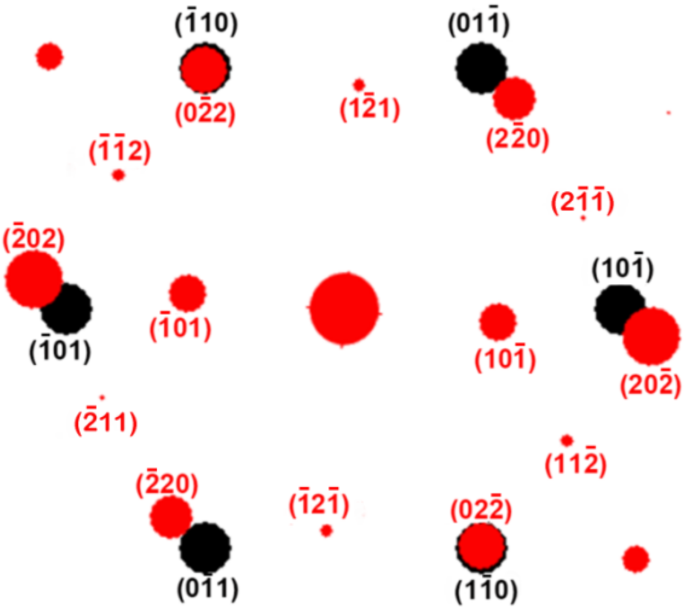

Fig. 5.7 Simulated diffraction patterns of YAP (dots and plane indices in red) and Fe (dots and plane indices in black) along the ⟨111⟩ zone axis for both.

In Fig.5.8a, {110} lattice planes of Fe are imaged clearly, and Moiré fringes appear in the oxide particle, which implies a semi-coherent relationship between YAP and ferrite. The diffraction of $(1\bar{2}1)_{YAP}$ and $(01\bar{1})_{Fe}$ are indexed in the corresponding FFT. It can be derived from the FFT that the $(1\bar{2}1)_{YAP}$ is not exactly parallel to $(01\bar{1})_{Fe}$, but there is a few degrees rotation between them. This can be illustrated in Fig. 5.7 where $(1\bar{2}1)_{YAP}$ and $(01\bar{1})_{Fe}$ appear simultaneously, because of the relaxation of Bragg diffraction in TEM. Due to the fact that the lattice spacings of $(1\bar{2}1)_{YAP}$ and $(01\bar{1})_{Fe}$ are different (2.62 Å and 2.12 Å, respectively), Moiré fringes appears because of the double diffraction from the two individual planes. To validate this ambiguous index caused by the interference of the channeling effect from the particle and superimposed matrix, a quantitative interpretation of the Moiré fringes is needed. When the orientation relationship between the particle and surrounding matrix gives rise to overlap of two gratings with different periodicities d_1 and d_2, Moiré fringes at the interface of the particle and matrix will emerge. The periodicity of the parallel Moiré pattern is given by:

$$D_{Moiré} = \frac{d_1 d_2}{|d_2 - d_1|} \tag{5.1}$$

The spacing of Moiré fringes measured on the particle is 9.76 Å and d_1 is the spacing of $(110)_{Fe}$, and from Eq. (5.1), d_2 is found to be either 2.64 Å or 1.72 Å for $d_2 > d_1$ or

$d_2 < d_1$,respectively. Comparing with the lattice parameters of YAP, only the former value is consistent with a YAP plane spacing, corresponding to the $(1\bar{2}1)_{YAP}$. This is indeed what has been indexed according to the FFT pattern.

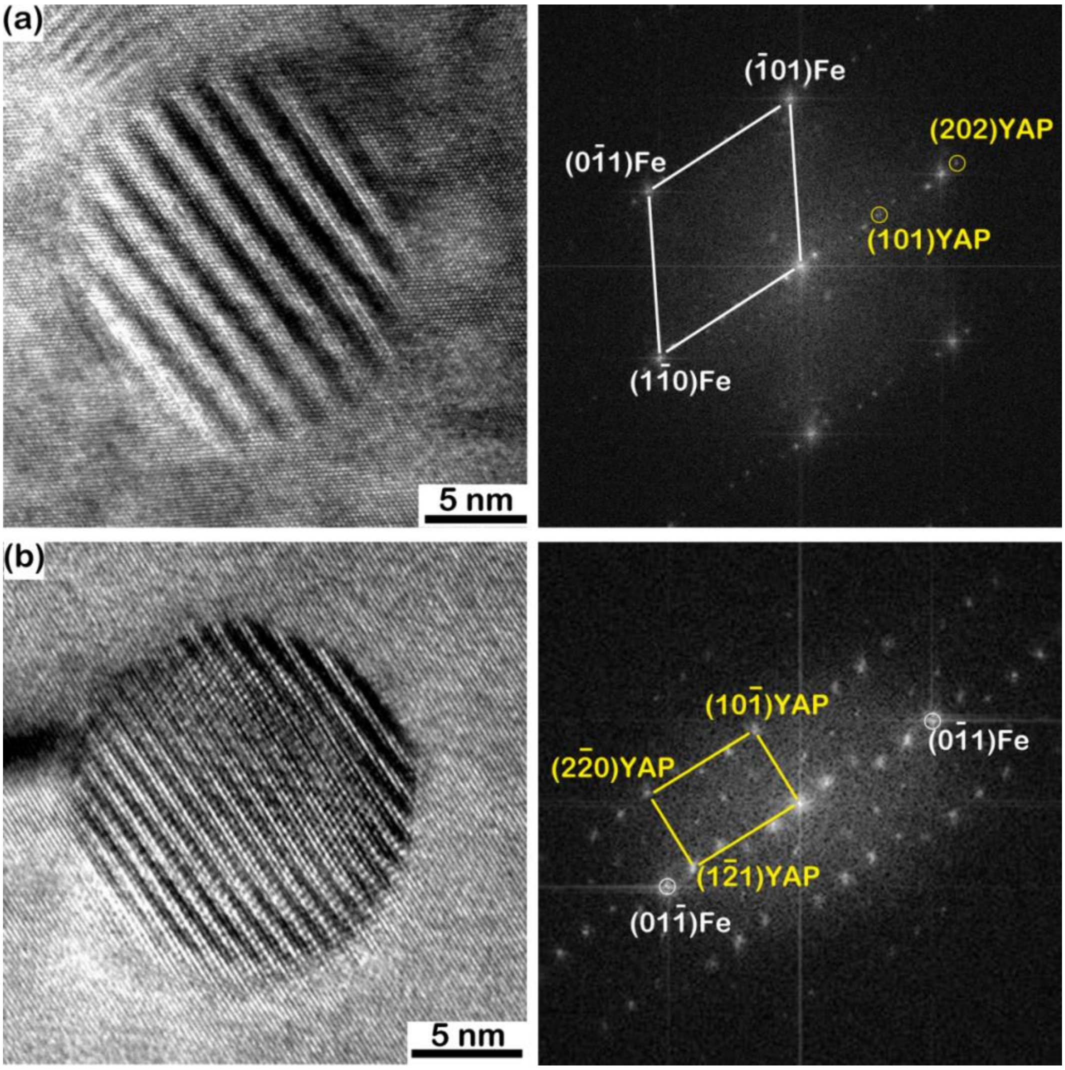

Fig. 5.8 HRTEM images and the corresponding FFTs showing two YAP particles and the ferrite matrix, with the incident electron beam along different zone axes, (a)$\langle 111 \rangle_{Fe}$ and near $\langle 111 \rangle_{YAP}$, (b) $\langle 111 \rangle_{YAP}$ and near $\langle 111 \rangle_{Fe}$.

Another example of the orientation relationship between an oxide nanoparticle and ferrite matrix is shown in Fig. 5.8b, in which Moiré patterns also emerge at the YAP particle. In this case, the $(110)_{Fe}$ is nearly parallel to $(022)_{YAP}$, and $(011)_{Fe}$ is nearly parallel to $(220)_{YAP}$. As quite a large mismatch between $(101)_{Fe}$ and $(202)_{YAP}$ exists, however, Moiré fringes emerge due to the different periodicities (2.12 Å and 1.86 Å, respectively) of these two individual gratings. By measuring the periodicity of Moiré fringes and employing the Eq. (5.1), the indexed results can be also verified. Therefore, it can be concluded that an approximate cuboid-on-cube orientation relationship between YAP nanoparticles and the ferrite matrix develops in the as received PM2000. However, because of the different symmetry of orthorhombic and cubic lattices, interfacial coherency is different viewed along different directions, especially as Bragg condition relaxation is considered in the TEM imaging.

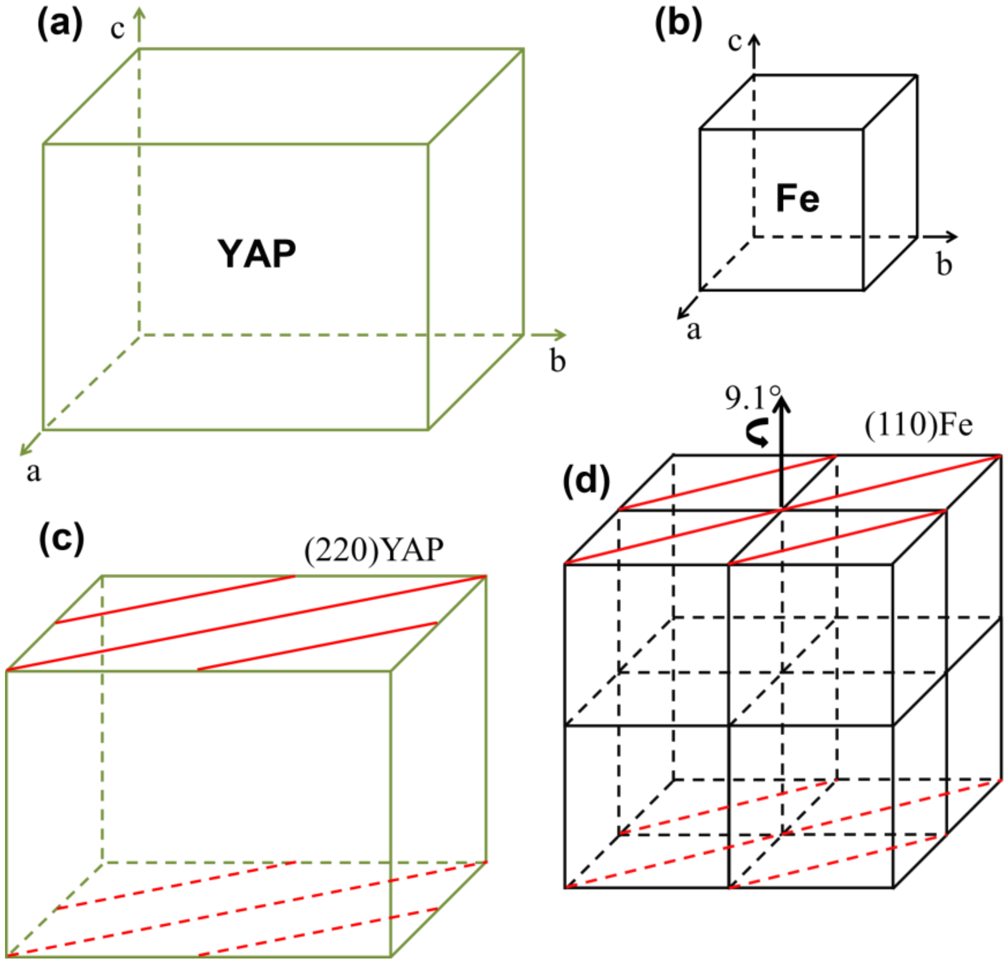

Fig. 5.9 Schematic diagrams showing the orientation relationship between a YAP nanoparticle and Fe matrix in PM2000. (a) unit cell of YAP, (b) unit cell of Fe, (c) unit cell of YAP with (220) plane traces shown in red lines, (d) four unit cells of Fe with (110) plane traces shown as red lines. The crystal of Fe is rotated about 9.1° along ***c***, resulting in $\boldsymbol{a}_{\mathrm{YAP}}$ and $\boldsymbol{a}_{\mathrm{Fe}}$ form an angle of 9.1°.

So far, it is evident that $(110)_{\mathrm{Fe}}//(220)_{\mathrm{YAP}}$ as derived from Fig. 5.6 , and $\langle 111\rangle_{\mathrm{Fe}}$ is nearly parallel to $\langle 111\rangle_{\mathrm{YAP}}$ as demonstrated in Fig. 5.8. A schematic diagram illustrating their true orientation relationship is shown in Fig. 5.9. The unit cells of YAP and Fe are shown with lengths proportional to their lattice parameters. Since the different crystal symmetry between YAP and Fe, the $(110)_{\mathrm{Fe}}$ and $(220)_{\mathrm{YAP}}$ are not exactly parallel when setting $\boldsymbol{a}_{\mathrm{YAP}}//\boldsymbol{a}_{\mathrm{Fe}}$, $\boldsymbol{b}_{\mathrm{YAP}}//\boldsymbol{b}_{\mathrm{Fe}}$ and $\boldsymbol{c}_{\mathrm{YAP}}//\boldsymbol{c}_{\mathrm{Fe}}$. A 9.1° rotation along the $\boldsymbol{c}_{\mathrm{YAP}}$ is necessary to make the $(110)_{\mathrm{Fe}}$ and $(220)_{\mathrm{YAP}}$ parallel, and this process is illustrated in Fig. 5.9d. After rotating 9.1° about $\boldsymbol{c}_{\mathrm{YAP},}$ the $\langle 111\rangle_{\mathrm{YAP}}$ and $\langle 111\rangle_{\mathrm{Fe}}$ have an angle of 5.6°, which is consistent with the observation in Fig. 5.8, and the orientation relationship between YAP is $(110)_{\mathrm{Fe}}//(220)_{\mathrm{YAP}}$ and $\langle 001\rangle_{\mathrm{Fe}}//\langle 001\rangle_{\mathrm{YAP}}$. However, as YAP has a different crystal symmetry with Fe, this orientation relationship can be expressed in another way as $\boldsymbol{c}_{\mathrm{YAP}}//\boldsymbol{c}_{\mathrm{Fe}}$, whilst $\angle\boldsymbol{a}_{\mathrm{YAP}},\boldsymbol{a}_{\mathrm{Fe}}=9.1°$, $\angle\boldsymbol{b}_{\mathrm{YAP}},\boldsymbol{b}_{\mathrm{Fe}}=9.1°$.

To summarize, the oxide nanoparticles in PM2000 are identified as $\mathrm{YAlO_3}$ with orthorhombic structure, and has a coherent lattice with ferrite matrix. The orientation relationship between YAP nanoparticles and the ferrite matrix developed during ball milling and consolidation and extrusion of the ball milled products is $(110)_{\mathrm{Fe}}//(220)_{\mathrm{YAP}}$ and $\langle 001\rangle_{\mathrm{Fe}}//\langle 001\rangle_{\mathrm{YAP}}$, i.e. they have nearly cuboid-on-cube orientation relationship.

5.1.4 Annealing behavior of the as-received PM2000

ODS steels are expected to be used at very high temperatureswith large temperature variations, and thus the thermal behavior of the ferrite matrix and oxide nanoparticles in PM2000 are of crucial importance. Therefore, the thermal stability of the materials is studied in this section. Additionally, the evolution of the orientation relationship between oxide nanoparticles and ferrite is of importance since any changes in these may alter the strengthening effect and the irradiation tolerance.

5.1.4.1 Thermal stability of the ferrite matrix

As seen from Fig. 5.1 and Fig. 5.2, the as-received PM2000 contains a large fraction of LABs and a high density of dislocations, which result from the hot consolidation and extrusion processes. These may induce thermal instability. The microstructure of PM2000, nevertheless, appears very stable when annealing at temperatures below 1000 °C for 1 hour. Orientation maps obtained by EBSD (Fig. 5.10) show the microstructure of PM2000 after annealing at 1150 °C and 1200 °C for 1 hour. After annealing at 1150 °C for 1 hour, the sample is almost fully recrystallized, and the sizes of recrystallized grains are in the order of millimeters. But there is a large white region that cannot be indexed when scanning with a large step size (20 μm) in Fig. 5.10a. An orientation map with a smaller step size (0.2 μm) was acquired (Fig. 5.10b) from this region. It is seen that the material in this region resembles the initial microstructure. After annealing at 1200 °C for 1 hour, the material is fully recrystallized

(Fig. 5.10c), and only two HABs were observed in the cross section of the whole sample (Ø6×9 mm). The size of the recrystallized grains is several millimeters. Apparently, as-received PM2000 does not show a standard recrystallization behavior. Instead, the recrystallization is characterized by a very high recrystallization temperature (~0.8 T_m, where T_m is the melting temperature) and, more importantly, very large recrystallized grains. This kind of phenomenon was also reported in the same and other ODS steels as well [157, 158].

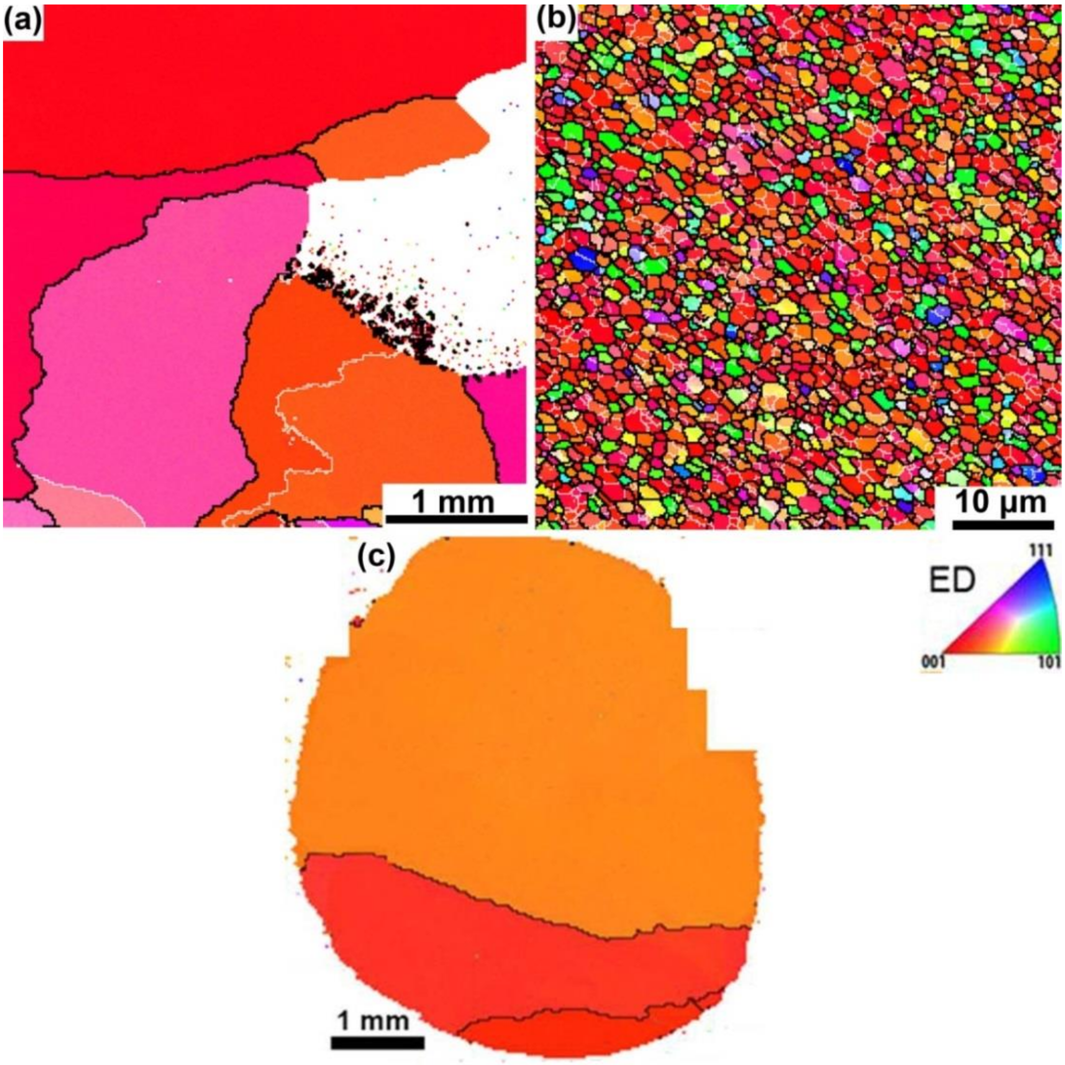

Fig. 5.10 Orientation maps obtained by EBSD of PM2000 in cross section after annealing at (a) and (b) 1150 °C for 1 hour, and (c) 1200 °C for 1 hour. Map (b) is from the region unindexed in (a) obtained with a smaller step size (0.2µm). Map (c) shows almost the entire specimen. The step size of (a) and (c) is 20µm. Black and white lines represent HABs and LABs, respectively.

During mechanical alloying, the powders experience a very large plastic strains (ε~9)[41], and the stored energy is thought to be very high (~1J/g) even after the consolidation and hot extrusion. Despite a high driving force for recrystallization, the alloys fail to recrystallize in practice except at very high temperatures close to the melting point [157-159]. This can be due to the nanoscale dispersoids which strongly pin dislocations and grain boundaries. Results from Fig. 5.10 demonstrate that even in the partially recrystallized sample with recrystallized grains size of several millimeters, the unrecrystallized region remain with their initial morphology. It is also claimed that [160] the microstructure of the material produced by high energy ball milling and powder metallurgy, characterized by submicron grain structure and high misorientations across the grain boundaries, contributes to such high thermal stability. Capdevila and Bhadeshia [34] proposed that for the material with this kind of structure, recrystallization happens by bowing out of a grain boundary. However, with such a small grain size, the boundary junctions themselves act as pinning sites for bowing out, and thereby preventing the formation of recrystallization nuclei at low temperatures. Once recrystallization nuclei form at very high temperatures, these nuclei can grow very rapid. Due to the fact that there are only very few recrystallized nuclei form, the recrystallized grains grow rapidly to a very large size [103, 160].

5.1.4.2 Thermal stability of the oxide nanoparticles

The thermal stability of the oxide nanoparticles in ODS steels is important to maintain their mechanical properties and irradiation tolerance at elevated temperatures. The oxide nanoparticles in PM2000 are generally very stable, because their coarsening requires a large thermal activation to enable long range diffusion of Y, Al and O. The as-received PM2000 was annealed at 1200 °C and above to study the thermal stability of the YAP nanoparticles. The Feret's diameter (distance between two parallel tangential lines of the particles) of the YAP nanoparticles was then measured in TEM thin foils. From Fig. 5.11 it is seen that after annealing at 1200 °C for 1 hour, the mean size of oxide nanoparticles does not increase compared to that prior to annealing (14.2 nm). Substantial coarsening happened when the material was annealed at 1300 °C. The average diameters of the oxide nanoparticles increase to 18.5 nm, 24.7 nm and 27.9 nm after annealing at 1300 °C for 1 hour, 10 hours and 100 hours, respectively. It is also evident from the size distribution histograms that the fraction of oxide nanoparticles with sizes smaller than 10 nm is largely reduced after annealing for 10 hours and 100 hours.

The thermal stability of the oxide nanoparticles has been examined for many ODS steels [36, 161, 162] . Miller *et al.*[161] reported that in some ODS steels containing Ti, such as 12YWT, 14YWT and MA957, the oxide nanoparticles do not coarsen even after annealing at 1300 °C for 24 hours. In other ODS steel with $YTaO_4$ nanodispersoids [162], significant coarsening was observed after the material was hot rolled at 1200 °C. For Al-alloyed ODS steels [48], little coarsening was observed after annealing at 1200 °C for 110 hours, and the diameter of the oxide nanoparticles increased from 15 nm to 26 nm, which is very similar to those observed in our current study. Such a big difference in the thermal stability of the oxide nanoparticles of different ODS steels is thought to result from the different compositions of the oxides. It is accepted that the presence of titanium in the oxide nanoparticles can refine the particles during consolidation [36, 163], and preserve their size to higher temperatures.

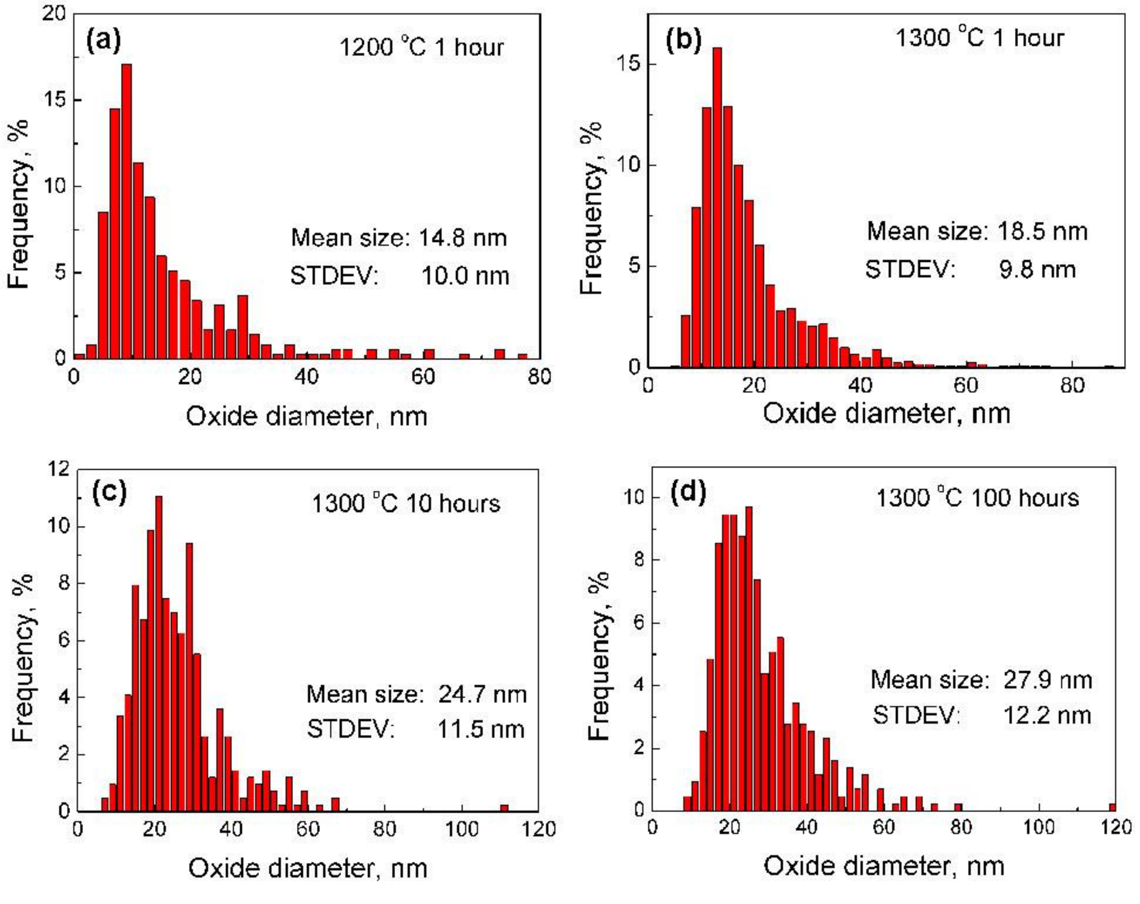

Fig. 5.11 Size distribution of the oxide nanoparticles in PM2000 after annealing at (a) 1200 °C for 1 hour, (b) 1300 °C for 1 hour , (c) 1300 °C for 10 hours, and (d) 1300 °C for 100 hours. Measurements were conducted in TEM thin foils, and at least 1000 particles with Feret's diameter were measured for each sample.

Interface and orientation relationship after annealing:1200 °C.

When PM2000 was annealed at high temperatures, the deformed structure in ferrite matrix coarsens, and the oxide nanoparticle can either shrink or grow. Any changes in the surrounding matrix and the particles themselves may alter the interface between the oxide nanoparticles and ferrite matrix. Besides, the oxide nanoparticles may have the potential to reorient at high temperatures in order to minimize the interfacial energy, thereby altering the interface and the orientation relationship between particle and matrix.

It has been shown in section 5.1.4.1 that after annealing at 1200 °C for 1 hour, the ferrite matrix significantly coarsens, which means that the orientation of the ferrite matrix surrounding most of oxide nanoparticles changes during annealing. However, at this stage, the average size of oxide nanoparticles does not increase considerably. The orientation relationships between the oxide nanoparticles and ferrite matrix indeed changes during annealing, and three typical examples are shown in Fig. 5.12 and Fig. 5.13.

Fig. 5.12 shows HRTEM images and corresponding FFTs and Inverse Fast Fourier Transformations (IFFTs) of two YAP nanoparticles in the sample after annealing at 1200 ℃ for 1 hour. In Fig. 5.12a, the incident electron beam is along $\langle 100\rangle_{Fe}$ and $\langle 112\rangle_{YAP}$, and the FFT of this HRTEM image is indexed accordingly. It can be seen that $(110)_{Fe}$ and $(02\bar{1})_{YAP}$ are almost parallel, and $(1\bar{1}0)_{Fe}$ forms an angle of 5° with $(2\bar{2}0)_{YAP}$. However, the lattice spacing of $(02\bar{1})_{YAP}$ is 2.90 Å, while the lattice spacing of $(110)_{Fe}$ is 2.12 Å. Due to such a large difference in spacing, the interface cannot remain coherent and misfit dislocations are expected at the interface. After filtering the background noise and selecting the diffraction from the $(02\bar{1})_{YAP}$, and$(1\bar{1}0)_{Fe}$ and $(110)_{Fe,}$ an IFFT image was constructed. The IFFT image more clearly reveals the periodical misfit dislocations around the YAP/Fe interface with a periodicity of 7.61 Å. The distance between misfit dislocations can also be calculated according to [164]:

$$D_{misfit} = \frac{(d_2 + d_1)^2}{4|d_2 - d_1|} \tag{5.2}$$

when two gratings with different periodicities as d_1 and d_2 are superimposed. With the values $d_{(021)YAP}$ and $d_{(110)Fe}$, the value of D_{misfit} can be derived as equal to 7.62 Å based on the Eq. (5.2), which is very consistent with the measured value.

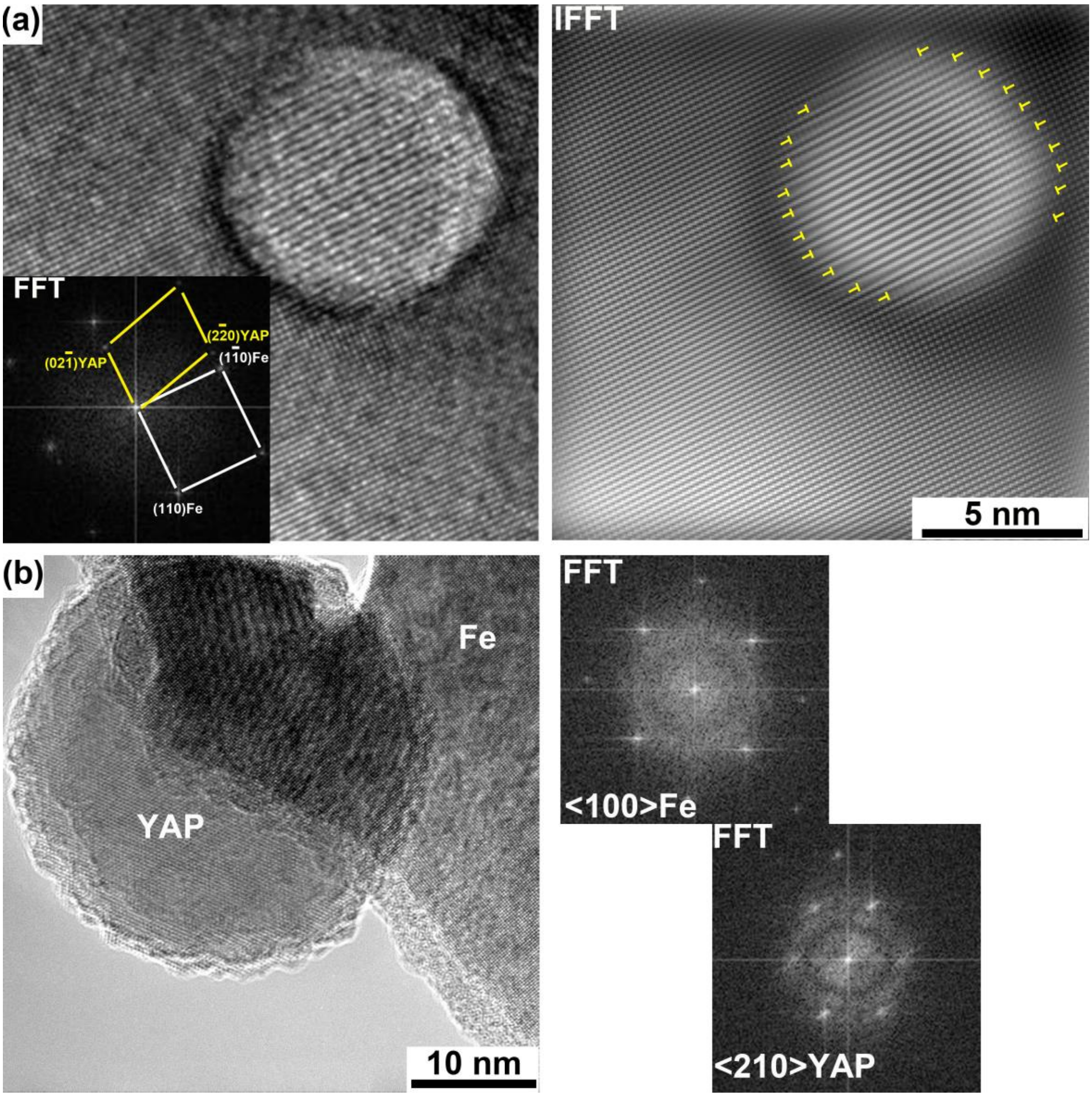

Fig. 5.12 HRTEM images and corresponding FFTs and IFFT of two oxide particles in PM2000 after annealing at 1200 ℃ for 1 hour. (a) A YAP nanoparticle with a semi-coherent interface with the ferrite matrix; its orientation relationship can be seen from the inset FFT, and the incident electron beam is approximately along the $\langle 100\rangle_{\mathrm{Fe}}$ and $\langle 112\rangle_{\mathrm{YAP}}$; an IFFT image after filtering the noise is shown at the right side, in which misfit dislocations around the interface are marked by yellow symbols. (b) A YAP nanoparticle with an incoherent interface with the ferrite matrix; the orientation relationship between them is demonstrated in the FFTs on the right side, the incident electron beam is approximately along the $\langle 100\rangle_{\mathrm{Fe}}$ and $\langle 210\rangle_{\mathrm{YAP}}$.

Fig. 5.12b presents another example of the YAP/Fe interface of a sample annealed at 1200 ℃ for 1 hour. As this YAP nanoparticle is on the edge of the TEM thin foil with part of it outside the ferrite matrix, the diffraction patterns of oxide and matrix can be obtained separately, and no interference originating from the channeling effect of particle and matrix occurs. Due to this advantage, the orientation relationship between YAP and Fe can be obtained easily. It is seen that the incident electron beam is along the $\langle 100\rangle_{Fe}$ and $\langle 210\rangle_{YAP}$, and that after indexing the FFTs no constant relationship between them can be derived. Furthermore, based on the superimposed region in the HRTEM image, no evidences of the coherent interface can be obtained. Therefore, this YAP nanoparticle has an incoherent interface and arbitrary orientation relationships with the ferrite matrix.

Another typical feature of the YAP nanoparticles in the sample after annealing at 1200 °C for 1 hour is shown in Fig. 5.13. Moiré fringes are frequently observed on the interface of YAP and Fe. As seen from the HRTEM image and the corresponding FFT (Fig. 5.13a), the incident electron beam is along a $\langle 100\rangle_{Fe}$, and very clear Moiré fringes appear on the interface of YAP and Fe due to the double diffraction. The visible plane of YAP under this condition is the $(202)_{YAP}$, which forms an angle of 19.1° with the $(110)_{Fe}$ plane. It is these two sets of planes with a rotation angle between them that leads to the formation of Moiré fringes when superimposed. To verify this speculation, a simple simulation (Fig. 5.13b) [165] is done by overlapping two sets of parallel gratings after a relative rotation of 19.1°, which are the counterparts of the planes of $(202)_{YAP}$ and $(110)_{Fe}$. The simulated Moiré pattern is in very good agreement with the observed HRTEM image, in terms of both the direction and the spacing of the Moiré fringes. Therefore, it is evident that these Moiré fringes originate from the double diffraction of $(202)_{YAP}$ and $(110)_{Fe.}$ In summary, the orientation relationship between the YAP nanoparticles and ferrite matrix is not conserved after annealing at 1200 °C.

Interface and orientation relationship after annealing: 1300 °C.

As seen from the size distribution of the oxide nanoparticles (Fig. 5.11), significant coarsening occurs in the samples annealed at 1300 °C for 10 hours and longer. In order to reveal the interface and orientation relationship between the recrystallized ferritic matrix and coarsened oxide particles, a sample after annealing at 1300 °C for 10 hours was characterized by HRTEM. Three examples with oxide diameters between 12 nm to 25 nm are shown in Fig. 5.14. It is evident from the HRTEM images that the morphology of the YAP particles changes from a near spherical shape to a clearer faceted shape after annealing. All facets in these three examples show very consistent alignment with one of two specific crystallographic planes of Fe, namely either $\{110\}_{Fe}$ or $\{200\}_{Fe}$. In Fig. 5.14, the incident direction of the electron beam is approximately along the zone axis of ⟨100⟩Fe, and the resulting diffraction patterns are indexed in the FFTs. Very periodical diffraction patterns with lower intensity than that of the ferrite are observed in the FFTs parallel to both $\{110\}_{Fe}$ and $\{200\}_{Fe}$. These diffraction patterns cannot be indexed as either Fe or YAP. They are supposed to originate from double diffractions of YAP particle and ferrite matrix.

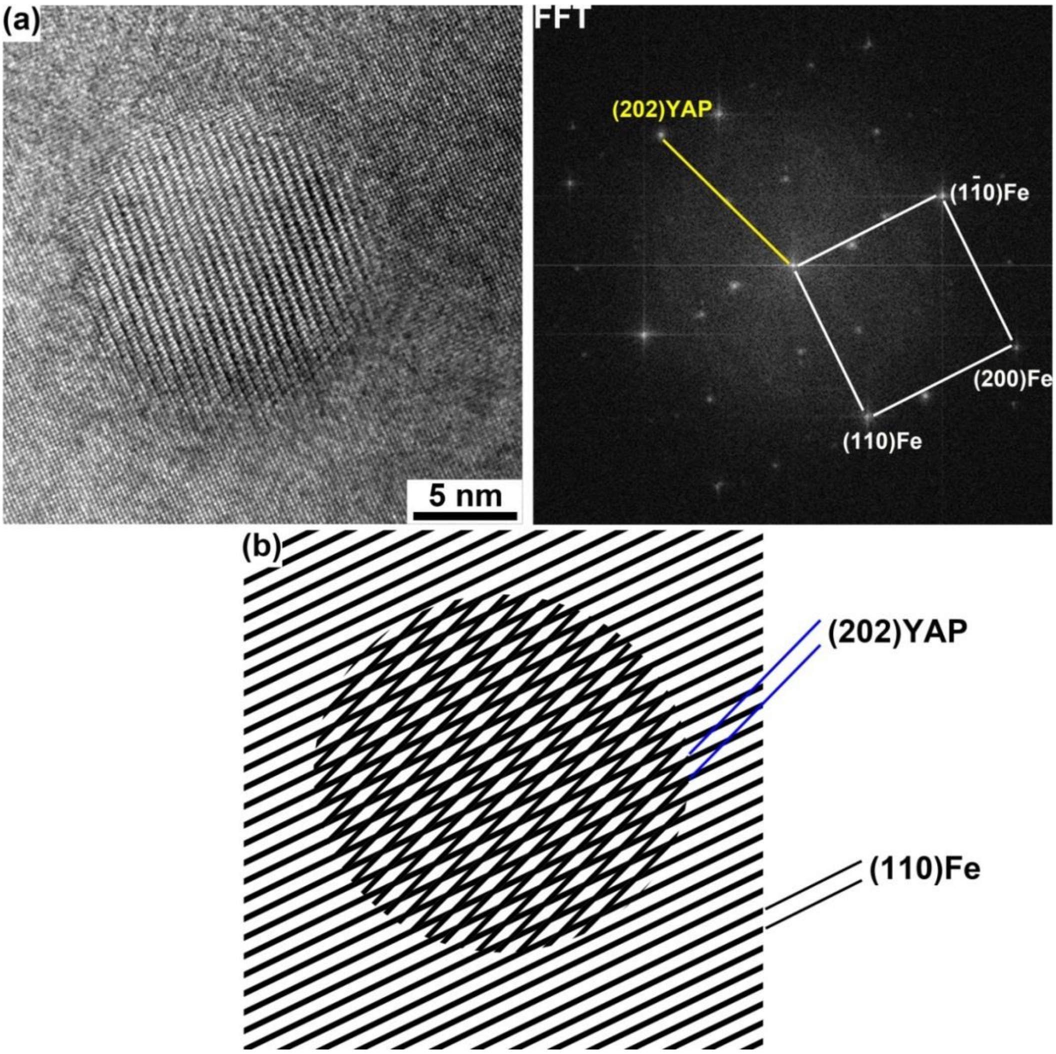

Fig. 5.13 (a) An HRTEM image and the corresponding FFT of a YAP nanoparticle in PM2000, which has an incoherent interface with the matrix, after annealing at 1200 ℃ for 1 hour. Moiré fringes appear on the interface of ferrite and YAP. (b) Simulated Moiré fringes from two superimposed sets of parallel gratings, corresponding to the planes of $(110)_{Fe}$ and $(202)_{YAP}$ with a relative rotation of 19.1° between them.

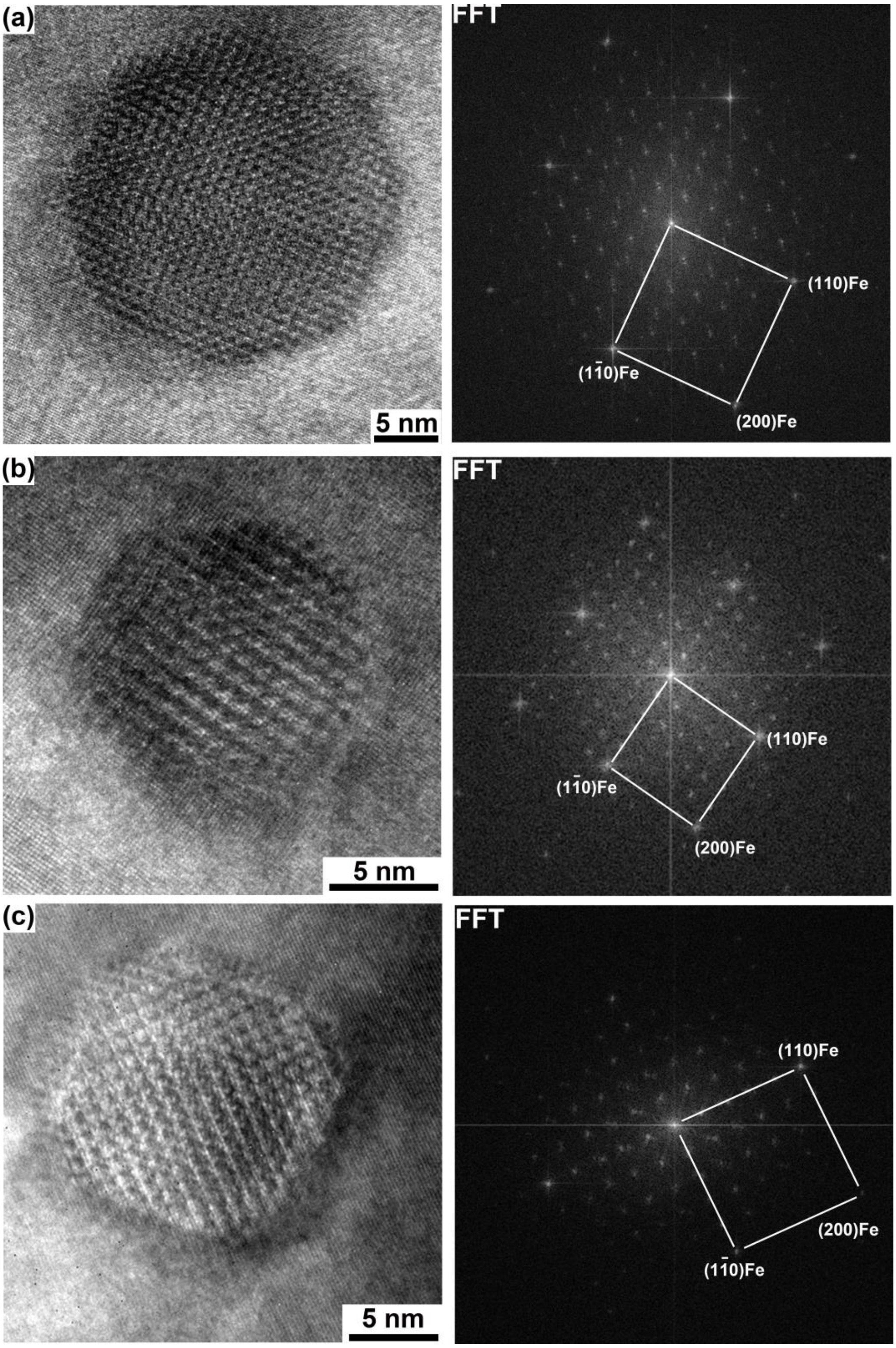

Fig. 5.14 HRTEM images of three YAP nanoparticles in PM2000 after annealing at 1300 °C for 10 hours. The diffraction patterns from the ferrite matrix are indexed in the corresponding FFTs. The incident electron beam is along the $\langle 001\rangle_{Fe}$ and $\langle 010\rangle_{YAP}$.

By masking the double diffraction patterns and the patterns from ferrite matrix, an IFFT image could be constructed after filtering the noise background. In the IFFT images shown in Fig. 5.15, the smaller and larger bright dots correspond to the atomic planes of ⟨100⟩$_{\mathrm{Fe}}$ and double diffraction product of superimposed ⟨010⟩$_{\mathrm{Fe}}$ and ⟨010⟩$_{\mathrm{YAP}}$. It is seen from the IFFT that the two facets of the YAP particle are parallel to the (110) and (200) planes of ferrite, resulting in a 135° angle between them. A schematic diagram interpreting the formation mechanism of such an image is presented in Fig. 5.16.

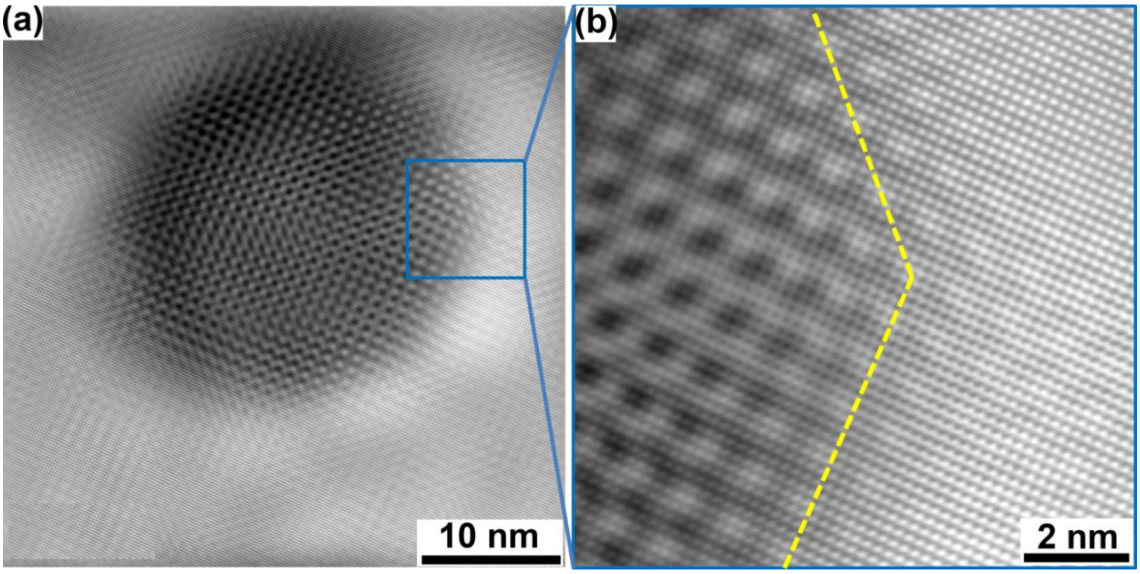

Fig. 5.15 (a) An IFFT image of the HRTEM image in Fig. 5.14a, with a filtering process to reveal the ferrite matrix and double diffraction products of superimposed ferrite and a YAP particle, (b) more detailed image from the framed region in (a), with yellow dash lines between the Fe and YAP particle.

As discussed earlier, when two gratings with different periodicities d_1 and d_2 are superposed, Moiré fringes emerge if the Bragg diffraction condition for the operating reflection is closely satisfied. As illustrated in Fig. 5.16 that two gratings representing the lattice planes of $(110)_{\mathrm{Fe}}$ and $(200)_{\mathrm{YAP}}$ are parallel and overlap along the horizontal direction, and those of $(1\bar{1}0)_{\mathrm{Fe}}$ and $(002)_{\mathrm{YAP}}$ are parallel and overlapping as well along the vertical direction. Because double diffraction takes place in two nonparallel directions, Moiré patterns with periodical dots can be observed in the image plane [166]. This is why periodical dots are generated in Fig. 5.15 instead of fringes. Due to the difference between $d_{(101)\mathrm{Fe}}$ and $d_{(200)\mathrm{YAP}}$, the matching planes are every $5d_{(101)\mathrm{Fe}}$ and $4d_{(200)\mathrm{YAP}}$ or $4d_{(002)\mathrm{YAP}}$, which is also the periodicity of the Moiré patterns. These simulated patterns are very similar to that observed in Fig. 5.15. However, due to the fact that $d_{(200)YAP}$ and $d_{(002)YAP}$ are slightly different, the superlattice originating from the double diffraction is distorted in some regions as seen in Fig. 5.15. The orientation relationship between the YAP particles and ferrite can be described as $(110)_{Fe}//(200)_{YAP}$ or $(002)_{YAP}$, and $\langle 100\rangle_{Fe}//\langle 202\rangle_{YAP}$. This orientation relationship is distinct from that in the sample prior to annealing. Schematic diagrams illustrating this difference in the orientation relationship between YAP and Fe due to annealing are presented in Fig. 5.17.

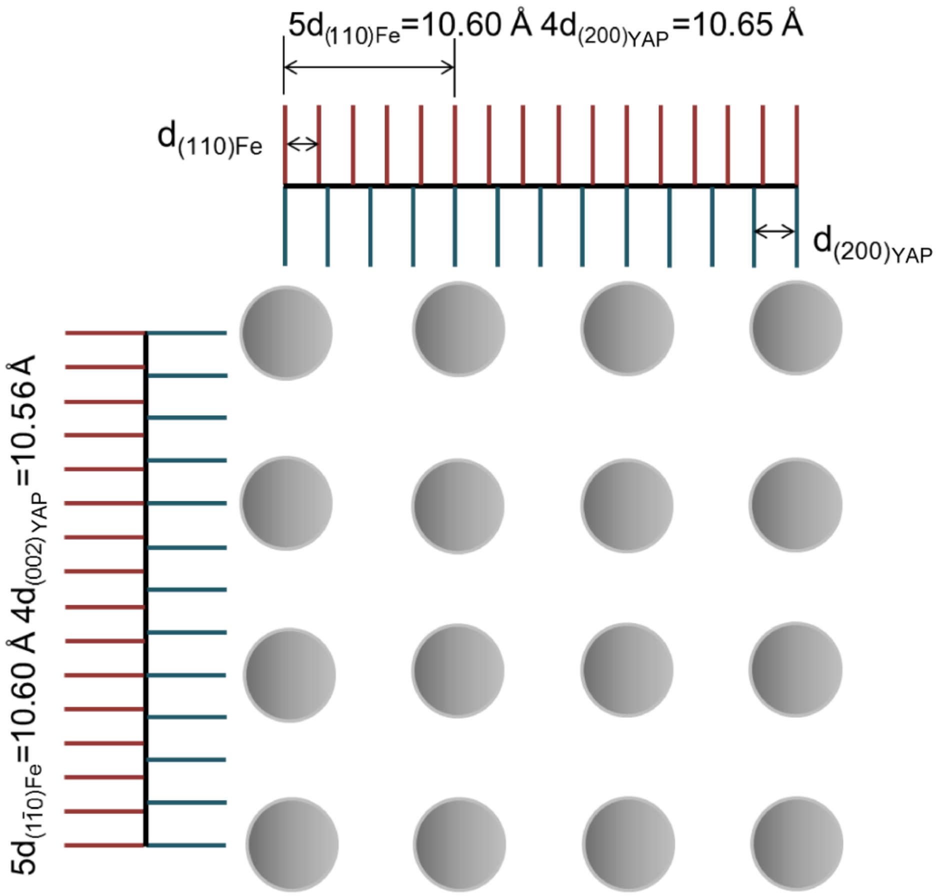

Fig. 5.16 Sketch illustrating the origin of the Moiré patterns observed in Fig. 5.15. Four sets of gratings, representing $(110)_{Fe}$, $(200)_{YAP}$, $(1\bar{1}0)_{Fe}$, and $(002)_{YAP}$ are superimposed in a way that $(110)_{Fe}//(200)_{YAP}$, and $(1\,\bar{1}\,0)_{Fe}//(002)_{YAP}$. The inspecting direction is along $[010]_{YAP}$ and $[001]_{Fe}$.

The orientation relationship between a YAP nanoparticle and Fe in the as-received sample is near cube-on-cuboid, with $(110)_{Fe}//(220)_{YAP}$ and $\langle 001\rangle_{Fe}//\langle 001\rangle_{YAP}$, as illustrated in the Fig. 5.17a. This orientation relationship changes to $(110)_{Fe}//(200)_{YAP}$ and $\langle 100\rangle_{Fe}//\langle 202\rangle_{YAP}$ after annealing at 1300 °C for 10 hours. It is seen from the diagram (Fig. 5.17b) that this new orientation relationship can be achieved by rotating the unit cell of Fe along the direction ***b*** by about 45°, while maintaining the initial orientation of the YAP unit cell.

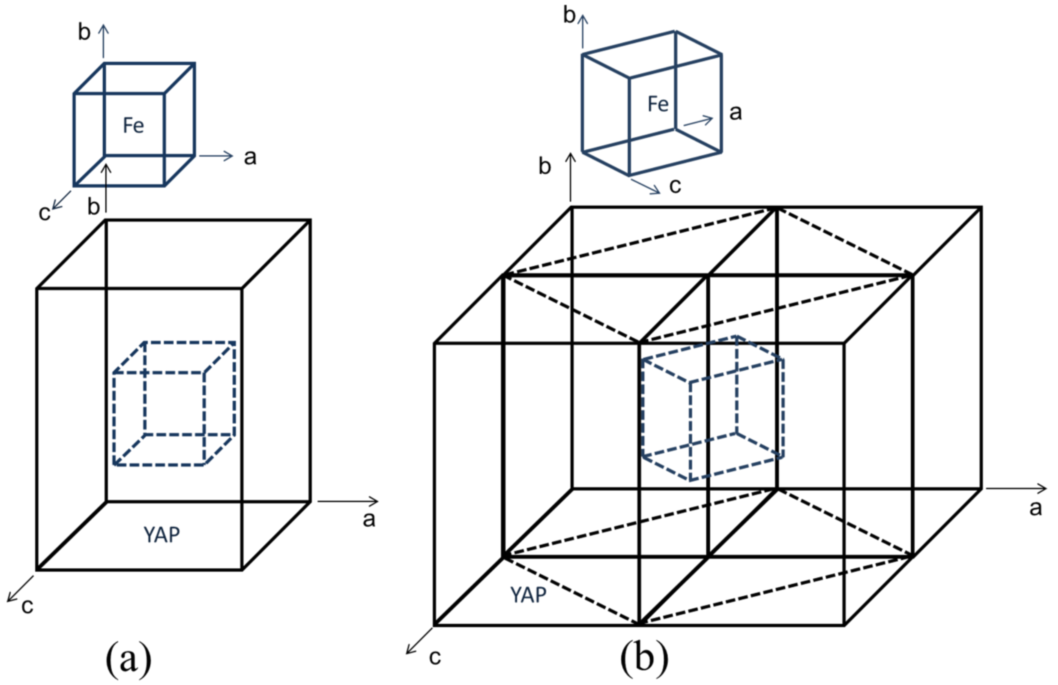

Fig. 5.17 Schematic diagrams showing the change of the orientation relationship between YAP and Fe. (a) Primitive crystal unit cell of Fe and YAP, and overlapped diagram with YAP and Fe showing the orientation relationship between them, in the as-received sample, and (b) unit cell of Fe and four unit cells of YAP illustrating the new orientation relationship that developed in the sample after annealing at 1300 °C for 10 hours. The black dashed lines in (b) represent the unit cell of the pseudo-cubic lattice.

From the schematic drawing of the newly developed orientation relationships between YAP and Fe in Fig. 5.17b, a more straightforward description regarding the orientation relationship is indicated by the dashed line. As already shown in section 5.1.2, YAP has an orthorhombic lattice structure. It is more straightforward to present the orientation relationship between the cubic and orthorhombic structure in the pseudo-cubic lattice of the orthorhombic crystal, especially considering that the lattice parameter of orthorhombic YAP has a relationship of $\boldsymbol{a}\cong\boldsymbol{c}$ and $\boldsymbol{b}\cong\sqrt{2}\boldsymbol{a}$. A sketch of the primitive crystal lattice of YAP as the orthorhombic lattice and pseudo-cubic lattice is shown in Fig.5.18 as solid and dashed lines, respectively. The merit of showing the YAP crystal in the pseudo-cubic lattice is that the pseudo-cubic unit cell of YAP is very close to cubic, and thereby reducing the difference between the crystallographic symmetry between YAP and Fe lattice. Important correspondences of indexed crystallographic orientations between the cubic and pseudo-cubic lattice are: $[100]=\frac{1}{2}[10\bar{1}]_{pc}$, $[101]=[001]_{pc}$, $[110]=\frac{1}{2}[121]_{pc}$, as illustrated in Fig. 5.18. Thus, the orientation relationship between ferrite and YAP in pseudo-cubic lattice in the sample after annealing at 1300 °C for 10 hours can be specified as: $(110)_{Fe}//(202)_{YAP\_pc}$, and $\langle 100\rangle_{Fe}//\langle 200\rangle_{YAP\_pc}$. Therefore, it can be concluded that a pseudo-cube-on-cube orientation relationship between the YAP and ferrite matrix develops in the sample after annealing at 1300 ℃ for 10 hours. This special orientation relationship is also reflected in the diagram in Fig. 5.17b.

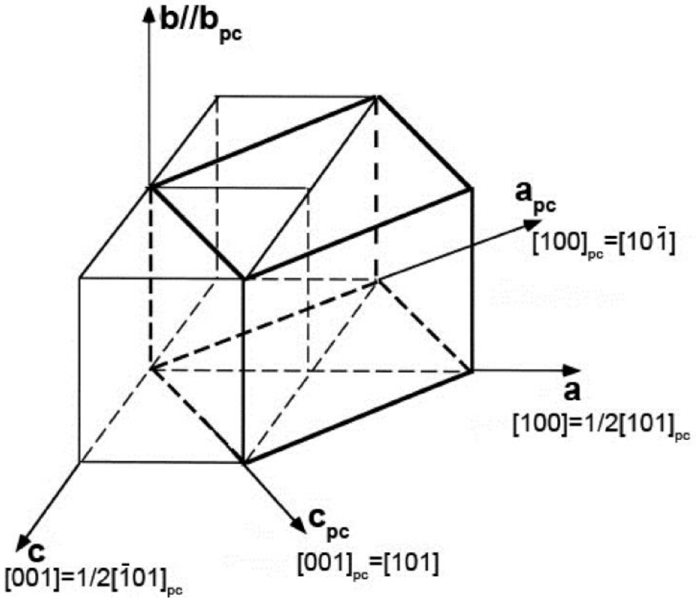

Fig. 5.18 Schematic drawing of the primitive crystal unit cell of YAP as orthorhombic and pseudo-cubic (pc) lattice.

5.1.5 Discussion

5.1.5.1 Identification of the oxide nanoparticles in PM2000

In terms of the type of oxide dispersoids, ODS steels can be divided into two main categories: ODS steel alloyed with Al, such as MA956 [167], PM2000 [48] *et al.*; and ODS steel alloyed with Ti but without Al, such as MA957 [45],ODS EUROFER [42], 14YWT [44, 47] *et al.*. In Al-alloyed ODS steel, the oxide dispersoids are generally characterized as yttrium-aluminum oxide, while in Ti-alloyed without Al the oxide dispersoids are yttrium-titanium oxide. Among the various ODS steels, high Cr- and Al-alloyed ODS ferritic steels are promising structural candidate materials for blankets, considering their better compatibility with dual coolant Pb-Li and He exposures [168-170]. However, there are only few investigations on this type of ODS steels with yttrium-aluminum oxide, and consequently the structure of the oxide dispersoids and their interfacial relationship with the matrix in Al-alloyed ODS steel are still unclear. As described above, there are at least four possible compounds, namely YAM, YAH, YAP, and YAG. These possibilities engender many controversial issues concerning the character of the oxide nanoparticles in Al-alloyed ODS ferrtic steel and their orientation relationship with ferrite matrix. By using electron energy loss spectroscopy technique, Kimenkov *et al*. [147] found the oxide dispersoids in a Fe-20Cr-5Al ODS steel are mainly YAG and YAP. However, in a similar ODS Fe-Cr-Al steel (MA956), the majority of oxide nanoparticles were identified as YAM by high resolution transmission electron microscopy (HRTEM) [171]. Recent studies by Dou *et al.* [153, 156] show that, in their Al-alloyed ODS steel, both YAH and YAP exist, and that the fraction of YAH increases with consolidation temperature. Consequently, the interface and orientation relationships between the oxide nanoparticles and ferrite matrix were reported with very large discrepancies.

The crystal structure of the majority of oxide nanoparticles in PM2000 has been identified as YAP phase by systematic HRTEM studies. Solid evidence has been gathered from the HRTEM images and a full agreement between their FFTs and simulated diffraction patterns of YAP. Taking advantage of the carbon extraction approach, the interference in indexing the oxide particles caused by ferrite matrix can be totally excluded. Nevertheless, one should be careful about the process of carbon extraction of oxide nanoparticles, because the etchant may react with the oxide particles during the process and thereby inducing artificial products. In this study, very consistent results about the crystal structure of oxide nanoparticles were obtained between TEM thin foils and carbon replicas. This demonstrates that the indexing results for the oxide nanoparticles in carbon replicas are valid.

Previous studies on the characterization of the oxide nanoparticles in Al-alloyed ODS steels show a large discrepancy. It is generally accepted that the formation mechanism of oxide dispersoids involves fragmentation of Y_2O_3 particles and then decomposition of Y_2O_3 fragments during ball milling, and reprecipitation of oxide nanoparticles during the consolidation process [36, 163]. YAP and YAH are the most frequently reported Y-Al-O nanoparticles in Al-alloyed ODS steel. However, YAH is thought to be an unstable product and would transform to YAP at elevated temperatures [156], and this is probably why YAH is not found in PM2000. YAG is also claimed to be identified in this material [48, 148], however, no solid evidence about the crystal structure was provided in these reports, and the HRTEM image in the report is wrongly indexed [148]. YAM was only determined in Al-alloyed ODS steel by Hsiung [151, 155], but since YAM is only thought to be formed at very high temperatures, we did not expect to find this product in PM2000. It is suggested that YAP is the dominant structure of the oxide nanoparticles in PM2000. It should be mentioned here that a small amount of quite large particles which was identified both in the current study and previous reports [148, 149]. These large particles are found to be alumina and titanium carbonitride. Due to their very small number fraction (<1%) and very large sizes (normally ≥100 nm), they play a small role in strengthening and enhancing the irradiation tolerance of the ODS steel. Thus they are not taken into consideration as nanoparticles in this study.

5.1.5.2 Interface and orientation relationship between oxide nanoparticles and ferrite matrix

When a second phase particle is precipitated, the interface of the particle/matrix can be classified as either coherent, semi-coherent or incoherent. In the hot consolidated state, coherent interfaces are observed between the YAP nanoparticles and the ferrite matrix in PM2000. This is proved by the HRTEM imaging along the different crystallographic directions of YAP. As the interfacial energy of a coherent particle is lower than an incoherent one (interphase boundary energy for coherent interfaces ranges from 5 to 200 mJ/m^2, while for incoherent interphases are between 800-2500 mJ/m^2 [164]), the nucleation of coherent precipitates is favored if the lattice mismatch between particles and matrix on certain planes is small. Coherent interfaces are thought to be more efficient in hindering the movement of dislocations and boundaries. This explains why there is no considerable structural coarsening of PM2000 when annealing below 1100 °C. The orientation relationship between YAP and ferrite matrix is, however, rarely reported. Only in a recent study by Dou *et al.* [156] presented that an orientation relationship between YAP and ferrite matrix is $[211]_{\mathrm{YAP}}//[111]_{\mathrm{Fe}}$ and $(1\bar{2}0)_{\mathrm{YAP}}//(\bar{1}10)$, which is different from the results of this study. However, the image from which this relationship was derived is blurred. The FFT pattern seems to be not correctly indexed in their paper. The orientation relationship shown in that image is very likely to be the same as shown in Fig. 5.7.

During annealing at 1200 °C, the driving force is sufficient to enable recovery and formation of recrystallization nuclei and recrystallization occurs. Considering the huge difference in grain size of PM2000 before and after annealing (1.1 μm to ~5 mm), the orientations of the majority of the initial ferrite matrix is expected to change after they are consumed by the recrystallizing grains. However, if the oxide nanoparticles do not reorient during this process, any initial coherency will be broken. Some particles develop semi-coherent interfaces, since the lattice mismatch is sufficient for coherent interface to relax to an unstrained condition with an array of misfit dislocations at the interface, as shown in Fig. 5.12a. In many cases, the misfit strain is too large and the atomic matching is sufficiently poor, so incoherent interfaces develop consequently.

During annealing at 1300 °C, reorientation of YAP nanoparticles occurs by the driving force of minimizing the interfacial energy, and thereby regaining the coherent/semi-coherent interface. The orientation relationship between YAP and Fe transfers from a cuboid-on-cube orientation to a pseudo-cube-on-cube orientation after annealing. One reason for this change could be reducing the mismatch of crystal lattice in three dimensions between the YAP and Fe. It should also be noticed that facets form at the surface of the oxide nanoparticles. It is well known that the equilibrium morphology of second phase particles embedded in a matrix is solely determined by the interfacial energy [172-174]. The interfacial energy consists of a compositional interface energy and misfit elastic strain energy, and the morphology is a result of a balance between them. The faceted shape developed in YAP/Fe system indicates that the elastic energy is predominant [175]. All facets have very consistent crystallographic planes, along either $(101)_{\mathrm{YAP}}$ or $(100)_{\mathrm{YAP}}$ planes, corresponding to $(100)_{\mathrm{Fe}}$ or $(110)_{\mathrm{Fe}}$, respectively, due to the pseudo-cube-on-cube orientation relationship between YAP and Fe. Therefore, it could be that the low energy facets are part of the driving force for reorientation.

5.1.6 Summary

The microstructure of PM2000 has been characterized, and ferritic grains with submicrometer size and nanoscale oxide dispersoids are observed in the as-received material. The majority of oxide nanoparticles in PM2000 are identified as orthorhombic $YAlO_3$ (YAP) by HRTEM. The interface between YAP and Fe is coherent, and the orientation relationship between them is $(110)_{\mathrm{Fe}}//(220)_{\mathrm{YAP}}$ and $\langle 001\rangle_{\mathrm{Fe}}//\langle 001\rangle_{\mathrm{YAP}}$, i.e. they have a near cuboid-on-cube orientation relationship. The hot consolidated PM2000 is thermally very stable, owing to the presence of well-dispersed oxide nanoparticles. Considerable structural coarsening occurs when the material is annealed at 1200 °C and above. A fully recrystallized structure with an average grain size in the millimeter range is obtained in the sample after annealing at 1200 °C for 1 hour.

The interfaces and orientation relationships between YAP nanoparticles and ferrite matrix change during annealing at high temperatures. Annealing at 1200 °C for 1 hour does not lead to any considerable coarsening of YAP nanoparticles, and semi-coherent or incoherent interface develop between the YAP and Fe. Substantial coarsening of the YAP nanoparticles takes place when the sample is annealed at 1300 °C, e.g. the mean size increases from 14.2 nm to 27.9 nm after annealing for 100 hours. The orientation relationship between YAP and Fe is transformed into a pseudo-cube-on-cube relationship, i.e. $(110)_{Fe}//(200)_{YAP}$ and $\langle 100\rangle_{Fe}//\langle 202\rangle_{YAP}$ or $(110)_{Fe}//(202)_{YAP\_pc}$, and $\langle 100\rangle_{Fe}//\langle 200\rangle_{YAP\_pc}$. Additionally, very clear facets along either $(100)_{YAP}$ or $(101)_{YAP}$ form at the surface of YAP nanoparticles, facing the planes of $(100)_{Fe}$ or $(110)_{Fe}$, respectively.

5.2 DPD-induced microstructure in PM2000

In this section, the microstructural evolution during DPD is characterized in detail regarding both the ferrite matrix and the oxide nanoparticles of PM2000. Two types of samples are subjected to DPD: the as-received PM2000 with a fine grain size, and the coarse grained PM2000 with an initial grain size of several millimeters obtained after annealing.

5.2.1 DPD-induced microstructure: as-received PM2000

Cylindrical samples, machined from the as-received PM2000 bar, with dimensions of Ø6×9 mm were compressed by DPD at room temperature. An equivalent strain of 2.1 was achieved after five passes. The orientation map obtained by EBSD (Fig. 5.19a) shows a nanoscale lamellar structure with lamellar boundaries nearly perpendicular to the CA. The microstructure is substantially refined after DPD, and the spacing of LABs and HABs measured along the compression direction is reduced to 76 nm and 137 nm, respectively. The misorientation distribution (Fig. 5.19b) shows the boundaries with a misorientation angle less than 4° occupy a very high fraction (18%). Nevertheless, there is a large fraction of boundaries with high misorientation, with f_{HAB}=52.8%. Pole figures (Fig. 5.20) obtained from the orientation data demonstrate that the deformed sample has a ⟨100⟩+⟨111⟩ duplex fibre texture.

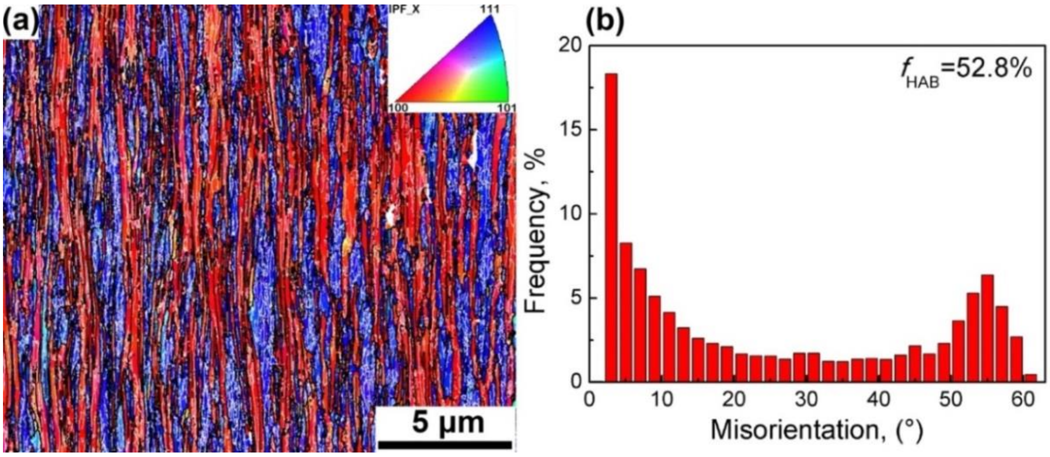

Fig. 5.19 (a) Orientation map obtained by EBSD of a longitudinal section of the as-received PM2000 after DPD to a strain of 2.1. The extrusion direction and CA is horizontal. It is colored according to the crystallographic direction of the CA with the color code shown in the inset. Black and white lines represent the LABs and HABs, respectively. (b) Distribution of misorientation angles of the boundaries in the map (a).

A TEM image from the longitudinal section of the deformed sample is shown in Fig. 5.21. Nanoscale lamellae with well-defined lamellar boundaries are observed in the microstructure. Statistical results for the lamellar thickness along the CA are presented in Fig. 5.21b. The mean thickness is about 72 nm, which is consistent with the EBSD result. The nanoscale lamellae contain a high density of dislocations and have interconnecting boundaries connecting the extended lamellar boundaries. Qualitatively, this lamellar structure is very similar to that observed for other metallic materials after deformation by rolling, quasi-static compression or DPD.

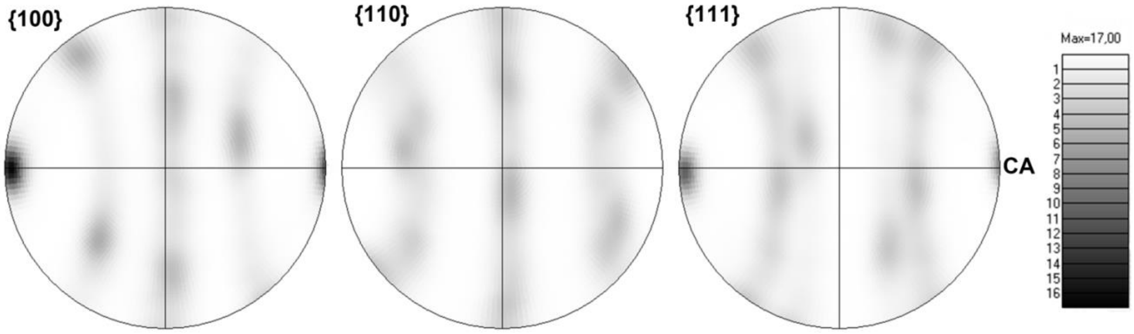

Fig. 5.20 {10 0}, {110} and {111} poles figures obtained from the EBSD orientation data for the as-received PM2000 after DPD to a strain of 2.1

Similar to the modified 9Cr-1Mo steel at high strains, PM2000 steel develops a nanoscale lamellar structure after DPD to high strains with a very pronounced ⟨100⟩+⟨111⟩ duplex fibre texture. The evolution of the morphology and microstructural parameters, observed in samples deformed from low to high strains is analogous for both steels. They both follow an evolution pattern with a dislocation cell structure formed at low and medium strains, and extended lamellar structure at high strains, as shown in section of 4.2. This indicates that although the PM2000 contains a high density of well-dispersed YAP nanoparticles, their effect on the microstructural evolution is not large enough to alter the deformation pattern during DPD. It is expected that at a low strain the dislocation structure is supposed to be more homogeneous due to the well-dispersed oxide nanoparticles [79]. However, since the initial microstructure contains a high density of dislocations, such a behavior (higher dislocation density and more homogeneous dislocation structure), which is prevalent in the single crystals with fine dispersoids [79], is not very clear in the current study. The much finer structure of DPD-processed PM2000 (72 nm) compared to the DPD-processed modified 9Cr-1Mo steel (98 nm) suggests that the presence of oxide nanoparticles facilitates structural refinement and leads to a finer deformation-induced microstructure [82].

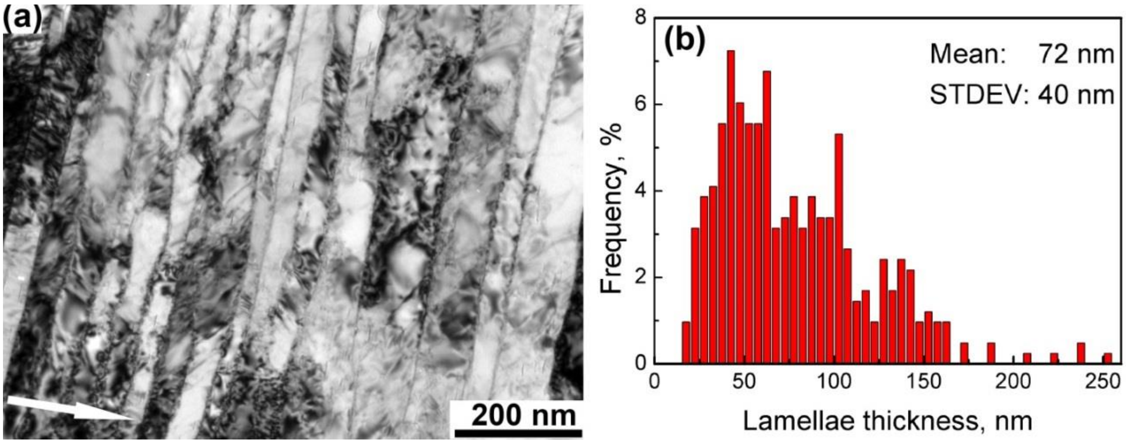

Fig. 5.21 (a) TEM image of a longitudinal section of the as-received PM2000 after DPD to a strain of 2.1. The CA is indicated by an arrow. (b) Distribution of the lamellae thickness along CA for 1250 lamellae.

5.2.2 DPD-induced microstructure evolution: coarse-grained PM2000

The microstructure of the as-received PM2000 is very fine and contains subgrains and a high density of dislocations, as shown in Fig. 5.1 and Fig. 5.2. The formation of nanoscale lamellae during DPD is supposed to partly benefit from fine initial grain size and high dislocation density in the initial structure. In this section, microstructural evolution of samples with coarsened recrystallized grains deformed by DPD to high strains is characterized. Comparison between the deformation-induced microstructure in both types of samples is made.

The as-received PM2000 is fully recrystallized after annealing at 1200 °C for 1 hour, as shown in Fig. 5.10. In addition to the existence of very coarse grains, another important feature of the fully recrystallized samples is that most of the grains have a ⟨100⟩ direction along the extrusion axis. An orientation map determined by EBSD of an annealed sample is shown in Fig. 5.22a. The area of this map is about 3.5 mm^2. It can be seen that in the measured area, no grain boundary or dislocation boundary with misorientation angle larger than 2° interior is present, which indicates that a fully recrystallized grain with a size of several millimeters formed after annealing. The corresponding pole figure (PF) demonstrates that this grain has an orientation with a ⟨100⟩ direction aligned with the initial extrusion axis.

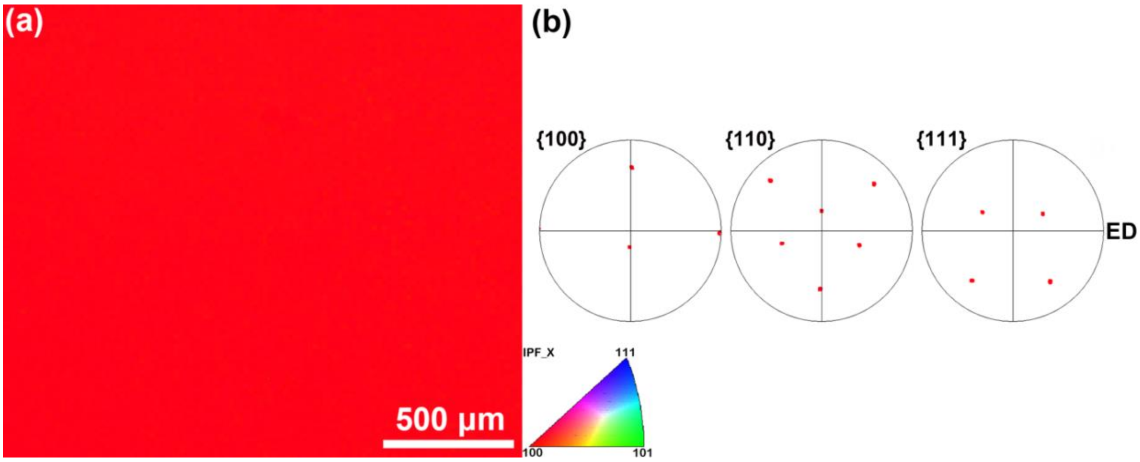

Fig. 5.22 (a) Orientation map of the as-received PM2000 in a longitudinal section after annealing at 1200 °C for 1 hour, showing no misorientation above 2° inside a large region. It is colored according to the crystallographic direction of the extrusion axis with the color code shown in the inverse pole figure. (b) {1 00}, {110} and {111} pole figures demonstrating a single orientation with ⟨100⟩ direction close to the initial extrusion direction.

5.2.2.1 Nanoscale lamellae after DPD to high strain

Cylindrical samples with dimensions of Ø6×9 mm were machined from the annealed bars, with longitudinal direction along the initial extrusion axis. These samples were compressed by DPD at room temperature, with a CA along the initial extrusion direction. This means that the compression is roughly along the ⟨100⟩ directions of the grains. An equivalent strain of 2.1 was achieved after five passes.

A typical microstructure of the sample after deformation is shown in Fig. 5.23. The deformed microstructure consists of two alternating types of lamellae closely aligned with the compression plane and having orientations with either a ⟨100⟩ direction along CA (red in Fig. 5.23a,b) or a ⟨111⟩ direction along CA (blue in Fig. 5.23a,b). The {110} pole figure in Fig.5.23b reveals that the ⟨111⟩ lamellae share one (110) pole with the ⟨100⟩ lamellae. This common pole is perpendicular to CA, i.e. the misorientation axis between the ⟨111⟩ and ⟨100⟩ lamellae is in the compression plane.

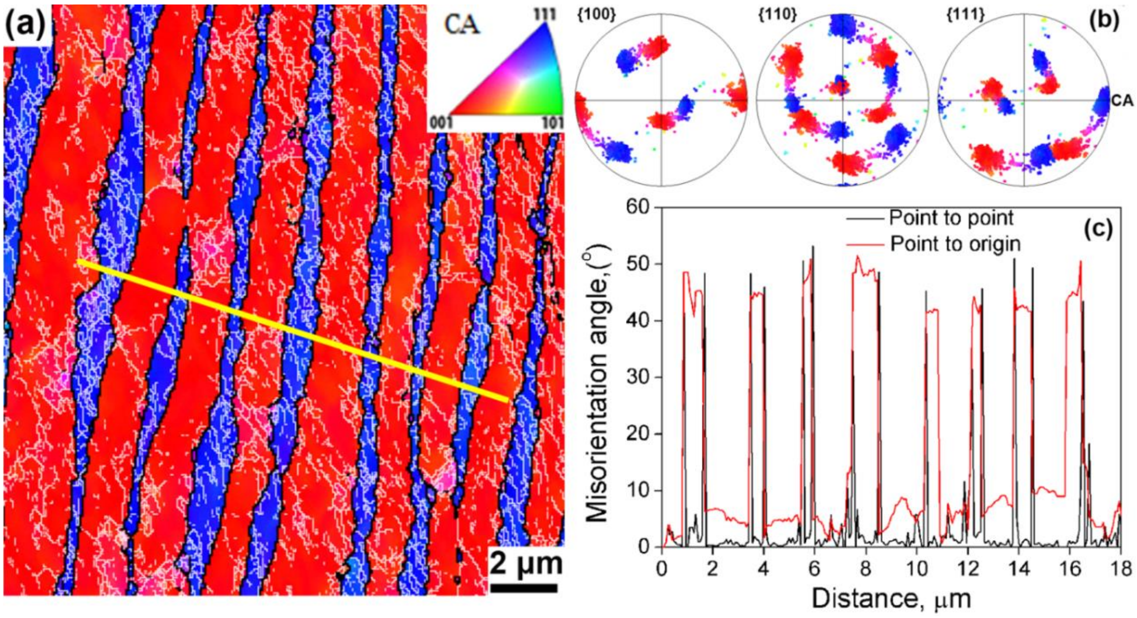

Fig. 5.23 Results from EBSD on a region containing comparatively broad lamellae in PM2000 of longitudinal section after DPD to a strain of 2.1: (a) orientation map colored according to the crystallographic direction along the CA using the color code in the inverse pole figure (see the inset). Black and white lines represent HABs and LABs, respectively. The CA is horizontal.; (b) [139], {110} and {111} pole figures; (c) a misorientation profile along the yellow line in (a).

Lamellae of the two different types are always separated by HABs, and contain LABs in their interior (see Fig. 5.23a, c). Distinct from the ⟨100⟩ and ⟨111⟩ lamellae formed in the as-received PM2000 after DPD, there is almost no misorientation between the individual ⟨100⟩ or ⟨111⟩ lamellae, as seen from Fig. 5.23b, c. This is not surprising for ⟨100⟩ as they originate from the initial orientation, but it is remarkable that all ⟨111⟩ lamellae have the same orientation. The ⟨100⟩ lamellae are wider than those with the ⟨111⟩ orientation. The average width of the ⟨100⟩ and ⟨111⟩ lamellae is 1.4 μm and 0.5 μm, respectively. The average boundary spacing along the CA in Fig. 5.23a is 0.3 μm. The microstructure is, however, not homogeneous, and considerable local variations are observed in the deformed sample. In some regions, original grains are subdivided by a much larger number of lamellar boundaries per unit area than in other regions. An example of such a well-refined region is shown in Fig. 5.24, where very narrow lamellae are observed. Here the average boundary spacing along the CA is 0.2 μm, and the average width of the ⟨100⟩ and ⟨111⟩ lamellae in this region is 540 nm and 110 nm, respectively, which is considerably smaller than the values obtained in the region shown in Fig. 5.23a. The width of the narrowest lamellae in Fig. 5.24 is about 40 nm. It should be mentioned that there might be many very fine lamellae represented in white color in Fig. 5.24, which are the regions not indexed by EBSD. Although the thicknesses of ⟨111⟩ and ⟨100⟩ lamellae are different for the different regions, the area fractions of the ⟨111⟩ lamellae are comparable, with 36% and 31% in the Fig. 5.23 and Fig. 5.24, respectively.

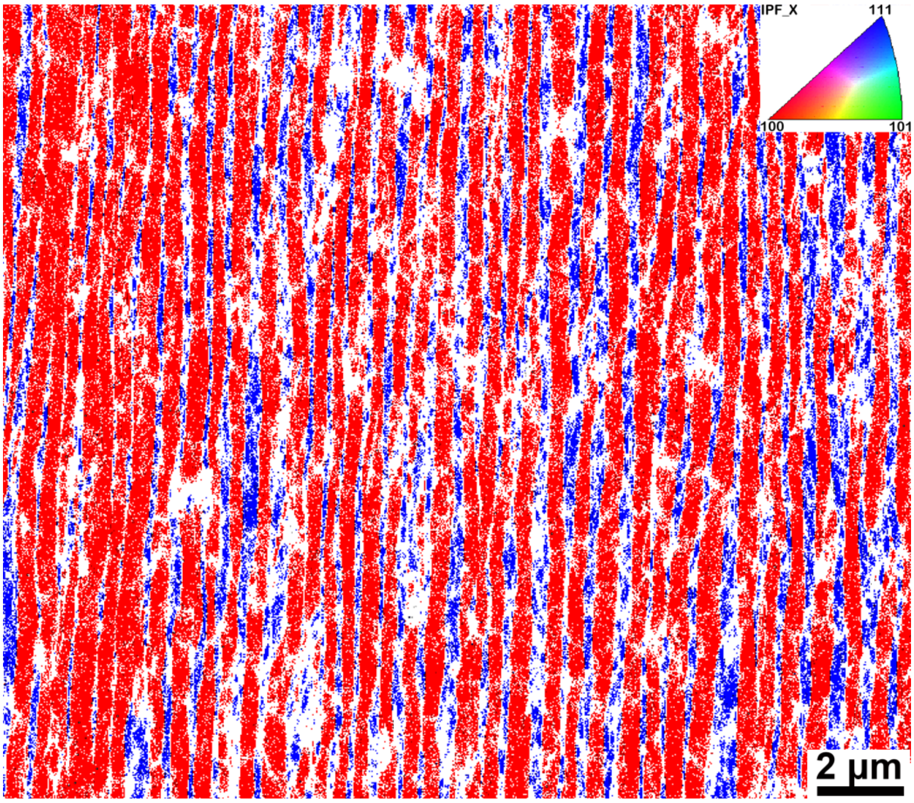

Fig. 5.24 Orientation map obtained by EBSD of the coarse-grained PM2000 in longitudinal section after DPD to a strain of 2.1. This map was acquired from a region with very fine lamellae, and the CA is horizontal. The color code for the crystallographic direction along CA is shown in the inset, and the white regions are not indexed.

TEM images (Fig. 5.25) provide clear evidence that the width of the very narrow lamellae can vary from 30 nm to 40 nm. Similar to the EBSD data, analysis of selected area diffraction patterns and dark field images demonstrate that these very narrow bands have a ⟨111⟩ direction aligned with the CA. It is also evident that there is a high density of dislocations within the lamellae. An example of further HRTEM characterization of these very fine lamellae is shown in Fig. 5.26. The HRTEM image (Fig. 5.26a) shows the microstructure of a ⟨111⟩ lamella and the neighboring ⟨100⟩ matrix. The HRTEM images from the left and right sides of the ⟨111⟩ lamella (Fig. 5.26b,c) shows a clear crystal lattice image of the ⟨100⟩ matrix. Based on these lattice images and the corresponding FFT patterns, the misorientation between the left and right sides is determined to be only 0.6°.

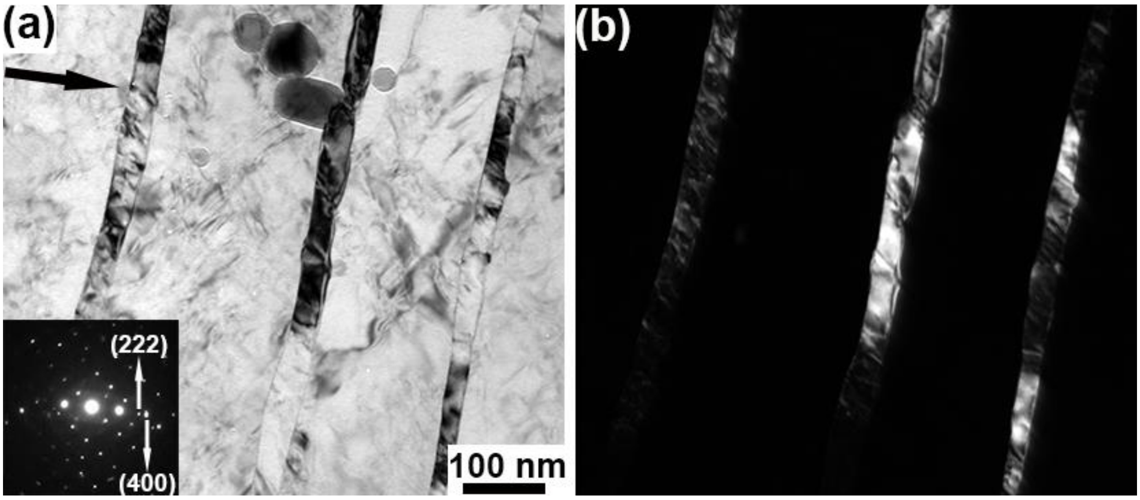

Fig.5.25 TEM micrographs from a longitudinal section of PM2000 after DPD to a strain of 2.1 showing comparatively wide ⟨100⟩ lamellae and very narrow ⟨111⟩ lamellae: (a) a bright field image with a selected area diffraction pattern in the inset; (b) a dark field image of the same region highlighting the ⟨111⟩ oriented lamellae. The CA is indicated by the black arrow in (a).

To conclude, very fine ⟨111⟩-oriented lamellae with thickness down to about 30 nm appear inside the initial ⟨100⟩-oriented matrix, forming alternating ultrafine ⟨100⟩- and ⟨111⟩-oriented lamellae with finer⟨111⟩ lamellae and coarser⟨100⟩ lamellae. As shown in section 5.2.1, a nanoscale structure with ⟨100⟩ and ⟨111⟩ oriented lamellae formed in the as-received sample after DPD to the same strain as well. However, a distinction between both structures is also evident. In the coarse grained samples, the newly-formed ⟨111⟩ lamellae have nearly identical orientation, and they do not form a fibre texture. Whereas, in the sample with the submicrometer initial grain size, only the ⟨111⟩ or the ⟨100⟩ directions of the crystals are aligned with the CA, but for the other directions, the crystallographic directions are arbitrary, i.e. they form a fibre texture. Another very interesting feature of the nanoscale lamellae developed in the coarse grained sample is that the deformation-induced ⟨111⟩ lamellae and the initial ⟨100⟩ grain share a common (110) pole and this pole is perpendicular to the CA, i.e. the orientation relationship between them has a misorientation axis of (110) in the compression plane. Besides, the lamellar boundaries are almost perpendicular to the CA after DPD to a strain of 2.1.

This means that the misorientation axis is in the boundary plane, and the lamellar boundaries between ⟨100⟩ and ⟨111⟩ lamellae have a tilt character. These special features make this lamellar structure very distinguished.

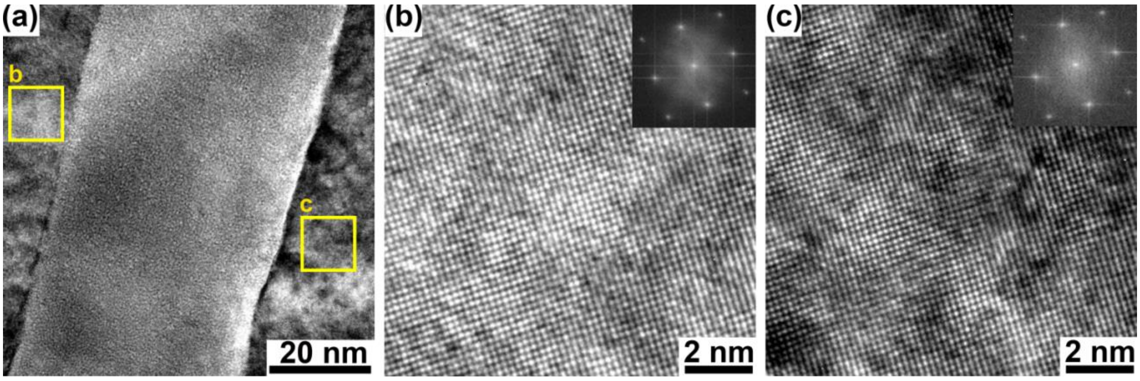

Fig. 5.26 HRTEM images around a very fine lamella in PM2000 of longitudinal section after DPD to a strain of 2.1. (a) Microstructure of a ⟨111⟩ lamella and the ⟨100⟩ matrix, (b) and (c) represent the two framed regions on left and right sides of the ⟨111⟩ lamella. The corresponding FFT patterns of (b) and (c) are shown in the insets.

5.2.2.2 Microstructural evolution during DPD with strain

Two coarse grained recrystallized samples after DPD to a strain of 0.5 and 0.9 were characterized to reveal the microstructural evolution and the evolution of the lamellae with strain. Orientation maps obtained by EBSD and the corresponding pole figures are shown in Fig. 5.27. In the sample after DPD to a strain of 0.5 (Fig. 5.27a), a lamellar structure starts to form. There are a large number of dislocation boundaries, where most of them are confined in isolated bands and thus lead to the formation of deformation bands. The lamellae are not well developed at this stage and the lamellar boundaries are not sharp, with LABs separating them from the initial matrix in some regions. Some lamellae can be detected by a slightly deviating orientation from the ⟨100⟩ matrix with pink color (the pink color indicates that they have a near ⟨311⟩ direction aligned with the CA). The {110} pole figure (Fig. 5.27c) shows the deformation-induced bands and the initial matrix have a common (110) pole perpendicular to the CA.

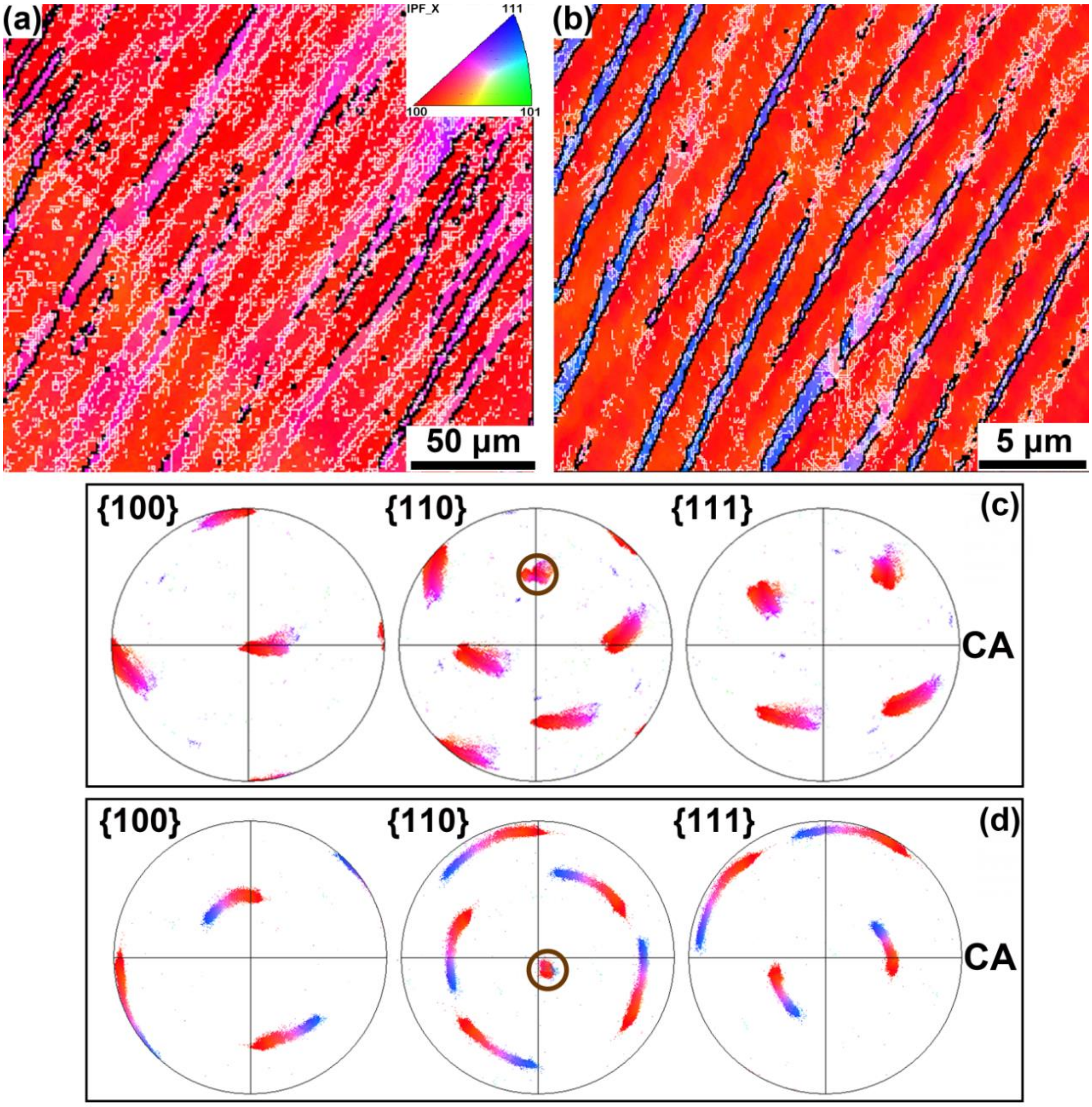

Fig. 5.27 Orientation maps obtained by EBSD from PM2000 in longitudinal section after DPD to a strain of (a) 0.5, and (b) 0.9. Black and white lines represent HABs and LABs, respectively, and the CA is horizontal. (c) and (d) are the corresponding pole figures of the orientation maps (a) and (b) respectively. The color code for the crystallographic direction along CA is shown in the inset in (a).

With increasing strain to 0.9, the lamellar structure gets finer and the boundaries become shaper, compared to that after a strain 0.5. Most deformation bands are separated by HABs from the matrix, while in some areas dislocation boundaries with low misorientations are arranged into isolated bands without sharp boundaries separating them from the matrix. The corresponding pole figures in Fig. 5.27d also demonstrate that the deformation bands and the matrix have ⟨110⟩ as their misorientation axis, and this axis is perpendicular to the CA.

However, compared to the samples after a strain of 2.1, the structure in the sample after lower strains are much coarser and the traces of developed lamellar boundaries have a lower inclination angle to the CA. This angle increases slightly with strain (about 5° from strain of 0.5 to 0.9) as seen from Fig. 5.27. It is also evident from the pole figures in Fig. 5.27c, d that with increasing of strain, the misorientation angle between the matrix and deformation bands increases. At a strain of 0.9, the deformation bands have a near ⟨554⟩ direction along the CA.

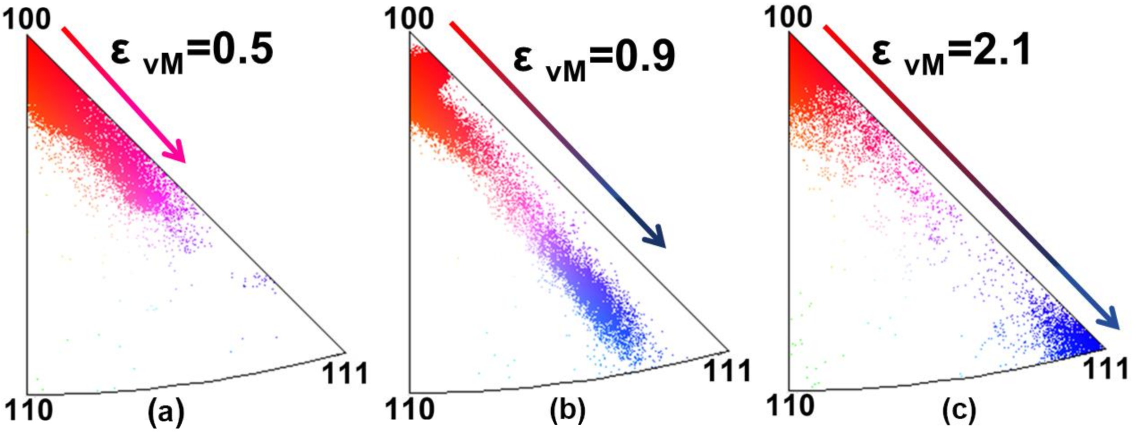

Fig. 5.28 Inverse pole figures obtained from the EBSD results of PM2000 after DPD to a strain of (a) 0.5, (b) 0.9, and (c) 2.1, showing the reorientation of the lamellar structure with strain.

The evolution of the orientation of the deformation bands with increasing of DPD strain can be more clearly seen in the inverse pole figures (Fig. 5.28). The initial orientation of the matrix is near a ⟨100⟩ along the CA, and part of the grain gradually shifts towards a ⟨111⟩ orientation with increasing strain by forming deformation bands. This ends up with a structure where ⟨111⟩ oriented lamellae alternate with bands of the initial ⟨100⟩ matrix. Specifically, as seen from Fig. 5.28, the orientation of the deformation bands moves from the ⟨100⟩ corner towards the ⟨111⟩ corner. This reorientation process follows a path such that crystal rotation occurs around a specific direction, namely a ⟨011⟩ axis, as indicated by the trace of the reorientation process taking place at low to high strains. It should also be mentioned that due to the slight difference in the initial orientations of the three samples, the path of the reorientation process in each inverse pole figures is slightly different: the orientation spread is almost along the ⟨100⟩-⟨111⟩ border line in the samples with strains of 0.5 and 2.1, whereas the orientation spread of the sample with a strain of 0.9 occurs along an arc slightly off this border line. Nevertheless, all traces are approximately normal to the [011] axis, and reorientations of the deformation bands will finally lead to the alignment of a ⟨111⟩ direction with the CA, because it is a stable orientation during compression.

It has been demonstrated in section 5.2.2.1 that the boundaries between the deformation bands and the initial matrix have tilt character in the sample after DPD to a strain of 2.1. This is derived from the microstructural analysis where lamellar boundaries are almost perpendicular to the CA. However, the boundary character is not evident in the samples after DPD to lower strains, in which the deformation-induced lamellar boundaries have a much smaller inclined angle to the CA. To reveal the boundary character at lower strains, additional analysis based on the EBSD results from the sample after DPD to a strain of 0.9 was carried out. As seen from the Fig. 5.27d, the rotation axis is almost along the viewing plane normal (*Z* axis), i.e. the crystallographic ⟨110⟩ orientation of both ⟨100⟩ and ⟨111⟩ lamellae is parallel to the *Z* axis. If the IPF orientation map is constructed along the *Z* axis, there must be no difference in color between the deformation bands and the initial matrix, as illustrated in Fig. 5.29. In this case, the misorientation axis is along the viewing plane normal, and the deformation bands and the initial matrix have the same crystal direction along the inspection direction. In general, three boundary characters are distinguished: tilt boundaries, twist boundaries or mixed boundaries. If the boundaries in Fig. 5.29 would have a twist character, the boundary traces should be invisible when viewing along the rotation axis of the boundary, since the rotation axis is perpendicular to the boundary plane. This is contradictory to the observation in Fig. 5.29, where the boundary traces are visible viewing along the rotation axis. Therefore, the possibility of twist boundaries is definitely excluded. Due to the fact that the lamellar boundaries in the sample after DPD to high strains have a tilt character and twist character is excluded, it is supposed that all boundaries between the deformation-induced ⟨111⟩ lamellae and the initial ⟨100⟩ oriented matrix have tilt character.

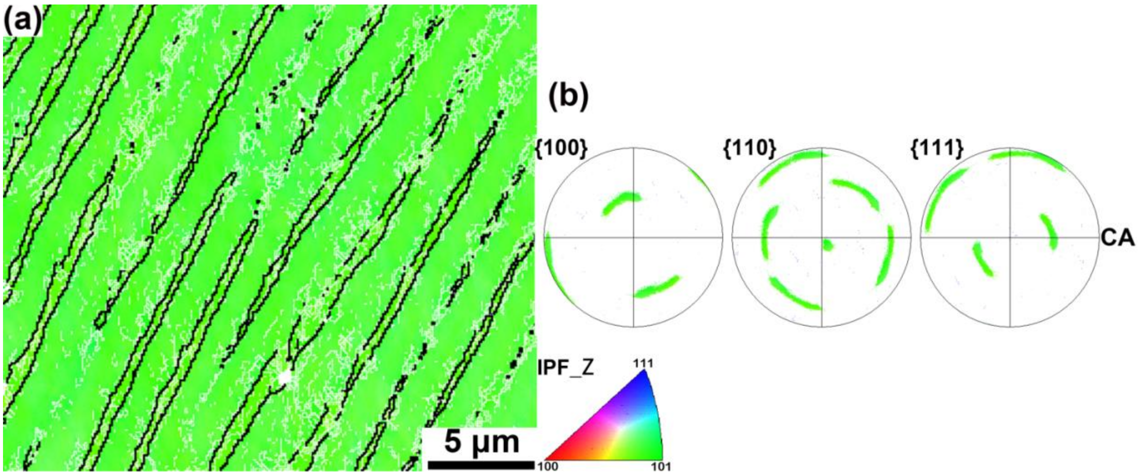

Fig. 5.29 Results obtained by EBSD from PM2000 in longitudinal section after DPD to a strain of 0.9 (same area as Fig. 5.27b). (a) orientation map colored according to the crystallographic direction along the viewing plane normal. Black and white lines represent HABs and LABs, respectively. (b) {1 00}, {110} and {111} pole figures

5.2.2.3 Discussion

In agreement with earlier findings reported for compressed body centered cubic materials [14,15], the texture developed in our sample is a combination of pronounced ⟨100⟩ and ⟨111⟩ components. These final texture components are spatially distributed in the form of alternating lamellae, where the ⟨100⟩ lamellae are significantly wider than the ⟨111⟩ lamellae. Considering that the dominant texture of the initial material was ⟨100⟩ parallel to the CA, it is suggested that the ⟨100⟩ component seen after DPD corresponds to the original orientation of the matrix, in which new and narrower ⟨111⟩ lamellae are formed. In general, since the ⟨100⟩ orientation is stable for *bcc* metals under comprssion, no reorientation of the lattice leading to a new ⟨111⟩ component should be expected. In this respect, the observation of ⟨111⟩ lamellae in grains with the ⟨100⟩ component appears surprising. It is proposed that small regions of the original grains reorient by rotation of 55° around a common (110) pole forming the ⟨111⟩ lamellae, as seen in the {110} pole figure (Fig. 5.23b). It is noteworthy that despite the existence of two crystallographically equivalent [110] directions in the compression plane, all ⟨111⟩ lamellae in Fig. 5.23a have almost identical orientations with their orientations rotated around the same [110] axis (see Fig. 5.23b).

The formation of ⟨111⟩ lamellae in the ⟨100⟩ matrix must result from a reorientation process during plastic deformation. It is evident from Fig. 5.28 that this reorientation process is realized by gradually increasing of the misorientation angle with strain. Such a continuous development indicates that this process is dominated by dislocation glide related mechanisms. For reorientation and texture evolution due to dislocation activity of metallic materials undergoing plastic deformation, Taylor-type theories are widely accepted and applied [114]. These theories assume an equal critical resolved shear stress for all slip systems and an equal strain for all grains in a polycrystalline aggregate. Under these assumptions, at least five active slip systems must be selected for satisfying the prescribed strain by minimizing the sum of shears. In Taylor models, all grains are assumed to be deformed homogeneously, and no grain splitting is considered. Taylor-type models have been successfully used to predict the macroscopic texture in a variety of materials deformed under different modes. However, Taylor theories fail to predict the local lattice reorientation, due to the fact that grains do not always deform uniformly, especially when grains are coarse. It has been found in many cases that grains split into different regions within which activated slip systems differ from one to another, and thereby forming banded structures delineating different regions [176-178]. Similarly, the formation of ⟨111⟩ lamellae in the ⟨100⟩ matrix is thought to originate from the orientation splitting of the interior of grains.

According to the Taylor theories, ⟨100⟩ is a stable orientation for *bcc* materials subjected to uniaxial compression, i.e. a grain with ⟨100⟩ direction oriented along the CA will not change its direction along the CA. After deformation to high strains, such grains are supposed to be subdivided into finer grains or subgrains, all having ⟨100⟩ directions along the CA. This should happen if all slip systems with the highest Schmid factor were activated equally, which may be not always the case.

When a crystal is compressed along a ⟨100⟩ direction, the activated slip systems can be calculated assuming pencil glide of dislocations with Burgers vectors ⟨111⟩ on all possible glide planes. There are four Burgers vectors, namely [111], $[\bar{1}11]$, $[1\bar{1}1]$, and $[11\bar{1}]$. For each given slip direction (Burgers vector), the most favored slip plane is the one leading to the highest Schmid factor. Four most favored slip systems with the same Schmid factor are obtained for the sample with ⟨100⟩ along CA (shown in Table 5.1).

Orientation data from EBSD could be used to determine the crystallographic plane of the lamellar boundaries. Due to the fact that lamellar boundaries have a tendency to rotate towards the compression plane with strain, the relationship between the slip systems and dislocation boundary plane will vanish at high strain, and therefore only the samples after DPD to low strains can be used for calculation of the boundary plane i, i.e. at the early stage of the boundary formation. The sample after DPD to a strain of 0.9 (Fig. 5.27b) was used with this purpose. The reason for choosing this sample is twofold: the boundaries in this sample are still at an early stage of their formation, since the orientation of the deformation bands has still not reach to ⟨111⟩ and there are many boundaries evolving from LABs to HABs as seen from Fig. 5.27b. In addition, in the sample after DPD to a strain of 0.9, the boundaries are viewed edge-on, which makes the calculation of the boundary plane very convenient and straightforward. The boundary trace direction forming an inclination angle of 62° with CA determined from orientation map is [0.5155   0.5811   -0.5199], and the rotation axis of the boundary is along [011]. Then the boundary plane normal can be determined as [1.1010   -0.5155   -0.5811] assuming pure tilt character of the boundary. Taking into consideration of the measuring errors of the Euler angles and misalignment of the sample during scanning, this plane normal is reasonable to be treated as $[2\bar{1}\bar{1}]$, which corresponds to an activated slip plane of slip system A.

Table 5.1 Most favored slip systems when a crystal is compressed along [100] or [111] direction for ⟨111⟩-pencil glide

CA	Slip systems	Schmid factor	CA	Slip systems	Schmid factor
[100]	A: $(2\bar{1}\bar{1})[111]$	0.47	[111]	(hkl)[111]	0
	B: $(211)[1\bar{1}\bar{1}]$			$\bar{B}$: $(211)[\bar{1}11]$	0.31
	C: $(21\bar{1})[1\bar{1}1]$			E: $(121)[1\bar{1}1]$	
	D: $(2\bar{1}1)[11\bar{1}]$			F: $(112)[11\bar{1}]$	

To determine which slip systems could cause crystal rotation around a ⟨110⟩ and thereby achieving reorientation from ⟨100⟩ to ⟨111⟩, the crystal rotations due to specific slip systems are analyzed using the velocity gradient. Taking the slip system *A* $(2\bar{1}\bar{1})[111]$ as an example, the velocity gradient can be expressed as:

$$L_A = \vec{b}_A \otimes \vec{n}_A \dot{\gamma}_A = \frac{1}{\sqrt{18}} \begin{pmatrix} 2 & \bar{1} & \bar{1} \\ 2 & \bar{1} & \bar{1} \\ 2 & \bar{1} & \bar{1} \end{pmatrix} \dot{\gamma}_A \tag{5.3}$$

where $\vec{b}_A$ and $\vec{n}_A$ are the Burgers vector and the slip plane normal of slip system *A*, respectively. $\dot{\gamma}_A$ is the shear strain rate. The rotation part of the gradient matrix is:

$$W_A = \frac{1}{2}(L_A - L_A{}^T) = \frac{1}{2}\frac{1}{\sqrt{18}}\begin{pmatrix} 0 & \bar{3} & \bar{3} \\ 3 & 0 & 0 \\ 3 & 0 & 0 \end{pmatrix}\dot{\gamma}_A \qquad (5.4)$$

The corresponding matrixes of other slip systems W_B, W_C and W_D can be calculated accordingly. The operation of different combinations of slip systems results in the crystal rotating along different axes. For convenience, δ symbol is introduced with δ equals to either 1, 0, or -1. Set $\dot{\gamma}_A = \delta_A \dot{\gamma}$, and analogy to δ_B, δ_c and δ_D.Then the matrix with combined slip systems could be expressed as:

$$L = L_A\delta_A + L_B\delta_B + L_C\delta_C + L_D\delta_D \qquad (5.5)$$

$\delta_i = 1$, 0, and -1 mean the slip system *i* (*i*=A, B, C, D) activated, not activated, and activated in the reverse direction. Then the rotation part of the matrix can be expressed as:

$$\begin{aligned} W &= \frac{1}{2}(L - L^T) \\ &= \frac{1}{2}\begin{pmatrix} 0 & -3\delta_A + 3\delta_B - \delta_c + \delta_D & -3\delta_A + 3\delta_B - 3\delta_c + 3\delta_D \\ 3\delta_A - 3\delta_B + \delta_c - \delta_D & 0 & 0 \\ 3\delta_A - 3\delta_B + 3\delta_c - 3\delta_D & 0 & 0 \end{pmatrix}\dot{\gamma} \end{aligned} \quad \ldots (5.6)$$

This leads to a rotation vector:

$$R = \begin{pmatrix} W_{23} \\ -W_{13} \\ W_{12} \end{pmatrix} = \begin{pmatrix} 0 \\ 3\delta_A - 3\delta_B + 3\delta_c - 3\delta_D \\ -3\delta_A + 3\delta_B - \delta_c + \delta_D \end{pmatrix}\dot{\gamma} \qquad (5.7)$$

It is clear that if $\delta_A = \delta_B = \delta_c = \delta_D = 1$, i.e. the four slip systems are equally activated, crystal rotation will not happen. This is consistent with the Taylor theory. If for instance, only one slip system is activated, the crystal will rotate around one of the crystallographic ⟨110⟩ axes. Operation of slip system B (211)[1$\bar{1}\bar{1}$] leads to a rotation of the crystal around [0$\bar{1}$1] from [100] towards [211]. However, the Schmid factor of this slip system decreases to zero with the crystal rotating from [100] towards [211]. Once the crystal rotates to [411], the activation of another two slip systems with Burgers vectors of [111] and [11$\bar{1}$] result in a net rotation towards [111]. Therefore the key factor controlling the crystal rotating from [100] to [111] is the preferential activation of slip system (211)$[1\bar{1}\bar{1}]$, with which the crystal can rotate from the [100] orientation corner (seen from the stereological triangle) towards [211].

The discrimination of activated slip systems results from the ambiguity in selection from equally favorable slip systems. This ambiguity becomes severe for compression along [100], because all four slip directions have the same Schmid factor for pencil glide. Any bias in selecting the slip systems will make this stable orientation as predicted by the Taylor-Bishop-Hill theory unstable. Therefore, a banded structure with alternating matrix and newly formed bands due to the lattice rotation forms. These deformation induced bands in single crystals and coarse grained polycrytals have been widely studied in *fcc* materials [176-181], and a few *bcc* materials [182-184]. However, it is the first time that such a nanoscale lamellar structure is reported with a high misorientation between all lamellae obtained by deformation-induced orientation splitting. The structural refinement is very efficient since the nanoscale lamellae with width finer than 40 nm could be obtained after DPD to a strain of 2.1. Such a nanoscale lamellar structure is not only of scientific interest, but might also have engineering significance, since such type of structure may result in high irradiation tolerance [185].

5.2.3 Behavior of oxide nanoparticles in PM2000 subjected to DPD

As the steel contains a high density of oxide nanoparticles, the behavior of these nanoparticles during DPD is a very important issue. Thus further detailed characterization by TEM and HRTEM are conducted to reveal the response of the oxide nanoparticles when the PM2000 was subjected to DPD.

5.2.3.1 Microstructure of oxide nanoparticles after DPD

Bright field TEM images of samples after DPD to strains of 1.0 and 2.1 are shown in Fig. 5.30. Enlarged images from the framed regions were presented as well to show more details. It is evident that the deformation microstructure contains dark elongated features, which can be seen more clearly in the magnified regions on the right-hand side of Fig. 5.30a and Fig. 5.30b. These features are aligned almost perpendicular to the CA. A dark field TEM image obtained by masking the diffraction from the oxide nanoparticles is shown in Fig. 5.31. The contrast in this image demonstrates that the elongated features have a crystal structure similar to the YAP nanoparticles. To support this claim, a HAADF STEM image of the DPD sample is shown in Fig. 5.32. Differently from the diffraction contrast in conventional TEM images, the HAADF STEM image mainly shows the mass contrast, i.e. regions with smaller atomic number and/or including lighter elements, for instance oxides in ferrite, have darker contrast and vice versa. It is seen from the STEM image that the elongated features are darker than the ferrite matrix, which indicates they contain lighter elements than Fe. An EDX line scan spectrum obtained from the region marked by the yellow line provides evidence that these features are enriched in Y and Al, but depleted in Fe and Cr, which suggests that they are indeed oxide nanoparticles. Their shape has been altered from the original spheres to disks due to compression by DPD. This indicates that the oxide nanoparticles become plastically deformed during DPD. The disk shape is further verified by observations of particles from a different section that contains the compression plane (see Fig. 5.33). It is seen that the disks do not appear perfectly round in the compression plane, which may be due to anisotropic deformation of individual particles.

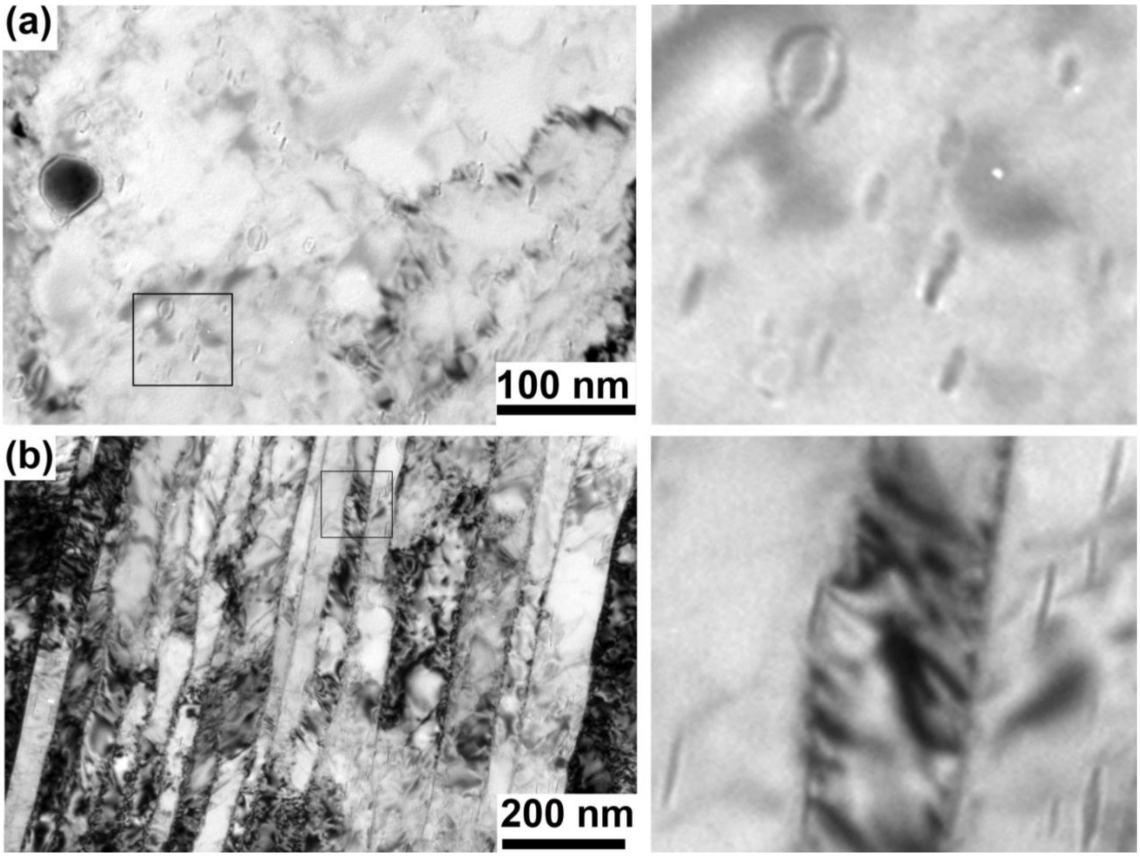

Fig. 5.30 TEM images from the longitudinal section of PM2000 after DPD to a strain of (a) 1.0 and (b) 2.1. Regions framed in the images on the left-hand side are magnified on the right-hand side to demonstrate deformed particles in more detail. The CA is horizontal.

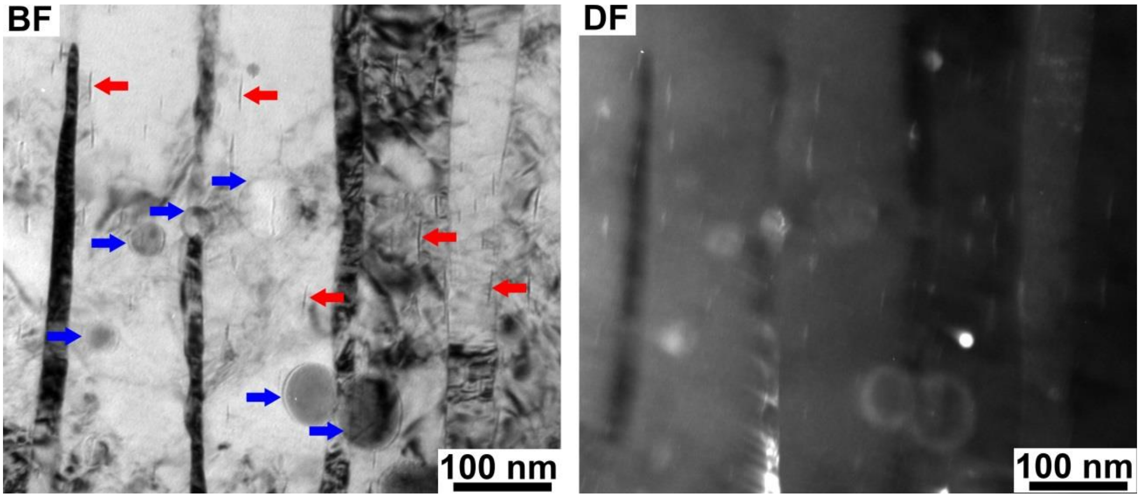

Fig. 5.31 TEM images from the longitudinal section of PM2000 after DPD to a strain of 2.1: bright field (BF) image, and dark field (DF) image by masking the diffraction from the oxide nanoparticles. Some oxide particles which change their shapes substantially are marked by red arrows; while those do not have appreciable changes are indicated by blue arrows. CA is horizontal.

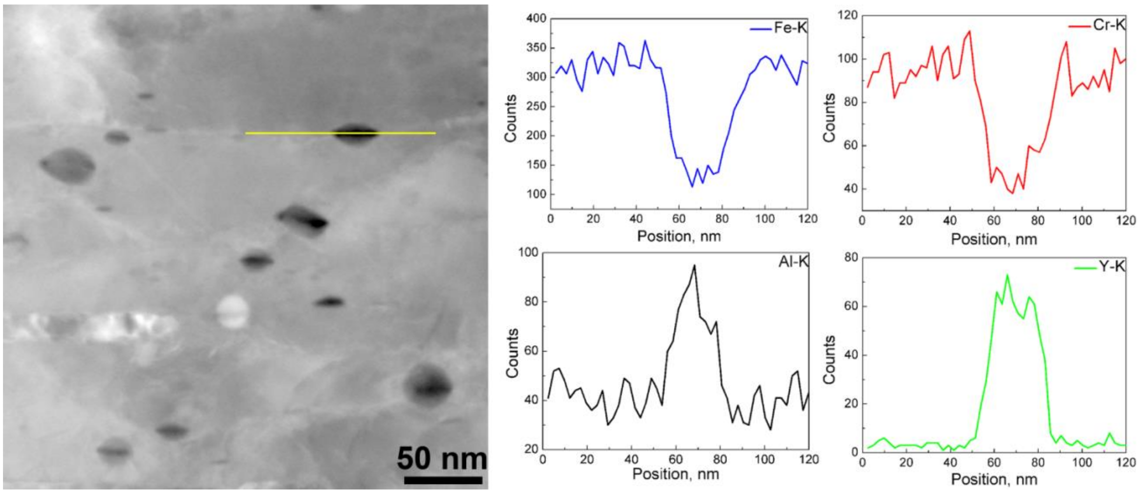

Fig. 5.32 STEM image of PM2000 in longitudinal section after DPD to a strain of 2.1. The EDX spectra, for the elements Fe, Cr, Al, and Y, on the right side are from the line scan marked yellow in the STEM image. The intensity in the profiles represents the relative concentration of a certain element. CA is vertical.

The aspect ratio (AR) characterizing the shape of oxide nanoparticles in the longitudinal section can be used to evaluate the plastic strain experienced by these particles during DPD. Statistical data illustrating the relationship between the particle size calculated as the equivalent circular diameter (ECD,) and AR for 160 and 240 particles in the samples after DPD to strains of 1.0 and 2.1, respectively, are shown in Fig. 5.34. Theseplots reveal three important findings: (i) the AR of oxide nanoparticles increases with increasing macroscopic strain; (ii) the AR tends to increase with decreasing particle size; and (iii) most ECDs of deformed particles with AR larger than 1.2 are less than 15 nm. The latter results can further be validated by comparing the frequencies of particles with an ECD below 15 nm in the as-received and DPD samples. The percentage of particles with an aspect ratio below 1.2 after DPD is 12%, which is substantially smaller than the frequency of such non-elongated particles of this size in the as-received condition (74%). The distributions of AR of the particles with AR larger than 1.2 in the sample after DPD to strains of 1.0 and 2.1 are presented in Fig. 5.35. Large variations can be seen in both cases, and the mean AR for the particles with AR>1.2 is 2.84 and 6.34 after DPD to strains of 1.0 and 2.1, respectively.

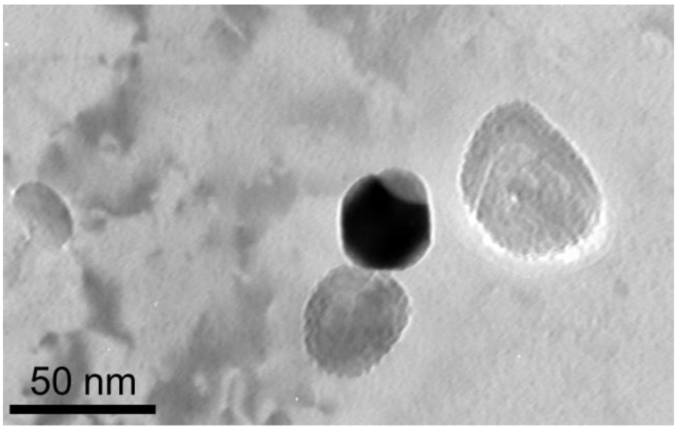

Fig.5.33 TEM image showing deformed particles in the compression plane of PM2000 after DPD to a strain of 2.1.

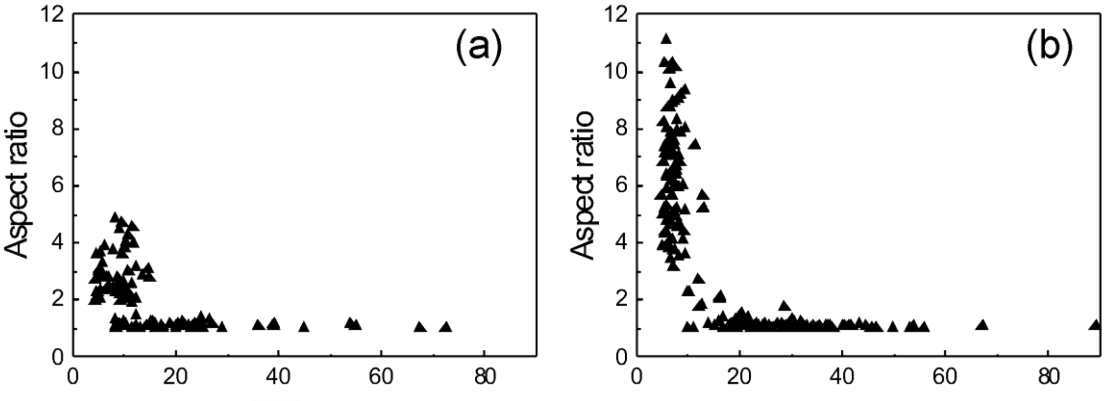

Fig. 5.34 Distribution of the aspect ratio versus the equivalent circular diameter (ECD) of oxide nanoparticles in the samples after DPD to strains of 1.0 (a) and 2.1 (b).

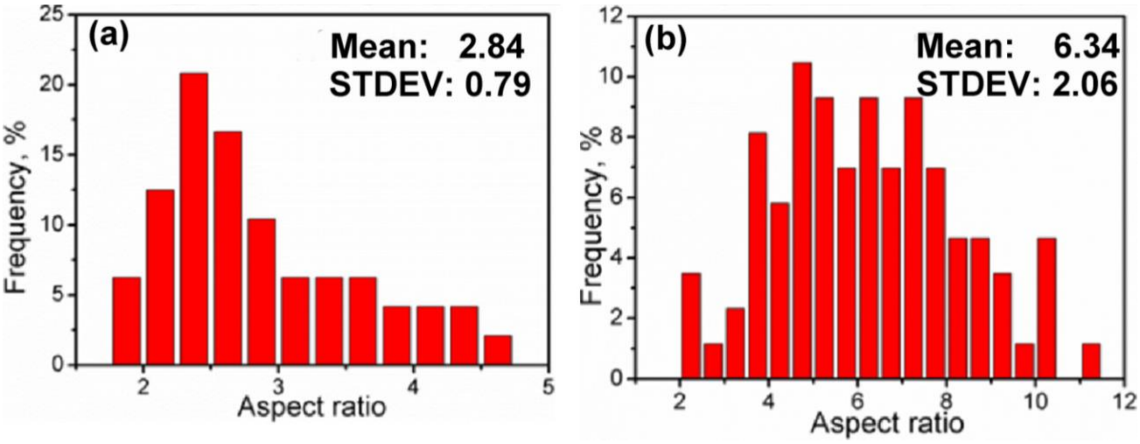

Fig. 5.35 Histogram of the aspect ratio of particles (with aspect ratios above 1.2) in the samples deformed by DPD to equivalent strains of (a) 1.0 and (b) 2.1.

Considering that the oxide nanoparticles had a nearly spherical shape before DPD, particles with aspect ratios above 1.2 are considered to be deformed during DPD. The true plastic strain of the particles after deformation is estimated from their aspect ratio as $\varepsilon_{part} = 2\ln AR/3$. The plastic strain calculated using this relation is shown in Fig. 5.36, which represents data only for particles with AR larger than 1.2, i.e. for the particles considered as deformed. The mean value of the equivalent plastic strain of the oxide nanoparticles is 0.7 and 1.2 for the samples deformed by DPD to strains of 1.0 and 2.1, respectively. Obviously, the average equivalent strain of the particles is substantially smaller than the macroscopic strain.

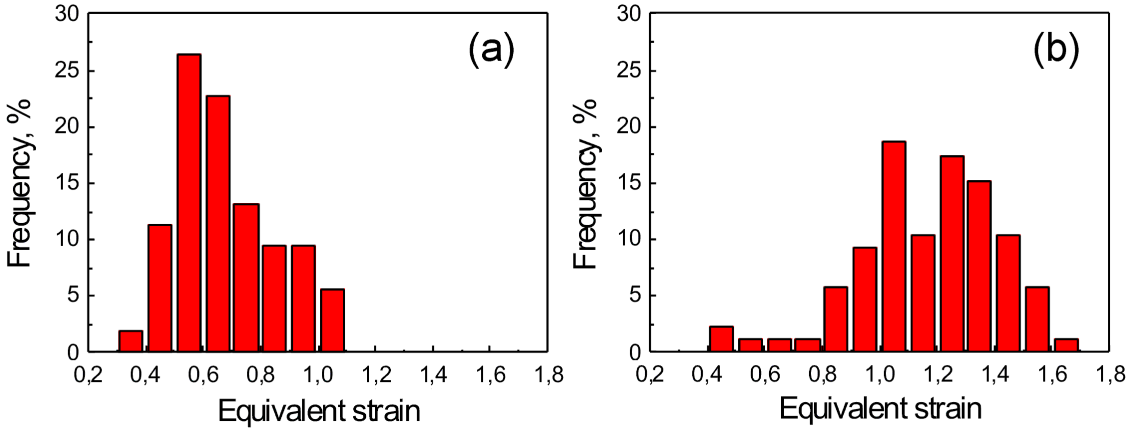

Fig. 5.36 Frequencies of particles (with aspect ratios above 1.2) in the samples deformed by DPD to equivalent strains of (a) 1.0 and (b) 2.1.

By excluding the oxide nanoparticles with aspect ratio higher than 1.2 (critical value, below which the oxide nanoparticles are thought to be not deformed), the distribution of the Feret's diameters of the oxide nanoparticles after DPD to a strain of 2.1 is shown in Fig. 5.37. Compared to the size distribution in the as received sample, a considerable difference can be seen. Quantitatively, the percentage of the particle size less than 10 nm and 20 nm are 43% and 81%, respectively, in the as received material, while the counterparts of the sample after DPD to a strain of 2.1 are 1% and 31%, respectively. This also indicates that most of the deformed oxide particles have a diameter less than 20 nm.

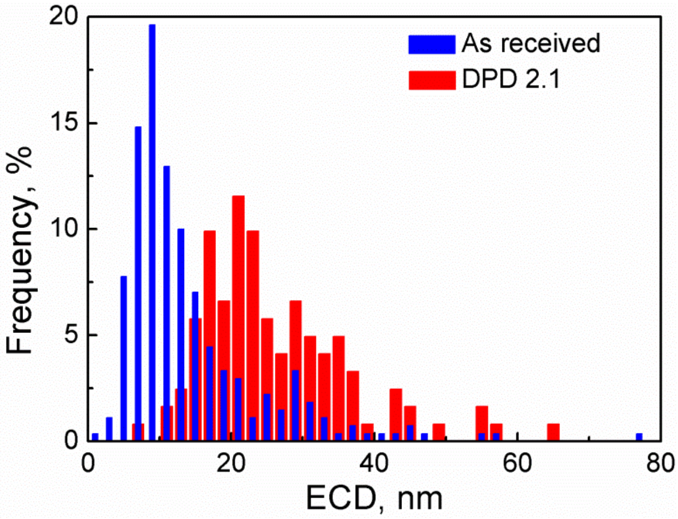

Fig. 5.37 Size distribution of the Feret's diameters of oxide nanoparticles in the as received sample and oxide nanoparticles with aspect ratio smaller than 1.2 in the sample after DPD to a strain of 2.1.

5.2.3.2 Deformation mechanisms of oxide nanoparticles

As described above, the oxide nanoparticles are found to be plastically deformed in the samples after DPD. This is, however, contradictory to the common view that oxide particles are both hard and brittle at ambient temperature. The mechanical parameters of bulk YAP is listed in Table 5.2 [186]. According to Pugh's criterion [187], a material is brittle if the ratio of bulk modulus/shear modulus is less than 1.75 and/or Poisson's ratio is less than 0.26. In case of YAP, these ratios are 1.55 and 0.23, respectively. Thus the bulk YAP is suggested to be intrinsically brittle at room temperature. Therefore, it is difficult to understand how the YAP could be substantially deformed at room temperature. To reveal the deformation mechanism of the YAP nanoparticles in PM2000, HRTEM characterization on the YAP nanoparticles deformed to low strains is conducted.

Table 5.2 Mechanical parameters of YAP at room temperature [186]

Bulk modulus (GPa)	Shear modulus (GPa)	Young's modulus (GPa)	Poisson's ratio	Hardness (GPa)
198.3	127.9	315.8	0.23	~19.5

Two examples of deformed YAP particles are presented and analyzed in Fig. 5.38. The HRTEM image and corresponding FFT and IFFT (Fig. 5.38a) show the existence of deformation twinning in the deformed nanoparticle, which is indicated by the yellow lines in the HRTEM image and IFFT image. The deformation twinning can be indexed as $(110)\langle 1\bar{1}2\rangle$ according to the FFT pattern, i.e. the twinning plane and twinning direction are (110) and $\langle 1\bar{1}2\rangle$, respectively. It is seen that this twinning involves shear displacement of 9 (220) planes along the $\langle 1\bar{1}2\rangle$ direction. Fig. 5.39 shows a simulated schema of the atomic structure of $(110)\langle 1\bar{1}2\rangle$ twinning in YAP viewed along the $[\bar{1}11]$ zone axis, and it is in a very good agreement with the observed structure in Fig. 5.38a.

Another example of a deformed YAP nanoparticle is shown in Fig. 5.38b. One twin boundary with the same twin character as that in Fig. 5.38a ($(110)\langle 1\bar{1}2\rangle$) is figured out and marked by yellow lines, based on analysis of the HRTEM image and its corresponding FFT and IFFT. In addition, another planar defect (indicated by blue lines) is observed in the same particle. As seen from the HRTEM and IFFT images, this defect resembles to a stacking fault in metallic materials. A stacking fault in pure metals involves only one displaced plane of atoms, i.e. it is a two dimensional defect. However, HRTEM images in the current study show the lattice structure instead of atomic structure of YAP - a lattice plane in the HRTEM corresponding to the atomic structure of a certain volume in the specimen. Therefore, this defect might not be able to be identified as stacking fault. In order to present the real structure of this defect, a schematic diagram (Fig. 5.40) is present to illustrate the atomic structure of this defect. Evidently, several planes of atoms are present in this defect, and these planes (as marked in the dash rectangle) have mirror relationship on both sides of the mother crystals. Therefore, this defect is similar to a deformation twin with the same character (twinning plane and twinning direction is (110) and $\langle 1\bar{1}2\rangle$, respectively), as those indicated by yellow lines. The only difference is that this twin involves three (110) lattice planes seen from the HRTEM image, i.e. this is the unit twin with minimum thickness which can form in the YAP crystal. It should be mentioned here that $(110)\langle 1\bar{1}2\rangle$ twin was frequently observed in slightly deformed YAP nanoparticles, and no evidence of other type of defects were found in them.

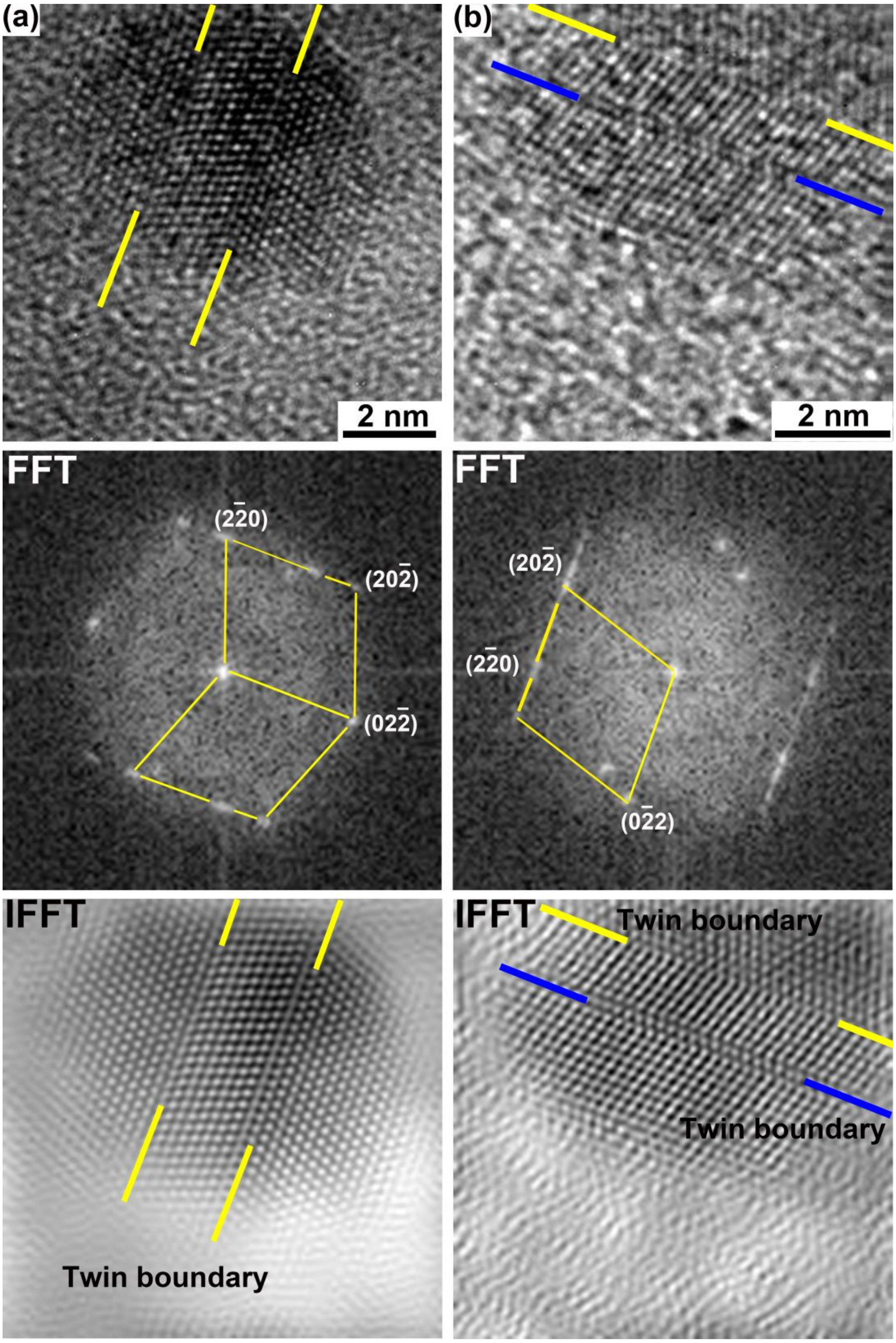

Fig. 5.38 HRTEM images of two oxide nanoparticles after deformation (a) and (b), and their corresponding FFTs. To better visualize the structure of the oxide nanoparticles, IFFT images are constructed by filtering the background noise from the HRTEM images. Twin boundaries are indicated by either yellow or blue lines.

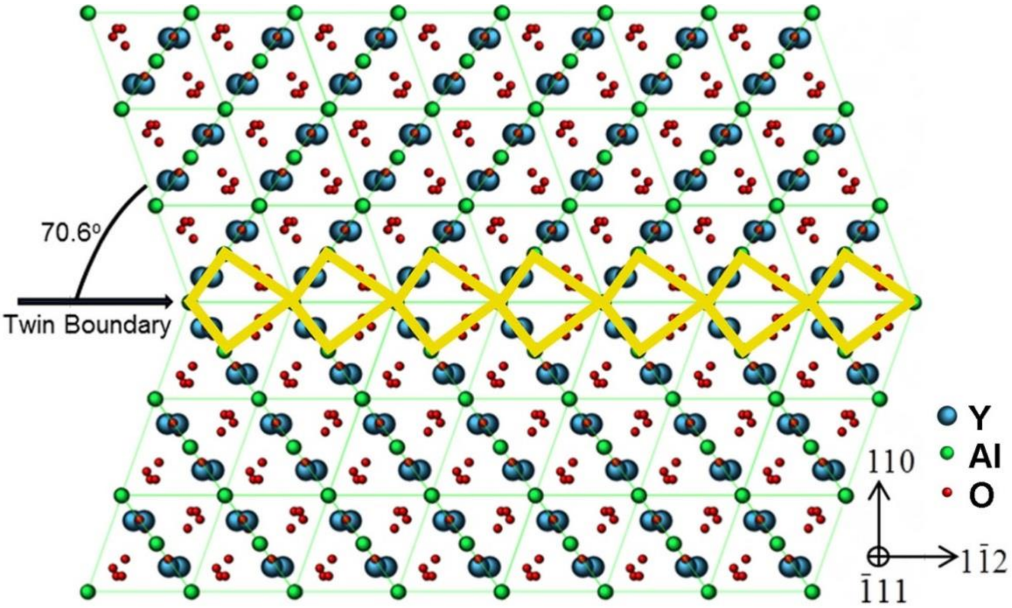

Fig. 5.39 Schematic diagram of $(110)\langle 1\bar{1}2\rangle$ twinning structure in YAP nanoparticle viewed from the $[\bar{1}11]$ direction, with mirror plane indicated. (Note that twin does not occur by pure shear, but may also require shuffling of O atoms)

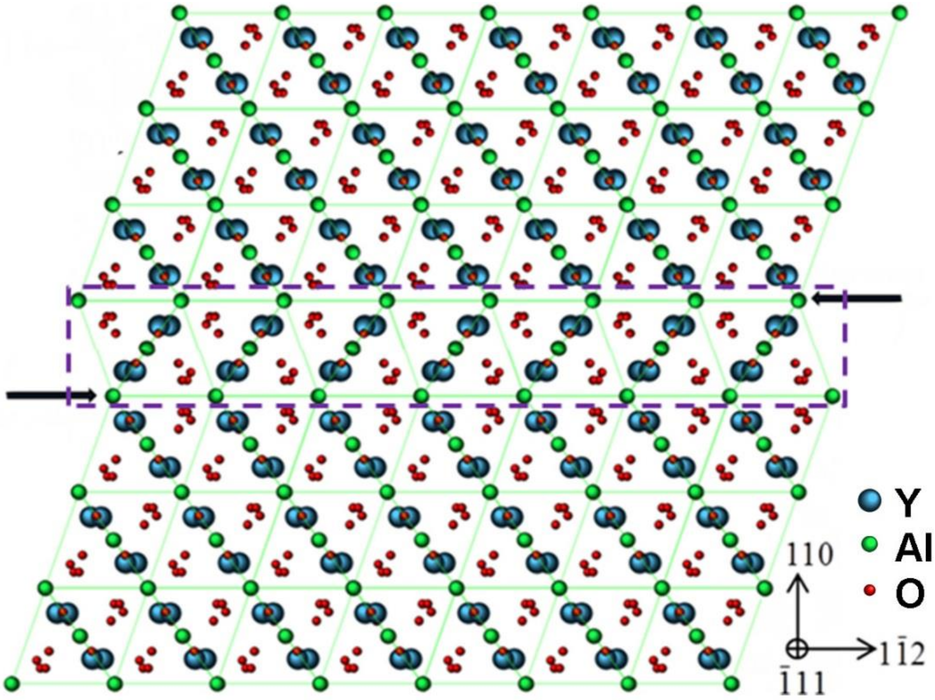

Fig. 5.40 A schematic diagram of $(110)\langle 1\bar{1}2\rangle$ twinning structure with a single layer of atoms in the twin of YAP nanoparticle viewed from the $[\bar{1}11]$ direction. Twinning boundaries are indicated by black arrows, and the twinning layer is marked by a dash rectangle. (Note that twin does not occur by pure shear, but may also require shuffling of O atoms).

The above results show that twins are the typical deformation induced defect in YAP nanoparticles after DPD to low strains. To totally clarify the deformation mechanism, the feature of the substantially deformed YAP nanoparticles would be required. However, the particles are deformed to very thin plates after DPD to high strains, so it is very difficult to view the particles edge-on. Furthermore, because of the high density of defects in the particles and the strong interference from the severely deformed ferrite matrix, no clear HRTEM images could be obtained on the largely deformed particles. Fig. 5.41 shows two YAP nanoparticles after deformation to larger strain.

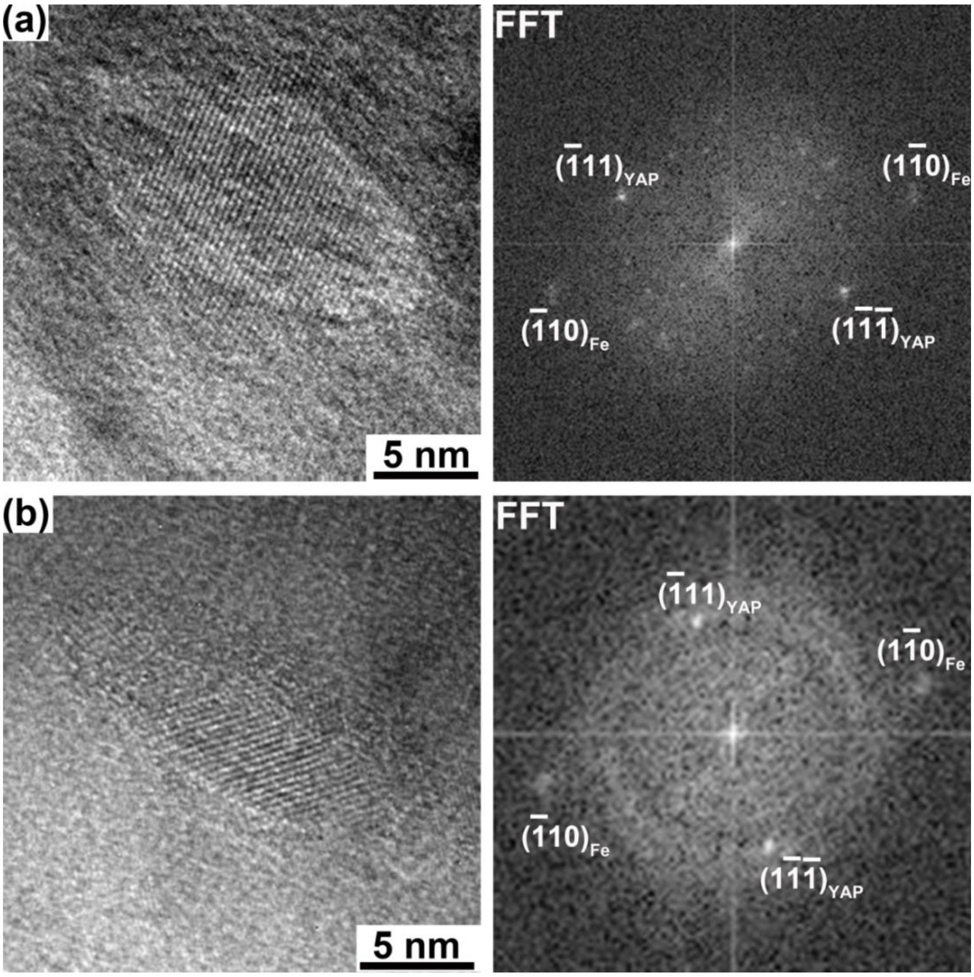

Fig. 5.41 HRTEM images and their corresponding FFTs of two oxide nanoparticles after deformation to high strains, with aspect ratios of (a) 2.2 and (b) 4.4. Diffraction from the crystalline YAP is indexed in the FFTs, which means the YAP particles still preserve its crystal structure after such high strains.

As the electron beam is not along the proper zone axes and the image is blurred due to the largely deformed structure, no deformation-induced defects can be observed clearly in these particles. Nevertheless, useful information could be derived from these images: the particles are still of crystalline structure, and FFT patterns demonstrate that the deformed particles still maintain the initial crystal structure; no amorphous or phase transformation occurs in these particles, as frequently observed in perovskite materials under high pressure. This indicates that deformation-induced twinning may still be the dominant mechanism at high strains.

5.2.3.3 Evolution of oxide nanoparticles with strain

Since the oxide nanoparticles are embedded in the ferrite matrix, stress and strain are directly imposed on the YAP nanoparticles by the surrounding ferrite matrix. Therefore, the correlated deformation between the YAP and Fe is of significance for understanding the deformation behavior of the oxide nanoparticles. In this section, the evolution of the oxide nanoparticles and the neighboring surrounding matrix with strain during DPD is characterized in detail, and to further clarify the deformation mechanism of the oxide nanoparticles.

TEM images in Fig. 5.42 show the microstructure of the samples after DPD to four strains, namely 0.6, 1.0, 1.6 and 2.1. It is seen in Fig. 5.42a that after deformation to a strain of 0.6, no appreciable deformation of the oxide particles can be observed. Interestingly, small voids extending in the compression plane on a nanoscale are seen at the interface, which are marked by arrows. These nanovoids indicate that decohesion between the oxide nanoparticles and the ferrite matrix. With increasing strain to 1.0, the oxide nanoparticles were slightly deformed to ellipsoidal shape and voids are still present at the interface. After DPD to a strain of 1.6, the YAP particles become further elongated, whereas nanovoids around some smaller YAP particles disappear. On the contrary, the nanovoids around relatively large particles are still present. In the sample after DPD to a strain of 2.1 (Fig. 5.42d), oxide nanoparticles are deformed substantially and most of the nanovoids at the interface disappeared.

The above results suggest that nanovoids developed around smaller particles heal during further deformation, whilst those around larger particles do not close. More evidence about such behaviors is shown in Fig. 5.43. It is seen from Fig. 5.43a that in the sample after DPD to a strain of 1.0, nanovoids form not only around the particles with size larger than 20 nm, but also around YAP particles with sizes less than 20 nm (about 8 nm), which are indicated by black arrows. After DPD to a strain of 2.1, the nanovoids around small particles disappear accompanying the deformation of the particles themselves which are thus present as black lines seen in Fig. 5.43b. The nanovoids around relatively larger particles (indicated by black arrows in Fig. 5.43b) with size larger than 20 nm, on the other hand, are preserved after deformation to such a high strain. These larger oxide nanoparticles almost do not change their initial spherical shape.

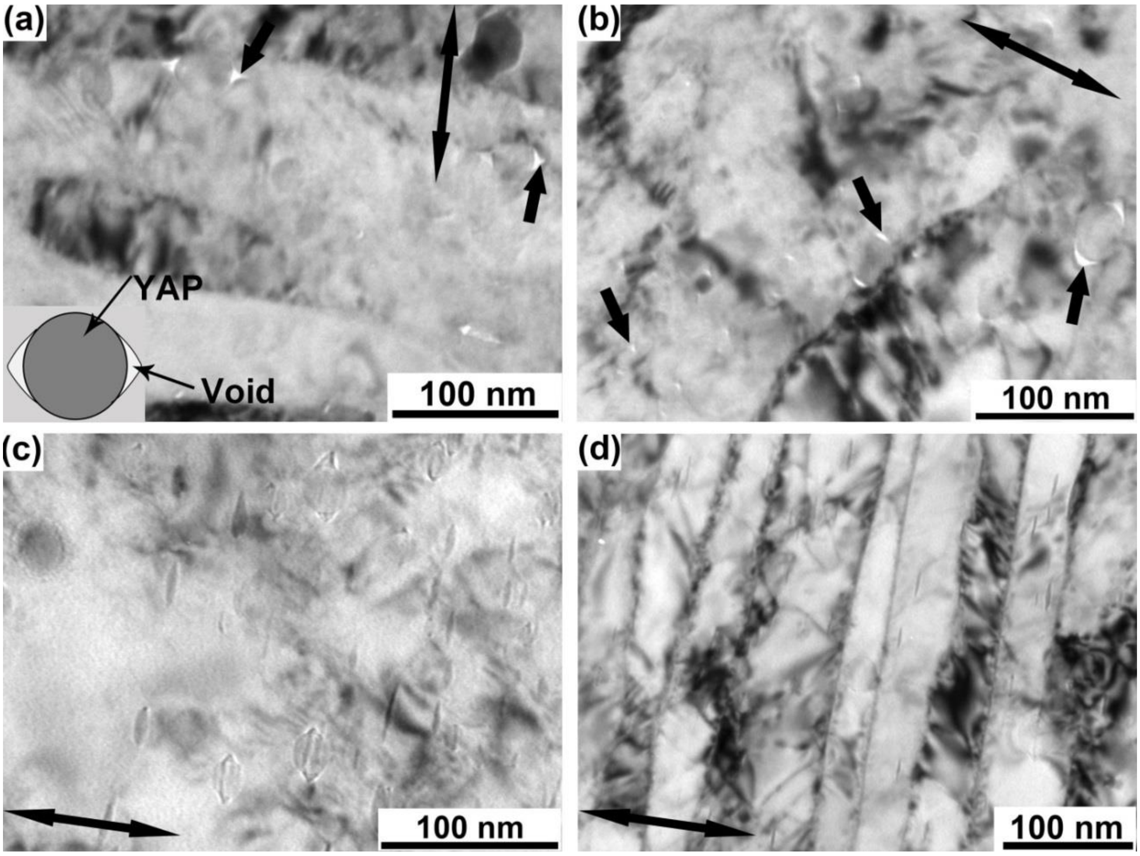

Fig. 5.42 TEM images of a longitudinal section of PM2000 after DPD to a strain of (a) 0.6, (b) 1.0, (c) 1.6, and (d) 2.1. The black arrows in (a) and (b) point at some voids formed around the interface of YAP/Fe. A schematic diagram illustrating the morphology of the void at a YAP/Fe interface is shown in (a). The CA is indicated by double arrows.

More evidence about the unclosed voids at the interface around the large oxide nanoparticles is presented in Fig. 5.44. HRTEM images show two oxide nanoparticles with nanovoids at the interface in the sample after DPD to a strain of 2.1. These two YAP particles have ECD of approximately (a) 26 nm and (b) 30 nm. No appreciable deviation from the equiaxed shape and hence no deformation is revealed for them and no deformation-induced defect is visible in the particles. Besides, nanovoids caused by debonding are still present at the Fe/YAP interface, as indicated by black arrows.

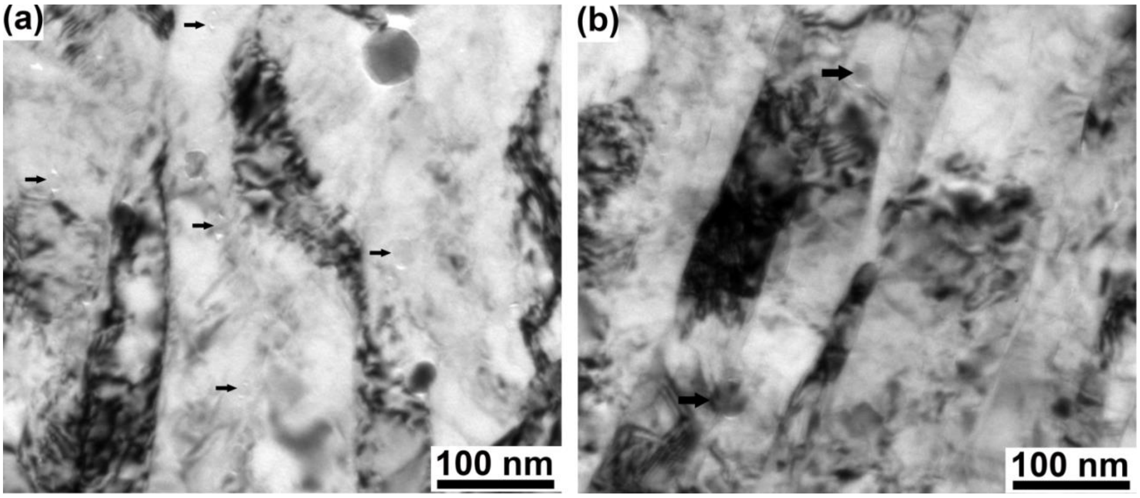

Fig. 5.43 TEM images of a longitudinal section of PM2000 after DPD to a strain of (a) 1.0, and (b) 2.1. Black arrows indicate some small particles which develop nanovoids around them in (a), and some larger particles in (b) where nanovoids are still preserved after DPD to a strain of 2.1. The CA is indicated by double arrows.

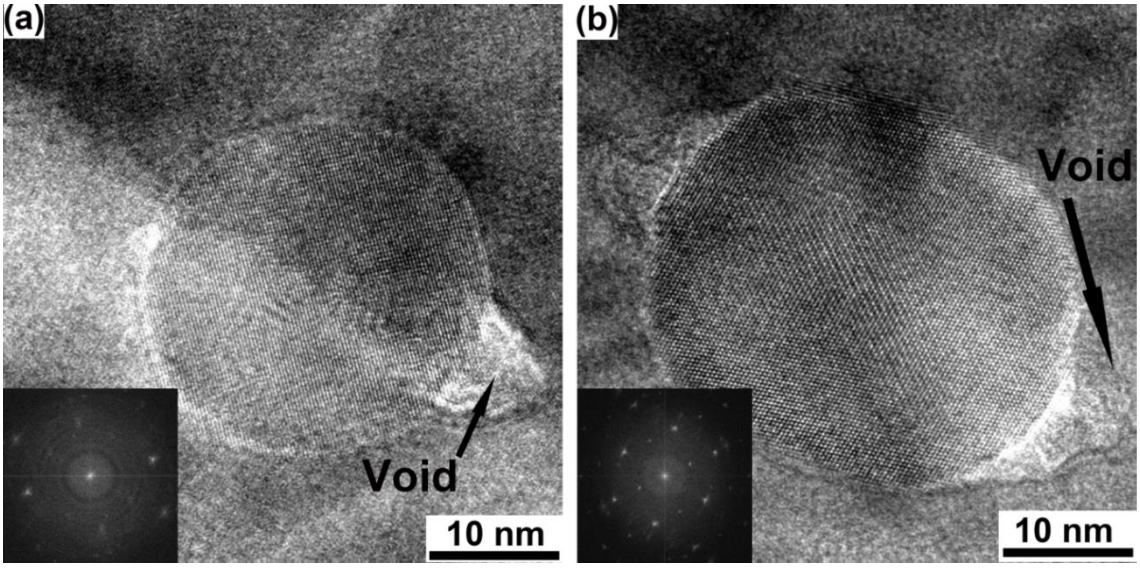

Fig. 5.44 HRTEM images of two oxide nanoparticles in the PM2000 after DPD to a strain of 2.1. Insets are the corresponding FFTs. Nanovoids at the interface are indicated by arrows.

It is so far evident that nanovoids form around all the oxide particles after DPD to low strains. With increasing deformation to high strains, the voids around the oxide particles with diameters smaller than 20 nm vanish, whilst those around the larger oxide particles do not disappear. The closing of the nanovoids is mainly attributed to the self-welding of the top and bottom surface of the voids due to the compressive stress imposed on them and the deformation of the matrix. It is also demonstrated that healing of the nanovoids is related to the deformation of nanoparticles, since the voids around the deformable particles become closed while those around large particles that do not deform are still open after DPD to high strains. A series of schematic diagrams (Fig. 5.45) show the envisaged evolution of nanovoids around the oxide nanoparticles with strain coupled to the deformation of oxide nanoparticles themselves.

There are two distinct categories of oxide nanoparticles in the ferrite matrix, namely small particles with sizes smaller than 20 nm which are substantially deformed during DPD, and large particles with sizes larger than 20 nm which do not deform appreciably with increasing strain. Debonding occurs near the interface between Fe/YAP along a line in the compression plane, where tensile normal stresses are the largest. Thereby voids having sizes proportional to the sizes of the particle form at the interface (Fig. 5.45b). Self-welding of the matrix close to the void tip takes place with the emergence of matrix flow from above and below the particle after deformation to a certain strain (Fig. 5.45c), resulting in the formation of conical nanovoids (when viewed in two dimensions). Progressively, the volume of the voids at the interface decreases with increasing external strain during DPD. Simultaneously, small YAP nanoparticles are plastically deformed, while large particles do not deform. After DPD to high strains (Fig. 5.45d), nanovoids around the small oxide nanoparticles shrink and vanish due to self-welding when the particles are substantially deformed, whereas the nanovoids around the particles that are not considerably deformed are still open. This suggests that the deformation of oxide nanoparticles is crucial for healing of the nanovoids.

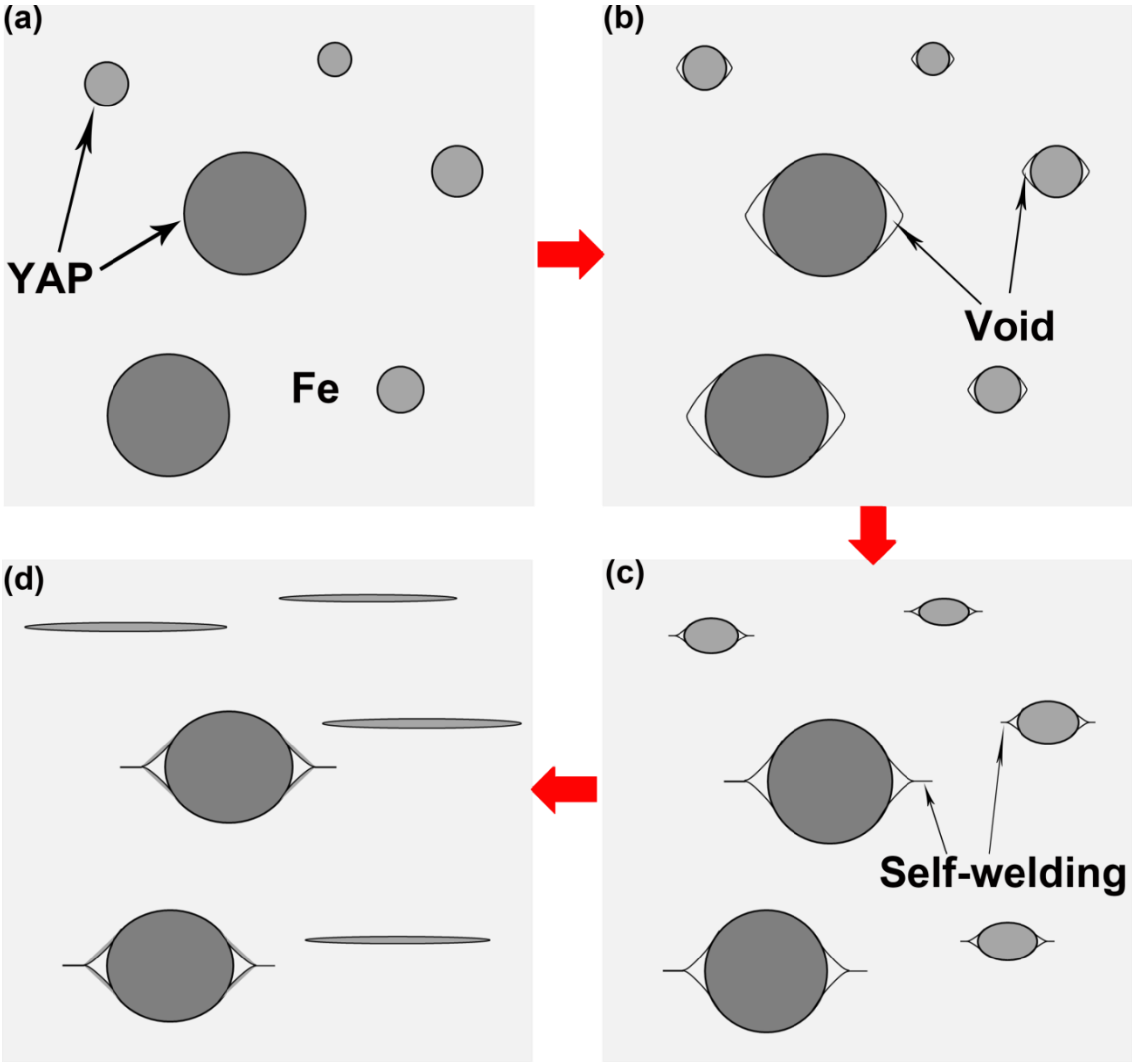

Fig. 5.45 Schematic diagram showing the envisaged evolution of oxide nanoparticles and the nanovoids generated at the interface. (a) YAP particles with sizes smaller than 20 nm and larger than 20 nm and the ferrite matrix before deformation, (b) nanovoids form at the interface around both large and small YAP particles after deformation to a low strain, (c) part of the nanovoids close due to self-welding caused by compressive stress after deformation to a medium strain, and (d) nanovoids around small particles disappear accompanied by the deformation of the particles, whilst the voids around large particle remain open.

5.2.3.4 Effect of interface on the deformation of oxide nanoparticles

The interface between the oxide nanoparticles and ferrite matrix may play an important role in the evolution of ferrite matrix and oxide particles, since the stress/strain is transferred from the matrix to the particles via the interface, and formation of voids around the particles results from debonding of the interface. These issues may be closely related to the character of the interface and its interfacial energy and bonding strength. In terms of the interface character, there are mainly three types, namely coherent, semi-coherent and incoherent. The interface between the YAP nanoparticles and the ferrite matrix is coherent in the as-received PM2000, as demonstrated in section of 5.1.2. Substantial deformation of YAP nanoparticles occurs in this sample during DPD. A question to be answered is whether the particles have a different type of interface with the matrix, e.g. an incoherent interface, whether can be plastically deformed or not.

Therefore a sample in which oxide nanoparticles have an incoherent interface with the ferrite matrix is prepared and deformed. As shown in section of 5.1.4, YAP oxide nanoparticles develop an incoherent interface with the matrix after annealing at 1200 °C for 1 hour. A cylindrical sample with dimensions of Ø6×9 mm was annealed at 1200 °C for 1 hour, and subsequently DPD was carried out on this sample at room temperature with strain rates of 10^2-10^3 s^{-1}. A TEM image from the sample after DPD to a strain of 2.1 is shown in Fig. 5.46.

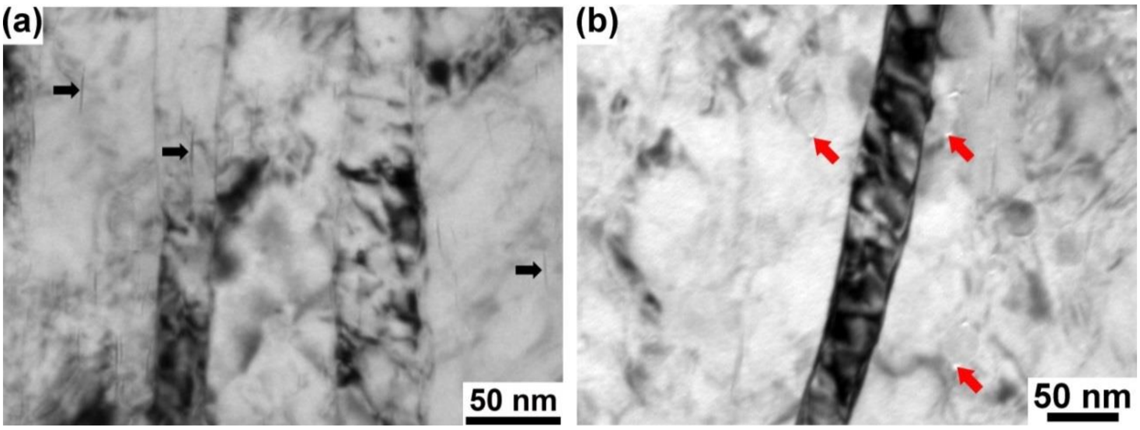

Fig. 5.46 TEM image of the longitudinal section of the as-received PM2000 after annealing at 1200 °C for 1 hour followed by subsequent DPD to a strain of 2.1: (a) the microstructure of deformed ferrite matrix and deformed YAP nanoparticles, which are indicated by black arrows in (a), and some remaining voids indicated by red arrows in (b).

It is seen that a very fine lamellar structure is formed after DPD. More importantly many black features, same as seen in the Fig. 5.30, are observed. Accordingly, these black features are deformed oxide nanoparticles as well. It is also evident that the considerably deformed oxide nanoparticles are those with sizes less than 20 nm.

Nanovoids are observed around undeformed oxide nanoparticles in this sample (Fig. 5.46b), whereas no voids can be seen in the substantially deformed oxide nanoparticles (Fig. 5.46a). Therefore, it can be concluded that no matter what interface the oxide nanoparticles have with the matrix (coherent or incoherent), the oxide nanoparticles are substantially deformed during DPD, i.e. the deformation of YAP nanoparticles does not depend on the character of the interface between the particles and ferrite matrix.

5.2.3.5 Effect of strain rate on the deformation of oxide nanoparticles

Since the deformation of oxide nanoparticles is not common place and has not been reported previously, it should be clarified whether the deformation of oxide nanoparticles is related to the high strain rates imposed by DPD or not. To evaluate the role of the strain rate on the particle deformation, a quasi-static compression (QSC) test with an initial strain rate of 10^{-4} s^{-1} was conducted on the as-received PM2000 samples. Cylindrical samples with dimension of Ø6×9 mm were compressed at room temperature to a strain of 2.1 in two passes, and the resulting microstructure was characterized. TEM images from the sample after QSC to a strain of 2.1 are shown in Fig. 5.47.

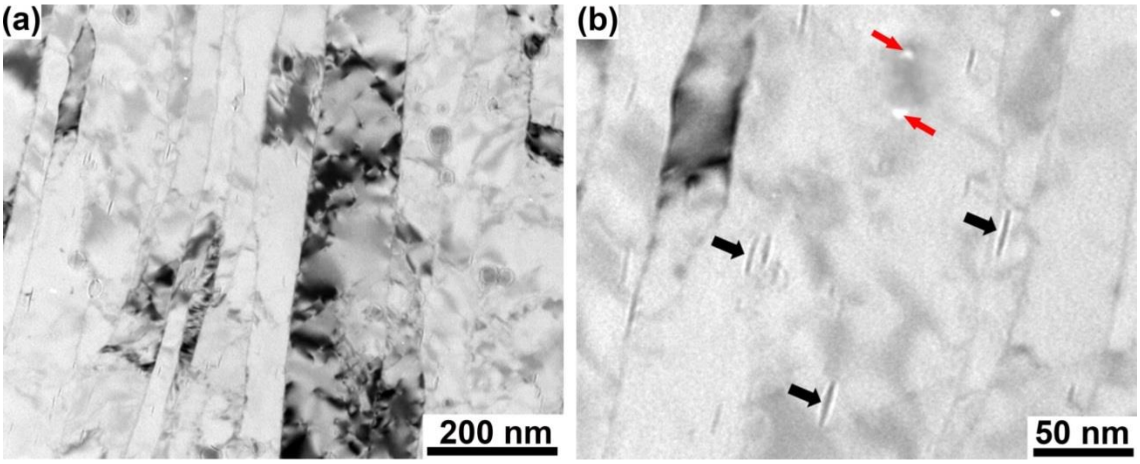

Fig. 5.47 TEM images of the as-received PM2000 in longitudinal section after QSC to a strain of 2.1 (a) microstructure of the deformed matrix, (b) deformed oxide nanoparticles are indicated by black arrows, and nanovoids around larger particles are indicated by red arrows.

A nanoscale lamellar structure developed after deformation, and more importantly deformed oxide nanoparticles are also observed in the TEM image (Fig. 5.47b). The average aspect ratio of the deformed oxide nanoparticles in the sample after QSC to 2.1 is about 6.17, which is very close to their counterparts in the DPD sample (6.34). Nanovoids remain open around a larger particle (about 25 nm), which is indicated by red arrows (Fig. 5.47b), whereas no voids are observed around the smaller particles. Therefore, the deformation of oxide nanoparticles occurs not only during DPD, but also during QSC at a much lower strain rate. It can be thus concluded that the deformation of YAP nanoparticles is a general phenomenon for PM2000 compressed at room temperature, and that it is not sensitive to the strain rate in the range investigated in the present work (from 10^{-4} s^{-1} to 10^{2} s^{-1}).

5.2.3.6 Discussion

Deformation of YAP nanoparticles

Particles or precipitations are used to strengthen metallic materials by depressing dislocation motion. For metallic materials with second phase precipitation, dislocations can interact with the precipitates in one or two ways [188]. Dislocations either tend to bow around large precipitates and form Orowan loops to pass-by [188], or cut through the precipitates when the size of precipitates is smaller than a critical size [189]. Relatively hard particles such as oxides and carbides in steels are thought to be unable to be sheared by gliding dislocations, and therefore Orowan looping is considered to be the dominant strengthening mechanism [190]. In ODS steels, oxide nanoparticles are generally treated as rigid bodies experiencing only little elastic strain, while plastic deformation is totally neglected for such nanoparticles [191, 192]. Models for the strengthening mechanism and dislocation interaction with oxide nanoparticles are based on this well accepted approach [193]. The present research, however, demonstrates that oxide nanoparticles are actually plastically deformable, and that they are able to sustain high plastic strains during deformation at room temperature, especially those with sizes smaller than 20 nm. Therefore, it is suggested that the previously proposed strengthening mechanism and the mode of dislocation-oxide interaction in ODS steels may not be appropriate, and the deformation of oxide nanoparticle should be taken into account.

In terms of the deformation mechanism of YAP nanoparticles, deformation twinning was observed in the deformed oxide nanoparticles. Twinning is commonly observed in materials with a perovskites structure, such as $BaTiO_3$ [194], $CaTiO_3$ [195], $SrTiO_3$ [196], etc. For orthorhombic perovskites, twin domains that are related by reflection operations with respect to {112} and {110} planes are reported in $MgSiO_3$ [197]and $LaGaO_3$ [198]. Both growth twins and transformation twins are well characterized in these materials, where transformation twins arerelated to changes in pressure and/or temperature [197]. In the current study, deformation twinning with twin boundary along (110) planes is thought to be the dominant mechanism accounting for the plastic deformation of YAP nanoparticles. Mechanical twinning is much less understood compared to transformation twinning in perovskite. Nevertheless, twining along (110) planes of tetragonal perovskite ($BiTiO_3$) was observed after nanoindentation [199], and twinning along (110) planes was found in an orthorhombic perovskite (YAP) after creep tests at 0.82-0.88 T_m [200]. Such a twinning behavior in a bulk perovskite material is very similar to that observed in the deformed YAP nanoparticles. Dislocations with a variety of Burgers vectors were found in the bulk YAP after creep test [200], but they were not observed in the nanoparticles after deformation, mainly as dislocations in perovskite are thought to be mobile only at high temperatures [201, 202].

Size dependent deformation of YAP nanoparticles

Besides the deformation mechanism of YAP nanoparticles, the underlying reason for the pronounced size effect on the deformation of YAP nanoparticles should be explored. Since there is no report on such a size effect for YAP particles, reviews on other materials are supposed to provide clues to rationalize such a phenomenon. It is well documented that a size effect on the strength, plasticity and deformation mechanism of metallic and non-metallic materials has been discovered in several systems [203-206]. For metallic nanopillars and nanoparticles, where dislocation or dislocation/twinning is the dominant deformation mechanism, smaller particles show a higher strength, which is attributed to dislocation source exhaustion [206, 207]. For non-metallic materials, such as Si nanoparticles [208, 209], smaller particles exhibit a higher hardness. In addition to the effect of sample size on strength and hardness, the plasticity is also found to be dependent on the sample size. For Si [210, 211] and SiC[212] with brittle character on macroscopic size, decent ductility was achieved when the sample size is decreasing to the nanometer scale. Chrobak *et al.* [211] claims that a shift from phase-transformation-dominated incipient plasticity to a dislocation driven one when the sample size decreases from the bulk to nanoscale contributes to this size dependent plasticity. Using molecular dynamic simulation, Zhang *et al.* [208] investigated the deformation mechanism of silicon nanoparticles with diameters from 40 nm to 5 nm, a change in deformation mechanism from a phase transformation and dislocation based activity to a phase transformation and amorphization dominated plasticity was reported when the particles size was smaller than 8 nm, which led to a reduced hardness with a decrease of the particle size. Therefore, it can be concluded that both size-dependent strength and plasticity are attributed to the distinct deformation mechanisms operated at different size scales. This may provide a hint to analyze the size-dependent deformation behavior of YAP nanoparticles.

As shown in section 5.2.3.1, YAP nanoparticles with sizes less than 20 nm are substantially deformed after DPD, and smaller particles are deformed to larger strains. It is suggested that this size dependence is related to different deformation mechanisms for particles of different sizes. It has been shown that deformation induced twinning is the dominant deformation mechanism of smaller particles. Due to the fact that particles with size larger than 20 nm were seldom deformed, it is not easy to obtain information on the deformation mechanism for such larger particles. One example showing a slightly deformed YAP particle with a diameter of ~26 nm is presented in Fig. 5.48. It is seen that this YAP particle contains several defects (Fig. 5.48a). An enlarged IFFT image (Fig.5.48b) corresponding to part of in the HRTEM image reveals a deformation-induced boundary. It is seen that the lattice is divided into two parts, and the boundary between them is not straight but zigzagging. The boundary between the two parts is coherent along the plane of $(020)_{YAP}$. The right side of the boundary is determined as YAP with the incident electron beam along $\langle 100\rangle_{YAP}$. However, the left side of the boundary cannot be identified as YAP along any zone axis. After comparing with the all possible yttrium-aluminum oxides, this crystal can be identified as $YAlO_3$ (yttrium aluminum hexagonal, YAH) inspected along its $\langle 221\rangle$ direction. YAH has the same composition as YAP, but has a different crystallographic structure. YAH is thought to be a transformation-induced product from YAP. This transformation is able to accommodate the strain imposed on the nanoparticle. Additionally, this transformation involves a change in the interface between the nanoparticle and the ferrite matrix. In the region between initial$\langle 100\rangle_{YAP}$ and ferrite, the lattice is still coherent with $(220)_{YAP}//(110)_{Fe}$ (Fig. 5.48c), which is identical to the orientation relationship in the undeformed sample. After the transformation, the YAH does not have a coherent lattice with the ferrite matrix anymore (Fig. 5.48d).

Pressure induced phase transformations are common in materials with perovskite structure [213]. For bulk YAP with orthorhombic perovskite structure, several possible pressure induced phase transformations have been examined [214]. It has been demonstrated that phase transformation is an important mode to accommodate the plastic deformation of YAP. Thus, it is suggested that in contrast to smaller particles with sizes less than 20 nm, larger YAP nanoparticles show a deformation-induced phase transformation as a deformation mechanism. This difference in deformation mechanisms may be the reason for the size-dependent deformation behavior of YAP oxide nanoparticles, i.e. that smaller particles are more vulnerable to deformation than larger particles. However, the reason for larger particles to deform by stress-induced phase transformations is still not clear. More detailed characterization by HRTEM and atomic STEM assisted with multiscale modeling required to understand the underlying mechanism.

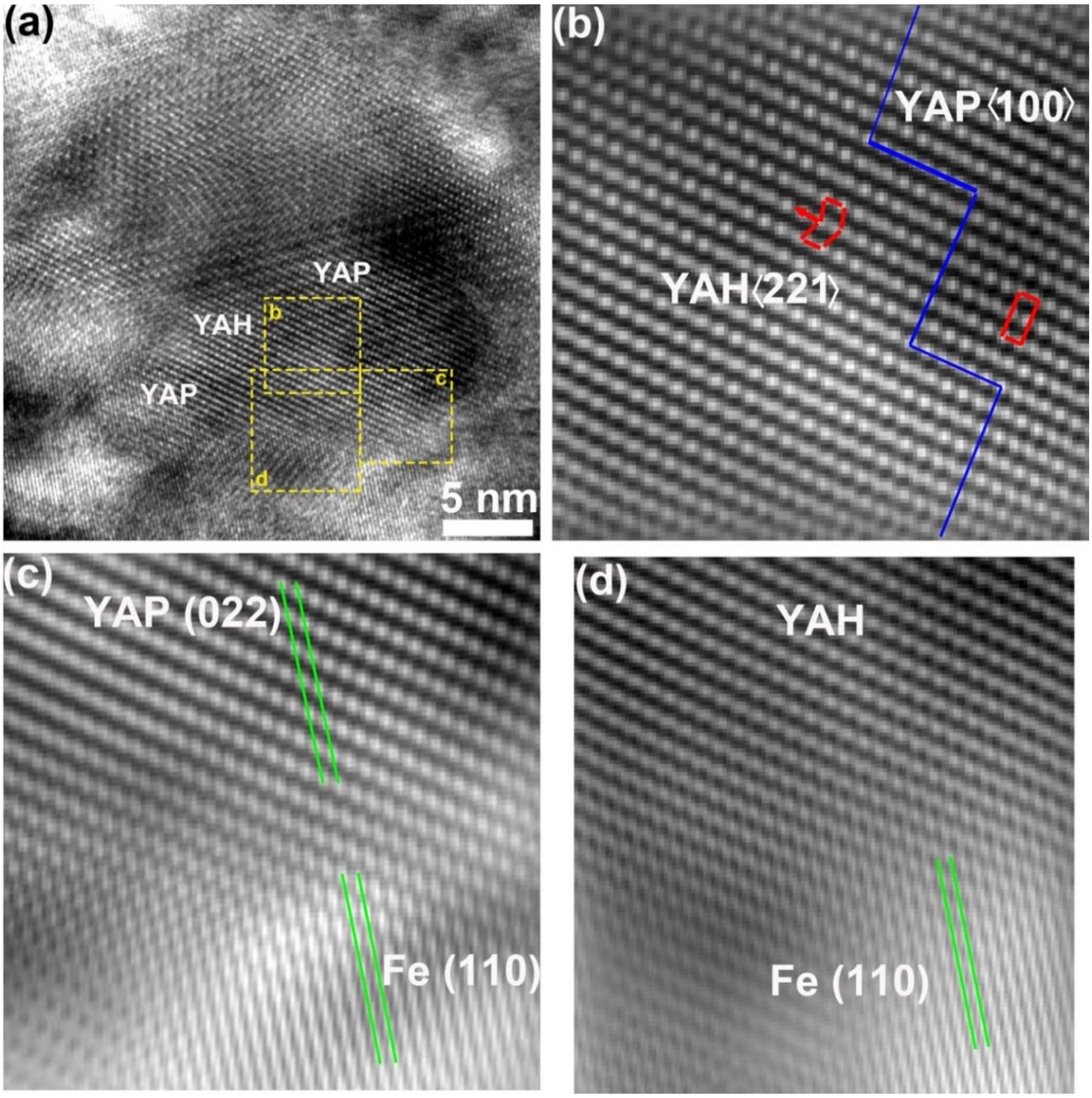

Fig. 5.48 (a) HRTEM image of an oxide nanoparticle after deformation, (b), (c) and (d) are the images corresponding to the enlarged frames of b, c and d in (a). (b), (c) and (d), with noise filtered using the IFFT method, highlight different information: (b) the boundary between $\langle 100\rangle_{YAP}$ and $\langle 221\rangle_{YAH}$ (marked by blue lines) in the interior of the particle; (c) interface between the YAP and the ferrite matrix; (d) interface between the transformed YAH and the ferrite matrix.

Nanovoids at YAP/Fe interface

Voids are found at the YAP and Fe interface after DPD to low strains. Previously, voids formed adjacent to non-metallic particles were reported in steels after rolling at low and high temperatures. From a systematic study of the deformation behavior of MnS in steels [215, 216], Charles *et al.* claimed that the formation of voids around the particle/matrix interface is caused by the inability of the steel matrix to flow around the particles and simultaneously maintain contact with them. If the interfacial strength is not sufficient to withstand the tensile stresses due to the deformation of matrix, decohesion between particles and matrix takes place, thereby forming a conical void at the interface. Waudby *et al* .[217] considered that decohesion is initiated by frictional forces acting tangentially to the surface of the inclusion. Combined with the force imposed by the flow of steel matrix, conical voids are created. Employing finite element method, Luo *et al.* [218] proposed that debonding would occur if the resolved normal stress at the interface reaches a critical value. Despite slight discrepancies in the formation mechanism of voids around non-metallic particles proposed by different researchers, there is a general agreement that it is the local heterogeneous flow due to the discontinuity at the interface between the particles and the matrix that causes the formation of voids. Consequently, the difference in yield stress between particles and matrix is the common reason for void initiation adjacent to the interface.

It is shown in present study that voids in nanoscale generate around YAP nanoparticles during DPD, and that the size of nanovoids is related to the diameter of the related particles. In the as-received PM2000, the ferrite matrix is much softer than the oxide nanoparticles. Therefore nanovoids form adjacent to the particle after DPD to a strain of 0.6. With increasing strain, the ferrite matrix is work hardened, and once the yield stress of the ferrite is comparable to that of the YAP nanoparticles, the particles start to deform simultaneously with the deformation of ferrite by a similar extent. During this process, nanovoids around deformable oxide nanoparticles close, while nanovoids associated with those particles that do not deformed considerably still remain open. A comparison between the strains of YAP nanoparticles and the ferrite matrix could verify this claim. The average strain experienced by the particles (estimated from their shape change) increases with increasing macroscopic strain, remaining always smaller than the imposed macroscopic strain. It should be mentioned that for spherical particles subjected to compression to strains of 1.0 and 2.1, an aspect ratio of 4.5 and 23.3 is expected, respectively. Apparently, the average values obtained for the YAP particles in the present experiment, 0.7 and 1.2, are much smaller than these values.

It should also be mentioned here that the YAP nanoparticles are much smaller than those non-metallic particles in steel (with a micrometer size) investigated for void formation. The formation of voids due to debonding at the oxide/ferrite interface was not expected for ODS steels, since the oxide particles are on the nanoscale and the heterogeneity was supposed to be easily mediated during plastic deformation. However, in the present study nanovoids are observed even around YAP particles smaller than 4 nm. This could be an important factor which deteriorates the ductility of ODS steel if the nanovoids coalesce and form macroscopic cracks, leading to the faster failure.

5.3Annealing behavior of deformed ODS steel

Nanostructured PM2000 is obtained after DPD to a strain of 2.1. The thermal stability of the nanostructured PM2000 is examined as service at elevated temperatures is expected. Besides, understanding of the annealing behavior of the nanostructured ODS steel is important to modify the structure and properties of this material. In addition, because the oxide nanoparticles were substantially deformed, the annealing response of the deformed oxide nanoparticles is of significance. This might be able to provide some insights in the possibilities of tailoring the size, morphology and distribution of the oxide nanoparticles by thermomechanical treatment and thereby altering the mechanical and physical properties. Hence, detailed studies on the microstructure evolution are carried out in this section.

5.3.1 Annealing behavior: ferrite matrix

The Vickers hardness is used to monitor the annealing behavior of the PM2000 after DPD. It is seen from the isochronal annealing curves in Fig. 5.49a that the hardness evolution can be divided into two regions: region I, where softening is slow, which mainly represents recovery; and region II, where recrystallization is the dominant process and the hardness decreases drastically. The transition temperature between these two regions is between 700 °C and 715 °C. The hardness after isothermal annealing at 715 °C shows a similar trend, with an obvious recovery region and a recrystallization region. DPD-processed PM2000 has a much higher hardness of 443 HV1,than the as-received material (332 HV1). However, the thermal stability is dramatically reduced, since the as-received PM2000 only shows considerable softening during annealing for 1 hour at 1150 °C and above. This deteriorated thermal stability is a consequence of the cold deformation, during which a large amount of energy was stored in the material. Orientation maps obtained by EBSD (Fig. 5.50) reflect the microstructure evolution during isothermal annealing.

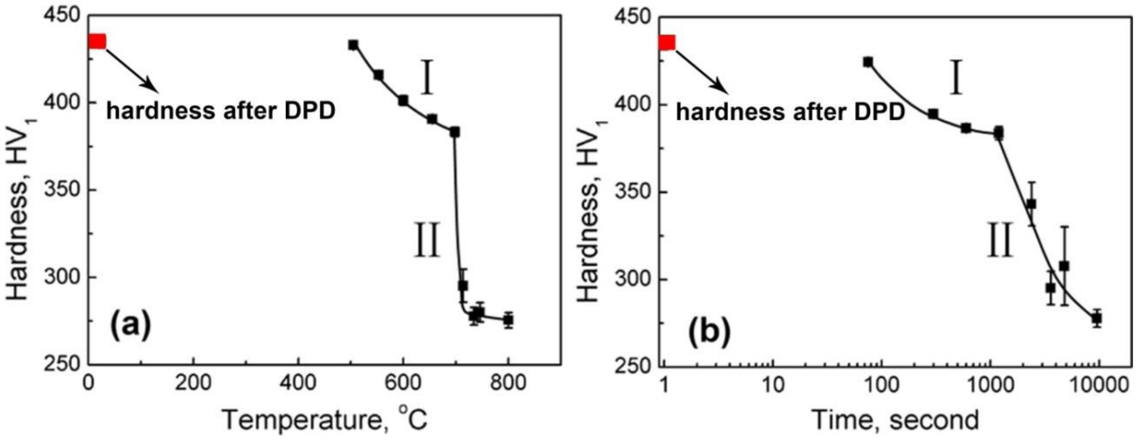

Fig. 5.49 Vickers hardness of the as-received PM2000 after DPD to a strain of 2.1 (a) isochronal annealing for 1 hour at temperatures ranging from 500 °C to 800 °C, and (b) isothermal annealing at 715 °C

It is seen from Fig. 5.50 that after annealing at 715 °C for 10 minutes, the microstructure of DPD-processed samples coarsen, The spacing of boundaries with misorientation angle higher than 2° increases from 76 nm in the DPD sample to 176 nm after annealing. The material is still mainly in recovered state and it contains a very high fraction of LABs (61.8%). Only one recrystallization nucleus is observed in the characterized area, which accounts for 1% of the total area. After annealing for 20 minutes at 715 °C, 68% of the material is recrystallized, and this leads to a significant increase in the boundary spacing ($d_{\theta>2°}$=750 nm, d_{HAB}=1215 nm). After annealing for 80 minutes, the material is almost fully recrystallized (f_{rex}=97%), with the spacing of $d_{\theta>2°}$ and d_{HAB} being 3754 nm and 4320 nm, respectively. Further structural coarsening takes place when the material is fully recrystallized after annealing at 715 °C for 160 min, after which the $d_{\theta>2°}$ and d_{HAB} spacing increases to 6851 nm and 7747 nm, respectively.

In addition to the structural parameters, information about the orientations of the recrystallized grains can be obtained from the orientation maps. It is evident that the majority of the recrystallized grains appear in blue colors, i.e. they have a ⟨111⟩ direction along the CA. To be more specific, the recrystallization nucleus in the Fig. 5.50a is of ⟨111⟩ orientation. In the 68% recrystallized sample, the fraction of ⟨111⟩ oriented recrystallized grains accounts for 72% of the total recrystallized region. In the fully recrystallized sample, ⟨111⟩ oriented grains occupy 67% of the whole sample. This might be a result of a strong oriented nucleation.

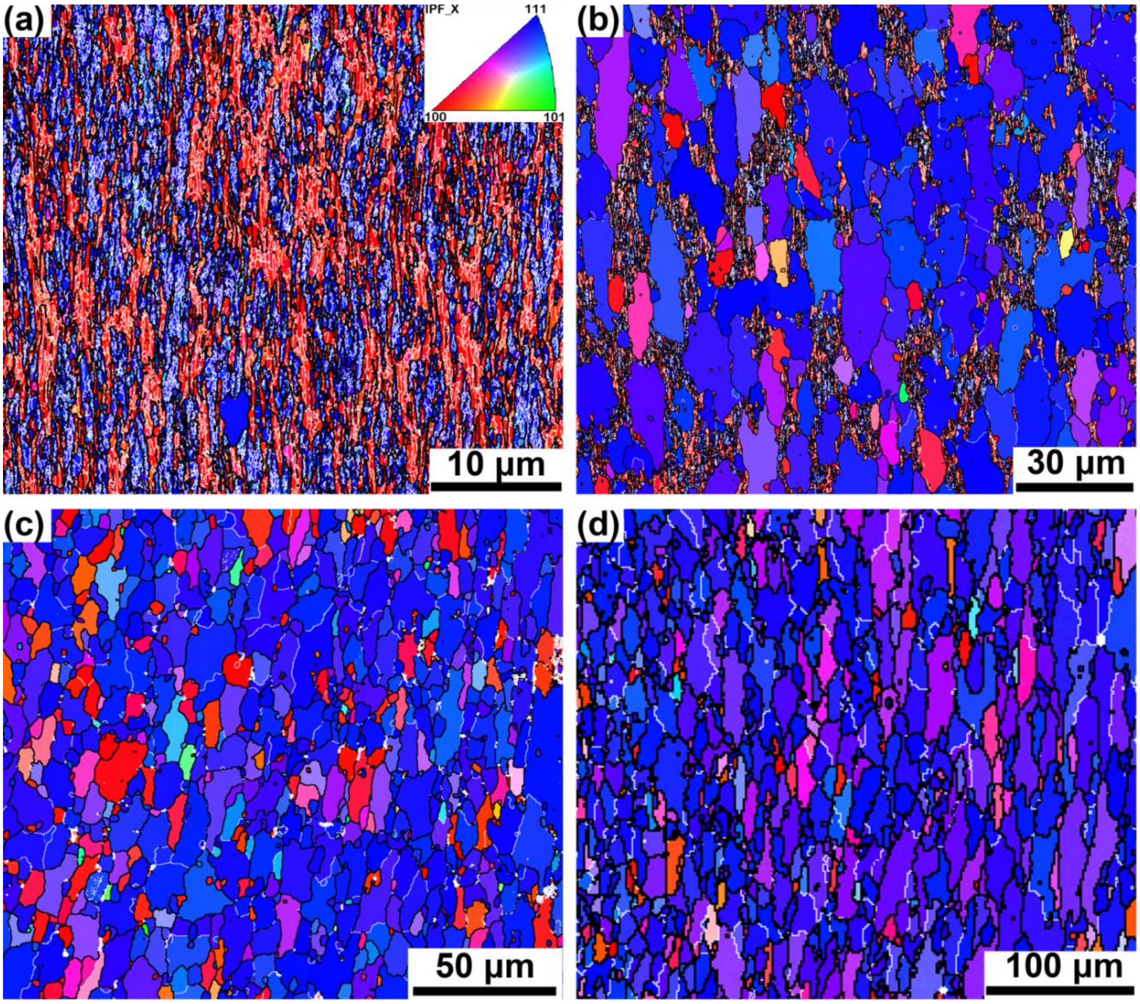

Fig. 5.50 Orientation maps obtained by EBSD for the DPD-processed PM2000 in longitudinal section after isothermal annealing at 715 °C for: (a) 10 minutes, (b) 20 minutes, (c) 80 minutes and (d) 160 minutes. Maps are colored according to the crystallographic direction along the CA using the color code in the inset. LABs and HABs are shown as white and black lines, respectively, and the CA is horizontal.

A TEM image from the sample annealed at 715 °C for 80 minutes is presented in Fig. 5.51. It is seen from Fig. 5.51a that the material is almost fully recrystallized with only a small recovered region. The magnified image in Fig. 5.51b of the framed region reveals a very fine lamellar structure with an average thickness of lamellae of 165 nm, and a high density of dislocations preserved in the deformed remainder of this 97% recrystallized sample.

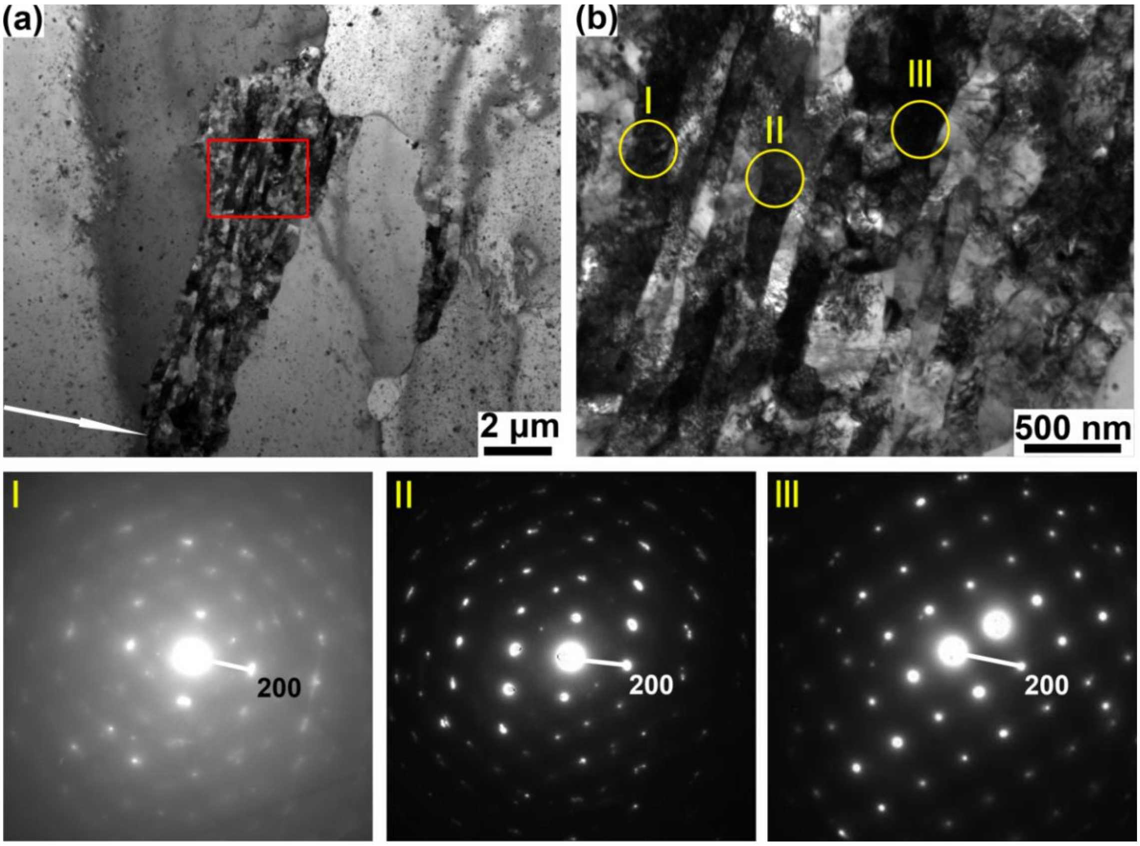

Fig. 5.51 Microstructure of DPD-processed PM2000 in longitudinal section after annealing at 715 °C for 80 minutes: (a) TEM image showing recrystallized grains and a small region still with the deformed microstructure (b) magnified image of the region marked by the red frame in (a). The selected area diffraction patterns presented at the bottom are from the regions with yellow circles I, II, and III. The initial CA is indicated by the arrow in (a).

Selected area diffraction analysis demonstrates that the surviving lamellar structure belongs to the ⟨100⟩ fibre texture component. This indicates that ⟨100⟩ lamellae are very sluggish in recovery and recrystallization, compared to that of ⟨111⟩ lamellae, and that the recrystallization nuclei are reluctant to consume the ⟨100⟩ deformed lamellae during recrystallization. This phenomenon is similar to that observed in the DPD-processed modified 9Cr-1Mo steel, where slow recovery was observed in the ⟨100⟩ lamellae. The difference between both texture components in the partially recrystallized sample, however, is more pronounced in PM2000 compared to the counterpart of modified 9Cr-1Mo steel in Fig. 4.19. The ⟨100⟩ oriented lamellae exhibit much slower recovery in PM2000 (Fig. 5.51) than those in modified 9Cr-1Mo steel (Fig. 4.19). The main difference between these two steels is that PM2000 has well-dispersed oxide nanoparticles, which are strong obstacles for dislocation rearrangement. Therefore, the more pronounced orientation dependence of recovery in PM2000 is attributed to the oxide nanoparticles, which are supposed to exert a strong effect on recovery.

It can be concluded that the recrystallization process in nanostructured PM2000 occurs very similar to that observed in the DPD-processed modified 9Cr-1Mo steel (Chapter 4), in which the ⟨100⟩+⟨111⟩ duplex fibre texture is replaced by ⟨111⟩ fibre texture when the deformed material is recrystallized. It is clear that the DPD-processed both modified 9Cr-1Mo steel and PM2000 steel have strong ⟨100⟩+⟨111⟩ fibre textures, and that both demonstrate a very pronounced orientation dependent recrystallization. The presence of oxide nanoparticles does appreciably affect neither the deformation texture nor the subsequent annealing behavior.

5.3.2 Annealing behavior: oxide nanoparticles

The deformed oxide nanoparticles have undergone substantial plastic deformation, and contain a high defect content and hence high stored energy. Besides, the coherency of the interface between the oxide and matrix was destroyed, and misfit elastic and plastic strains are generated around the interface. The stored energy may act as driving force for changing the oxide nanoparticles during annealing. Detailed characterizations by TEM were carried out to reveal changes of the substantially deformed oxide nanoparticles during annealing.

TEM images in Fig. 5.52 illustrate the morphology of the deformed oxide after annealing at 650 °C for 1 hour. It is seen that the material is mainly recovered with slight a structure coarsening and only a few recrystallization nuclei. No changes of the oxide nanoparticles can be observed in the regions where little structural recovery takes place in the surrounding ferrite matrix (Fig. 5.52b). In the regions with appreciable recovery (Fig. 5.52c), some deformed particles still maintain their shape but a few small nearly equiaxed particles (indicated by red arrows) appear, which are thought to result from deformed disc-shaped particles. In recrystallized grains, many of deformed oxide particles have such a nearly equiaxed shape, with the aspect ratio largely reduced compared to the state after DPD. The diameter of the annealed particles is even smaller than the initial nanoparticles before deformation. Further annealing at higher temperatures provides more clear evidence about the evolution of the deformed oxide nanoparticles during annealing.

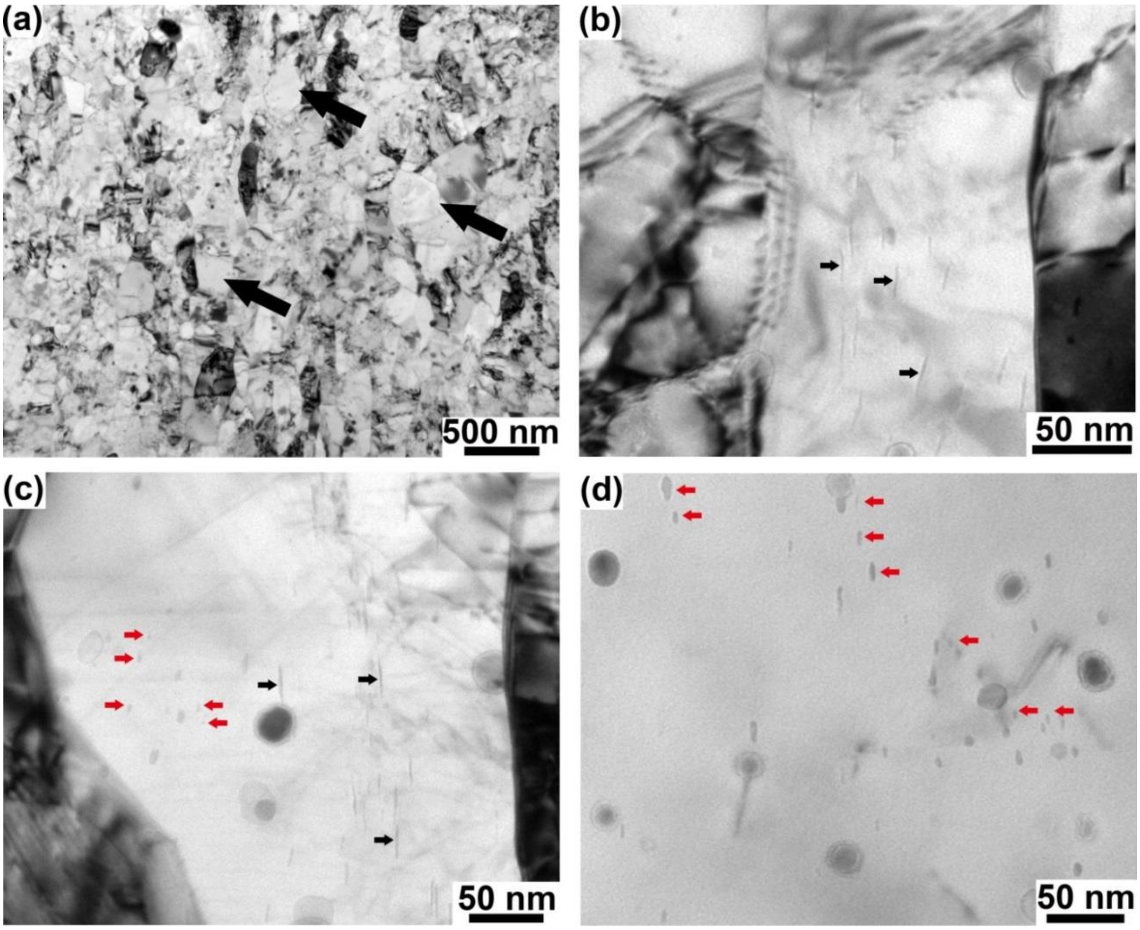

Fig. 5.52 TEM images of the DPD-processed PM2000 in longitudinal section after annealing at 650 °C for 1 hour. (a) TEM image showing mainly a recovered microstructure with a few recrystallization nuclei (indicated by arrows), (b) deformed oxide nanoparticles, indicated by black arrows, in a recovered region, (c) oxide nanoparticles in a region with an extensively recovered microstructure. Deformed oxide nanoparticles which did not change their shape appreciably are marked by black arrows and those which change their shape significantly are marked by red arrows. (d) TEM image inside a recrystallizing grain, some oxide nanoparticles which do not maintain their elongated shape after deformation are marked by red arrows.

After annealing at 750 °C for 1 hour, the DPD-processed PM2000 is almost fully recrystallized, with about 3% unrecrystallized area, as shown in Fig. 5.53a. In the recrystallized grains, the aspect ratio of the deformed oxide decreases significantly, when comparing the oxide nanoparticles in Fig. 5.53b to those in Fig. 5.31. As seen from Fig. 5.53c, some elongated particles have broken into several parts (indicated by white arrows), and some of the separated parts developed into a nearly equiaxed shape (indicated by red arrows). These nearly equiaxed nanoparticles are much smaller than the initial particles. In some regions, there is almost no feature of the deformed oxide nanoparticle retained, and the aspect ratio of these oxide nanoparticles is close to one, similar to that of oxide nanoparticles in the as-received material.

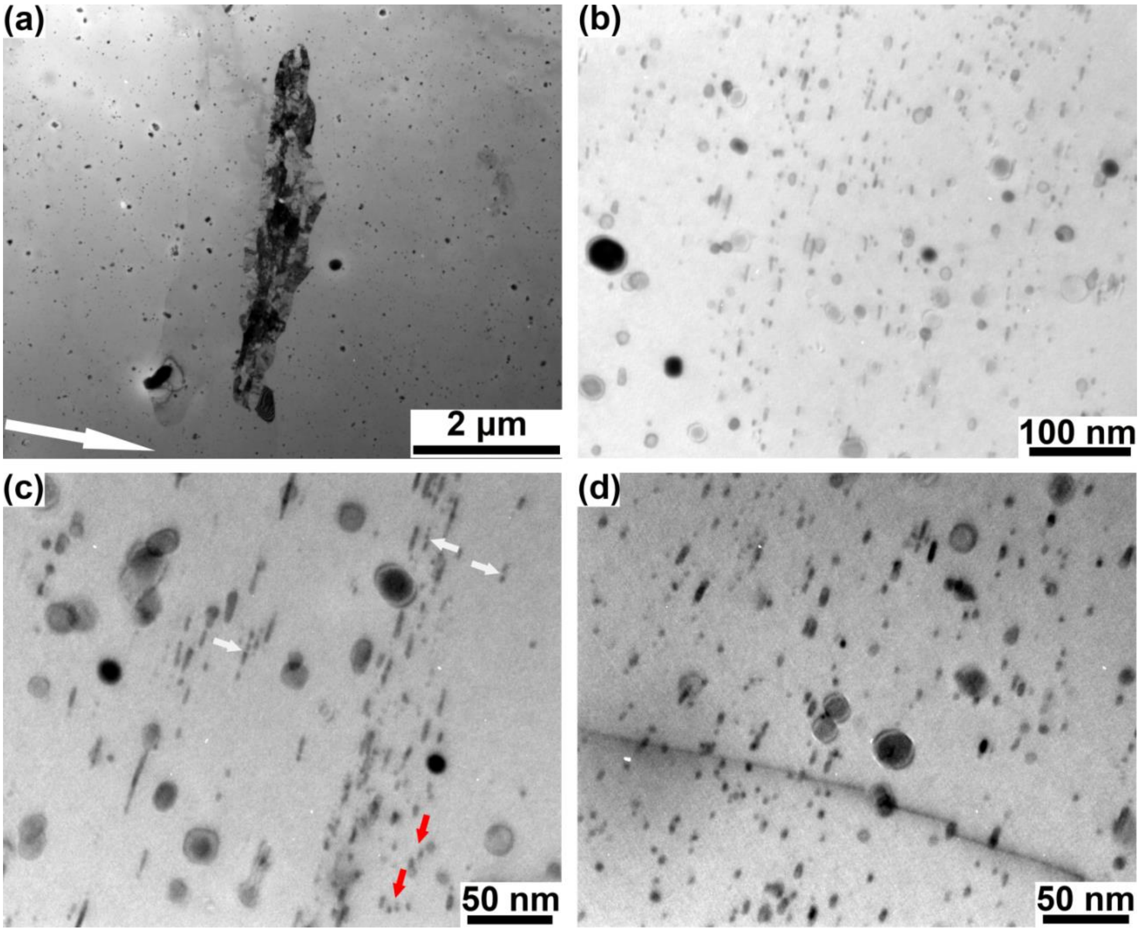

Fig. 5.53 TEM images of the DPD-processed PM2000 in longitudinal section after annealing at 750 °C for 1 hour. (a) TEM image showing almost fully recrystallized material with a small region still in deformed state, (b) TEM image from a recrystallized grain showing the morphology of the oxide nanoparticles, (c) a region where some deformed oxide nanoparticles broken into several parts (indicated by white arrows), or further developed a nearly equiaxed shape (indicated by red arrows), (d) a region with most of deformed oxide nanoparticles alter their shape considerably. The initial CA is indicated by an arrow in (a).

After measuring the Feret's diameters of 650 particles with nearly equiaxed shape in the annealed sample, the size distribution is obtained (Fig. 5.54a). The mean diameter of the oxide nanoparticles is about 7.4 nm, and the fraction of particles with size smaller than 4 nm is about 63%. Comparing with the particle size distribution in the as-received materials (Fig. 5.54b), a significant refinement of the particles is apparent. The mean diameter of the oxide particles decreases from 14.2 nm to 7.4 nm, and more significantly a much narrower size distribution is observed in the sample after DPD and annealing. Oxide particles with sizes in the range of 2 nm to 4 nm represent about 60% of all measured particles. It can be concluded that the oxide nanoparticles are substantially refined after a combination of DPD and subsequent annealing at 750 °C for 1 hour.

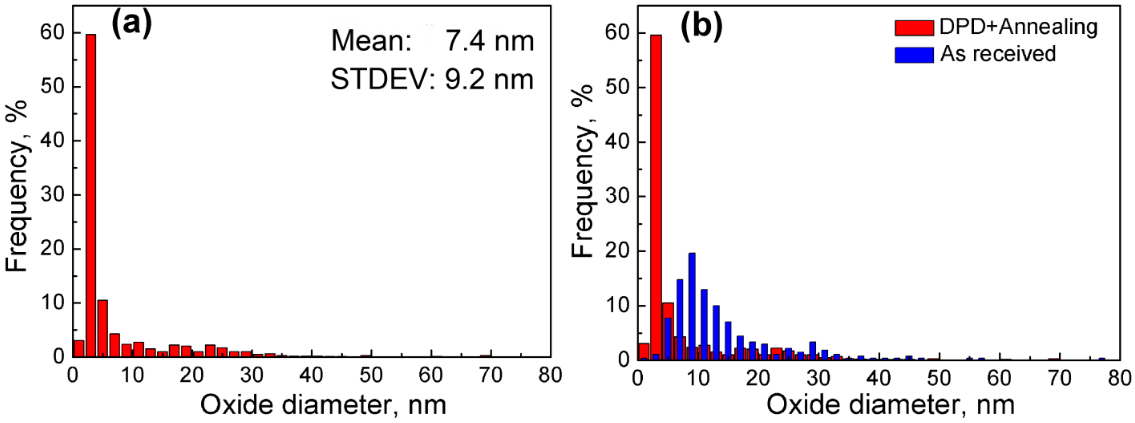

Fig. 5.54 (a) Size distribution of oxide nanoparticles in the DPD-processed PM2000 after annealing at 750 °C for 1 hour and (b) comparison with size distribution of the oxide nanoparticles in the as-received material.

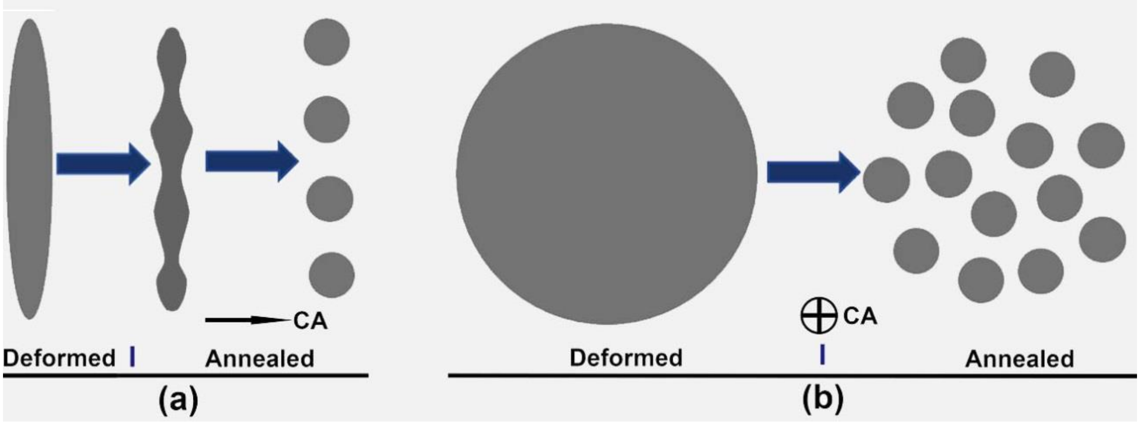

Fig. 5.55 Schematic diagram illustrating the evolution of deformed oxide nanoparticles from a disc to several small nearly equiaxed particles. (a) Diagram showing the evolution from a disc into separated equiaxed fragments, as seen in the longitudinal section of the DPD sample, where CA is horizontal, and (b) diagram showing the evolution from a disc into final small particles viewing along the CA.

The evolution of the deformed oxide nanoparticles during annealing suggests that the deformed disc-shaped oxide nanoparticles are firstly broken into several parts and then those isolated parts evolve into nearly equiaxed shape during further annealing. A series of diagrams in Fig. 5.55 illustrate this process. The deformed oxide nanoparticles have a disc shape. Viewing from the longitudinal section of the DPD-processed sample, the oxide nanoparticles are viewed edge on the discs as needles. They evolve into several smaller particles. If the deformed and annealed samples are imaged along the initial CA (cross section), the deformed oxide nanoparticle should have a pancake shape, while after annealing it should consist of several smaller particles. In this manner, each oxide nanoparticle is transformed into several smaller particles after DPD and annealing, and the number density of the oxide nanoparticles increases compared to that of the as-received sample as observed in Fig. 5.53d.

5.3.3 Discussion on tuning the size of oxide nanoparticles

Al-alloyed ODS steels, like PM2000 and MA956, have better compatibility with dual coolant Pb-Li and He exposures [168-170], compared to those without aluminum. However, compared to those ODS steels with yttrium-titanium oxide as dispersoids, such as MA957, 14YWT, Eurofer, *et al*., the yttrium-aluminum oxide in Al-alloyed ODS steels is somewhat coarser. This is attributed to the fact that titanium is very effective in refining the oxide precipitation, while aluminum does not have such an effect [36, 219]. This drawback of Al-alloyed ODS steels constraints their application as irradiation-tolerant materials, since the irradiation tolerance can be largely enhanced by decreasing the size of oxide particles [1]. Unfortunately, these coarser oxide particles originate from the intrinsic character of composition and structure of the yttrium-aluminum oxide, which means that the size of oxide particles can hardly be refined during the reprecipitation process of fabrication. Therefore, PM2000 and MA956 are thought to be not as promising as other ODS steels for nuclear reactors. By a combination of DPD and annealing, the size of oxide nanoparticles is substantially reduced. Very remarkably, the average diameter of the yttrium-aluminum oxide particles after modification by the proposed approach is around 7 nm, and the fraction of oxide nanoparticles below 4 nm is 63%. Such a size distribution of the oxide nanoparticles is comparable to those in the ODS steels without aluminum where the average size of the oxide nanoparticles is about 5 nm [112]. Our findings provide a novel approach to effectively refine the oxide nanoparticles in Al-alloyed ODS steels and remedy the main drawback of this type of ODS steels, and thereby making these steels very promising for application as an irradiation-resistant material.

For particle strengthening, the finding that smaller particles result in a higher strength at a constant volume fraction is only valid when the particles are undeformable. If particles are deformable, stress and strains at the particle/matrix interface can be easily relived by deformation of the particle, and the corresponding strengthening effect becomes weak. Yttrium-aluminum oxide nanoparticles in PM2000 are demonstrated to be deformable, especially those with a size smaller than 20 nm. This indicates that particle strengthening from these oxide nanoparticles is not as high as expected if all the oxide particles are assumed to be undeformable. For deformable particles at a constant volume fraction, a smaller particle size does not usually result in higher strength, and the strengthening effect from particles attain a maximum at a certain critical particle size [32]. The present studies show that annealing at high temperatures could be used to modify the size of oxide nanoparticles in PM2000. For instance after annealing at 1300 °C for 100 hours, the fraction of the oxide nanoparticles with size smaller than 20 nm is largely reduced (from 81% to 26%). Thus the particle size could be tailored by annealing to achieve an optimized strengthening effect from the oxide nanoparticles when a higher strength is the desired property.

5.4 Summary

In this chapter, the ferrite matrix, oxide nanoparticles, and the interface between oxide nanoparticles and the ferrite matrix in a ferritic ODS steel, PM2000, were investigated in the as-received, DPD-processed, and subsequent annealed conditions. The main findings can be summarized as follows:

1. The oxide nanoparticles in the as-received PM2000 are identified as $YAlO_3$ with an orthorhombic perovskite (YAP) structure. The interface between YAP and Fe is coherent, with an orientation relationship of $(110)_{Fe}//(220)_{YAP}$ and $\langle 001\rangle_{Fe}//\langle 001\rangle_{YAP}$.
2. YAP nanoparticles are found to be very stable, and no considerable coarsening is observed in the sample during annealing below 1300 °C. The interface lost coherency during annealing at 1200 °C for 1 hour, since the ferrite matrix dramatically coarsens but no change of the oxide nanoparticles is observed. Coarsening of YAP nanoparticles commence in the sample during annealing at 1300 °C, and after annealing at 1300 °C for 10 hours the orientation relationship changes to $(110)_{Fe}//(200)_{YAP}$ and $\langle 100\rangle_{Fe}//\langle 202\rangle_{YAP}$.
3. Nanoscale ⟨100⟩ and ⟨111⟩ lamellae form in the as-received PM2000 after DPD to a strain of 2.1. In the ⟨100⟩ oriented sample with a large grain size, very fine

⟨111⟩lamellae with widths down to 40 nm form in the interior of the ⟨100⟩ matrix, leading to a lamellar structure with alternating ⟨100⟩ and ⟨111⟩ oriented lamellae. These newly formed ⟨111⟩ lamellae have nearly identical orientation, and share a common [110] pole with the ⟨100⟩ matrix. This common pole is perpendicular to the CA. The boundaries between these two lamellae have tilt character, with a misorientation of 54.7°[110]. The formation of this novel structure is thought to be due to the preference in selecting certain slip systems from slip systems of the same Schmid factor.

4. Oxide nanoparticles with diameters less than 20 nm are substantially deformed after DPD to a strain of 2.1, whereas for larger dispersoids no deformation is observed. Mechanical twinning is found to be the main deformation mechanism for the smaller oxide nanoparticles. The deformation of oxide nanoparticles is found to be independent of the imposed strain rate and the coherency between the YAP nanoparticles and ferrite matrix.
5. Nanosize voids form at the interface of YAP and Fe during DPD to a small strain, because of the heterogeneous plastic flow between them. Most voids around the nanoparticles with sizes smaller than 20 nm are closed after DPD to high strain, due to the deformation of nanoparticles at large strains, whereas voids around the undeformed particles are still open after DPD to a strain of 2.1.
6. Pronounced orientation dependent recrystallization behavior is observed in the DPD-processed PM2000 during annealing. Similar to that of DPD-processed modified 9Cr-1Mo steel, the ⟨100⟩+⟨111⟩ duplex fibre texture is replaced by a dominant ⟨111⟩ fibre texture after full recrystallization. Advantages in recovery and nucleation of recrystallization grains in the ⟨111⟩ oriented lamellae, are thought to be the main reason for this orientation dependent phenomenon.
7. The deformed oxide nanoparticles change their morphology during annealing. Driven by minimizing the interfacial energy, the disc-shaped YAP nanoparticles break up into smaller parts and shrink to a nearly equiaxed shape during annealing at 750 °C for 1 hour, which leads to a substantial refinement and hence an increase in the number density of the YAP nanoparticles, compared to those in the as-received PM2000. Specifically, the average size of the oxide nanoparticles is reduced from 14.2 nm to 7.4 nm, where 63% of oxide nanoparticles have size smaller than 4 nm after DPD and annealing. These findings provide a promising approach to refine the size of oxide dispersoids in Al-alloyed ODS steels by thermomechanical treatment.

Chapter 6

General comparison: deformation microstructure and annealing behavior

In this chapter, a general comparison between the modified 9Cr-1Mo steel and PM2000 with respect to the DPD induced microstructure, the mechanical properties and their evolution during annealing is presented to provide an overview of the effect of microstructural parameters on the mechanical behavior and thermal stability of these steels as candidate materials for nuclear reactors.

6.1 DPD-induced microstructure and mechanical properties

The similarities between the DPD processed modified 9Cr-1Mo steel and PM2000 are: 1) nanoscale lamellar structures developing after high strains; 2) pronounced ⟨100⟩+⟨111⟩ duplex fibre texture after deformation; 3) pronounced orientation dependence of recrystallization leading to a very strong ⟨111⟩ fibre texture after recrystallization.

Table 6.1 summarizes the microstructural parameters and the strength of the modified 9Cr-1Mo steel and PM2000 prior to and after DPD to high strains. The modified 9Cr-1Mo steel has a much coarser initial structure than PM2000, with both LAB and HAB spacings about 3 times larger in the former material.

Table 6.1 Microstructural parameters ($d_{\theta>2°}$, d_{HAB} and f_{HAB}) obtained from EBSD data, and ultimate tensile strength (UTS) of the modified 9Cr-1Mo steel and PM2000 in the as-received (AR) condition and after DPD to high strains

Condition	Microstructure	$d_{\theta>2°}$, nm	d_{HAB}, nm	f_{HAB}, %	UTS, MPa
9Cr-1Mo: AR	Tempered martensite	1110	2430	46	675±6
9Cr-1Mo: DPD 2.3	⟨100⟩+⟨111⟩ lamellae	111	200	50	1247±16
PM2000: AR	Ferrite and dispersoids	368	754	44	932±5
PM2000: DPD 2.1	⟨100⟩+⟨111⟩ lamellae	76	136	43	1553±12

After DPD to high strains, the difference in the boundary spacing of these two steels is reduced. The ultimate tensile strength of the modified 9Cr-1Mo steel and PM2000 increases by a factor of 1.8 and 1.7, respectively, due to DPD. The fraction of HABs in both DPD-processed materials is similar, 43 and 50% (see Table 6.1). The smaller boundary spacing and higher tensile stress of the DPD-processed PM2000 compared to the modified 9Cr-1Mo steel is attributed to two factors: one is the finer initial structure of PM2000, and another is the presence of well-dispersed oxide nanoparticles in PM2000, which suppress dynamic recovery and thus leads to a smaller saturation value for the boundary spacing.

6.2 Thermal stability and annealing behavior

Even though the modified 9Cr-1Mo steel and PM2000 have either carbides or oxide nanoparticles as stabilizers of the microstructure, the thermal stability of both steels is largely reduced after nanostructuring by DPD, due to the very high stored energy in the form of a high density of dislocations and deformation-induced boundaries. Fig. 6.1 shows the Vickers hardness of the DPD processed modified 9Cr-1Mo steel and PM2000 during isochronal annealing for 1 hour at different temperatures. Although PM2000 has a much finer deformation structure and higher hardness, its hardness drops less drastically than that of the modified 9Cr-1Mo steel. This is attributed to a pinning effect from the oxide nanoparticles hindering GB migration. Significant softening accompanying the onset of recrystallization takes place at 700 °C and above for PM2000, while for the modified 9Cr-1Mo steel recrystallization occurs already at 625 °C. Thus, both DPD-processed steels do not remain nanostructured at these elevated temperatures and do not maintain their properties at the level desired for application in nuclear reactors (650 °C and above).

From Fig. 6.1 it is evident that the dependence of Vickers hardness on temperature is quite different for the modified 9Cr-1Mo steel and PM2000. To be more specific, the hardness decrease of PM2000 can be divided into two distinct regions. Below 700°C, the hardness decreases only slightly; whereas a very sharp drop occurs at temperatures above 700 °C. The lower temperature region corresponds to recovery of the deformed microstructure, while the high temperature region corresponds to recrystallization. For the modified 9Cr-1Mo steel, the recrystallization induced softening (above 625 °C) is less drastic than for PM2000 and, therefore, the transition between the two softening stages is less distinct. This indicates that these two nanostructured steels behave somewhat differently during recovery and recrystallization.

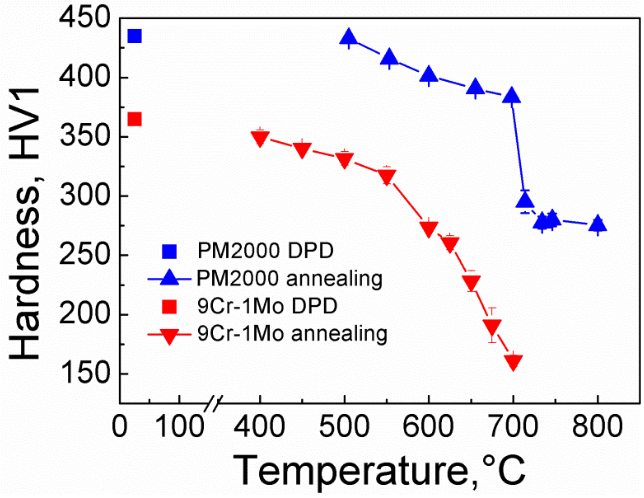

Fig. 6.1 Vickers hardness of the modified 9Cr-1Mo steel and PM2000 after deformation by DPD to strains of 2.3 and 2.1 (, respectively, and after isochronal annealing at different temperatures for 1 hour.

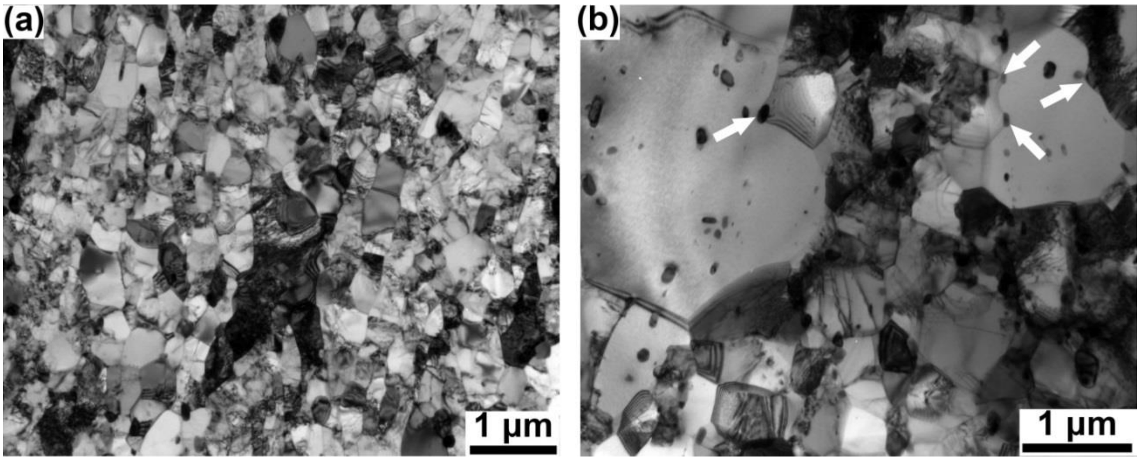

Fig. 6.2 TEM images from the longitudinal section of modified 9Cr-1Mo steel deformed by DPD to a strain of 2.3 after annealing for 1 hour at (a) 600 °C and (b) 650 °C. Recrystallizing grains with cusped boundaries at particles (indicated by arrows)

These differences are also reflected in the microstructure. The recovered structure of the modified 9Cr-1Mo steel after annealing at 600 °C for 1 hour (Fig. 6.2a) contains subgrains with relatively clean interiors (a low dislocation density), whereas PM2000 annealed at 600 °C for 1 hour still contains a very fine lamellar structure (Fig. 6.3a) with a high dislocation density. After annealing at 650 °C for 1 hour, the lamellar microstructure of PM2000 is transformed into a subgrain structure, but the dislocation density is still very high. This indicates that annihilation of dislocations and their rearrangement into subgrain boundaries is more sluggish in the DPD-processed PM2000 than in the modified 9Cr-1Mo steel, which is attributed to a pinning effect from the well-dispersed oxide nanoparticles. Once recrystallization nuclei form, their boundaries can migrate at a very high rate resulting in rapid recrystallization and a drastic reduction in hardness. For the modified 9Cr-1Mo steel, however, the motion of grain boundaries during recrystallization is retarded by the relatively large carbides (as shown in Fig. 6.2b), and therefore the recrystallization is less rapid. This is consistent with the notion that very fine particles are effective in pinning dislocations, but large particles are strong obstacles for boundary migration.

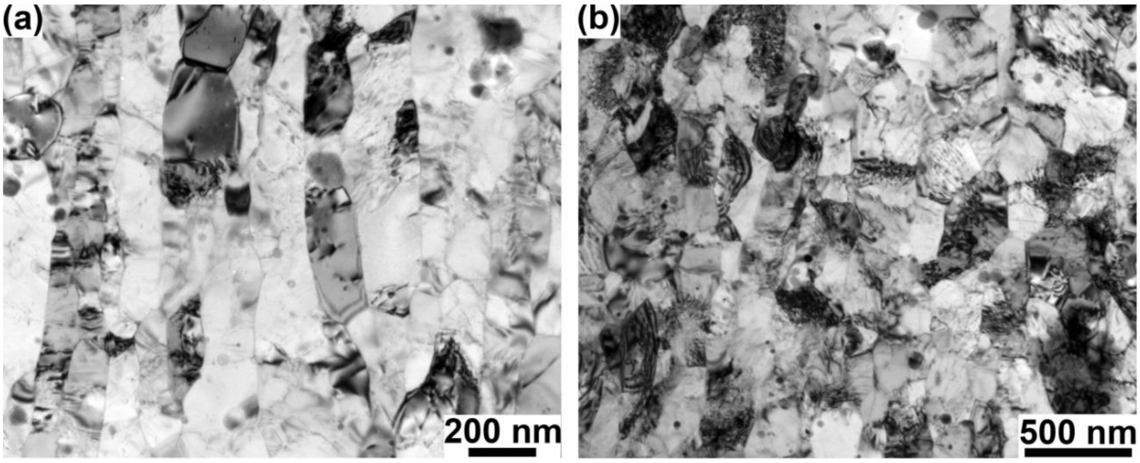

Fig. 6.3 TEM images from the longitudinal section of PM2000 deformed by DPD to a strain of 2.3 after annealing for 1 hour at (a) 600 °C and (b) 650 °C.

A pronounced effect of the oxide nanoparticles on recovery is indirectly reflected in the orientation dependent recrystallization process, since the formation of recrystallization nuclei can be retarded due to the sluggish recovery. As shown in Fig. 5.51, PM2000 is almost fully recrystallized (98%), but several isolated ⟨100⟩ regions are still showing a nanoscale lamellar structure and have not undergone recrystallization. Fig. 6.4 highlights this phenomenon in three examples. Some regions with the ⟨100⟩ fibre texture still contain lamellar remnants of the deformation microstructure. Other recrystallizing grains of the ⟨111⟩ fibre texture component have not grown into these lamellae. It is evident that the boundaries between these survived lamellar regions and recrystallizing grains (marked by yellow dash lines) form very pronounced retrusions (see Fig. 6.4), especially in Fig. 6.4c, where the isolated ⟨100⟩ oriented deformation structure is embedded in one well recrystallized grain. Interestingly, a very high dislocation density is also evident in these preserved ⟨100⟩ lamellae (Fig. 5.51b and Fig. 6.4), which means that even recovery rarely happens in these regions.

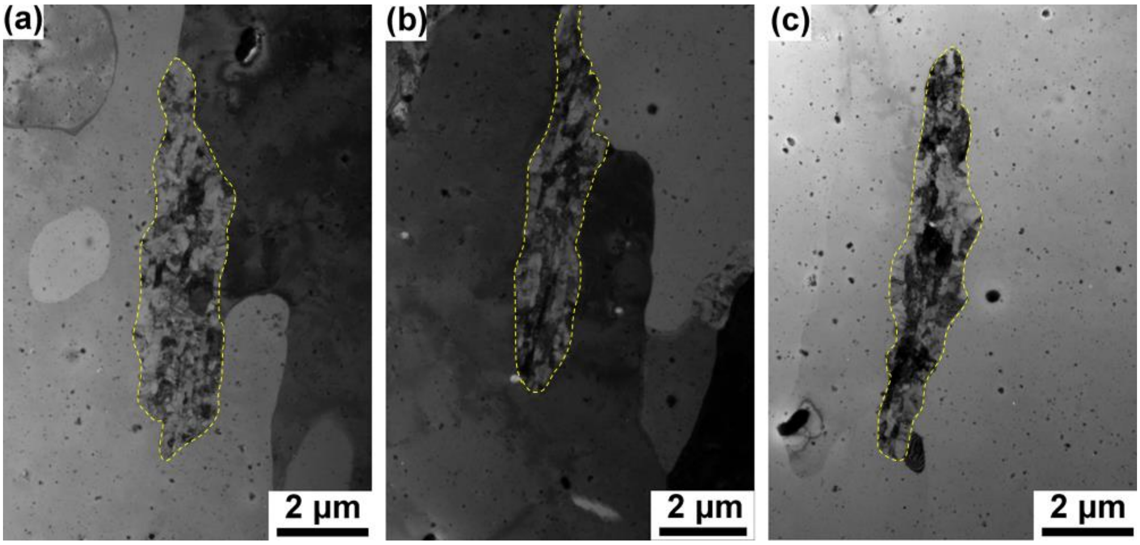

Fig. 6.4 TEM images from the longitudinal section of the DPD-processed PM2000 with a strain of 2.1 and after annealing at 750 °C for 1 hour. Regions with ⟨100⟩ directions along the CA are still in deformed state. The boundaries between these regions and the recrystallizing grains are marked in yellow dash lines.

As proposed in Chapter 4, the differences in recovery within the dominant components of the compression texture are responsible for the different recrystallization kinetics for the ⟨100⟩ and ⟨111⟩ oriented structures, namely that faster recovery within the ⟨111⟩ oriented regions results in preferential formation of ⟨111⟩ recrystallization nuclei in the modified 9Cr-1Mo steel (see Fig. 4.23 and Fig. 4.24). The difference in the recovery and nucleation behavior of the ⟨100⟩ and ⟨111⟩ oriented regions seems to be much more pronounced in the DPD-processed PM2000. In general, recovery can involve dislocation rearrangement, short-range boundary migration and subgrain coalescence. The well-dispersed oxide nanoparticles are suggested to impose considerable constrains on this process, and to retard recovery of the ⟨100⟩ oriented regions in DPD-processed PM2000. This is suggested to be the cause that survived ⟨100⟩ structure in the largely recrystallized sample rarely experiences recovery. The reason accounting for the slow migration of the recrystallizing grain boundaries into the ⟨100⟩ oriented regions, even though these regions may have higher stored energy and the boundaries between them have a preferential geometry for moving remains unclear.

In summary, the deformation structures and textures of the DPD processed modified 9Cr-1Mo steel and PM2000 are generally similar. The somewhat finer structure of the PM2000 after DPD is mainly attributed to the well-dispersed oxide nanoparticles. Orientation dependence of recrystallization is also similar in both materials after DPD, however, the presence of oxide nanoparticles in PM2000 appears to retard the recovery, which leads to more pronounced differences between the ⟨100⟩ and ⟨111⟩ oriented structures in the annealed PM2000 than in the annealed modified 9Cr-1Mo steel. These results indicate that a combination of both small and large particles, where the small particles are effective in stabilizing the dislocation structure and the large particles prevent grain boundary migration, might be beneficial for achieving higher thermal stability in particle strengthened materials.

Chapter 7

Summary, conclusions and perspectives

In this study, two promising candidate materials — a modified 9Cr-1Mo ferritic/martensitic steel and a PM2000 ODS steel—have been processed and studied with respect to their deformation-induced microstructures and their annealing behaviors. The main objective of the present work s to obtain a nanostructure in these two steels by DPD, to evaluate their propensity to be used at elevated temperatures, and to provide new insights into possible way to tailor their microstructure and properties by thermomechanical treatments. The main findings of this study and conclusions are summarized in this chapter.

Deformation-induced microstructure and annealing behavior: ferrite matrix

1) Nanoscale lamellar structures with a pronounced ⟨100⟩+⟨111⟩ duplex fibre texture along the CA develop in both the modified 9Cr-1Mo steel and PM2000 after DPD to a strain of 2.3 and 2.1, respectively. The modified 9Cr-1Mo steel is transformed from a martensitic structure into a typical lamellar structure with a lamellar boundary spacing of 98 nm along CA; PM2000 is refined from a nearly equiaxed ferritic structure of submicron grain size to a lamellar nanostructure with a lamellar thickness of 72 nm. No considerable difference is observed in the deformation texture of these two steels.

2) For annealed PM2000 having coarse grains with crystallographic ⟨100⟩ directions along the CA, very narrow ⟨111⟩ lamellae with a width down to 40 nm form in the interior of ⟨100⟩ grains after DPD to a strain of 2.1, which results in alternating ⟨100⟩ and ⟨111⟩ oriented lamellae. These newly formed ⟨111⟩ lamellae all have nearly identical orientation, and share a common [110] pole with the ⟨100⟩ matrix. This common pole is perpendicular to the CA.

3) Whereas the tensile strength of both nanostructured steels is largely improved compared to their counterparts prior to deformation, the thermal stability of the DPD-processed materials is reduced. Annealing at 600 °C and above leads to structural coarsening and mechanical softening. After recrystallization, the ⟨100⟩+⟨111⟩ duplex texture is replaced by a strong ⟨111⟩ fibre texture. Detailed characterization and analysis of the DPD-processed modified 9Cr-1Mo steel

demonstrates that both oriented nucleation in the ⟨111⟩ oriented lamellae and oriented growth of the ⟨111⟩ oriented recrystallizing grains contributes to the strong recrystallization ⟨111⟩ texture. It is found that after annealing at 600 °C for 1 hour, the ⟨111⟩ oriented regions are transformed into nearly equiaxed subgrains, whereas subgrains in the ⟨100⟩ oriented regions are still elongated. The structure with equixed subgrains is more prone to form recrystallization nuclei. This different annealing behavior between ⟨100⟩ and ⟨111⟩ oriented lamellae is attributed to a much higher stored energy in the ⟨111⟩ oriented lamellae. Based on the extended Cahn-Hagel method, it is found that growth rates of the ⟨111⟩-oriented recrystallizing grains are higher in the beginning of recrystallization. The underlying mechanism is suggested to be related to two phenomena: ⟨111⟩ and ⟨100⟩ oriented recrystallizing grains nucleate within the ⟨111⟩ and ⟨100⟩ oriented lamellar regions, respectively; the ⟨111⟩ oriented recrystallizing grains have better conditions for growth since they are surrounded by nearly equiaxed subgrains. The recrystallization behavior of DPD-processed PM2000 can be rationalized in a similar way. However, due to the presence of well-dispersed oxide nanoparticles, PM2000 shows an even more sluggish recovery in the ⟨100⟩ oriented lamellae than that of the modified 9Cr-1Mo steel.

Deformation-induced microstructure and annealing behavior: oxide nanoparticles

4) The majority of oxide nanoparticles in the as-received PM2000 are $YAlO_3$ with orthorhombic perovskite (YAP) structure. The interface between YAP and Fe is coherent in the as-received material, with an orientation relationship of (110)Fe//(220)YAP and ⟨001⟩Fe//⟨001⟩YAP (cube-on-cuboid). YAP nanoparticles are thermally quite stable, and no considerable coarsening takes place during annealing at temperatures below 1300 °C. The interface coherency is however lost during annealing at 1200 °C for 1 hour since the ferrite matrix coarsens dramatically, but neither size, nor morphology of the YAP particles change. Coarsening of YAP nanoparticles is observed in the sample after annealing at 1300 °C. The orientation relationship changes to (110)Fe//(200)YAP and ⟨100⟩Fe//⟨202⟩YAP (pseudo-cube-on-cube) after annealing at 1300 °C for 10 hours.

5) Oxide nanoparticles with diameters less than 20 nm are substantially deformed during DPD to a strain of 2.1, whereas for larger particles no appreciable

deformation is revealed. It is suggested that (110) $\langle 1\bar{1}2\rangle$ mechanical twinning is the main deformation mechanism for the YAP nanoparticles smaller than 20 nm. The deformation of oxide nanoparticles occurs later than the deformation of the surrounding ferrite matrix. Considerable deformation of particles occurs in the sample during DPD to a strain of 0.6 and above. In the sample after DPD to a strain of 2.1, the mean equivalent strain of oxide nanoparticles is only 1.2. Due to heterogeneous flow between the YAP nanoparticles and ferrite matrix, nanovoids form at the interface of YAP and Fe at a low strain. Most voids around the nanoparticles smaller than 20 nm close after DPD to high strain, due to deformation of the nanoparticles at high strains. On the other hand, voids around the undeformable particles are still open after DPD to a strain of 2.1. As proven by the experiments, the deformation behavior of oxide nanoparticles and its co-deformation with the ferrite matrix are independent of the imposed strain rate and the interfacial coherency between the YAP nanoparticles and ferrite matrix.

6) The deformed oxide nanoparticles change their morphology significantly during annealing. To minimize the interfacial energy, disc-shaped YAP nanoparticles break up into smaller fragments and become nearly equiaxed during annealing at 750 °C for 1 hour, which reduces the average size of the YAP nanoparticles and leads to an increase in the their number density as compared to the as-received condition. Specifically, after DPD to strain of 2.1 and subsequent annealing at 750 °C for 1 hour the average size of the oxide nanoparticles is reduced from 14.2 nm to 7.4 nm, and 63% of oxide nanoparticles are smaller than 4 nm.

Based on the above findings, some suggestions for future work are proposed:

1) More detailed analysis of recovery in materials with ⟨100⟩ + ⟨111⟩ fibre texture

Both DPD-processed modified 9Cr-1Mo steel and PM2000 exhibit very pronounced orientation dependent recovery and recrystallization behavior. Experimental results suggest that the preference in the recovery of the ⟨111⟩ oriented lamellae contributes to advantageous formation of ⟨111⟩ oriented nuclei and their subsequent growth. However, the reason for this oriented recovery and nucleation is still unclear. More experimental work to study recovery of ⟨111⟩ and ⟨100⟩ oriented structures should be done, e.g. by using in-situ characterization to provide direct evidence. Understanding of the mechanism controlling the orientation dependency of recovery and recrystallization is not only important for compressed *bcc* metals and alloys, but also for the *bcc* materials annealed after rolling, since the oriented nucleation in ⟨111⟩ fibre component is very pronounced in rolled materials as well.

2) Nanoscale lamellar structure formed in the coarse-grained PM2000

Very fine lamellar structure with alternating ⟨100⟩ and ⟨111⟩ lamellae are produced in coarse grained PM2000 after DPD to a high strain. The annealing behavior of this structure is very interesting. As seen from the preliminary result in Fig. 7.1, after annealing at 900 °C for 1 hour recrystallization takes place only in the interior of the ⟨111⟩ lamellae. The lamellar boundaries between the ⟨100⟩ and ⟨111⟩ bands are preserved after annealing, which indicates that these boundaries are relatively stable. This structure is of high scientific interest in terms of both the formation mechanism and annealing behavior, which should be explored in more detail. Due to the fact that this lamellar structure is quite stable, it might be interesting to evaluate the irradiation performance of this material.

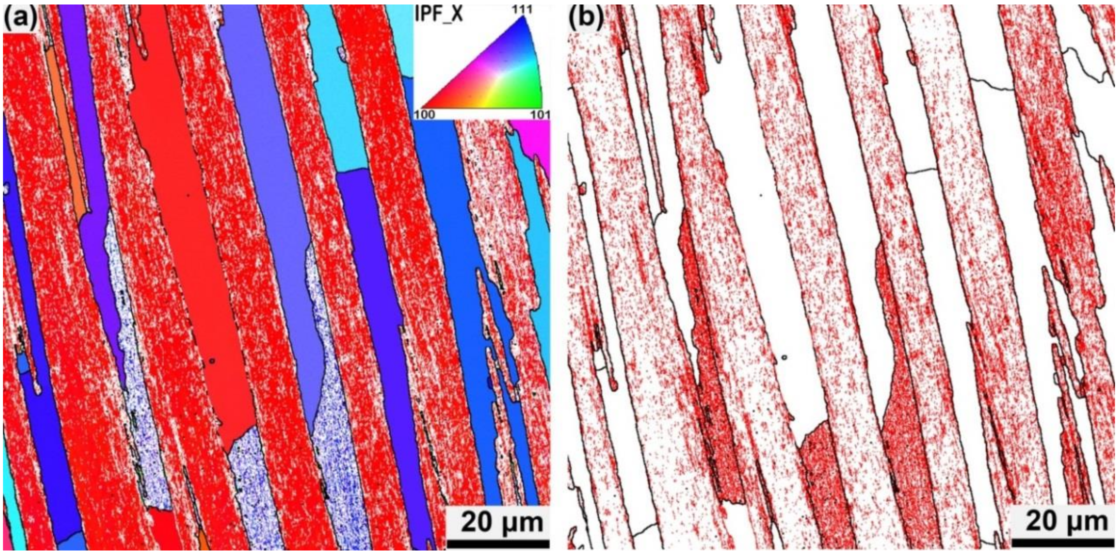

Fig. 7.1 Microstructure from the longitudinal section of coarse-grained PM2000 deformed by DPD to a strain of 2.1 after annealing at 900 °C for 1 hour. (a) Orientation map colored according to the crystallographic direction along the CA using the color code in the inverse pole figure (see the inset). Black and white lines represent HABs and LABs, respectively; (b) Boundary map from the same region as (a), with black and red lines representing HABs and LABs, respectively. Large white regions in (b) are recrystallized grains.

3) Deformation of oxide nanoparticles and its size dependence

The plastic deformation of YAP nanoparticles in the Al-alloyed ODS steels is of significance, with regard to the processing of these steels by deformation and understanding the strengthening mechanism of ODS steels. Deformation induced twinning is suggested to be the main mechanism for the deformation of YAP nanoparticles, but the reason for the size dependent deformation behavior is not clear. Further characterization by STEM with atomic resolution and atomic scale modeling should be carried out to reveal the deformation-induced defects and structures, and to better understand the deformation mechanism.

4) Thermomechanical treatment to refine oxide nanoparticles

The irradiation tolerance of ODS steels typically improves with decreasing size of oxide dispersoids. Therefore, many efforts have been dedicated to produce ODS steels with nanoscale oxide particles. In Al-alloyed ODS steels oxide particles are much coarser than those in the Ti-alloyed ODS steels, which makes Al-alloyed ODS steel less applicable as irradiation-resistant materials. The present study opens a novel approach, namely employing DPD and subsequent annealing, by which the yttrium aluminum oxide can be substantially refined and their homogeneity can be enhanced to a large extent. Since DPD can only produce small laboratory samples, further experiments should be conducted using an industrial deformation process, e.g. cold rolling. It is also necessary to investigate how size distribution of particles can be controlled by combinations of plastic deformation and annealing. Finally, the irradiation performance and mechanical properties of materials produced using this new approach should be characterized in detail.

Appendix I Calculation of heating during compression

1. Solution of diffusion equation

The function $u(x,t)$ that describes the temperature at a given location (x), can be expressed as:

$$u(x,t) = \int_0^t ds \int_{-\infty}^{\infty} dy \, \frac{p(y,s)}{2\sqrt{\pi(t-s)}} \exp\left(-\frac{(x-y)^2}{4(t-s)}\right) \tag{I.1}$$

where p(y,s) is the source term. For cylindrical sample with diameter of L under compression at constant strain rate the source term is constant across the sample. Then Eq(I.1) can be expressed as:

$$u(x,t) = p\int_0^t ds \int_{-L/2}^{L/2} dy \, \frac{1}{2\sqrt{\pi(t-s)}} \exp\left(-\frac{(x-y)^2}{4(t-s)}\right) \tag{I.2}$$

2. Heat equation

$$\frac{\partial T}{\partial t} - \frac{\kappa}{\rho c_p}\frac{\partial^2 T}{\partial x^2} = \frac{\dot{q}}{\rho c_p} \tag{I.3}$$

With scaled time $\tilde{t} = t\frac{\kappa}{\rho c_p}$ and source term $p = \frac{\sigma\dot{\varepsilon}}{\kappa}$

$$\frac{\partial T}{\partial \tilde{t}} - \frac{\partial^2 T}{\partial x^2} = \frac{\dot{q}}{\kappa} = \frac{\sigma\dot{\varepsilon}}{\kappa} \tag{I.4}$$

Where k is the thermal conductivity, ρ is the mass density, c_p is the specific heat capacity, σ is the yield strength of the material. $\dot{\varepsilon}$ is the strain rate. The parameters of the modified 9Cr-1Mo steel are listed as following:

k = 43W/mK
ρ = 7.9×10^3 kg/m^3
c_p= 0.49 kJ/kgK
σ= 900 MPa

Then the temperature increase in the modified 9Cr-1Mo steel during compression at specific strain rates can be estimated. Fig. I.1 shows the temperature increase in the samples during compression at strain rates of 5 s^{-1}, 1 s^{-1}, 0.1 s^{-1}, 0.01 s^{-1}, 0.001 s^{-1} and

0.0001 s^{-1}. It can be seen that the specimen is about 50 K above the room temperature during deformation at a strain rate of 0.1 s^{-1}, whereas under strain rate of 0.01 s^{-1}, the temperature is about 25 K. For the slowest strain rate used in this study (0.0001 s^{-1}), the increase in temperature is less than 4 K. It should be mentioned that all calculations are done with contact to same material, the grips are assumed to be infinitive and there is not heat transition coefficient which should reduce the out-flux.

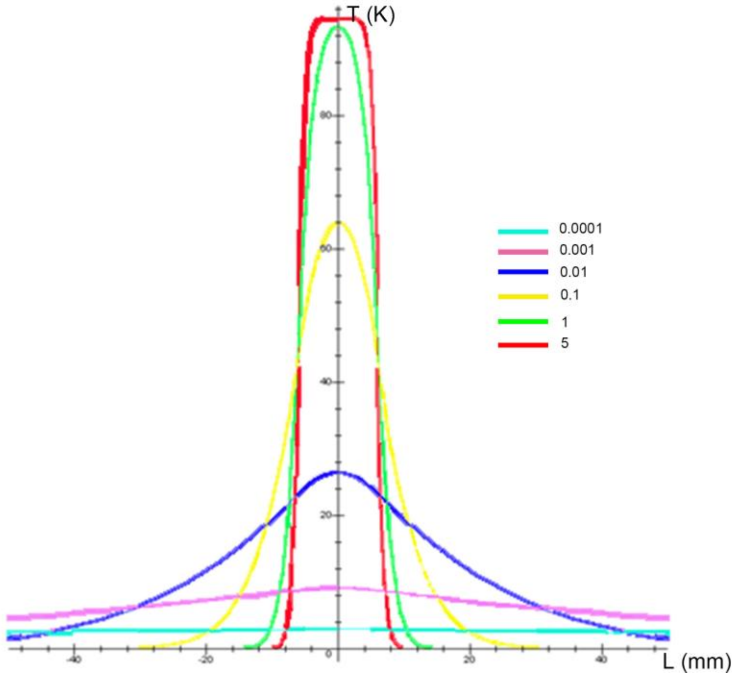

Fig. I.1 The increase in temperature of the modified 9Cr-1Mo steel after compression to a strain of 0.5 at strain rates of 5 s^{-1}, 1 s^{-1}, 0.1 s^{-1}, 0.01 s^{-1}, 0.001 s^{-1} and 0.0001 s^{-1}.

References

[1] Odette, G.R., Alinger, M.J., and Wirth, B.D., Recent developments in irradiation-resistant steels, Ann. Rev. Mater. Res. 2008. p. 471.

[2] Guerin, Y., Was, G.S., and Zinkle, S.J., Materials Challenges for Advanced Nuclear Energy Systems. MRS. Bull., 2009. 34 (1):10.

[3] Zinkle, S.J. and Was, G.S., Materials challenges in nuclear energy. Acta Mater., 2013. 61 (3):735.

[4] Klueh, R.L. and Bloom, E.E., The Development of Ferritic Steels for Fast Induced-Radioactivity Decay for Fusion-Reactor Applications. Nucl. Eng. Des., 1985. 2 (4):383.

[5] Klueh, R.L., Elevated temperature ferritic and martensitic steels and their application to future nuclear reactors. Int. Mater. Rev., 2005. 50 (5):287.

[6] Klueh, R.L. and Nelson, A.T., Ferritic/martensitic steels for next-generation reactors. J. Nucl. Mater., 2007. 371 (1-3):37.

[7] Ukai, S. and Fujiwara, M., Perspective of ODS alloys application in nuclear environments. J. Nucl. Mater., 2002. 307–311, Part 1 (0):749.

[8] Ukai, S., Nishida, T., Okada, H., Okuda, T., Fujiwara, M., and Asabe, K., Development of oxide dispersion strengthened ferritic steels for FBR core application .1. Improvement of mechanical properties by recrystallization processing. J. Nucl. Sci. Technol., 1997. 34 (3):256.

[9] Ukai, S., Nishida, T., Okuda, T., and Yoshitake, T., R&D of oxide dispersion strengthened ferritic martensitic steels for FBR. J. Nucl. Mater., 1998. 258:1745.

[10] Hansen, N., Mehl, R., and Medalist, A., New discoveries in deformed metals. Metall. Mater. Trans. A, 2001. 32 (12):2917.

[11] Bai, X.M., Voter, A.F., Hoagland, R.G., Nastasi, M., and Uberuaga, B.P., Efficient Annealing of Radiation Damage Near Grain Boundaries via Interstitial Emission. Science, 2010. 327 (5973):1631.

[12] Singh, B.N., Effect of Grain-Size on Void Formation during High-Energy Electron-Irradiation of Austenitic Stainless-Steel. Philos. Mag. A, 1974. 29 (1):25.

[13] Chimi, Y., Iwase, A., Ishikawa, N., Kobiyama, A., Inami, T., and Okuda, S., Accumulation and recovery of defects in ion-irradiated nanocrystalline gold. J. Nucl. Mater., 2001. 297 (3):355.

[14] Rose, M., Balogh, A.G., and Hahn, H., Instability of irradiation induced defects in nanostructured materials. Nucl. Instr. Meth. Phys., 1997. 127:119.

[15] Song, M., Wu, Y.D., Chen, D., Wang, X.M., Sun, C., Yu, K.Y., Chen, Y., Shao, L., Yang, Y., Hartwig, K.T., and Zhang, X., Response of equal channel angular extrusion processed ultrafine-grained T91 steel subjected to high temperature heavy ion irradiation. Acta Mater., 2014. 74 (0):285.

[16] Wang, Y., Chen, M., Zhou, F., and Ma, E., High tensile ductility in a nanostructured metal. Nature, 2002. 419 (6910):912.

[17] Song, M., Zhu, R., Foley, D.C., Sun, C., Chen, Y., Hartwig, K.T., and Zhang, X., Enhancement of strength and ductility in ultrafine-grained T91 steel through thermomechanical treatments. J. Mater. Sci., 2013. 48 (21):7360.

[18] Huang, F., Tao, N.R., and Lu, K., Effects of Strain Rate and Deformation Temperature on Microstructures and Hardness in Plastically Deformed Pure Aluminum. J.Mater.Sci.Techn, 2011. 27 (1):1.

[19] Odette, G.R., On Mechanisms Controlling Swelling in Ferritic and Martensitic Alloys. J. Nucl. Mater., 1988. 155:921.

[20] Kimura, A., Kasada, R., Morishita, K., Sugano, R., Hasegawa, A., Abe, K., Yamamoto, T., Matsui, H., Yoshida, N., Wirth, B.D., and Rubia, T.D., High resistance to helium embrittlement in reduced activation martensitic steels. J. Nucl. Mater., 2002. 307:521.

[21] Leslie, W.C., Iron and Its Dilute Substitutional Solid-Solutions. Metall. Trans., 1972. 3 (1):5.

[22] Viswanathan, R. and Bakker, W., Materials for ultrasupercritical coal power plants-boiler materials: Part 1. J. Mater. Eng. Perform., 2001. 10 (1):81.

[23] Viswanathan, R. and Bakker, W., Materials for ultrasupercritical coal power plants - Turbine materials: Part II. J. Mater. Eng. Perform., 2001. 10 (1):96.

[24] Swindeman, R.W., Santella, M.L., Maziasz, P.J., Roberts, B.W., and Coleman, K., Issues in replacing Cr-Mo steels and stainless steels with modified 9Cr-1Mo-V steel. Int. J. Pres. Ves. Pip., 2004. 81 (6):507.

[25] Gupta, G. and Was, G.S., Improved Creep Behavior of Ferritic-Martensitic Alloy T91 by Subgrain Boundary Density Enhancement. Metall. Mater. Trans. A, 2008. 39 (1):150.

[26] Klueh, R.L., Reduced-activation bainitic and martensitic steels for nuclear fusion applications. Curr.Opin.Solid State Mater.Sci., 2004. 8 (3-4):239.

[27] Salavy, J.F., Aiello, G., Aubert, P., Boccaccini, L.V., Daichendt, M., De Dinechin, G., Diegele, E., Giancarli, L.M., Lasser, R., Neuberger, H., Poitevin, Y., Stephan, Y., Rampal, G., and Rigal, E., Ferritic-Martensitic steel Test

Blanket Modules: Status and future needs for design criteria requirements and fabrication validation. J. Nucl. Mater., 2009. 386-88:922.

[28] Jitsukawa, S., Tamura, M., van der Schaaf, B., Klueh, R.L., Alamo, A., Petersen, C., Schirra, M., Spaetig, P., Odette, G.R., Tavassoli, A.A., Shiba, K., Kohyama, A., and Kimura, A., Development of an extensive database of mechanical and physical properties for reduced-activation martensitic steel F82H. J. Nucl. Mater., 2002. 307:179.

[29] Lindau, R. and Schirra, M., First results on the characterisation of the reduced-activation-ferritic-martensitic steel EUROFER. Fusion Eng. Des., 2001. 58-59:781.

[30] Huang, Q., Li, C., Li, Y., Chen, M., Zhang, M., Peng, L., Zhu, Z., Song, Y., and Gao, S., Progress in development of China Low Activation Martensitic Steel for fusion application. J. Nucl. Mater., 2007. 367:142.

[31] Dieter, G.E., Mechanical metallurgy. 1976: McGraw-Hill.

[32] Arzt, E., Overview no. 130 - Size effects in materials due to microstructural and dimensional constraints: A comparative review. Acta Mater., 1998. 46 (16):5611.

[33] Schroder, J.H. and Arzt, E., Weak Beam Studies of Dislocation Dispersoid Interaction in an Ods Superalloy. Scr. Metall., 1985. 19 (9):1129.

[34] Capdevila, C. and Bhadeshia, H., Manufacturing and microstructural evolution of mechanuically alloyed oxide dispersion strengthened superalloys. Adv. Eng. Mater., 2001. 3 (9):647.

[35] Benjamin, J.S., Dispersion Strengthened Superalloys by Mechanical Alloying. Metall. Trans., 1970. 1 (10):2943.

[36] Alinger, M.J., Odette, G.R., and Hoelzer, D.T., On the role of alloy composition and processing parameters in nanocluster formation and dispersion strengthening in nanostuctured ferritic alloys. Acta Mater., 2009. 57 (2):392.

[37] Miller, M.K., Kenik, E.A., Russell, K.F., Heatherly, L., Hoelzer, D.T., and Maziasz, P.J., Atom probe tomography of nanoscale particles in ODS ferritic alloys. Mater. Sci. Eng. A, 2003. 353 (1-2):140.

[38] Mukhopadhyay, D.K., Froes, F.H., and Gelles, D.S., Development of oxide dispersion strengthened ferritic steels for fusion. J. Nucl. Mater., 1998. 258:1209.

[39] Ukai, S., Yoshitake, T., Mizuta, S., Matsudaira, Y., Hagi, S., and Kobayashi, T., Preliminary tube manufacturing of oxide dispersion strengthened ferritic steels with recrystallized structure. J. Nucl. Sci. Technol., 1999. 36 (8):710.

[40] Chou, T.S. and Bhadeshia, H., Crystallographic texture in mechanically alloyed oxide dispersion-strengthened MA956 and MA957 steels. Metall. Trans. A, 1993. 24 (4):773.

[41] Chou, T.S. and Bhadeshia, H., Recrystallization temperatures in mechanically alloyed oxide-dispersion-strengthened MA956 and MA957 steels. Mater. Sci. Eng. A, 1994. 189 (1-2):229.

[42] Williams, C.A., Marquis, E.A., Cerezo, A., and Smith, G.D.W., Nanoscale characterisation of ODS-Eurofer 97 steel: An atom-probe tomography study. J. Nucl. Mater., 2010. 400 (1):37.

[43] Miller, M.K., Hoelzer, D.T., Kenik, E.A., and Russell, K.F., Stability of ferritic MA/ODS alloys at high temperatures. Intermetallics., 2005. 13 (3-4):387.

[44] Hirata, A., Fujita, T., Wen, Y.R., Schneibel, J.H., Liu, C.T., and Chen, M.W., Atomic structure of nanoclusters in oxide-dispersion-strengthened steels. Nature Mater., 2011. 10 (12):922.

[45] Wu, Y., Haney, E.M., Cunningham, N.J., and Odette, G.R., Transmission electron microscopy characterization of the nanofeatures in nanostructured ferritic alloy MA957. Acta Mater., 2012. 60 (8):3456.

[46] Ribis, J. and de Carlan, Y., Interfacial strained structure and orientation relationships of the nanosized oxide particles deduced from elasticity-driven morphology in oxide dispersion strengthened materials. Acta Mater., 2012. 60 (1):238.

[47] Hirata, A., Fujita, T., Liu, C.T., and Chen, M.W., Characterization of oxide nanoprecipitates in an oxide dispersion strengthened 14YWT steel using aberration-corrected STEM. Acta Mater., 2012. 60 (16):5686.

[48] Krautwasser, P., Czyrska-Filemonowicz, A., Widera, M., and Carsughi, F., Thermal stability of dispersoids in ferritic oxide-dispersion-strengthened alloys. Mater. Sci. Eng. A, 1994. 177 (1–2):199.

[49] Ackland, G., Controlling Radiation Damage. Science, 2010. 327 (5973):1587.

[50] Hull, D. and Bacon, D.J., Introduction to Dislocations. 2001: Elsevier Science.

[51] Kuhlmann-Wilsdorf, D. and Hansen, N., Geometrically necessary, incidental and subgrain boundaries. Scr. Metall., 1991. 25 (7):1557.

[52] Hansen, N. and Jensen, D.J., Deformed metals - structure, recrystallisation and strength. Mater. Sci. Technol., 2011. 27 (8):1229.

[53] Li, B.L., Godfrey, A., Meng, Q.C., Liu, Q., and Hansen, N., Microstructural evolution of IF-steel during cold rolling. Acta Mater., 2004. 52 (4):1069.

[54] Huang, X., Kamikawa, N., and Hansen, N., Strengthening mechanisms and optimization of structure and properties in a nanostructured IF steel. J. Mater. Sci., 2010. 45 (17):4761.

[55] Hughes, D.A. and Hansen, N., Microstructure and strength of nickel at large strains. Acta Mater., 2000. 48 (11):2985.

[56] Godfrey, A. and Liu, Q., Stored energy and structure in top-down processed nanostructured metals. Scripta Mater., 2009. 60 (12):1050.

[57] Huang, X. and Hansen, N., Grain orientation dependence of microstructure in aluminium deformed in tension. Scripta Mater., 1997. 37 (1):1.

[58] Huang, X. and Winther, G., Dislocation structures. Part I. Grain orientation dependence. Philos. Mag. A, 2007. 87 (33):5189.

[59] Hansen, N., Huang, X., Pantleon, W., and Winther, G., Grain orientation and dislocation patterns. Philos. Mag. A, 2006. 86 (25-26):3981.

[60] Le, G.M., Godfrey, A., Hong, C.S., Huang, X., and Winther, G., Orientation dependence of the deformation microstructure in compressed aluminum. Scripta Mater., 2012. 66 (6):359.

[61] Haldar, A., Huang, X., Leffers, T., Hansen, N., and Ray, R.K., Grain orientation dependence of microstructures in a warm rolled IF steel. Acta Mater., 2004. 52 (18):5405.

[62] Winther, G. and Huang, X., Dislocation structures. Part II. Slip system dependence. Philos. Mag. A, 2007. 87 (33):5215.

[63] Raabe, D. and Lucke, K., Textures of Ferritic Stainless-Steels. Mater. Sci. Technol., 1993. 9 (4):302.

[64] Hosford, W.F., Mechanical Behavior of Materials. 2005: Cambridge University Press.

[65] Dillamore, I.L., Katoh, H., and Haslam, K., The Nucleation of Recrystallisation and the Development of Textures in Heavily Compressed Iron-Carbon Alloys. Texture, 1974. 1 (3):151.

[66] Valiev, R.Z. and Langdon, T.G., Principles of equal-channel angular pressing as a processing tool for grain refinement. Prog. Mater. Sci., 2006. 51 (7):881.

[67] Vorhauer, A. and Pippan, R., On the homogeneity of deformation by high pressure torsion. Scripta Mater., 2004. 51 (9):921.

[68] Saito, Y., Utsunomiya, H., Tsuji, N., and Sakai, T., Novel ultra-high straining process for bulk materials - Development of the accumulative roll-bonding (ARB) process. Acta Mater., 1999. 47 (2):579.

[69] Kocks, U.F., Laws for work-hardening and low-temperature creep. J. Eng. Mater. Technol. ASME, 1976. 98 (1):76.

[70] Kocks, U.F., Argon, A.S., and Ashby, M.F., Thermodynamics and kinetics of slip. Prog. Mater. Sci., 1975. 19:1.

[71] Li, Y.S., Tao, N.R., and Lu, K., Microstructural evolution and nanostructure formation in copper during dynamic plastic deformation at cryogenic temperatures. Acta Mater., 2008. 56 (2):230.

[72] Huang, F., Tao, N.R., and Lu, K., Effects of Impurity on Microstructure and Hardness in Pure Al Subjected to Dynamic Plastic Deformation at Cryogenic Temperature. J.Mater.Sci.Techn, 2011. 27 (7):628.

[73] Ashby, M.F., Deformation of plastically non-homogeneous materials. Philos. Mag. A, 1970. 21 (170):399.

[74] Liu, X.C., Zhang, H.W., and Lu, K., Strain-Induced Ultrahard and Ultrastable Nanolaminated Structure in Nickel. Science, 2013. 342 (6156):337.

[75] Martin, J.W., Micromechanisms in Particle-Hardened Alloys. 1980: Cambridge University Press.

[76] Humphreys, F.J. and Hirsch, P.B., Work-Hardening and Recovery of Dispersion Hardened Alloys. Philos. Mag. A, 1976. 34 (3):373.

[77] Bahk, S. and Ashby, M.F., Stored energy of cold work in internally oxidized copper, and some of its consequences. Scr. Metall., 1975. 9 (2):129.

[78] Humphreys, F.J. and Hatherly, M., Recrystallization and Related Annealing Phenomena (Second Edition). 2004, Oxford: Elsevier.

[79] Lewis, M.H. and Martin, J.W., The Effect of Internal Oxidation on the Structure of Some Deformed Copper Alloys. J. Electrochem. Soc., 1963. 110 (3):C62.

[80] Hansen, N. and Bay, B., Effect of particle content, particle distribution and cold deformation on recrystallization of low oxide Al-Al_2O_3 products. J. Mater. Sci., 1972. 7 (12):1351.

[81] Barlow, C.Y. and Hansen, N., Deformation Structures in Aluminum Containing Small Particles. Acta Metall., 1989. 37 (5):1313.

[82] Barlow, C.Y., Hansen, N., and Liu, Y.L., Fine scale structures from deformation of aluminium containing small alumina particles. Acta Mater., 2002. 50 (1):171.

[83] Humphreys, F.J., Local Lattice Rotations at 2nd Phase Particles in Deformed Metals. Acta Metall., 1979. 27 (12):1801.

[84] Doherty, R.D., Hughes, D.A., Humphreys, F.J., Jonas, J.J., Jensen, D.J., Kassner, M.E., King, W.E., McNelley, T.R., McQueen, H.J., and Rollett, A.D., Current issues in recrystallization: a review. Mater. Sci. Eng. A, 1997. 238 (2):219.

[85] Lian, J., Valiev, R.Z., and Baudelet, B., On the enhanced grain growth in ultrafine grained metals. Acta Metall., 1995. 43 (11):4165.

[86] Yu, T.B., Hansen, N., and Huang, X.X., Recovery by triple junction motion in aluminium deformed to ultrahigh strains. Proc. R. Soc. London, Ser. A, 2011. 467 (2135):3039.

[87] Ridha, A.A. and Hutchinson, W.B., Recrystallization mechanisms and the origin of cube texture in copper. Acta Metall., 1982. 30 (10):1929.

[88] Doherty, R.D., Recrystallization and texture. Prog. Mater. Sci., 1997. 42 (1-4):39.

[89] Oyarzabal, M., Martinez-De-Guerenu, A., and Gutierrez, I., Effect of stored energy and recovery on the overall recrystallization kinetics of a cold rolled low carbon steel. Mater. Sci. Eng. A, 2008. 485 (1-2):200.

[90] Khatirkar, R., Vadavadagi, B., Shekhawat, S.K., Haldar, A., and Samajdar, I., Orientation Dependent Recovery in Interstitial Free Steel. ISIJ Int., 2012. 52 (5):884.

[91] Khatirkar, R., Kestens, L.A.I., Petrov, R., and Samajdar, I., Controlled Warm Working: Possible Tool for Optimizing Stored Energy Advantage in Deformed gamma-fiber (ND//< 111 >). ISIJ Int., 2009. 49 (1):78.

[92] Martinez-de-Guerenu, A., Arizti, F., Diaz-Fuentes, M., and Gutierrez, I., Recovery during annealing in a cold rolled low carbon steel. Part 1: Kinetics and microstructural characterization. Acta Mater., 2004. 52 (12):3657.

[93] Humphreys, F.J., Nucleation of recrystallization at 2nd phase particles in deformed aluminum. Acta Metall., 1977. 25 (11):1323.

[94] Doherty, R.D. and Martin, J.W., Effect of a dispersed second phase on recrystallization of aluminium-copper alloys. J. Inst. Met., 1963. 91 (10):332.

[95] Hansen, N. and Bay, B., Effect of particle-size on recrystallization temperature of dispersion-strengthened aluminum aluminium-oxide alloys. Scr. Metall., 1974. 8 (11):1291.

[96] Humphrey.Fj and Martin, J.W., Effect of dispersed silica particles on recovery and recrystallization of deformed copper crystals. Acta Metall., 1966. 14 (6):775.

[97] Humphrey.Fj and Martin, J.W., Effect of dispersed phases upon annealing behaviour of plastically deformed copper crystals. Philos. Mag. A, 1968. 17 (146):365.

[98] Mandal, D. and Baker, I., On the effect of fine second-phase particles on primary recrystallization as a function of strain. Acta Mater., 1997. 45 (2):453.

[99] Mishin, O.V., Godfrey, A., Juul Jensen, D., and Hansen, N., Recovery and recrystallization in commercial purity aluminum cold rolled to an ultrahigh strain. Acta Mater., 2013. 61 (14):5354.

[100] Hart, E.W., Theory of the tensile test. Acta Metall., 1967. 15 (2):351.

[101] Yan, F.K., Liu, G.Z., Tao, N.R., and Lu, K., Strength and ductility of 316L austenitic stainless steel strengthened by nano-scale twin bundles. Acta Mater., 2012. 60 (3):1059.

[102] Schneibel, J.H., Heilmaier, M., Blum, W., Hasemann, G., and Shanmugasundaram, T., Temperature dependence of the strength of fine- and ultrafine-grained materials. Acta Mater., 2011. 59 (3):1300.

[103] Capdevila, C., Chen, Y.L., Lassen, N.C.K., Jones, A.R., and Bhadeshia, H., Heterogeneous deformation and recrystallisation of iron base oxide dispersion strengthened PM2000 alloy. Mater. Sci. Technol., 2001. 17 (6):693.

[104] Humphreys, F.J., Review - Grain and subgrain characterisation by electron backscatter diffraction. J. Mater. Sci., 2001. 36 (16):3833.

[105] Wu, G.L. and Jensen, D.J., Automatic determination of recrystallization parameters based on EBSD mapping. Mater. Charact., 2008. 59 (6):794.

[106] Christiansen, G., Bowen, J.R., and Lindbo, J., Electrolytic preparation of metallic thin foils with large electron-transparent regions. Mater. Charact., 2002. 49 (4):331.

[107] Kurdjumow, G. and Sachs, G., About the mechanism of hardening steel. Z.Phys, 1930. 64 (5-6):325.

[108] Morito, S., Tanaka, H., Konishi, R., Furuhara, T., and Maki, T., The morphology and crystallography of lath martensite in Fe-C alloys. Acta Mater., 2003. 51 (6):1789.

[109] Kitahara, H., Ueji, R., Tsuji, N., and Minamino, Y., Crystallographic features of lath martensite in low-carbon steel. Acta Mater., 2006. 54 (5):1279.

[110] Lojkowski, W., Djahanbakhsh, M., Burkle, G., Gierlotka, S., Zielinski, W., and Fecht, H.J., Nanostructure formation on the surface of railway tracks. Mater. Sci. Eng. A, 2001. 303 (1-2):197.

[111] Gridnev, V.N. and Gavrilyuk, V.G., Cementite decomposition in steel under plastic-deformation (a review). Phys. Met., 1982. 4 (3):531.

[112] Song, M., Sun, C., Jang, J., Han, C.H., Kim, T.K., Hartwig, K.T., and Zhang, X., Microstructure refinement and strengthening mechanisms of a 12Cr ODS steel processed by equal channel angular extrusion. J. Alloy. Compd., 2013. 577 (0):247.

[113] Mishin, O.V., Östensson, L., and Godfrey, A., Comparative microstructural characterization of a friction-stir-welded aluminum alloy using TEM and SEM-based techniques. Metall. Mater. Trans. A, 2006. 37 (2):489.

[114] Hosford, W.F., The Mechanics of Crystals and Textured Polycrystals. Oxford Engineering Science Series. 1993: Oxford University Press.

[115] Rosenber, J.M. and Piehler, H.R., Calculation of Taylor factor and lattice rotations for *bcc* metals deforming by pencil glide. Metall. Trans., 1971. 2 (1):257.

[116] Godfrey, A., Cao, W.Q., Hansen, N., and Liu, Q., Stored energy, microstructure, and flow stress of deformed metals. Metall. Mater. Trans.A, 2005. 36A (9):2371.

[117] Read, W.T. and Shockley, W., Dislocation models of crystal grain boundaries. Phys. Rev., 1950. 78 (3):275.

[118] Murr, L.E., Interfacial Phenomena in Metals and Alloys. 1975: Addison-Wesley Educational Publishers Inc.

[119] Huang, X., Morito, S., Hansen, N., and Maki, T., Ultrafine Structure and High Strength in Cold-Rolled Martensite. Metall. Mater. Trans.A, 2012. 43A (10):3517.

[120] Ueji, R., Tsuji, N., Minamino, Y., and Koizumi, Y., Ultragrain refinement of plain low carbon steel by cold-rolling and annealing of martensite. Acta Mater., 2002. 50 (16):4177.

[121] Ueji, R., Tsuji, N., Minamino, Y., Koizumi, Y., and Saito, Y., Mechanical properties of nano-structured plain low-carbon steels produced by conventional cold-rolling and annealing of martensite starting microstructure. Ultrafine Grained Materials Ii, 2002:399.

[122] Ueji, R., Tsuji, N., Minamino, Y., and Koizumi, Y., Effect of rolling reduction on ultrafine grained structure and mechanical properties of low-carbon steel thermomechanically processed from martensite starting structure. Sci. Technol. Adv. Mater., 2004. 5 (1-2):153.

[123] Yu, T., Hansen, N., Huang, X., and Godfrey, A., Observation of a New Mechanism Balancing Hardening and Softening in Metals. Mater. Res. Lett., 2014. 2 (3):160.

[124] Alfonso, A., Juul Jensen, D., Luo, G.N., and Pantleon, W., Recrystallization kinetics of warm-rolled tungsten in the temperature range 1150–1350°C. J. Nucl. Mater., 2014. 455 (1–3):591.

[125] Hu, H., Texture of metals. Texture, 1974. 1:26.

[126] Dillamore, I.L. and Katoh, H., The Mechanisms of Recrystallization in Cubic Metals with Particular Reference to Their Orientation-Dependence. Metal Sci., 1974. 8 (1):73.

[127] Samajdar, I., Verlinden, B., Van Houtte, P., and Vanderschueren, D., gamma-fibre recrystallization texture in IF-steel: an investigation on the recrystallization mechanisms. Mater. Sci. Eng. A, 1997. 238 (2):343.

[128] Hutchinson, B. and Ryde, L. Mechanisms, kinetics and crystallography of recrystallization in cold rolled steels. in 16th Risø International Symposium on Materials Science: Microstructure and Crystallographic Aspects of Recrystallization. 1995. Roskilde, Denmark: Risø National Laboratory.

[129] Park, J.T. and Szpunar, J.A., Evolution of recrystallization texture in nonoriented electrical steels. Acta Mater., 2005. 51 (11):3037.

[130] Sanchez-Araiza, M., Godet, S., Jacques, P.J., and Jonas, J.J., Texture evolution during the recrystallization of a warm-rolled low-carbon steel. Acta Mater., 2006. 54 (11):3085.

[131] Dillamore, I.L., Smith, C.J.E., and Watson, T.W., Oriented Nucleation in the Formation of Annealing Textures in Iron. Metal Sci., 1967. 1 (1):49.

[132] Every, R.L. and Hatherly, M., Oriented Nucleation in Low-Carbon Steels. Texture, 1974. 1 (3):183.

[133] Li, X.L., Liu, W., Godfrey, A., Jensen, D.J., and Liu, Q., Development of the cube texture at low annealing temperatures in highly rolled pure nickel. Acta Mater., 2007. 55 (10):3531.

[134] Magnusson, H., Jensen, D.J., and Hutchinsson, B., Growth rates for different texture components during recrystallization of if steel. Scr. Mater., 2001. 44 (3):435.

[135] Raabe, D. and Lucke, K., Rolling and Annealing Textures of *bcc* Metals. Proceedings of the 10th International Conference on Textures of Materials, Pts 1 and 2 - ICTOM-10, 1994. 157-:597.

[136] Jensen, D.J., Growth of nuclei with different crystallographic orientations during recrystallization. Scr. Metall., 1992. 27 (5):533.

[137] Cahn, J.W. and Hagel, W.C., Divergent Pearlite in a Manganese Eutectoid Steel. Acta Metall., 1963. 11 (6):561.

[138] Fan, G.H., Zhang, Y.B., Driver, J.H., and Jensen, D.J., Oriented growth during recrystallization revisited in three dimensions. Scr. Mater., 2014. 72-73:9.

[139] BS EN 10088-1, Elevated temperature physical properties of steel. 2005

[140] Kocks, U.F. and Mecking, H., Physics and phenomenology of strain hardening: the FCC case. Prog. Mater. Sci., 2003. 48 (3):171.

[141] Hsu, H., Texture, 1974. 1.

[142] Luo, Z.P., Mishin, O.V., Zhang, Y.B., Zhang, H.W., and Lu, K., Microstructural characterization of nickel subjected to dynamic plastic deformation. Scr. Mater., 2012. 66 (6):335.

[143] Fan, Z.Q., Hao, T., Zhao, S.X., Luo, G.N., Liu, C.S., and Fang, Q.F., The microstructure and mechanical properties of T91 steel processed by ECAP at room temperature. J. Nucl. Mater., 2013. 434 (1-3):417.

[144] Hao, T., Fan, Z.Q., Zhao, S.X., Luo, G.N., Liu, C.S., and Fang, Q.F., Strengthening mechanism and thermal stability of severely deformed ferritic/martensitic steel. Mater. Sci. Eng. A, 2014. 596:244.

[145] Gray, G.T., High-Strain-Rate Deformation: Mechanical Behavior and Deformation Substructures Induced. Ann. Rev. Mater. Res., 2012. 42:285.

[146] Darken, L.S. and Gurry, R.W., Physical chemistry of metals. 1953, New York: McGraw-Hill.

[147] Klimenkov, M., Moslang, A., and Lindau, R., EELS analysis of complex precipitates in PM 2000 steel. Eur. Phys. J-appl. Phys, 2008. 42 (3):293.

[148] Klimiankou, M., Lindau, R., Moslang, A., and Schroder, J., TEM study of PM2000 steel. Powder Metall., 2005. 48 (3):277.

[149] Shen, Y.Z., Zou, T.T., Zhang, S., and Sheng, L.Z., Identification of Oxide Phases in Oxide Dispersion Strengthened PM2000 Steel. ISIJ Int., 2013. 53 (2):304.

[150] Fabrichnaya, O., Seifert, H.J., Ludwig, T., Aldinger, F., and Navrotsky, A., The assessment of thermodynamic parameters in the Al_2O_3-Y_2O_3 system and phase relations in the Y-Al-O system. Scand. J. Metall., 2001. 30 (3):175.

[151] Hsiung, L.L., Fluss, M.J., and Kimura, A., Structure of oxide nanoparticles in Fe-16Cr MA/ODS ferritic steel. Mater. Lett., 2010. 64 (16):1782.

[152] Lee, J.H. and Kim, J.H., Characterization of Oxide Nanoparticles in Al-Free and Al-Containing Oxide Dispersion Strengthened Ferritic Steels. J.NanoNanotechnol., 2013. 13 (9):6169.

[153] Dou, P., Kimura, A., Kasada, R., Okuda, T., Inoue, M., Ukai, S., Ohnuki, S., Fujisawa, T., and Abe, F., TEM and HRTEM study of oxide particles in an Al-alloyed high-Cr oxide dispersion strengthened steel with Zr addition. J. Nucl. Mater., 2014. 444 (1-3):441.

[154] Zhang, C.H., Kimura, A., Kasada, R., Jang, J., Kishimoto, H., and Yang, Y.T., Characterization of the oxide particles in Al-added high-Cr ODS ferritic steels. J. Nucl. Mater., 2011. 417 (1-3):221.

[155] Hsiung, L.L., Fluss, M.J., Tumey, S.J., Choi, B.W., Serruys, Y., Willaime, F., and Kimura, A., Formation mechanism and the role of nanoparticles in Fe-Cr ODS steels developed for radiation tolerance. Phys. Rev. B, 2010. 82 (18).

[156] Dou, P., Kimura, A., Okuda, T., Inoue, M., Ukai, S., Ohnuki, S., Fujisawa, T., and Abe, F., Polymorphic and coherency transition of Y-Al complex oxide particles with extrusion temperature in an Al-alloyed high-Cr oxide dispersion strengthened ferritic steel. Acta Mater., 2011. 59 (3):992.

[157] Chen, C.L., Tatlock, G.J., and Jones, A.R., Effect of annealing temperatures on the secondary re-crystallization of extruded PM2000 steel bar. J. Microscopy, 2009. 233 (3):474.

[158] Capdevila, C., Toda-Caraballo, I., Pimentel, G., and Chao, J., Influence of plastic deformation on recrystallized microstructure of Fe-base ods alloy. Met. Mater-int., 2012. 18 (5):799.

[159] Chou, T.S. and Bhadeshia, H., Grain control in mechanically alloyed oxide dispersion-strengthened MA-957 steel. Mater. Sci. Technol., 1993. 9 (10):890.

[160] Capdevila, C., Chen, Y.L., Jones, A.R., and Bhadeshia, H., Grain boundary mobility in Fe-base oxide dispersion strengthened PM2000 alloy. ISIJ Int., 2003. 43 (5):777.

[161] Miller, M.K., Hoelzer, D.T., Kenik, E.A., and Russell, K.F., Stability of ferritic MA/ODS alloys at high temperatures. Intermetallics., 2005. 13 (3–4):387.

[162] Mao, X., Kim, T.K., Kim, S.S., Oh, K.H., and Jang, J., Thermal stability of oxide particles in 12Cr ODS steel. J. Nucl. Mater., 2012. 428 (1-3):82.

[163] Alinger, M.J., On the formation and stability of nanometer scale precipitates in ferritic alloys during processing and high temperature service. PhD thesis. Univ. Calif., Santa Barbara, 2004.

[164] Howe, J.M., Interfaces in materials: atomic structure, thermodynamics and kinetics of solid-vapor, solid-liquid and solid-solid interfaces. 1997: Wiley.

[165] Krumm, J. and Shafer, S.A., A Sampled-grating Model of Moire Patterns from Digital Imaging. 1989: Carnegie Mellon University, the Robotics Institute.

[166] Creath, K. and Wyant, J.C., Moire and fringe projection techniques, in Optical Shop Testing, 2nd Edition, D. Malacara, Editor. 1992, Wiley: New York.

[167] Read, H.G., Murakami, H., and Hono, K., Al partitioning in MA 956, an ODS ferritic stainless steel. Scr. Mater., 1997. 36 (3):355.

[168] Hosemann, P., Thau, H.T., Johnson, A.L., Maloy, S.A., and Li, N., Corrosion of ODS steels in lead-bismuth eutectic. J. Nucl. Mater., 2008. 373 (1-3):246.

[169] Takaya, S., Furukawa, T., Aoto, K., Muller, G., Weisenburger, A., Heinzel, A., Inoue, M., Okuda, T., Abe, F., Ohnuki, S., Fujisawa, T., and Kimura, A., Corrosion behavior of Al-alloying high Cr-ODS steels in lead-bismuth eutectic. J. Nucl. Mater., 2009. 386-88:507.

[170] Takaya, S., Furukawa, T., Inoue, M., Fujisawa, T., Okuda, T., Abe, F., Ohnuki, S., and Kimura, A., Corrosion resistance of Al-alloying high Cr-ODS steels in stagnant lead-bismuth. J. Nucl. Mater., 2010. 398 (1-3):132.

[171] Hsiung, L.L., Fluss, M.J., Tumey, S.J., Choi, B.W., Serruys, Y., Willaime, F., and Kimura, A., Formation mechanism and the role of nanoparticles in Fe-Cr ODS steels developed for radiation tolerance. Phys. Rev. B, 2010. 82 (18):184103.

[172] Voorhees, P.W., Mcfadden, G.B., and Johnson, W.C., On the Morphological Development of 2nd-Phase Particles in Elastically-Stressed Solids. Acta Metall., 1992. 40 (11):2979.

[173] Maheshwari, A. and Ardell, A.J., Morphological Evolution of Coherent Misfitting Precipitates in Anisotropic Elastic Media. Phys. Rev. Lett., 1993. 70 (15):2305.

[174] Ardell, A.J. and Nicholso.Rb, On Modulated Structure of Aged Ni-Al Alloys. Acta Metall., 1966. 14 (10):1295.

[175] Onaka, S., Kobayashi, N., Fujii, T., and Kato, M., Energy analysis with a superspherical shape approximation on the spherical to cubical shape transitions of coherent precipitates in cubic materials. Mater. Sci. Eng. A, 2003. 347 (1-2):42.

[176] Wert, J.A., Huang, X., and Inoko, F., Deformation bands in a [110] aluminium single crystal strained in tension. Proc. R. Soc. London, Ser. A, 2003. 459 (2029):85.

[177] Chin, G.Y. and Wonsiewi.Bc, Deformation Banding and Stability of (100)-(111) Fiber Textures of Fcc Metals. Trans. Metall. Soc. AIME, 1969. 245 (4):871.

[178] Lee, C.S., Duggan, B.J., and Smallman, R.E., A Theory of Deformation Banding in Cold-Rolling. Acta Metall. 1993. 41 (8):2265.

[179] Sawkill, J. and Honeycombe, R.W.K., Strain Hardening in Face-Centred Cubic Metal Crystals. Acta Metall., 1954. 2 (6):854.

[180] Lee, C.S., Duggan, B.J., and Smallman, R.E., Deformation Banding in Copper. Phil. Mag. Lett., 1993. 68 (4):185.

[181] Wonsiewi.Bc and Chin, G.Y., Inhomogeneity of Plastic Flow in Plane Strain Compression of (111) [112] Crystals. J. Metal, 1969. 21 (3):A19.

[182] Zhu, L., Seefeldt, M., and Verlinden, B., Deformation banding in a Nb polycrystal deformed by successive compression tests. Acta Mater., 2012. 60 (10):4349.

[183] Dorner, D., Adachi, Y., and Tsuzaki, K., Periodic crystal lattice rotation in microband groups in a *bcc* metal. Scr. Mater., 2007. 57 (8):775.

[184] Dorner, D., Adachi, Y., and Tsuzaki, K., Slip system partitioning as a possible mechanism for ultrafine grain formation in Fe-3%Si bicrystals. ISIJ Int., 2008. 48 (8):1102.

[185] Han, W.Z., Demkowicz, M.J., Mara, N.A., Fu, E.G., Sinha, S., Rollett, A.D., Wang, Y.Q., Carpenter, J.S., Beyerlein, I.J., and Misra, A., Design of Radiation Tolerant Materials Via Interface Engineering. Adv. Mater., 2013. 25 (48):6975.

[186] Huang, Z., Feng, J., and Pan, W., First-principles calculations of mechanical and thermodynamic properties of YAlO3. Comp. Mater. Sci., 2011. 50 (10):3056.

[187] Pugh, S.F., Relations between the elastic moduli and the plastic properties of polycrystalline pure metals. Philos. Mag. A, 1954. 45 (367):823.

[188] Ardell, A.J., Precipitation hardening. Metall. Trans. A, 1985. 16 (12):2131.

[189] Callister, W.D., Fundamentals of Materials Science and Engineering. 2004: Wiley.

[190] Agon, A.S., ed. Plastic deformation of inhomogeneous metals. Physical Metallurgy Fourth Edition, ed. R.W. Cahn. 1996.

[191] Eshelby, J.D., The determination of the elastic field of an ellipsoidal inclusion, and related problems. Proc. Roy. Soc.A, 1957. 241 (1226):376.

[192] Song, M., Sun, C., Jang, J., Han, C.H., Kim, T.K., Hartwig, K.T., and Zhang, X., Microstructure refinement and strengthening mechanisms of a 12Cr ODS steel processed by equal channel angular extrusion. J. Alloy. Compd., 2013. 577:247.

[193] Takahashi, A. and Sato, S., Discrete dislocation plasticity analysis of dispersion strengthening in oxide dispersion strengthened (ODS) steels. J. of Central South Uni., 2014. 21 (4):1249.

[194] White, E.A.D., Twinning in barium titanate crystals. Acta Crystall., 1955. 8 (12):845.

[195] Calleja, M., Dove, M.T., and Salje, E.K.H., Trapping of oxygen vacancies on twin walls of $CaTiO_3$: a computer simulation study. J. Phys-Condens. Mat., 2003. 15 (14):2301.

[196] Buckley, A., Rivera, J.P., and Salje, E.K.H., Twin structures in tetragonal $SrTiO_3$: The ferroelastic phase transition and the formation of needle domains. J. Appl. Phys., 1999. 86 (3):1653.

[197] Wang, Y.B., Guyot, F., Yeganehhaeri, A., and Liebermann, R.C., Twinning in $MgSiO_3$ perovskite. Science, 1990. 248 (4954):468.

[198] Wang, W.-L. and Lu, H.-Y., 〈111〉 Rotation Twins in an Orthorhombic $LaGaO_3$ Perovskite. J. Am. Ceram. Soc., 2007. 90 (1):264.

[199] Gaillard, Y., Macias, A.H., Munoz-Saldana, J., Anglada, M., and Trapaga, G., Nanoindentation of $BaTiO_3$: dislocation nucleation and mechanical twinning. J. Phys. D, 2009. 42 (8).

[200] Wang, Z.C., Dupas-Bruzek, C., and Karato, S., High temperature creep of an orthorhombic perovskite - YAlO3. Phys. Earth. Planet. In, 1999. 110 (1-2):51.

[201] Besson, P., Poirier, J.P., and Price, G.D., Dislocations in $CaTiO_3$ perovskite deformed at high-temperature: A transmission electron microscopy study. Phys. Chem. Miner., 1996. 23 (6):337.

[202] Wang, Z.C., Karato, S., and Fujino, K., High-Temperature Creep of Single-Crystal Strontium-Titanate ($SrTiO_3$) - a Contribution to Creep Systematics in Perovskites. Phys. Earth. Planet. In, 1993. 79 (3-4):299.

[203] Yu, Q., Shan, Z.W., Li, J., Huang, X.X., Xiao, L., Sun, J., and Ma, E., Strong crystal size effect on deformation twinning. Nature, 2010. 463 (7279):335.

[204] Zheng, H., Cao, A.J., Weinberger, C.R., Huang, J.Y., Du, K., Wang, J.B., Ma, Y.Y., Xia, Y.N., and Mao, S.X., Discrete plasticity in sub-10-nm-sized gold crystals. Nat. Commun., 2010. 1.

[205] Uchic, M.D., Dimiduk, D.M., Florando, J.N., and Nix, W.D., Sample dimensions influence strength and crystal plasticity. Science, 2004. 305 (5686):986.

[206] Greer, J.R. and Nix, W.D., Nanoscale gold pillars strengthened through dislocation starvation. Phys. Rev. B, 2006. 73 (24).

[207] Shan, Z.W., Mishra, R.K., Asif, S.A.S., Warren, O.L., and Minor, A.M., Mechanical annealing and source-limited deformation in submicrometre-diameter Ni crystals. Nat. Mater., 2008. 7 (2):115.

[208] Zhang, N., Deng, Q.A., Hong, Y., Xiong, L.M., Li, S., Strasberg, M., Yin, W.Q., Zou, Y.J., Taylor, C.R., Sawyer, G., and Chen, Y.P., Deformation mechanisms in silicon nanoparticles. J. Appl. Phys., 2011. 109 (6).

[209] Gerberich, W.W., Michler, J., Mook, W.M., Ghisleni, R., Ostlund, F., Stauffer, D.D., and Ballarini, R., Scale effects for strength, ductility, and toughness in "brittle" materials. J. Mater. Res., 2009. 24 (3):898.

[210] Han, X., Zheng, K., Zhang, Y., Zhang, X., Zhang, Z., and Wang, Z.L., Low-temperature in situ large-strain plasticity of silicon nanowires. Adv. Mater., 2007. 19 (16):2112.

[211] Chrobak, D., Tymiak, N., Beaber, A., Ugurlu, O., Gerberich, W.W., and Nowak, R., Deconfinement leads to changes in the nanoscale plasticity of silicon. Nat. Nanotechnol., 2011. 6 (8):480.

[212] Han, X.D., Zhang, Y.F., Zheng, K., Zhang, X.N., Zhang, Z., Hao, Y.J., Guo, X.Y., Yuan, J., and Wang, Z.L., Low-temperature in situ large strain plasticity of ceramic SiC nanowires and its atomic-scale mechanism. Nano Lett., 2007. 7 (2):452.

[213] Thomas, H. and Müller, K.A., Structural Phase Transitions in Perovskite-Type Crystals. Phys. Rev. Lett., 1968. 21 (17):1256.

[214] Wu, X., Qin, S., and Wu, Z.Y., Generalized gradient approximation calculations of the pressure-induced phase transition of YAlO3 perovskite. J. Phys-Condens. Mat., 2006. 18 (16):3907.

[215] Gove, K.B. and Charles, J.A., Further aspects of inclusion deformation. Met. Technol., 1974. 1 (1):425.

[216] Baker, T.J., Gave, K.B., and Charles, J.A., Inclusion deformation and toughness anisotropy in hot-rolled steels. Met. Technol., 1976. 3 (1):183.

[217] Waudby, P.E., Salter, W.J.M., and Pickerin.Fb, Study of reaction between silicate inclusions and aluminum in molten iron. J. Iron Steel Inst., 1973. 211 (JUL):486.

[218] Luo, C., Evolution of voids close to an inclusion in hot deformation of metals. Comp. Mater. Sci., 2001. 21 (3):360.

[219] Ukai, S., Harada, M., Okada, H., Inoue, M., Nomura, S., Shikakura, S., Asabe, K., Nishida, T., and Fujiwara, M., Alloying Design of Oxide Dispersion-Strengthened Ferritic Steel for Long-Life Fbrs Core Materials. J. Nucl. Mater., 1993. 204:65.

DTU Vindenergi er et institut under Danmarks Tekniske Universitet med en unik integration af forskning, uddannelse, innovation og offentlige/private konsulentopgaver inden for vindenergi. Vores aktiviteter bidrager til nye muligheder og teknologier inden for udnyttelse af vindenergi, både globalt og nationalt. Forskningen har fokus på specifikke tekniske og videnskabelige områder, der er centrale for udvikling, innovation og brug af vindenergi, og som danner grundlaget for højt kvalificerede uddannelser på universitetet.

Vi har mere end 240 ansatte og heraf er ca. 60 ph.d. studerende. Forskningen tager udgangspunkt i ni forskningsprogrammer, der er organiseret i tre hovedgrupper: vindenergisystemer, vindmølleteknologi og grundlag for vindenergi.

Danmarks Tekniske Universitet
DTU Vindenergi
Nils Koppels Allé
Bygning 403
2800 Kgs. Lyngby
Telefon45 25 25 25

info@vindenergi.dtu.dk
www.vindenergi.dtu.dk